THE UNIVERSITY of EDINBURGH

Title	On the host galaxies of quasars
Author	Floyd, David James Elford.
Qualification	PhD
Year	2004

Digitisation Notes:

- pages xx, xxi missing from original. Pages 154, 196 are blank - not scanned

On The Host Galaxies of Quasars

DAVID JAMES ELFORD FLOYD

Institute for Astronomy

School of Physics

A thesis submitted to the University of Edinburgh

for the degree of Doctor of Philosophy

April 2004

Abstract

I present the results of three distinct, but inter-connected studies of the nature and evolution of the host galaxies of quasars. These three are: i) An HST V-band study of a sample of 17 quasars at $z \approx 0.4$, with absolute magnitudes in the range $-24 \geq M_V \geq -28$; ii) An HST rest-frame U-band study of matched subsamples of radio-loud and radio-quiet quasars at $z \approx 1$ and $z \approx 2$; and iii) A UKIRT K-band imaging study of a sample of ULIRG's and IR-bright QSO's A 2-dimensional modelling technique has been developed, and used throughout to disentangle the host galaxies from the nuclear-dominated UV, optical and infrared images.

The first study allows an investigation of host galaxy properties across a decade in quasar luminosity, but at a single redshift, and forms a crucial low-z baseline against which to compare future host galaxy studies at higher z. Previous imaging studies of AGN hosts have focussed primarily on quasars of moderate luminosity, but the most powerful objects in this sample have powers comparable to the most luminous quasars found at high redshifts. All the radio-loud quasars, and all the radio-quiet quasars with nuclear luminosities $M_V < -24$, are found to have massive bulge-dominated galaxies, confirming and extending the trends deduced from previous studies. From the best-fitting model host galaxies I have estimated spheroid and hence black-hole masses, and the efficiency (with respect to the Eddington luminosity) with which each quasar is emitting radiation. The largest inferred black-hole mass in our sample is $m_{BH} \simeq 3 \times 10^9 \mathrm{m}_\odot$, comparable to the mass of the black holes at the

centres of M87 and Cygnus A. No evidence is found for super-Eddington accretion rates in even the most luminous objects. The role of the scatter in the black-hole:spheroid mass relation in determining the ratio of quasar to host-galaxy luminosity is addressed by generating simulated populations of quasars lying in hosts with a Schechter mass function. Within the subsample of the highest-luminosity quasars, the observed variation in nuclear-host luminosity ratio is consistent with being the result of the scatter in the black-hole:spheroid relation. Quasars with high nuclear-to-host luminosity ratios can be explained in terms of sub-Eddington accretion rates onto black holes in the high-mass tail of the black-hole:spheroid relation. The results imply that, owing to the Schechter function cutoff, host mass should not continue to increase linearly with quasar luminosity, at the very highest luminosities. Any quasars more luminous than $M_V = -27$ should be found in massive elliptical hosts which at the present day would have $M_V \simeq -24.5$.

The second study is used in concert with existing rest-frame V-band data to calculate $U - V$ colours for the host galaxies, and thus provide the first unbiased estimates of quasar host galaxy evolution out to cosmologically significant distances. The host galaxy colours are found to be broadly consistent with the assumption of passive evolution, but with a small amount ($< 1\%$) of ongoing star-formation. The hosts of the radio-quiet quasars are found to evolve slightly more rapidly than those of the radio-louds.

Finally, the same modelling technique is applied to a sample of ULIRG's and a control sample of IR-bright QSO's, matched in terms of their 60μm luminosity. Using UKIRT K-band imaging to detect the presence of any well-evolved stellar population, the possibility of an evolutionary link between ULIRG's and Quasars is explored. Large K-band bulges are found to be present in all of the quasars, with the majority of the ULIRG's being best-fit by a disc. Despite the apparent difference, a significant overlap exists between the two populations in terms of their nuclear luminosity. A significant unresolved nuclear component is present in all of the objects, and this is found to correlate with the

luminosity of the K-band host across the sample. In general, the ULIRG's do not appear to be on their way to becoming fully-fledged quasars, nor the first-ranked massive ellipticals that we have come to expect to find quasars situated in. It seems likely that such systems are the dusty equivalents of the Seyfert galaxies, and while some may end up as quite large ($\lesssim L^{\star}$) ellipticals, many have more in common with the disk galaxy population.

Taken as a whole, this thesis pushes the study of Quasar Host Galaxies in three new directions, allowing a number of interesting questions on cosmology and galaxy evolution to be addressed.

Declaration

I hereby declare that this thesis ~~entitled~~ is not substantially the same as any that I have submitted for a degree or diploma or other qualification at any other University. I further state that no part of my thesis has already been or is being concurrently submitted for any such degree, diploma or other qualification.

This thesis is the outcome of my own work except where specifically indicated in the text.

David Floyd,

Edinburgh,

April 2004.

Acknowledgements

Firstly, my thanks must go to Jim, for the immense wisdom, freedom, inspiration and guidance he has offered me, (as well as the finest office in the Observatory) throughout my 3 years as his student. I gratefully acknowledge also the input and assistance of all my collaborators at ROE, Oxford, and Space Telescope. Ross McLure, Marek Kukula, Will Percival, Lance Miller, Chris O'Dea and Stefi Baum have all provided invaluable input to the work presented in this thesis. To Thor and Olga for their steady UKIRT-guiding hands in rough weather. In addition, I thank Alan Heavens for his superviserly support through some difficult years, and encouragement in times of need.

Second, I'd like to thank my parents, close friends and housemates - all people who have put up with my mood-swings; enthusiasm, frustration and unholy work hours.

Next, a big thanks to my fellow inmates at "HM"OE, and other "institutions" around the world. In particular to Ben for clicky-ball-game entertainment on dismal Tuesday afternoons, to Ian and Olivia for IDL and liquid assistance, to Stephen for ORACDR help, Tara for infinite UNIX wisdom, Dan for pictures of Crocodiles, and Thomas for Danish 'Gangsta' rap. Ralph, who will be sorely missed for many years to come. Liz for keeping the place on the straight and narrow. Also to all the Cargese massive for such a memorable summer school.

Thanks to BFS for hilltop silliness and for making Edinburgh the magical place that it is. To EUWSC for beachy fun and games, trips to Tiree, Machrihanish, Cornwall and France: Crusties

forever! Thanks to Mike for beautiful west-coast sailing jaunts, and the opportunity to tinker on boats. To Endeavour, her captain and crew, and the BBC2 history team for the tropical voyage of a lifetime and for making me look hairy, scary and dopey in front of 3 million people. To Andy for green-fingered fun, and to Penny for her great understanding.

I gratefully acknowledge the support of PPARC through a three-year studentship at the University of Edinburgh, and to the University itself for educating and putting up with me for 8 whole years(!). Two of the main datasets presented are based on observations with the NASA/ESA's marvellous *Hubble Space Telescope*, (program ID's 7447, 8609 and 9085) obtained at the Space Telescope Science Institute, which is operated by The Association of Universities for Research in Astronomy, Inc. under NASA contract No. NAS5-26555. The final dataset originates from UKIRT in January 2002. Data was analysed using starlink's ORACDR and NOAO's IRAF software, on STARLINK and IfA machines at the Royal Observatory, Edinburgh. This research has made use of the NASA/IPAC Extragalactic Database (NED) which is operated by the Jet Propulsion Laboratory, California Institute of Technology, under contract with NASA.

Finally, I extend my thanks to the late-night dedication of the staff of Edinburgh's many and varied chippies and other eateries, without whose life-saving sustanance I almost certainly would not be here today. Of particular note are "Franks" and "Salvatoris" for their exemplary salt-and-sauce, the thought of which makes my mouth water even as I write these words.

Contents

List of Figures

CHAPTER 1

Introduction

This thesis is primarily concerned with the kinds of galaxies in which we find a broad range of very obvious nuclear activity; the Quasars. Until comparatively recently the study of quasars, and of their host galaxies, was viewed as a rather esoteric branch of astrophysics. Their extreme luminosity made them useful cosmological probes, but the cause of their extreme luminosity was poorly understood, difficult to investigate, and anyway seemed very far removed from the big cosmological questions that have begun to be tackled in the past half-century. In recent years however, the study of quasars has moved away from the realm of interesting exotica, and taken centre stage in the keystone astrophysical study of the formation and evolution of galaxies. We are increasingly seeing the evolution of galaxies not simply in terms of the optically dominant gas and starlight, but in terms of a complex interplay between many different components, each of which evolve independently and in concert with the others, and may be more or less significant at different stages through a galaxy's evolution.

In particular, the notion that black holes play a pivotal role in the evolution of galaxies now appears

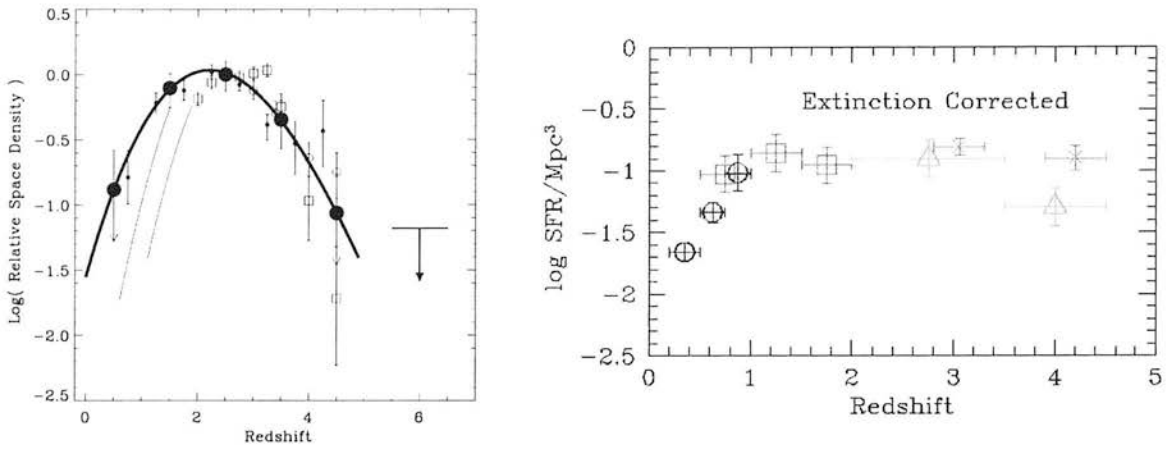

Figure 1.1: **Left:** Quasar comoving number density as a function of redshift (from Shaver et al. 1996). **Right:** The well-known "Madau plot" showing the star formation history of the Universe, as updated by Steidel et al. (1999) to correct for extinction.

to be inescapable. AGN activity is now quite broadly explained by the accretion of material onto a massive central object, that we believe is too compact to be anything but a Black Hole. But now we are finding evidence for such compact objects in many quiescent, or inactive galaxies as well (section 1.3). In nearby galaxies at least, a correlation is found between the presumed mass of the black-hole, and two important bulk properties of the galaxy: The mass (luminosity) of the velocity dispersion, σ of the Spheroid (or bulge component). Such a correlation suggests a deep connection between the evolution of the black-hole and of the bulge. Furthermore, although clear indications of activity are seen in only about 1% of local galaxies, low-level activity has been observed in many - possibly as many as 40% (Miller et al. 2003), and as we look into the deeper, more distant past, we find significant evolution in these numbers. Much has been made of the apparent broad similarity between the evolution of the quasar number density and the comoving star-formation rate of the Universe (figure 1.1), suggesting that quasar activity traces the evolution of galaxies back to its peak at around $z \approx 2$.

Thus, far from being a rare phenomenon, it now appears that we have been observing the rare luminous, or highly active tail of a highly abundant, and rapidly evolving population. This evolution

appears to be connected to the evolution of the galaxy population at large (section 1.4, though models remain controversial, and observations weakened by incompleteness. Thus the last five years have seen the merger of a number of fields into a combined study of "The coevolution of galaxies and black-holes", acknowledging the complex interrelationships between black-holes, stars and the gas and dust of the interstellar medium, in directing the evolution of galaxies.

I therefore present the following background information starting with galaxies, and working on to active galaxies and the evidence for supermassive black-holes in the galaxy population at large. Galaxy evolution in the context of current cosmological models is briefly discussed at a level which highlights the relevance of the study of quasars. Host galaxy studies, and their aims and key results are then discussed at some length, before describing the work in this thesis, and its part in an ongoing study of the evolution of quasar host galaxies out to redshift 4.

1.1 Galaxies

Strictly, there is no such thing as a normal galaxy, but there are a number of ways of classifying them. In particular, Active Galaxies (section 1.2) stand out as so different from the others that "normal" has come to refer to the others, regardless of how exceptional they may be!

Galaxies are, in general, dominated in terms of their emission by starlight, which lies mainly inside the visible window, and is perhaps the reason that optical astronomy remains such a rewarding field in the current era of multi-wavelength observations. The second major component of a galaxy's emission is from the gas of the interstellar medium (ISM). Again, since the majority of atomic electron transitions have energies of a few electronvolts, much of the gas emission is observable in the optical. Much of our basic terminology came about originally from examination of visible light and photographic plates. As a continually developing study, astronomy mustn't lose sight of the limita-

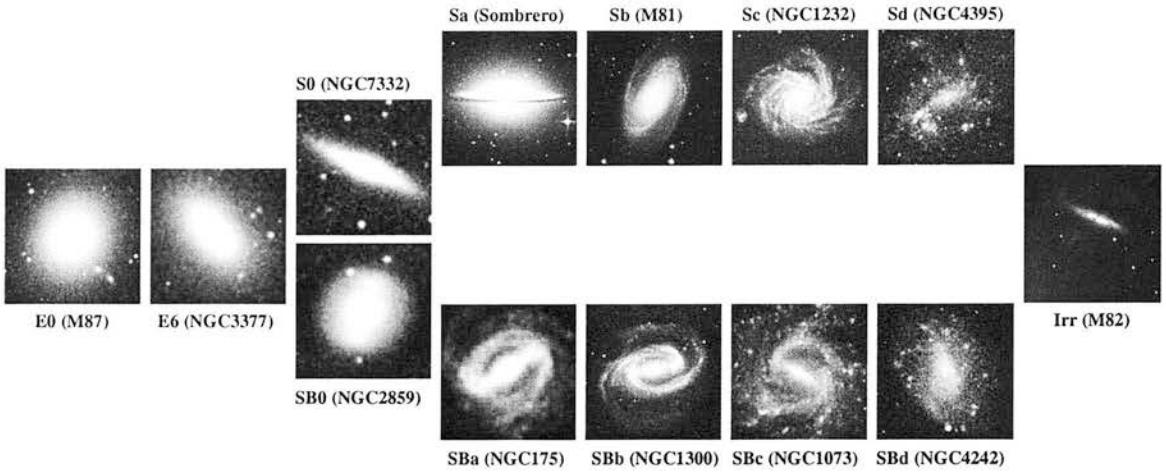

Figure 1.2: **The Hubble Tuning Fork.** Hubble believed that his classification scheme reflected evolution of the galaxies, from left to right, and we still refer to galaxies as being "Earlier" or "Later" types, the further to the left or right they are respectively.

tions imposed by earlier studies using inferior technology. Whilst visible observations therefore form the basis for our understanding of galaxies, we must not lose sight of the profound implications of emission in the radio, infrared, UV, X- and $\gamma-$rays, and the recently uncovered sub-mm.

1.1.1 Morphology - the Hubble Classification Scheme

Given the immense diversity observed in the galaxy population, it may come as something of a surprise that there can exist any simple classification scheme. However, Edwin Hubble in the 1920' and 30's worked assiduously to classify and order the local galaxy population. He pioneered the study of galaxies based on simple appearance (Hubble 1926), dividing them into three major categories: Elliptical, Spiral, and Irregular. These are sub-divided in a fashion that is known today as the "Hubble Tuning Fork" (figure 1.2).

Elliptical galaxies

Triaxial spheroidal galaxies, having an appearance on the sky of elliptical disks, with a smooth light distribution traditionally approximated by the de Vaucouleurs $r^{1/4}$ law:

$$I(r) = I_0 \exp\left\{ -\left(\frac{r}{R_0}\right)^{1/4} \right\} \tag{1.1}$$

Where R_0 is the effective "scalelength" of the galaxy. More commonly from an observational point of view we use the **half-light radius**, $R_{1/2} = 3459R_0$, and the surface brightness at this radius, $I_{1/2}$. Clearly any such relation may be integrated exactly to obtain the total luminosity:

$$L = 20160 I_0 r_0^2 = 22.7 I_{1/2} R_{1/2}^2 \tag{1.2}$$

In recent years it has been found that the $r^{1/4}$ law only really applies to a subset of the Elliptical population. A better fit is obtained using the Sèrsic profile, which allows for an additional third parameter, β, controlling the overall shape of the radial profile (Sersic 1968):

$$I(r) = I_0 \exp\left\{ -\left(\frac{r}{r_0}\right)^{\beta} \right\} \tag{1.3}$$

This equation must be integrated numerically, and Lima Neto et al. (1999) present a useful set of calculations.

Elliptical galaxies are classified by the elongation of their apparent projected image, in terms of their **Ellipticity**:

$$n = 10(1 - \varepsilon)$$

where $\varepsilon = b/a$, is the eccentricity (a = semi-major, and b = semi-minor axis). Thus E0's appear

circular, and E7's (the most eccentric ellipticals found) have an eccentricity of $\varepsilon = 0.3$. The measure is a somewhat subjective one. The true ellipticity of a galaxy cannot be determined because we do not know the orientation of a given galaxy.

Ellipticals do not rotate globally, but their constituent stars follow individual orbits, resulting in bulk velocity dispersions that are approximately Virialised. They typically exhibit quite red colours, containing old stellar populations. The precise formation mechanism of ellipticals is controversial, and of major importance to cosmology (see section 1.4).

Spiral galaxies

May be "Normal" (SA or simply S) or "Barred" (SB). Both have spiral-shaped arms. Generally they have two arms arranged symmetrically about the centre of rotation. These galaxies have a "discy" profile, that is well described by an exponential function of the Freeman (1970) form:

$$I(r) = I_0 \exp\left\{-\frac{r}{R_0}\right\} \tag{1.4}$$

The spiral arms are then small fluctuations in surface brightness, superimposed onto this basic form. In ordinary spirals, the arms emerge directly from the nucleus. In the barred spirals, a bar of material cuts through the centre, and the arms originate from the ends of the bar. The fraction of barred spirals is found to be independent of environment, but declines rapidly with increasing redshift, suggesting that the process that results in the formation of bars is an internal one. At higher redshifts, the spirals may simply be too dynamically hot for such a global instability to arise. Both types show similar variations in terms of the tightness of their spiral arms, and compactness of central bulge, and are subdivided accordingly a-c (see figure 1.2). Old and young stellar populations coexist in all spirals, but the proportion of young, population I objects increases from a through c. Subtypes d and m

("Magellanic") were added by Gerard de Vaucouleurs and are progressively less and less tight.

Spiral galaxies are found to rotate, and in order to explain the rotation curves observed at large radii, we invoke the presence of invisible or "Dark" matter in a halo. The nature of this dark matter is one of the deepest mysteries, and biggest problems facing 21st century astrophysics.

Lenticular, or S0 galaxies

Galaxies that contain significant bulge and disk contributions, and thus appear as an "evolutionary bridge" in Hubble's tuning fork. They are flatter than E7, having a thin disk and a large spheroidal bulge. Edge-on they look like a convex lens - hence the name.

Peculiars

These galaxies differ in some significant way from the Hubble Tuning Fork prototypes. Most luminous nearby galaxies fit very well with Hubble's simple picture, but as we go to higher and higher redshifts we find more and more galaxies that need to be "shoehorned" into one class or another. The fraction of peculiar galaxies increases rapidly with increasing redshift, and the types of peculiarity exhibited by early and late type galaxies differs.

Irregulars

Irregular galaxies are so different to the basic Hubble prototypes that they can no longer be shoehorned into any such morphology. There are 2 distinct types of Irregular:

- **Irr I:** Have resolved HII regions, and population I (OB type) stars.
- **Irr II:** Ambiguous classification; amorphous appearance, can't be resolved into stars, marked absorption by interstellar dust, significant gaseous emission.

1.1.2 Basic Physical Description of Galaxies

In the case of both main galaxy morphologies, there exists a well-documented, but none-the-less remarkable empirical relationship between the luminosity of a given galaxy, and the motion of its contents. These differ somewhat between the ellipticals and the spirals, and we shall consider each in turn.

The Tully-Fisher relationship

It was empirically found by Tully and Fisher (1977), that the rotation velocity of a spiral galaxy, as measured in the 21cm HI line, is tightly correlated with its luminosity:

$$L \propto \Delta v^4 \tag{1.5}$$

The effect is also seen in the optical and infrared, with the latter giving the smallest scatter. Now known as the **Tully-Fisher** relation, it is poorly understood, but has long been used as a "standard candle" distance indicator.

The Faber-Jackson Relation

As was mentioned above, Elliptical galaxies do not globally rotate, their stars instead having random orbital velocities, yielding an overall stellar velocity dispersion which is greatest in the central regions of the galaxy, observable through the Doppler width of spectral lines; σ_v. In the case of Ellipticals, σ_v is found to correlate with galaxy luminosity:

$$L \propto \sigma_v^{\alpha} \tag{1.6}$$

with $\alpha \simeq 3-4$ (Faber and Jackson 1976). Again the reasons for such a relationship are poorly understood, but the empirical finding has made for an extremely useful distance estimation tool.

The Kormendy Relation

In the case of Elliptical galaxies, a second empirical relationship is found between the characteristic scale-length of a galaxy, $R_{1/2}$ say, and the surface brightness at that radius, $\mu_{1/2}$. Originally due to Kormendy (1977), this relationship has been well studied for nearby galaxies. The most recent determination from the Sloan Digital Sky Survey (SDSS), and drawn from 9000 early-type galaxies (Bernardi et al. 2003) is:

$$\mu_{1/2} = (3.33 \pm 0.09) \log_{10} R_{1/2} + C$$

The Fundamental Plane

Thanks to a decade of observations with the Hubble Space Telescope, we now have a wealth of both structural and spectral information on the nearby galaxy population, and we are beginning to understand the physics behind the Tully-Fisher relation, the Faber-Jackson relation, and the Kormendy relation. It is found empirically that the three observables, $I_{1/2}, R_{1/2}, \sigma v$ are closely correlated, such that the population of elliptical galaxies live on a **"fundamental plane":**

$$L \propto I_0^x \sigma_v^y \tag{1.7}$$

with $(x,y) \simeq (-0.7,3)$ (Dressler et al. 1987, Djorgovski and Davis 1987). Thus the Kormendy and Faber-Jackson relations are simply projections of this deeper relationship.

Such a relationship is anticipated, if we assume firstly that galaxies are self-gravitating systems

satisfy the Keplerian relation:

$$\sigma_v^2 \propto \frac{M}{R} \tag{1.8}$$

And secondly, that as a population, ellipticals share a weakly-varying mass-to-light ratio, $M/L \propto M^a$ (ie. they are homologous).

Following these two basic assumptions, we obtain a result that looks very like the Fundamental Plane, a relation between luminosity, surface brightness and velocity dispersion:

$$L^{1+a} \propto \sigma_v^{4-4a} I_0^{a-1} \tag{1.9}$$

So we should expect a fundamental plane for any family of self-gravitating systems with roughly constant mass-to-light ratio. The existence of this relation has been used for some time as a "standard ruler" in cosmology. However, it tells us something fundamental about the formation of galaxies, and is a useful diagnostic tool in comparing families of galaxies.

The Faber-Jackson relationship can then be recovered, by assuming that it is the result of collapse in a gravitational hierarchy (Faber 1982): Let σ_0 be the rms density variation $(\delta\rho/\rho)$ in the Universe (after smoothing by a box of mass M). We know that gravitational collapse occurs when $\delta\rho/\rho \approx 1$, and the density contrast evolves as $(1+z)^{-1}$. Assuming a power-law distribution, $\sigma_0 \propto M^{-\lambda}$, the collapse redshift scales as

$$1 + z \propto \nu M^{-\lambda}$$

where $\nu \equiv (\delta\rho/\rho)/\sigma_0$ is a dimensionless measure of the perturbation size. At collapse, the density of the galaxy is some multiple of the background density:

$$M/r_0^3 \propto (1+z)^3$$

Eliminating z and using the FP equations derived above, we find

$$L^{2-3\lambda} \propto \nu^{-3(1+a)} \sigma_v^{6(1+a)}$$

A low value of λ ($\sim 1/6$) gives roughly the observed relation, and in addition, the scatter in ν expected for peaks in random density perturbations accounts for the ~ 1 magnitude of scatter in the relation.

1.2 Active Galaxies

We define Active Galaxies in the broadest sense as galaxies in which there is a significant contribution to the total energy output that cannot be accounted for by stellar, or normal (single temperature) thermal radiation. This definition is sufficiently vague to cover an enormous range of objects, from starburst galaxies in which the activity can be accounted for by a vigorous "burst" of star formation, to radio-loud quasars in which we see colossal "quasi-stellar" optical emission drowning out an entire galaxy, as well as incredible radio structures that dwarf the galaxy in scale. This unusual behaviour, although exhibited through a broad range of phenomena, is usually connected with the galactic nucleus, hence the term Active Galactic Nucleus (AGN). In recent years we have come to understand the majority of these phenomena in terms of just one underlying physical process: the accretion of gas onto a SMBH (section 1.2.2).

1.2.1 AGN types

Many of the distinctions among the various flavors of AGN rely on spectroscopic clues (see the montage of optical spectra in figure 1.3). What follows is a census of the main types of AGN, with a brief discussion of their observed properties, and the manner of their discovery.

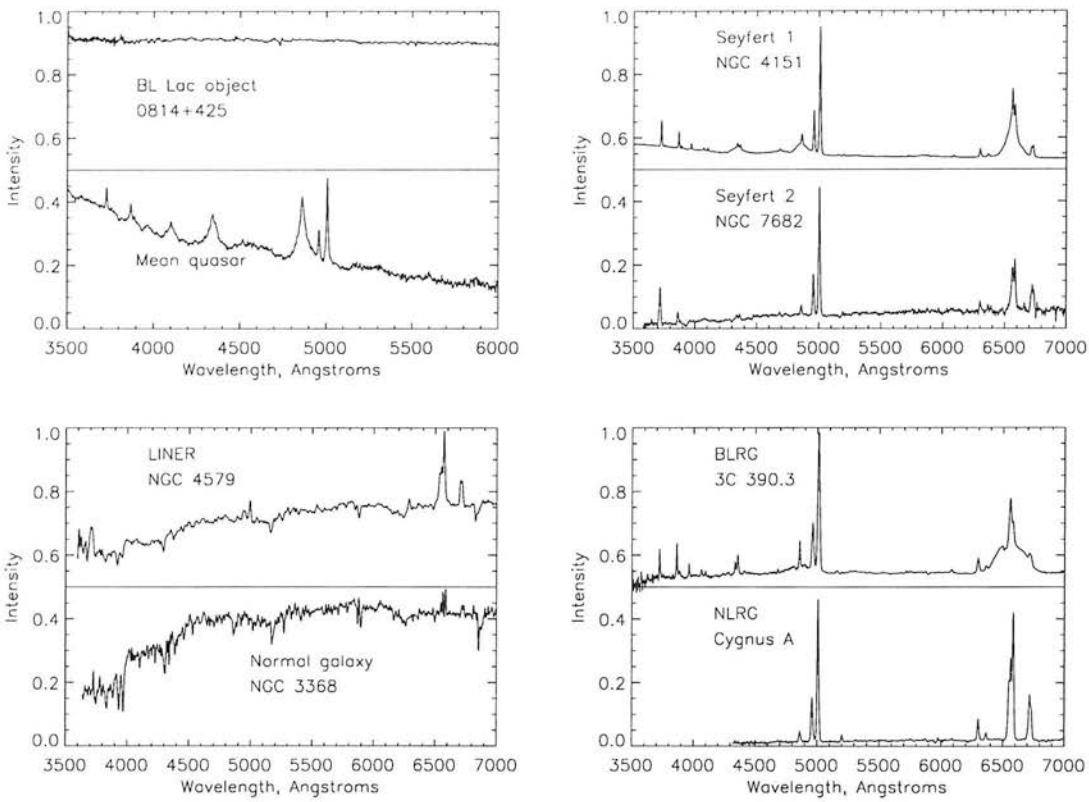

Figure 1.3: **Montage of optical spectra of different types of AGN** shown at their emitted wavelengths for ease of comparison. See main text for details. Specific object names are given in each case, except for the quasar, which is a composite spectrum made up of the average of many spectra. A "normal" galaxy spectrum (of early-type spiral NGC3368) is also provided for comparison. (Figure taken from http://www.astr.ua.edu/keel/agn/ and references therein).

Seyfert Galaxies

The first discovery of AGN was by Fath (1908), who discovered the unusually bright nucleus in NGC1068. A number of other objects followed, and it was found that their spectra exhibited a number of unusual properties. However, it was not until 1943 that Seyfert (1943) identified six such objects as a distinct class, defined by their unusually bright central surface-brightness and broad emission lines. Today, Seyferts are defined (somewhat arbitrarily) to be active galaxies whose optical nuclei have $M_V < -23.5$. Brighter nuclei are generally classed as quasars.

Seyferts have been very well studied due to their relative closeness. Virtually all are hosted by

normal spiral galaxies, and are distinguished by their bright "starlike" nuclei. Their spectra reveal strong emission lines from highly ionised species, and a featureless, "non-thermal" AGN continuum. The strength of the continuum and the relative properties of the emission lines are used to subdivide the Seyferts into two types:

- **Seyfert 1's** Exhibit two sets of emission lines, narrow and broad, and a strong AGN continuum.
- **Seyfert 2's** Exhibit only the narrow emission lines, and have a weaker AGN continuum.

Further investigation has revealed that the separation between these two classes is less than clear-cut. Intermediate types have been classified by Osterbrock (1981) as types 1.5, 1.8 or 1.9, depending on the relative strengths of the broad and narrow line emission components, and there appears to be a continuum of properties, with close inspection of the spectra revealing that the broad line component never completely disappears.

Quasars

The discovery of quasars (a compaction of "quasi-stellar radio source"), can be directly attributed to the leaps in radio technology made throughout the second world war. The first catalogues that reached the flux limit of 9Jy were the 3C (3rd Cambridge) and the 3CR (Revised) catalogues, at 158MHz and 178MHz respectively. In the early days, the spatial resolution in the radio was so poor, that observers had to wait for their objects to be occulted by the moon in order to get an accurate position. The vast majority of these radio sources were associated with resolved Elliptical galaxies (the radio galaxies - see below), but a small number did not have obvious optical counterparts. When optical counterparts were eventually identified, they appeared to be stellar (Matthews and Sandage 1963). These "Radio Stars" had blue spectra relative to normal stars, and their spectra were even stranger. Unlike any stellar spectrum previously recorded, they featured strong broad emission lines that could not be attributed

to any known element.

It was Schmidt (1963) who first successfully identified some of the lines in 3C273 as heavily redshifted Balmer lines, at the then unprecedented redshift of $z = 0.158$. Many others soon followed. If the redshift was cosmological in nature, then some of these objects had luminosities more than a hundred times larger than that of the most luminous known galaxies. In addition was the enigma of scale; The "quasi-stellar" source was obviously too small to resolve, but could produce luminosities $\approx 10^2$ times brighter than a typical galaxy. Examination of photographic plates spanning years of observations showed many objects' emission lines to systematically vary, on timescales from months right down to just a few days. Whatever was powering these objects was not only too small to be resolved - it was perhaps only as large as the Solar system. This causality argument led to early suggestions (e.g Zel'dovich and Novikov 1964, Lynden-Bell 1969) that the quasars might be powered by black-holes, but there was little solid evidence to back up the argument until comparatively recently (section 1.3).

The strong blue colour, and "UV excess" was soon being used to identify another class of quasar, that did not exhibit the same vast radio luminosity as the originally discovered "Radio Loud Quasars" (RLQ's). These latter, now known as "Radio Quiet Quasars" (RQQ's), exhibit the same bright optical nuclear point sources as the RLQ's, exhibiting broad emission lines, variability, and the generally flat spectrum that has come to identify quasars above all other properties. Empirically, the spectrum of a quasar nucleus is found to follow the general power-law form:

$$f_\nu \propto \nu^{-\alpha} \tag{1.10}$$

with a spectral index in the range $0 < \alpha < 1$ giving its rather flat shape, and the peculiarly strong (w.r.t. starlight) blue and UV flux. The UV excess technique has now been successfully used to uncover a

large population of QSO's that may not have been identified in the radio. RQQ's are found to be some ~ 10 times more abundant than their RLQ counterparts. RLQ's have been successfully unified with radio-galaxies, and are classified in the same way (see below). The reason for the "radio loudness dichotomy" remains unclear, and an active field of research.

Today, the term "quasar" is often used quite slackly to refer to active galaxies in general. In the strictest sense, a quasar is defined as being an active galaxy with an extremely bright nucleus, with $M_B < -23$, although it must be admitted that this is rather an arbitrary cutoff with no good physical basis. Quasars exhibit a strong nonthermal continuum, with broad permitted and narrow forbidden lines (see figure 1.3 for an averaged quasar spectrum).

As the number of known quasars has increased, progressively greater and greater redshifts have been identified, but no blueshifts, and it is now clear that their distribution is isotropic on the sky. They must therefore be assumed to be extragalactic, and their redshifts assumed to be cosmological. As of the start of 2004, the highest observed redshift is that of a quasar at $z = 6.41$.

Radio Galaxies

Critical to the discovery of AGN, and typically found to be hosted by giant elliptical galaxies, some being associated with quasars. Two types of radio galaxy exhibit *optical* spectra that we associate with AGN activity. These are the Broad Line and Narrow Line Radio Galaxies (BLRG's and NLRG's) and exhibit spectra that are analogous to those of the Seyfert 1's and 2's respectively.

The radio emission typically exhibits two components, which are both produced by synchrotron radiation, and follow the power-law form of equation 1.10 with different spectral indices:

- **Flat-spectrum:** $0.0 < \alpha < 0.5$, typically compact ($<$ 1arcsec) and coincident with the nucleus of the host galaxy. Thought to originate from the flat turnover in the synchrotron spectrum from

multiple sources.

- **Steep-spectrum:** $0.5 < \alpha < 1.0$ characteristic of optically thin synchrotron emission. Observed in the large (kpc-scale) jets and lobes displayed by some sources.

Depending on the relative contributions of the core and lobe components to the total radio luminosity, radio galaxies are often classified as core- or lobe-dominated.

The lobe-dominated radio galaxies are the most impressive and are further classified on the basis of their extended radio emission morphology, after Fanaroff and Riley (1974):

- **FRI's:** Characterised by *twin* jets that are straight and highly linear for a few kpc, then deviate and turn into diffuse radio lobes. Typically associated with less powerful radio sources, of $L_{178GHz} < 2 \times 10^{25} h^{-2} \mathrm{WHz}^{-1}\mathrm{Sr}^{-1}$.
- **FRII's:** Highly powerful radio sources ($L_{178GHz} \gtrsim 2 \times 10^{25} h^{-2} \mathrm{WHz}^{-1}\mathrm{Sr}^{-1}$, distinguished by their powerful, highly linear *one-sided* jets.

FRI's are generally associated with large bright (D, cD) Elliptical galaxies, with a slightly flatter light distribution than a typical Elliptical, and often located in rich clusters with extreme X-ray emission - formerly attributed to cooling flows. FRII's on the other hand are generally associated with normal looking $\sim L^*$ elliptical galaxies, but not the first-ranked D, cD cluster galaxies, and exhibit no enhanced clustering.

Blazars

Radio-loud objects, exhibiting flat radio spectra, strong polarisation, and large variability at all wavelengths. Their rarity, and their alignment make them highly consistent with being RLQ's in which we are staring directly down the beam. However there are two important subtypes, believed to reflect two different parent populations.

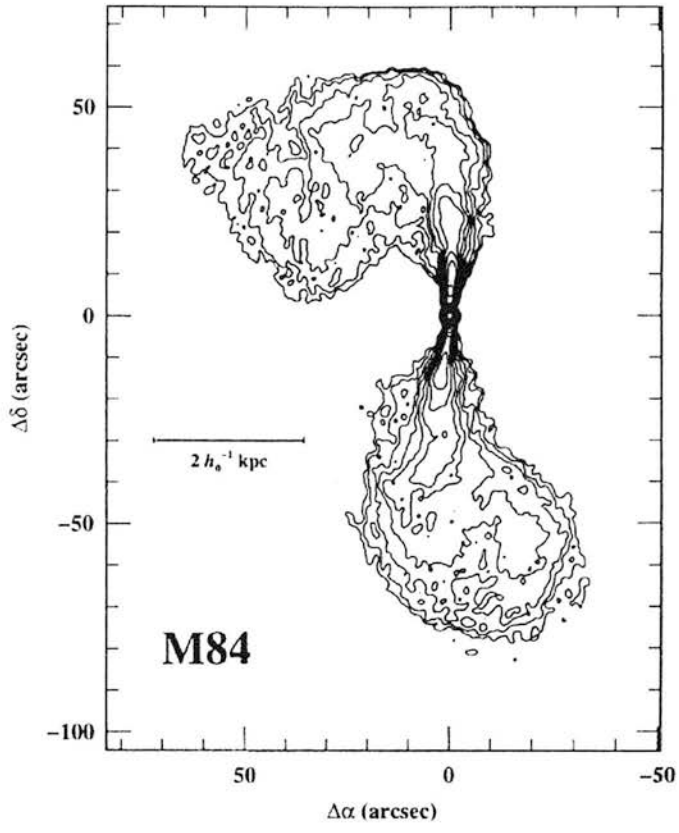

Figure 1.4: **Top:** FRI radio morphology in M84, a lenticular galaxy in the Virgo cluster, at $z = 0.003536$. **Bottom:** FRII radio morphology 3C175. This RLQ has an optical counterpart at z=0.768, and the linear extension is some $212h^{-1}$kpc. Note the Doppler-induced brightening of the jet on one side.

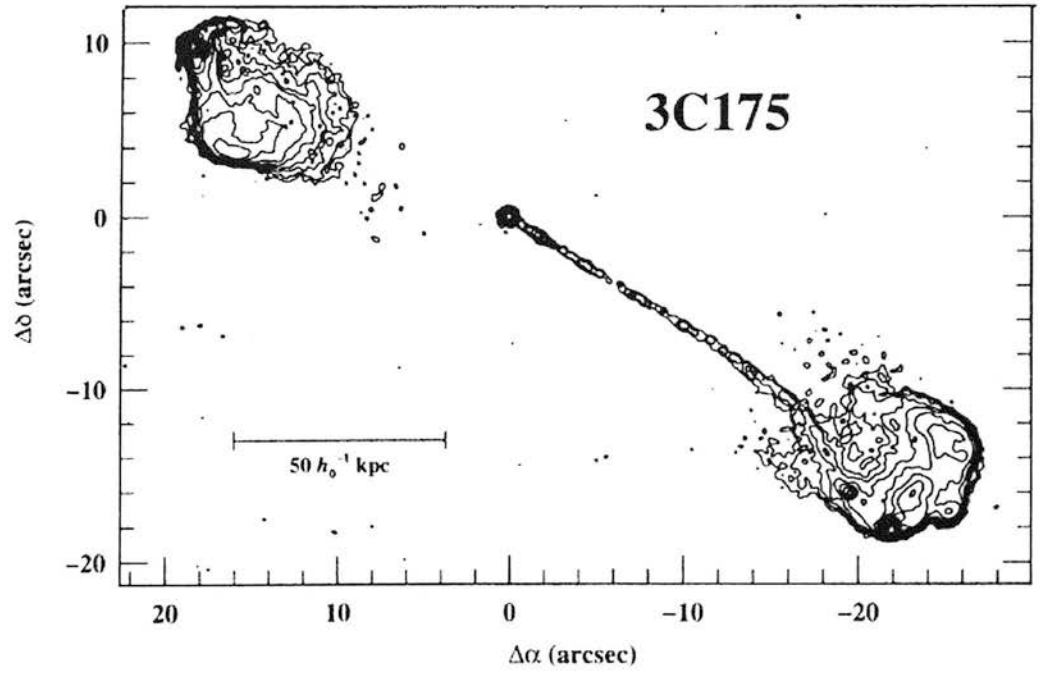

- **BL Lacs** Named after the prototype object BL Lacertae, originally identified as a variable star in our own galaxy. There is a flat, nonthermal continuum, well modelled by a simple power law, and decreasing steadily from the flat radio component, right through the optical and into the X-ray. Emission lines are either weak or absent entirely (see fig 1.3) The luminosity function of the BL Lacs overlaps that of the quasars at the faint end (see for example Robson 1996), and BL Lacs are believed to be the beamed members of a lower luminosity parent population, most likely the FRI radio galaxies.

- **Optically Violent Variable quasars (OVV's)** OVV's share many of the same defining features of the BL Lacs, with a number of important differences. Primarily, the OVV's do have strong emission lines in their spectra, typical of other quasars. In addition, they are more luminous and have thus been detected at much greater redshifts than the BL Lacs. They are also found to have a stronger X-ray emission component, suggesting that a clearer view of the central emission region is available in the OVV's. They are believed to be the beamed population of the powerful FRII radio galaxies.

Starburst galaxies

A different kind of active galaxy, in which a violent burst of star formation close to the centre results in a brightened, unusually blue nucleus. Starbursts may well contribute to the nuclear flux observed within other types of AGN, such as the quasars, and it is possible that the action of one of these two types of activity could assist in triggering the other. However, there is significant ongoing controversy surrounding the issue, and it is revisited in section 1.4.

LINERs

At lower activity levels, many galaxies (and ~50% of bright spirals) contain nuclear emission regions known as LINERs (Low-Ionization Nuclear Emission-Line Regions), which are in at least some cases a lower-luminosity version of the processes seen in more traditional active nuclei. For example, NGC 4579, (spectrum shown in the figure), has a very faint Seyfert 1-like broad component to its H-alpha emission, and a modestly bright ultraviolet central source. 2 types of LINER are observed - analogous to the 2 Seyfert types. A significant fraction of LINERs are powered by black-holes, but many also exhibit a stellar ionization contribution.

ULIRGs

During the 1980's, the IRAS satellite discovered a population of hitherto unobserved objects that emit vast quantities of energy in the infrared: $L_{IR} > 10^{12} L_{\odot}$, comparable with the bolometric luminosity of a UV-excess selected QSO. Some of these "Ultra Luminous Infrared Galaxies" have now been identified with Quasars, but many more have not, being found instead to originate from spectacular mergers of galaxies, very rich in gas and dust. Although the optical spectra of ULIRGs is consistent with a major starburst and interposing dust, this cannot account for all of the IR luminosity alone. The current assumption is that the gas, either from the merger, or from the subsequent starburst is fuelling a central nucleus at a high rate, but that the light from this AGN is being absorbed by the same dust that is helping to fuel the starburst (and/or AGN). However, this link has not been explicitly made, and it remains unclear whether all ULIRG's will end up as a QSO, or whether a QSO is a plausible explanation for the FIR luminosity in all ULIRG's. This question forms the basis for a UKIRT study presented in chapter 4.

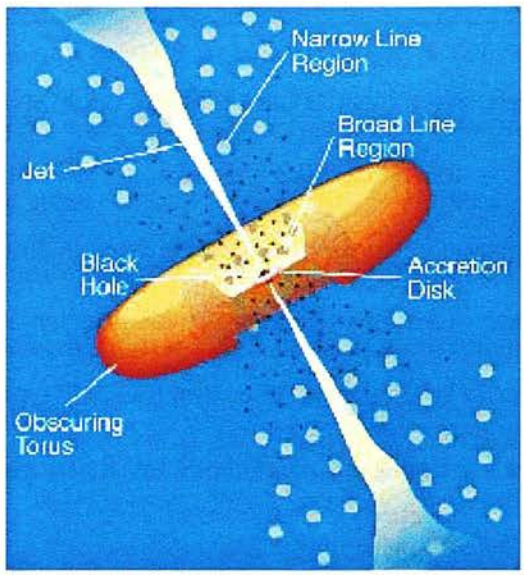

Figure 1.5: **The Standard Model for AGN emission.**

1.2.2 The "Standard Model": Toward a Physical Understanding of AGN

Today, we believe that we have a broad physical understanding of how many of the radiative phenomena in AGN come about, and that black-holes are the only likely candidate for such diverse and extreme behaviour. However, we lack a detailed picture, and much work is still being done to to refine the model. Our general understanding centres upon an optically thick disc or torus of material that is accreting onto a supermassive black hole, and the effect that this has on the galactic environment - see figure 1.5.

The Black-Hole

The process of accretion is now understood to be behind much of the radiation from active galaxies. Material radiates as it loses gravitational potential energy in falling onto a large mass. The luminosity

that we can obtain from accretion is expressible as

$$L = \mu \dot{M} c^2 \tag{1.11}$$

The luminosity does not depend upon the central mass, M, only the fuelling rate $\dot{M}$. In principle we could generate as large an energy as we required, provided that we could supply enough fuel. The efficiency, μ, is dependent on how much of the gravitational energy can be converted into radiation, and how far into the centre the radiation can be observed.

In accretion onto a black-hole, the innermost radius we could possibly hope to see radiation from, is of course the Schwarzschild radius, or "event horizon":

$$R_{\mathrm{Sch}} = \frac{2GM}{c^2} \tag{1.12}$$

In actual fact, General relativity tells us that there is a stricter limit to the radius at which we can expect to see radiation - the "innermost stable circular orbit" (ISCO), which for a non-rotating black-hole is $3R_{\mathrm{Sch}}$. The situation is more complicated for rotating black-holes, but we do not here have the space to go into a detailed discussion. As a rough estimate, μ is found to be approximately 6% for a non-rotating black-hole, and up to 42% in the case of a maximally rotating black-hole.

However, there is an upper limit to the luminosity of a celestial object of given mass, resulting from the radiation pressure generated by the object's own luminosity preventing the infall of more material. This limit occurs when the outward radiation pressure and the inward pull of gravitation balance each other out:

$$\frac{L\sigma_T}{4\pi R^2 c} = \frac{GM_H m_p}{R^2}$$

and is known as the Eddington limit:

$$L_{\max} = L_{\text{Edd}} = \frac{4\pi G M_H m_p c}{\sigma_T} = 1.25 \times 10^{31} \frac{M_H}{M_\odot} = 6.31 M_H (\text{Watts}) \tag{1.13}$$

Eddington-limited accretion onto a supermassive black-hole of can explain a luminosity of 10^{39}W with a relatively modest fuelling rate of

$$\dot{M}_{\text{Edd}} = \frac{2.2 \times 10^{-9}}{\mu} M_{BH} \text{yr}^{-1}$$

Where μ is now the efficiency with respect to the Eddington limit. At 10% of the Eddington limit, we require an accretion rate of just $2M_\odot \text{yr}^{-1}$ onto a $10^8 M_\odot$ black-hole to explain the observed luminosity. Such an object can also explain the rapid variability, having a Schwarzschild radius of less than a light hour.

The Accretion Disc

A blackbody radiator, whose total luminosity (given by the Stefan-Boltzmann law $L = A\sigma T^4$) is the Eddington luminosity of a supermassive black hole of mass M_{BH}, has a characteristic temperature:

$$T = 3.8 \times 10^7 \left(\frac{M_\odot}{M_{BH}} \right)^{1/4} \text{K}$$

Thus a $10^8 M_\odot$ black-hole yields temperatures of $\sim 10^5$K (radiation at around 110Å, in the UV and soft X-rays), close to the peak observed in the broad "Blue Bump" in the SED of quasars. Note that a smaller black-hole results in a higher temperature, with a solar mass one giving $T \sim 10^7$K - well into the hard X-rays.

However, such a simple model cannot explain the breadth of the Blue Bump. Our favoured model

is that of an optically thick disc or torus of material, acting as a multi-temperature blackbody radiator. In the simplest toy model we assign each location in a disc a simple blackbody temperature, $T(R)$, based on its radius (distance from the hole) and the assumption that all gravitational potential energy lost by infalling material is radiated immediately from a flat disc:

$$T(R) = (\frac{GM_{BH}\dot{m}}{8\pi R^3\sigma})^{1/4}$$

Each annulus thus acts as a blackbody radiator, with a surface brightness given by Planck's radiation law:

$$I_\nu = B[\nu, T] = \frac{2\pi h\nu^3}{c^2(e^x - 1)}; \qquad x = \frac{h\nu}{kT} \tag{1.14}$$

The total luminosity of the disc is then obtained by integrating:

$$L_\nu = \int_{R_{in}}^{R_{out}} I_\nu A dR$$

yielding a function which rises steadily as

$$L \propto \nu^{1/3}$$

between the Rayliegh-Jeans tail of the outermost radiator and the Wien cutoff of the innermost one. This model succeeds in describing the steady rise of flux to a near-UV peak, but the predicted $\sim \nu^{1/3}$ rise is not observed. The typical slope in the optical-UV SED of a quasar is typically in the range $0 > \alpha > -0.5$. Interestingly, cataclysmic variables *do* exhibit the $\nu^{1/3}$ rise in flux calculated above, suggesting that nature is capable of producing simple accretion discs

Radio emission

The polarisation and shape of the radio SED in RLQ's and RG's are best explained by an ensemble of Synchrotron-emitting electrons, which themselves have a power-law distribution of energies. The mechanism for jet formation is still highly controversial, but it is clear that enormous magnetic fields are required, and it is believed that these are supplied by the mass of rotating charged material that forms the accretion disk. There is not the scope to go into this vast field here - see any good AGN textbook, or the review by Ferrari (1998).

X-ray continuum

The hardest radiation is observed in the "X-ray bump", another feature of the SED of quasars (see Mushotzky et al. 1993 for a review). Variations are observed to be far more rapid, suggesting a smaller region close to the nucleus. This radiation is believed to originate from ion-pair plasma in the very central region. Extremely hot coronal gas found above and below the disc, and bombarded by hard radiation from the disc and from the nucleus itself. The majority of AGN are found to emit predominantly soft X-rays, with a few emitting at harder levels.

IR bump

Heated dust at large distances from the nucleus. The IR bump is another broad feature in the quasar SED, but it does not vary, and this suggests diffuse gas of a range of temperatures, and presumably at a large range of distances from the nucleus.

Emission lines

Permitted and forbidden lines are present, and these have quite different mechanisms for their production. We believe that quite different regions, with very different physical conditions, must be behind

these two features.

- **The Narrow Line Region (NLR):** Narrow lines ($v \sim 500\text{kms}^{-1}$) are seen that include many forbidden lines. These are lines that would be collisionally de-excited in any but the rarest of environments, and are therefore not seen in labs on earth. Must be from a region of extreme low density, $n_e \sim 10^{10}\text{m}^{-3}$.

- **The Broad Line Region (BLR):** Broad ($v \sim 10000\text{kms}^{-1}$) high-ionization emission lines of permitted species only, including strong H, NII, SII, OIII and weak OII. We also see substantial emission from *very* high excitation lines such as OVI (113.8eV; $T \sim 340000K$) and HeII (54.4eV; $T \sim 160000K$).

Both gases have temperatures $\sim 10000K$, but occur at different locations, judging by their line width. The BLR is believed to originate in the central parsec or so, explaining the Doppler-broadened lines, with the NLR at distances of tens of kiloparsecs.

1.2.3 Unification

Unification attempts, depending on viewing angle, and hence relative obscuration of the nuclear region have had some success. However, the "Grand" unification schemes, aiming to unify radio-loud and radio-quiet objects under one basic object type, have yet to make a breakthrough. Full discussions of AGN unification schemes can be found in review articles by Antonucci (1993) and Urry and Padovani (1995). Here I present a brief summary, with illustrative figures to serve as a reminder of the basic paradigms.

Radio-Quiet Unification

Unification by orientation had its first real success with the detection by Antonucci and Miller (1985) of broad emission lines in the polarised flux of Sy2's. This detection forms the strongest piece of evidence that the Seyferts are all fundamentally the same object, and differ only in terms of relative obscuration of the active nucleus. It is clear that at least some classic Sy2's are in fact obscured Sy1's.

Radio-Loud Unification

The radio loud unification schemes for FRI and FRII type radio galaxies are shown in figure 1.6. Depending on the viewing angle, we will see a radio galaxy (no bright nucleus) if observed edge-on, a quasar (clear view of the nucleus) or a BL Lac (beamed frontal view of the nucleus). From statistical surveys we know that the radio galaxy population in general is consistent with being the subset of RLQ's that are observed side-on, and we believe that the differences observed in the FRI and FRII populations can be accounted for with a different geometry for the obscuring torus, and hence a different angle required for a direct view of the nucleus.

1.2.4 A note on the Radio Loudness Dichotomy

The existence of a bimodality in the radio-to-optical flux ratio (R) distribution in AGN was long thought to be a well-established, "text book" result (e.g. Peterson 1997). However, recent results from Cirasuolo et al. (2003) have placed a question mark over the existence of this dichotomy. Controversy rages as people use different measures, the FIRST survey for example, being only sensitive to the compact core emission, which is more susceptible to beaming, and due to the incompleteness and intrinsic bias in current samples of radio-observed, optically selected QSO's Blundell (2003).

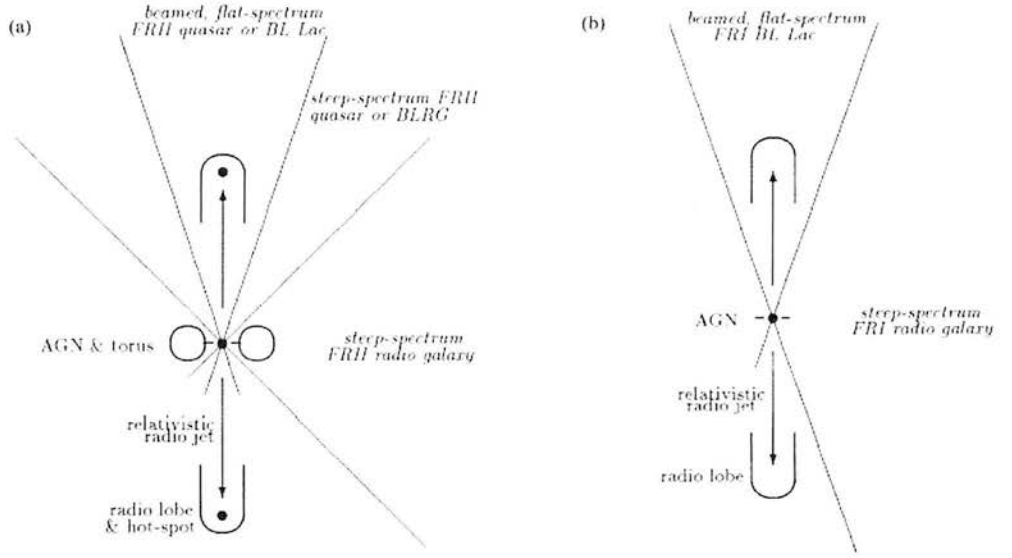

Figure 1.6: **Radio-loud unification schemes** from Jackson and Wall (1999). (a) For FRII sources. (b) for FRI sources.

1.3 Evidence for Super-Massive Black-Holes

In this section we look at the evidence for the presence of Supermassive black-holes in galactic centres. This field is well-documented with a number of good reviews appearing in recent years (e.g. Begelman 2003, Kormendy 2001, Kormendy and Gebhardt 2001, Nelson 2000, Rees 1998, Kormendy and Richstone 1995). The following therefore serves as a quick census, rather than as a detailed review in its own right

It should also be emphasised that our current evidence for black-holes is almost entirely circumstantial. We identify regions of space that are too dense to be explained through classical physical processes, and thus infer the presence of a massive dark object (MDO), with a deep potential well. Such evidence tells us nothing about the metric in the region around the MDO, and thus does not directly confirm the presence of a black-hole. The only distinguishing feature of a black hole is the event horizon, and this is by its nature rather hard to detect. Some success has been had with stellar

mass black holes (See for example Garcia et al. 2001).

1.3.1 Evidence from AGN

Gravity Power

The first suggestions that black-holes may be responsible for the activity observed in AGN came about early on as a means of explaining such vast luminosities from such small objects (e.g.Zel'dovich and Novikov 1964, Lynden-Bell 1969). A quick rest-mass energy calculation yields an illuminating insight: Quasars typically exhibit bolometric luminosities in excess of 10^{39} Watts. From the lobes of RLQ's and RG's we know that this emission must be stable over timescales of $\sim 10^8$ years, yielding a total energy of some 10^{54} Joules. To generate such energy with 100% efficient ($\mu = 1$) conversion of the rest mass energy,

$$E = \mu mc^2$$

would require $\sim 10^7 M_\odot$ of material. Given that the most efficient nuclear reaction known (Hydrogen fusion to form Helium) only has an efficiency, $\mu = 0.007$, we would require a mass of $\sim 10^9 M_\odot$ to generate such power in nuclear reactions. However, from variability studies, we know that such a mass must be confined within a region just light-days across; $R \sim 10^{13}$m. The total binding energy of such a configuration is

$$E_{\rm bind} = \frac{GM^2}{R} \sim 10^{55}\mathrm{J}$$

In other words, the object must be so compact, that *more* energy is available gravitationally, from collapse, than is available through its rest-mass energy in nuclear burning.

Stellar cusps

M87 is a massive elliptical galaxy, found at the centre of the nearby Virgo cluster. It exhibits a spectacular optical jet, and its comparative closeness ($\sim 15Mpc$, $z = 0.004360$) mean that it has been well-studied, and there have been long-held suspicions that it might harbour a supermassive black-hole. Young et al. (1978) demonstrated an unusually cuspy central surface brightness, and spectroscopy revealing an increase in the stellar velocity distribution toward the nucleus. However, it required the high-resolution of the re-furbished HST to finally convince a sceptical astronomical community (e.g. Macchetto et al. 1997, Harms et al. 1994, Ford et al. 1994). Macchetto et al. require a black-hole of mass $(3.2 \pm 0.9) \times 10^9 M_\odot$ to account for their observed rotation curve. Other active galaxies have been studied in a similar manner (see summary in Nelson 2000), notably:

- **NGC4151:** A large central mass of $\sim 10^9 M_\odot$ is found, but not all is attributable to the black-hole, as the Keplerian region is found to be extended. The best estimate of the black-hole mass is $M_{BH} = 3 \pm 0.2 \times 10^7 M_\odot$ (Nelson and Whittle 1995).
- **Cen A:** Infrared VLT (ISAAC) spectroscopy (Marconi et al. 2001), yielding $M_{BH} = 2 \times 10^8 M_\odot$.
- **NGC6251** $M_{BH} = (6 \pm 2) \times 10^8 M_\odot$ (Ferrarese and Ford 1999).
- **NGC4261** $M_{BH} = (4.9 \pm 1) \times 10^8 M_\odot$ (Ferrarese et al. 1996). HST has made a direct detection of a dusty disk-like structure surrounding the nucleus in this object (figure 1.7).
- **NGC1023** $M_{BH} = (1.5 \pm 1) \times 10^9 M_\odot$ (Bower et al. 1997).

Asymmetric Iron line profiles

The only really direct evidence for the presence of supermassive black-holes comes from X-ray spectroscopy of extremely broad, and highly variable emission lines originating very close to the nucleus.

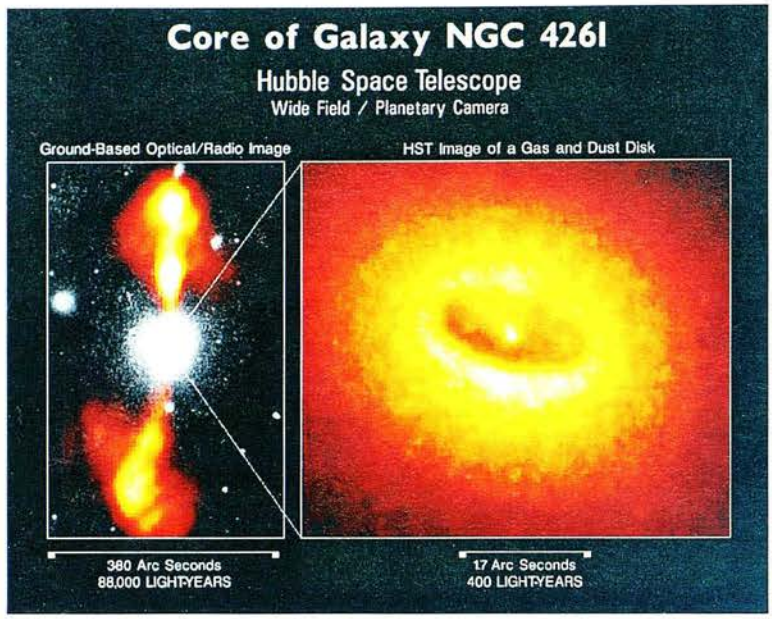

Figure 1.7: **NGC4261: Direct evidence for an accretion disk.** See section 1.3.1.

The best-studied example is the Seyfert galaxy MSG-6-30-15. XMM spectroscopy (figure 1.8) of the iron Kα line reveals an extremely broad ($v \sim 1 \times 10^5 \mathrm{kms}^{-1}$) feature with a highly asymmetric gravitational redshift (Tanaka et al. 1995, Fabian et al. 2002). Such lines are thought to originate in relatively cool, optically thick gas in the inner part of an accretion disk orbiting a black hole. The gas is bombarded by hard X-rays from hotter, optically thin coronal gas, making the cooler disk material fluoresce.

H_20 Megamasers

Using VLBI observations, Miyoshi et al. (1995) have shown that the Doppler shifts in the water vapour maser emission from NGC 4258 are perfectly consistent with Keplerian orbits around a central mass of $3.6 \times 10^7 M_\odot$, contained within just 0.1pc. The maser emission structure appears to be highly flattened, posing problems for the standard model of a thick dusty torus around the central black hole.

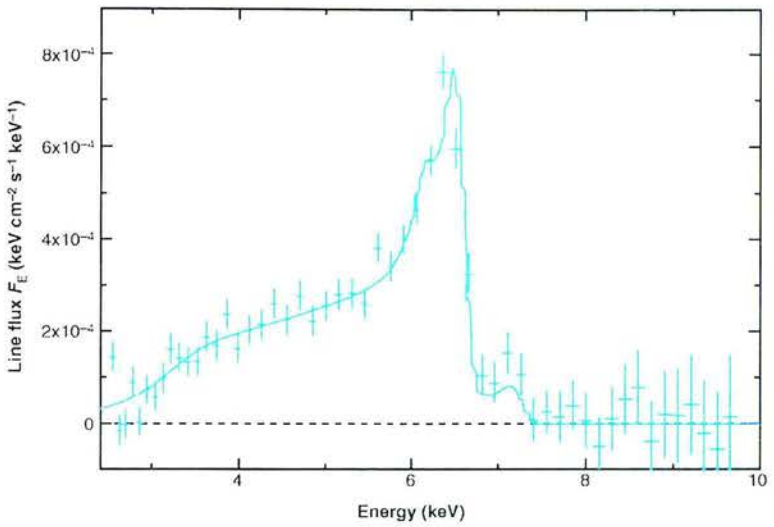

Figure 1.8: **Broad Fe Kα line spectrum in MCG-6-30-15.** Note the highly asymmetric broadening of this line, indicative of a disc-like flow close to the last stable orbit of a SMBH. The red wing is preferentially broadened through a combination of gravitational redshift and transverse Doppler shifting., whereas the narrow blue wing exhibits boosting due to the radial Doppler shift. This evidence is the best, and most direct for the existence of a black-hole to date. Taken from Fabian et al. (2002)

1.3.2 Evidence from quiescent galaxies

More and more normal quiescent galaxies are being associated with AGN behaviour, albeit at lower levels than we see in Quasars, or Seyferts, and we have now begun to expect to find SMBH's to be present in many galaxies, by association with AGN. In addition, a number of techniques have been employed to weigh the central dark mass.

Stellar absorption line kinematics

Long-slit spectroscopy is used to measure the breadth of a given absorption feature at different locations across a galaxy. The Doppler shift is used to determine the Keplerian rotation velocities at different distances from the centre. Using Schwarzschild (1979)'s numerical orbit superposition method, several groups have constructed dynamical models that establish black-hole masses. Most notable are the "Nuker" team, who together have studied more than half of the 20 objects studied in

this way (Gebhardt et al. 2003).

Optical emission lines

Emission line gas in the nuclei of around 100 galaxies within 100Mpc has been observed with HST. However, only $\sim 20\%$ seem to have circular rotation, and few black-hole masses have been published. The best example is M87 (Macchetto et al. 1997), for which HST has actually resolved the gas disc in optical images. Again, a Keplerian rotation is assumed, and a model created to describe the observed rotation curve.

The Galactic Centre

Perhaps the most astonishing and graphic demonstration of the existence of a black hole is the tracking of stellar orbits close to Sgr A* at the heart of our own galaxy. Using IR Keck observations spanning several years, Ghez et al. (2003) plotted the paths of 90 stars and calculated the central mass required to generate the highly eccentric Keplerian orbits observed. Along with an earlier paper by Genzel et al. (1997), the inferred central density of at least $10^{12} M_{\odot} \mathrm{pc}^{-3}$, exceeds the volume-averaged mass densities found at the centre of any other galaxy, and provides overwhelming evidence for a SMBH of $\approx 2.6 \times 10^{6} M_{\odot}$ at the position of Sgr A*. Figure 1.9 illustrates the orbit of the star S2, which comes to within 2000 Schwarzschild radii of the position of Sgr A* (Eisenhauer et al. 2003).

Sgr A* is an X-ray source close to the bright star Sgr A. It is somewhat fainter than is expected for such a massive black hole as inferred above. However, Baganoff et al. (2001) find strong evidence for an X-ray flux, and most importantly, a rapid flaring of this emission. Together, these observations provide compelling evidence of accretion of gas onto a SMBH. See Melia and Falcke (2001) for a full review of evidence for a black hole at the Galactic centre.

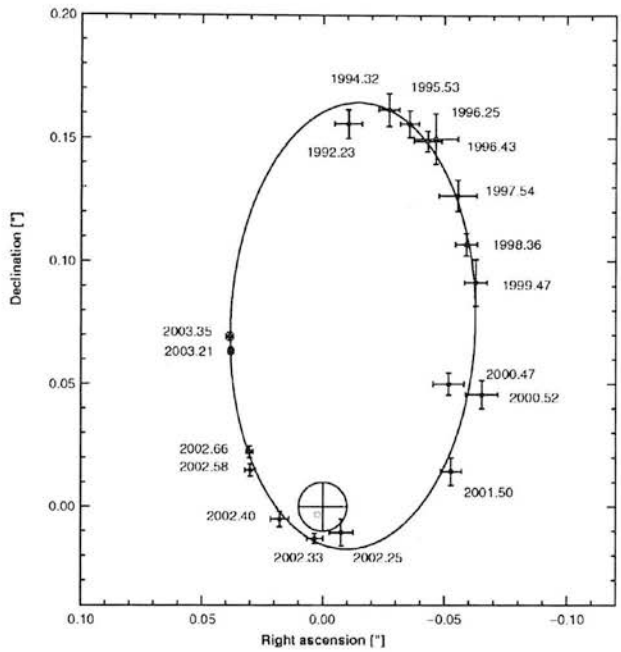

Figure 1.9: **Orbit of the star S2 around Sgr A*.** The smooth curve shows the best-fit Keplerian orbit, which has a period of 15.6 years, and comes to within 2000 $R_{\rm Sch}$ of the position of Sgr A* (denoted by the cross inside a circle). The small blue circle marks the focus of the elliptical orbit (Eisenhauer et al. 2003).

Globular Clusters

Measurement of resolved stellar kinematics is also possible in nearby GC's. Recent work by van der Marel et al. (2002) demonstrated the existence of an intermediate mass black-hole (IMBH) of mass $4.5\times10^3 M_\odot$ in M15, using STIS spectroscopy to obtain radial velocities of stars in the central arcsecond region. However, significant controversy surrounds this measurement, with different interpretations of the measured increase in the mass-to-light ratio toward the centre.

1.3.3 The Black-Hole: Spheroid mass relation

Early attempts to relate black-hole mass to the global properties of their host galaxies focused on the bulge luminosity, L_B (Kormendy and Richstone 1995, Magorrian et al. 1998). It was later shown by two groups, that there exists a tighter correlation between M_{BH} and the galaxy velocity dispersion, σ

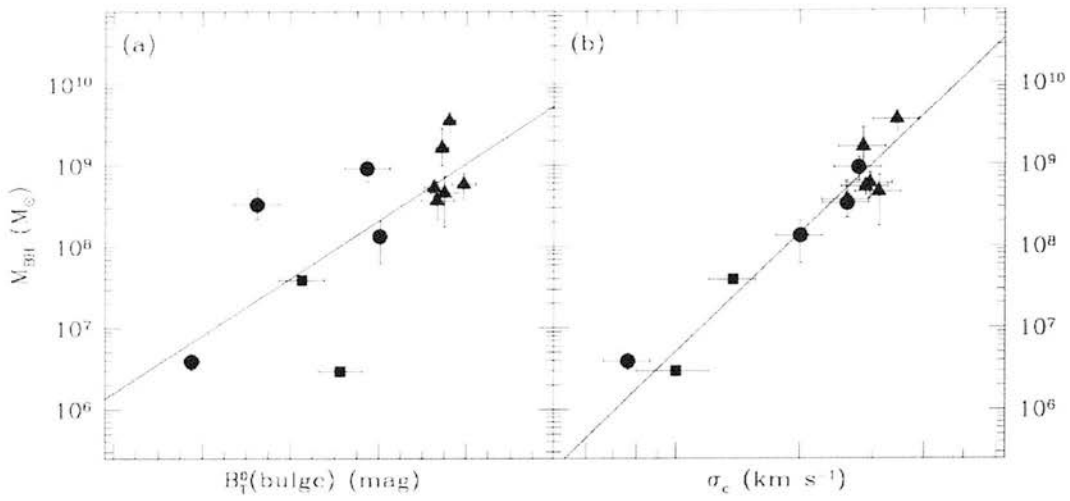

Figure 1.10: **a:** black-hole mass vs spheroid mass (luminosity).
b: black-hole mass vs stellar velocity dispersion. Adapted from Ferrarese and Merritt (2000)

(Ferrarese and Merritt 2000, Gebhardt et al. 2000) - see figure 1.10. We now have direct evidence, and good mass estimates for black-holes at the centre of 57 nearby inactive ellipticals, and both relationships are looking to hold, with a roughly 0.3dex scatter on the $M_{BH} - L_B$ "Magorrian" relation, and a somewhat tighter correlation of M_{BH} with σ.

However, it is important to stress that this finding is relatively new, and there is still much work to be done. Note in particular, that very few objects have been studied using more than one technique, to check and confirm consistency. In at least one case (IC1459) the black-hole masses determined from gas motions is significantly lower than that derived from stellar motions. And late type galaxies are still heavily under-represented. However, all of the evidence so far uncovered points to black-holes, far from being some rare exotica, are as ubiquitous as the galaxies that litter the cosmos, and that the two are connected in terms of their formation and evolution.

1.4 Galaxy Formation and the Black-Hole Connection

From the cosmologist's point of view, galaxies can be viewed as the end-point of the evolution of density fluctuations that arose in the very early Universe. A detailed account of the cosmological models that give rise to such density fluctuations is outwith the scope of this thesis, but for a comprehensive introduction see for example Peacock (1999). We cannot directly observe the processes that occurred before matter-radiation decoupling, and which shaped the subsequent evolution of our Universe. Tracing the evolution of the galaxies as far back as we *can* observe, has therefore become one way of constraining cosmological models, and exploring the effects which govern the structure of the Universe on the largest scales. The formation mechanism of elliptical galaxies, in particular, remains a fundamental and controversial issue in cosmology.

The traditional approach to modelling galaxy evolution has been to treat protogalaxies and protoclusters as conglomerations of gas and dust which simply evolve within their own potential well, defined early on by a dark matter halo (after decoupling from the dominant radiation field). Such evolution is punctuated by bursts of star formation, often triggered through mergers, which will depend in turn on the presence of other nearby halos. As we have seen, however, there is now significant evidence that supermassive black-holes play a key role in the evolution of a galaxy.

Current cosmological models are dominated by ΛCDM. This framework leads to a hierarchical picture of galaxy formation, which naturally explains the rise in number density of quasars at early times in terms of the growth of host galaxies through mergers, to a scale at which they can sustain a QSO nucleus (see for example Efstathiou and Rees 1988). The subsequent drop after $z \sim 2$ is a reflection of the lower density of the Universe overall, and the reduced frequency of mergers. In such a hi-

erarchical scenario, elliptical galaxies are predicted to grow typically in mergers of intermediate-mass discs at low-redshift (Kauffmann and Haehnelt 2000), However, there is considerable disagreement over whether this hierarchy is actually observed, with evidence that at least some massive ellipticals are formed in a rapid ($\leq$1Gyr) starburst at $z > 3$ (Nolan et al. 2001). Steidel et al. (1999) suggested that the formation of present day ellipticals has already been observed at optical wavelengths through the discovery of the Lyman break population at $z \approx 2-4$, but these objects are undetected with SCUBA, and thus it appears that the star formation rates are too low to explain the peak observed in the Madau plot (figure 1.1). Indeed, the sub-mm data point to a population of very massive, rapidly star-forming galaxies at $z > 2$ (Dunlop 2001, Ivison et al. 2002, Aretxaga et al. 2003, Chapman et al. 2003), which are more reminiscent of the traditional "Monolithic collapse" models of galaxy evolution than of the hierarchical buildup. However, the monolithic model cannot be fitted into a consistent picture of galaxy evolution from density perturbations in the early Universe. Something is clearly missing.

The possible role of active nuclei in galaxy formation and evolution was noted early on by Burbidge et al. (1963), but largely ignored until very recently. We now see that the central region could play a critical role in regulating the amount of star formation that can occur in a given protogalaxy. A new generation of galaxy evolution scenarios has thus emerged, in which there is a partnership between the protogalactic gas and dust, and the central black hole. The black hole provides an additional feedback mechanism thanks to winds generated by the radiation pressure (equation 1.13) from radiating infalling matter (Silk and Rees 1998). If this wind becomes strong enough, material will be ejected from the protogalaxy, enriching the IGM, reducing the protogalaxy's capacity to form stars, and cutting off the black-hole's fuel supply. Thus there is a natural upper limit to the size of black-hole that can be found in an efficiently star-forming galaxy. With the discovery of quasars at redshifts of 5, 6, and beyond, the existence of seed black-holes at even greater redshifts has become undeniable. Assuming roughly Eddington accretion, we would require a seed of $\sim 10^5 M_\odot$ at $z \approx 9$ in order

to produce a $10^9 M_\odot$ hole by $z \approx 5$, and it is possible that black-holes form before stars, as the first sub-galactic structures.

Such a hypothesis has a number of intriguing consequences for subsequent star formation, and evolution of both the protogalaxy itself, and the surrounding region. Firstly, the hard UV radiation from the hole is effective at destroying molecular gas, H_2, and will thus inhibit star formation, and the formation of dwarf galaxies within the vicinity. However, the densest regions will be able to form stars effectively, and this includes parts of the accretion disk itself. Being optically thick, we would expect to find regions of cool molecular gas, and any material falling into the middle region should be converted to stars with high efficiency. Outflow from such stars would help both in seeding further star-formation directly (as in classical pictures of galaxy evolution) and in fuelling the black hole, and thus the quasar-driven winds. This wind in turn can spread the enriched material far further than is classically possible, even ejecting it from the protogalaxy altogether, and enriching the IGM.

This field is a complex one with many inter-relating aspects, many of which we do not possess a complete isolated physical picture for. However, it is an appealing toy model which we can refine by holding it up to the light of observational evidence. Fabian (1999) demonstrated that the hard X-ray background is consistent with being emitted by a population of black holes that are heavily obscured throughout most of their growth. Fabian's is a development of Silk & Rees's quasar-driven wind model, with a more detailed consideration of the obscured growth phase. He posited a large population of hitherto unobserved quasars which, it is arguable, are now being detected by SCUBA and Chandra (Barger et al. 1998, Hughes et al. 1998, Blain et al. 1999, Alexander et al. 2002), and possibly in some of the more FIR-luminous ULIRGs. The unobscured objects that we know as quasars would then simply be a relatively short-lived post-obscuration phase of the AGN activity, lasting only from when the AGN becomes bright enough to blow off the remaining obscuring material until the accretion disc empties itself out into the black-hole. If true, this model means that the major black-hole

growth phase has not yet been directly observed.

Until we possess a detailed model of the physics of AGN - galaxy interaction, it is probably too early to expect our models of galaxy evolution to accurately recreate the visible Universe. However, there have been attempts. Kauffmann and Haehnelt (2000) were the first to incorporate black-hole growth into their semi-analytic models of galaxy evolution. They assume fuelling occurs only during major mergers. Whilst we know that mergers are an effective way of fuelling star-formation, and that both mergers themselves, and outflow from star-forming regions might provide efficient ways to feed an AGN, it is far from clear that there is causal link between mergers and AGN activity. More recently, Granato et al. (2004) have coupled a model of AGN feedback with their semi-analytical treatment of cosmic galaxy evolution to successfully reproduce the observed sub-mm number counts, redshift distributions and the epoch-dependent K-band luminosity function of spheroidals - an important indicator of the stellar population.

The study of quasar host galaxies of quasars is therefore intimately tied to the ongoing study of the evolution of the galaxy population at large. There is a lot of complex and poorly understood physics governing the interaction between AGN and galaxies, and detailed observational work at all wavelengths will be necessary before this issue is resolved.

1.5 Host Galaxy Studies

Host galaxy studies began over a decade after the initial discovery, although the true point-like nature of the quasars was questioned early on by Matthews and Sandage (1963). The first hard evidence that quasars were connected with galaxies came in the early 1970's, with the discovery of fuzzy halos of light surrounding some of the nearest ones (Kristian 1973). However, nothing physical was discernible about these hosts. The fact that they were definitely there represented a major breakthrough at the time.

Boroson and Oke (1982) used off-nuclear spectroscopy of 3C48 showed that this fuzz was stellar in nature.

The first successful attempt at obtaining actual physical parameters of quasar host galaxies was made by Smith et al. (1986). Using 1D profile fitting to a sample of 31 RLQs and RQQs at $z < 0.3$, they found all hosts to be from the luminous exponential tail ($L \geq L^*$) of the Schechter function (equation 2.10). A 0.7-0.8 magnitude deficit in the hosts of radio-quiet with respect to radio-loud quasars was also found. Furthermore, a morphological discrimination was found between the hosts of these two types of quasars; while RQQ's were found to prefer disc-like hosts, their Radio-Loud counterparts preferred early-type hosts. This finding was taken as evidence that RQQ's and RLQ's were simply luminosity-scaled versions of the low-redshift Seyfert and Radio galaxies respectively. Another interesting finding in this pioneering study was that some 50% of all the hosts showed signs of disturbance, suggesting that galactic interactions might play a crucial role in triggering AGN activity.

Many of these findings have been reinforced, and become standard results, although using R and I-band imaging, Veron-Cetty and Woltjer (1990) found that *both* RLQ *and* RQQ hosts have somewhat bluer colours than normal galaxies. This was the first real suggestion that the simple unification of Seyferts and RQQ's was not the full picture, though the idea has lingered in the literature to the present day. The difference in host luminosity of RLQ's and RQQ's is also hotly debated, and may be a false result imposed by inherent bias in the samples (section 1.6.1).

The first sub-arcsecond-seeing images of quasar hosts arrived courtesy of Hutchings and Neff (1992). Once again, radial profile fitting was the order of the day, and morphologies were found for 18 of the 28 quasars; mainly ellipticals, 4 exponential discs and the remainder too highly disturbed to distinguish. This work led to the conclusion that a significant proportion of RQQ's are in fact found in early types, along with the majority of RLQ's. The body of evidence suggesting a connection between AGN activity and galaxy mergers was continuing to grow.

The infrared revolution of the 1980's led to further breakthroughs. Observing quasars in the near-infrared minimises the nuclear to host ratio, and allows us to cut through obscuring dust. Dunlop et al. (1993) used deep K-band imaging of carefully statistically matched (see section 1.6.1) samples of RLQ's and RQQ's at $z \simeq 0.2$. This study was the first to compare the two populations whilst avoiding inherent selection bias. Unlike in previous studies, no significant difference was found between the luminosities of the hosts of RLQ's and RQQ's. All were found to be from the high-luminosity exponential tail of the galaxy luminosity function. An H-band study (McLeod and Rieke 1994a,b) found an average luminosity of $2L^*$ for 26 low redshift quasars, including five radio-loud ones. However, the data were too poor to allow morphological discrimination, despite using NIR observations to minimise the nuclear to host ratio.

By the mid-90's it was becoming clear that the 1D approach was insufficient for morphological discrimination of host galaxies, and in Taylor et al. (1996) a new, fully 2-dimensional technique (adopted and developed in this study - see chapter 2) was presented. This work took the matched RLQ/RQQ sample of Dunlop et al. (1993), and an additional sample of powerful RG's at the same redshift, matched in radio properties to be statistically indistinguishable from the RLQ sample. All three AGN subsamples were shown to have large, luminous hosts. However, no difference was detected between the host luminosities of the three subsamples, supporting (in the case of the RG and RLQ samples) the model for radio-loud unification through orientation of the host. The other significant finding of this study was that the majority of RQQ's dwell within elliptical, rather than the hitherto expected disc type galaxy. Within the RQQ sample, it was further found that the probability of finding an early type host was an increasing function of the quasar luminosity.

By this time HST was finally on the scene, but without the much-vaunted FOC coronograph. Instead, Bahcall et al. (1994, 1995b,a, 1996) made use of WFPC2 in the first HST host galaxy study to examine a statistically meaningful number of objects. Results were initially controversial and the

study received a great deal of publicity (see for example Disney 1998). Of the first eight objects studied, just three gave positive identifications of underlying hosts, leading the team to the conclusion that they were seeing naked quasars (ie before substantial star formation had occurred), or that the host galaxies were far dimmer than had previously been accepted. Re-analysis of the data by McLeod and Rieke (1995) demonstrated that the problem had been in over-subtraction of the nuclear emission, and that the hosts were in fact detectable at very low surface-brightness. Saturation in the central region had meant that PSF normalisation had to be performed too far out - at a point where the host galaxy made a significant contribution to the overall light. Once this problem was settled and a new empirical PSF had been obtained, Bahcall et al. (1997) made use of PSF subtraction and 1D and 2D modelling of the residual flux, leading to the detection of 18 out of the 20 hosts. They were found to be a mixed bag (Ellipticals, Discs and Irregulars all present). RLQ hosts were once again found to be almost a magnitude fainter than the hosts of their radio-loud counterparts, contradicting the evidence of Dunlop et al. (1993), Taylor et al. (1996).

A more distant sample ($0.4 < z < 0.6$) was investigated by Hooper et al. (1997), using the WFPC2 Planetary Camera. This chip offers superior resolution of the PSF, compared with the Wide Field chips, but the smaller pixels also result in higher read noise and lower saturation levels. Using a 2D modelling technique they found hosts for each one of their 16 quasars, all of which were luminous ($L > L^*$). In this study, objects were matched and no difference was found in the luminosity of hosts of RLQ's and RQQ's. Nuclear and host luminosities were found to be weakly correlated. In contrast, Boyce et al. (1998) once again found the hosts of RLQ's to be consistently brighter (by ≈ 0.7 magnitudes) than their radio-quiet counterparts. The majority were best fit by early-type galaxies, and once again, all were found to be luminous.

By the late 1990's, HST had a new tool in the form of NICMOS. At last it was possible to use Hubble to probe right down into the infrared. This study gave the benefits of some earlier ground

based studies, in being able to minimise the nuclear to host ratio, and get really firm host galaxy detections. It also allowed host galaxy studies to be taken to greater redshifts.

A major new HST study into the evolution of quasar hosts was launched with the publication of McLure et al. (1999), McLure (1999), Kukula et al. (1999) (see section 1.6). In McLure et al. (1999), the matched samples of $z \simeq 0.2$ RLQ's, RQQ's and RG's from Taylor et al. (1996), Dunlop et al. (1993) were examined once again, this time in R-band using WFPC2, using the 2D modelling technique of Taylor et al. (1996). The resulting R-K colours were found to be consistent with mature stellar populations. This paper also provided the first unambiguous evidence that all RLQ's, and all RQQ's brighter than $M_R = -24$ reside in giant ellipticals, eliminating the possibility that the radio-loudness dichotomy could be resolved simply through host galaxy morphology. black-hole masses, and Eddington luminosities were calculated using the black-hole - spheroid mass relationship (Magorrian et al. 1998), and comparing to estimates made from radio properties (Franceschini et al. 1998). Meanwhile, high redshift quasars were the subject of Kukula et al. (1999). Using NICMOS, J and H band images were taken of two quasar samples at redshifts of $\simeq 1$ and $\simeq 2$ respectively, corresponding to a restframe waveband around V. At these redshifts, it is hard to make a distinction between different morphologies, but the host and nuclear luminosities were recoverable.

Today people are pushing out to redshifts of 2 and beyond, using NICMOS (Ridgway et al. 2001), and attempting to use the new generation, 8m ground-based telescope equipped with adaptive optics (Guyon et al. 2001).

1.5.1 Key issues

There is still plenty of contradictory evidence circulating, although signs of a consensus have finally emerged. All results are now consistent with the picture of AGN only being hosted by the most

luminous of galaxies ($L \geq L^*$). The evidence of McLeod and McLeod (2001), Hamilton et al. (2000), McLure et al. (1999) suggests that the hosts of RLQ's and RQQ's are indistinguishable in terms of Luminosity. This point is controversial, but it seems plausible that other studies may disagree due to inherently biased samples (see section 1.6.1). If it is the case, then how do we explain the vast range (over 5 decades) in optical nuclear activity observed within radio loud objects? Rather than a dependence upon host galaxy, the key must lie with the black-hole itself, and perhaps the rate of accretion of material onto the black-hole. A correlation between host and nuclear luminosity is seen at the low-luminosity, Seyfert end of the scale, and some studies report its continuation into the quasar regime (Dunlop et al. 2003), whilst others reject it (Percival et al. 2001). The problem here is that there are insufficient luminous AGN to make statistically meaningful tests in the local Universe, which has been studied so far. This issue is addressed in chapter 2.

The issue of morphological difference is still a little unclear. It has long been supposed that RLQ's reside in elliptical galaxies, and RQQ's in spirals. However this conclusion has recently been show to be a result of intrinsic bias in the populations in early studies (Dunlop et al. 2003). The parent population of quasars, both radio-loud and radio-quiet, appears to be relatively normal massive elliptical galaxies. Evidence for RQQ's being found in spirals appears to be diminishing, with the majority of such objects not actually quite making the quasar grade, but rather falling short of the $M_V = -23.5$ quasar-Seyfert cutoff. The requirement for a massive spheroidal galaxy may now be seen as a requirement for a supermassive black hole. It appears that a black-hole of mass in excess of $5 \times 10^8 M_\odot$ is prerequisite for a quasar, whilst radio loudness demands one in excess of $10^9 M_\odot$.

However, there is evidence for a difference in the evolution of the host galaxies. From their optical luminosities it appears that RLQ hosts are consistent with the pure luminosity evolution of a mature stellar population (e.g. Dunlop et al., 2003). RQQ hosts, however, appear to show little or no change in luminosity between $z \sim 2$ and 0.2. However, the significance of this finding is currently

of marginal significance, and dependent on cosmology. It is to this issue that we turn in chapter 3. Broad absorption lines, just blue-ward of strong nuclear emission lines, are observed in $\sim$10% of RQQ spectra. These are indicative of a gas outflow close to the central source, and were thought to be absent in the spectra of RLQ's. However, even this difference has been thrown into doubt with the discovery by Wills et al. (1999) of possible BAL features in the powerful RLQ 1004+130. The reason for the broad range in radio properties of AGN remains an intriguing puzzle for astrophysicists. Radio emission cannot be obscured by dust, but is it possible that something in the galaxy stunts the growth of jets, or indeed that such a process results in a change in the star formation process inside the galaxy.

Mergers remain a prime candidate for the triggering of starbursts, supported by observational evidence from ULIRGs, and the predominance of quasars and potential quasar hosts in rich cluster environments. It seems that starbursts, mergers and active nuclei are very closely intertwined. **?** suggest that mergers are more ubiquitous in active galaxies than we have been led to believe. Using VLA 21cm mapping of neutral hydrogen, we see what cannot be seen in the optical; virtually all local active galaxies ($z < 0.07$) show signs of ongoing or remnant tidal interactions. Most low-z AGN are not in fact descendants of their high-z counterparts, but rather represent a newly triggered population of AGN. However, in an HST survey of 76 low-z, X-ray selected quasars, no evidence was found for *any* strong interaction or merger activity (Schade et al. 2000). Perhaps we are seeing the remnants from mergers long ago, and recent such events are not requisite for current AGN activity.

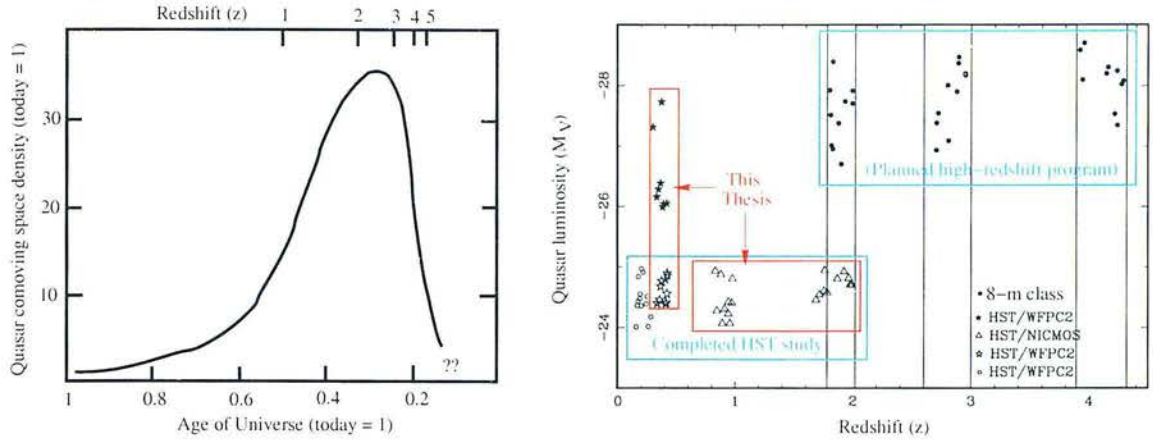

Figure 1.11: **The scope of this study:** Exploration of the evolution of quasar hosts from their heyday at $z \approx 2$ to the present. Chapter 2 focuses on observations at $z \approx 0.4$, including a sample of the most luminous nearby quasars. Chapter 3 looks at new U-band imaging at $z \approx 1$ and 2, and examines evolution of the hosts through cross-Lyman-break $(U - V)$ colours.

1.6 This Thesis, and its place in our Ongoing Study of Host Galaxy Evolution

I am working as part of an international collaboration to investigate the evolution of quasar hosts from the present, back to the quasar era at $z \simeq 2$, and hopefully further, using adaptive optics and large telescopes. We aim to make definitive, unbiased experiments using the best possible instrumentation and to investigate a good range of subject types.

For ease of comparison with previous work I have adopted an Einstein-de Sitter universe with $H_0 = 50$ km s^{-1} Mpc^{-1}.

1.6.1 Statistical matching

In order to avoid any inherent bias in our AGN subsamples (RLQ's, RQQ's, RG's) we want to ensure that we're comparing like with like. We therefore aim to make the samples indistinguishable from one

another with respect to the properties of definition:

- For RLQ's and RQQ's, we match **optical** properties by ensuring that the 2D distribution on the $V-z$ plane are indistinguishable.

- For RG's and RLQ's we match **radio** properties, through their distributions on the $P-z$ and $\alpha-z$ planes.

1.6.2 Redshift evolution

We have taken samples at a range of redshift bands (illustrated in figure 1.11):

Work at $z \simeq 0.2$:

Quasar model fitting has been performed upon a large sample of nearby quasars in R-band, using HST (McLure et al. 1999, McLure 1999) and K-band using UKIRT (Taylor et al. 1996). $R-K$ colours have been calculated for the host galaxies, to allow us to begin investigating the stellar populations of quasar hosts, and their evolution.

Work at $z \simeq 0.4$: Chapter 2

Examining the apparent correlation between host and nuclear luminosity observed in Seyferts, to see whether it continues into the quasar regime, or plateau's off as nuclei are reaching Eddington (radiation-pressure limited) accretion. This work will provide valuable information for unification schemes. At present the data is very sketchy (Dunlop et al. 2003) as the study only goes out to redshift 0.2, within which volume very few sufficiently luminous quasars are observed.

Work at $z \simeq 1$ and 2: Chapter 3

The samples have already been observed with NICMOS in J and H band respectively, and host properties recovered. However, morphological discriminations could not be made (Kukula et al. 1999) at these rest-frame V-band wavelengths. The samples are revisited here in V and I band respectively (rest-frame near-UV). This work allows stellar population modelling and testing of evolutionary models, in particular the Passive evolution model assumed by Kukula et al.

Further work:

We have been awarded time on Gemini North to look at samples at redshifts of 2, 3, and 4. As in all our samples, careful filter selection is essential in order to catch as much host galaxy light as possible, illustrated for these high-redshift samples on the right of figure 1.11.

1.6.3 Thesis structure

This thesis is divided into 3 main chapters.

In chapter 2 I present the 2-dimensional host galaxy modelling technique used throughout this work. This technique is then applied to a sample of quasars at $z \approx 0.4$ in a Hubble Space Telescope optical imaging project. The sample includes some of the most luminous quasars at $z < 0.4$, and forms a useful baseline for studies of quasars at higher redshift. The scatter in the host vs nuclear luminosity distribution is considered a some length.

Chapter 3 revisits the sample of Kukula et al. (2001) at $z \approx 1$ and $z \approx 2$. The U-band imaging presented here is used in concert with Kukula et al.'s V-band imaging to obtain host galaxy $U - V$ colours. These are compared with Simple Stellar Population synthesis models in order to test the key assumption of Passive Evolution.

Chapter 4 is an K-band UKIRT imaging study taking a sample of ULIRG's and comparing them with a control sample of IR-bright QSO's. By observing in K-band we are able to uncover smooth host galaxies from even the most disturbed (in the optical) objects. The possibility of an evolutionary link between the ULIRG's and the QSO's is investigated.

All of the modelling images, including the reduced HST and UKIRT frames, the best-fitting quasar models, and the underlying best-fit host galaxies, are presented in the appendices in order to save space in the body of the thesis.

Finally, chapter 5 sums up the work that has been done, looking at what has been learnt, and what new questions have been posed. A number of possible directions for ongoing work are proposed, several of which are already being actively pursued.

CHAPTER 2

An HST imaging study of Luminous Quasar Hosts at z=0.4

In this chapter, I present the results of a deep HST/WFPC2 imaging study of 17 quasars at $z \sim 0.4$, designed to determine the properties of their host galaxies. The sample consists of quasars with absolute magnitudes in the range $-24 \geq M_V \geq -28$, allowing us to investigate host galaxy properties across a decade in quasar luminosity, but at a single redshift. The most powerful objects in this $z = 0.4$ sample are comparable to the luminous quasars found at very high redshifts. Most previous imaging studies of AGN hosts have largely focussed on lower-luminosity quasars, where the disentanglement of host galaxy and PSF light is less problematic. As in previous studies, I find that the host galaxies of all radio-loud quasars, and all radio-quiet quasars more luminous than $M_V = -25$, are massive ellipticals with luminosities $> L^{\star}$. From the model host galaxies I have estimated spheroid and black hole masses, and the efficiency (with respect to the Eddington luminosity) at which each quasar is

accreting material. I find that the increase in nuclear luminosity of a factor of 10 across the quasar sample is the result of an increase in both black-hole mass and fuelling efficiency. Through some simple Monte-Carlo simulations, I investigate the role of scatter on the black-hole:spheroid mass relation in affecting the observed nuclear-host luminosity distribution. Statistical limits are placed on the possibility of a fixed fuelling rate for quasars, and the first evidence is presented for a high-luminosity turnover in the host galaxy population.

This is the first time that the host galaxy morphologies of such luminous quasars have been successfully recovered, and represents an important step in the investigation of quasar history out to larger, more cosmologically significant distances.

2.1 Introduction

As the most powerful class of active galactic nucleus (AGN), quasars provide a striking example of the complex interrelationship between galaxies and the supermassive black holes in their centres. Thanks largely to the Hubble Space Telescope (HST) the last five years have seen huge advances in our understanding of the host galaxies of the nearest ($z < 0.3$) quasars (Bahcall et al. 1997, Hooper et al. 1997, Boyce et al. 1998, McLure et al. 1999, Hamilton et al. 2000, McLeod and McLeod 2001, Dunlop et al. 2003). HST observations have demonstrated that low-z quasar hosts are luminous ($L > L^{\star}$) galaxies, confirming the results of earlier ground-based studies. But the key advantage of HST has been its ability to distinguish between disc and elliptical morphologies, leading to the finding that all radio-loud quasars (RLQs) and the majority of radio-quiet quasars (RQQs) occur in massive elliptical galaxies.

With recent improvements in the capabilities of both HST and ground based telescopes, new studies are beginning to shed light on the evolution of quasar hosts from high redshifts ($z > 1$) down

to the present day (Lehnert et al. 1999, Falomo et al. 2001, Stockton and Ridgway 2001, Ridgway et al. 2001, Kukula et al. 2001, Hutchings et al. 2002). At the same time it has become increasingly clear from studies of inactive galaxies that black hole and galaxy formation and growth are intimately linked processes, resulting in the now well-established correlation between black-hole mass and the mass of the host galaxy's stellar bulge (Magorrian et al. 1998, Gebhardt et al. 2000, Merritt and Ferrarese 2001).

Most previous studies of quasar hosts have concentrated on quasars of relatively low luminosity, largely because it is much easier to disentangle the host and nuclear light in such objects. However, the quasar population spans luminosities ranging from the (admittedly somewhat arbitrary) transition from Seyfert galaxies at $M_V = -23$ through to the most luminous objects, with absolute magnitudes $M_V \sim -30$; a factor of > 1000 in terms of luminosity. The majority of quasars currently known at large redshifts belong to the high end of the luminosity function. This is due to the degeneracy between redshift and luminosity in flux-limited samples, a situation which is beginning to be rectified as modern deep surveys detect low-luminosity, high-z quasars in increasing numbers. However, to understand the behaviour of the most massive galaxies and their black holes in the cosmologically-interesting high redshift regime ($z > 2$) will inevitably require the study of the most luminous quasars at these redshifts.

The aim of the current study is to break the degeneracy between quasar luminosity and redshift by studying a sample of quasars at a single redshift that spans an appreciable fraction of the quasar luminosity range (see Figure 2.1). The lowest redshift at which this work can be done is $z \sim 0.4$, since the volume of the local universe is too small to contain examples of the most luminous quasars, with $M_V < -27$, comparable to the most luminous quasars at very high redshifts.

Not only does this strategy allow us to explore the relation between quasar luminosity and the properties of their host galaxies, but the most luminous objects in this programme will also provide a

low redshift baseline against which to compare the hosts of luminous high-z quasars in future studies.

The key issue is, of course, the disentanglement of any structure in the image that is associated with the PSF from that which is actually intrinsic to the quasar's host galaxy. The very earliest studies merely recognised the presence of a faint "fuzz" around quasars (Kristian 1973) but the technology did not yet exist to characterise this light. Various techniques have been developed and tested over the past 3 decades, keeping apace of technological developments. Techniques include simple PSF subtraction (Smith et al. 1986, Dunlop et al. 1993) 1-dimensional (radial-profile) fitting (Wright et al. 1998), and of course full 2-D fitting of a model host galaxy (e.g. Taylor et al. 1996).

2.2 The quasar sample

This work is part of a larger project making use of HST to study the cosmological evolution of quasar host galaxies out to $z \simeq 2$ (see Figure 2.1). The sample was selected from the quasar catalogue of Veron-Cetty and Veron (1993a) and comprises two subsamples, both in the redshift range $0.29 < z < 0.43$ (Table 2.1).

The first, "low luminosity" subsample consists of a random selection of five radio-loud and five radio-quiet quasars (RLQs & RQQs) with absolute magnitudes $-24 > M_V > -25$. All of the RLQs have total 5GHz radio luminosities $> 10^{24}$W Hz^{-1}sr^{-1} and steep radio spectra to ensure that their radio luminosity is not boosted by relativistic beaming. The RQQs have all been surveyed in the radio at sufficient depth to ensure that their total 5GHz luminosities are indeed $< 10^{24}$W Hz^{-1}sr^{-1} (see Table 2.2). Previous HST studies of quasar hosts (McLure et al. 1999, Kukula et al. 2001, Dunlop et al. 2003) concentrated on quasars of similar, relatively low luminosity $M_V > -25$ but having a range of redshifts out to $z \simeq 2$ (Figure 2.1), and looking in particular at systematic differences between RLQ's and RQQ's.

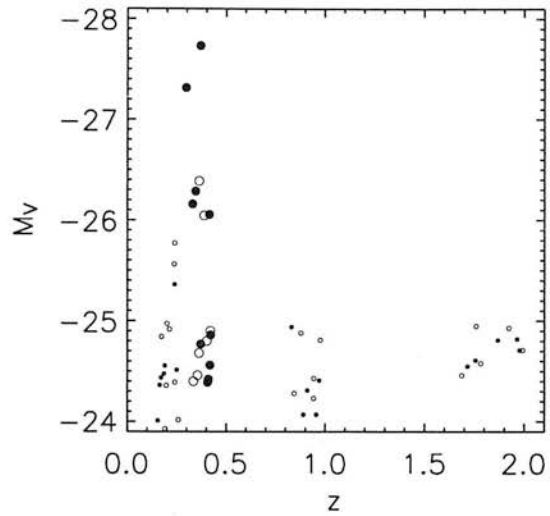

Figure 2.1: **Absolute magnitude versus redshift** for quasars observed to date in our HST host-galaxy imaging programmes. Filled circles represent radio-quiet quasars (RQQs) and open circles radio-loud quasars (RLQs). Our earlier work (small symbols) concentrated mainly on quasars of relatively low luminosity (typically $M_V > -25$) in three redshift regimes ($z \simeq 0.2, 1$ & 2), allowing us to probe the evolution of the host galaxies over a large fraction of cosmic history (Mclure et al. 1999; Kukula et al. 2001; Dunlop et al. 2002). The current study (large symbols) is designed to explore an orthogonal direction in the $M_V - z$ plane, by sampling a large range of quasar luminosities at a single redshift, $z \simeq 0.4$. This is the lowest redshift at which very luminous quasars (those with $M_V < -27$) can be found, comparable to the most luminous quasars in the high-redshift universe.

The second, "high luminosity" subsample consists of all known quasars in this redshift range with absolute magnitudes $M_V < -26$, and includes 2 quasars with absolute magnitudes $M_V \simeq -28$ (0624+691 & E1821+643). It also includes one object, 1404−049, that turned out to be an inactive spiral at $z = 0.04$ (Figure 2.2).

The low-luminosity RLQ and RQQ subsamples were selected in such a way as to match their optical luminosity - redshift distribution, in the same manner as the $z \simeq 0.2, 1,$ & 2 samples of Dunlop et al. (2003). This selection is not described in detail here, since the full sample does not constitute a well-matched selection of RLQ's and RQQ's. These selection criteria were explained in the introductory chapter (section 1.6.1) and are discussed again in chapter 3 where we revisit the high-redshift samples of Dunlop et al. (2003).

Table 2.1: **Quasars in the current study.** J2000 co-ordinates were obtained from the Digitised Sky Survey plates maintained by the Space Telescope Science Institute. Redshifts and apparent V magnitudes are from the quasar catalogue of Veron-Cetty and Veron (2000). For consistency we use a B1950 IAU format to refer to the quasars in this sample; the name under which each object appears in the HST Archive is given in the final column and additional names are given in the description of each object in Section 2.7. The low-luminosity subsample was observed in HST Cycle 7, using the WF2 chip and the F814W filter. The high-luminosity subsample was observed in Cycle 9 using the WF3 chip, and the slightly narrower F791W filter. This latter observing run included one additional object, 1404−049, an inactive spiral galaxy at redshift 0.04 which had been misclassified as a quasar (Figure 2.2). This object has been omitted from the analysis presented in this paper.

Name (B1950)	Type	z	RA (J2000)	Dec (J2000)	V	M_V	Observing date	HST archive name
Low-luminosity subsample (Cycle 7; F814W)								
1237−040	RQQ	0.371	12 : 39 : 39.0	−04 : 16 : 38.5	16.96	−24.77	Feb 12 1999	1239−041
1313−014	RQQ	0.406	13 : 16 : 09.0	−01 : 54 : 54.1	17.54	−24.39	Feb 01 1999	Q1313−0138
1258−015	RQQ	0.410	12 : 58 : 13.9	−02 : 00 : 09.3	17.53	−24.42	Feb 19 1999	1258−015
1357−024	RQQ	0.418	14 : 00 : 06.4	−02 : 42 : 22.6	17.43	−24.56	Mar 01 2000	1400−024
1254+021	RQQ	0.421	12 : 57 : 05.9	+01 : 49 : 46.8	17.14	−24.86	Feb 11 1999	1257+015
1150+497	RLQ	0.334	11 : 53 : 22.3	+49 : 30 : 21.4	17.10	−24.40	Nov 25 2000	LB2136
1233−240	RLQ	0.355	12 : 35 : 39.6	−25 : 11 : 31.1	17.18	−24.46	Aug 09 1997	PKS1233−24
0110+297	RLQ	0.363	01 : 13 : 22.0	+29 : 58 : 58.8	17.00	−24.68	Feb 02 1999	B2−0110+29
0812+020	RLQ	0.402	08 : 15 : 21.3	+01 : 55 : 44.8	17.10	−24.80	Feb 18 1999	PKS0812+02
1058+110	RLQ	0.423	11 : 00 : 49.3	+10 : 47 : 00.3	17.10	−24.90	Apr 02 1999	AO1058+11
1313+705	Star	0	13 : 38 : 58.0	+70 : 16 : 32.1	12.77	–	Feb 25 2000	PSF-STAR
High-luminosity subsample (Cycle 9; F791W)								
0624+691	RQQ	0.370	06 : 30 : 08.6	+69 : 05 : 40.0	14.20	−27.73	May 25 2000	HS0624+6907
1821+643	RQQ	0.297	18 : 22 : 02.8	+64 : 20 : 05.3	14.10	−27.31	Aug 17 2000	E1821+643
1252+020	RQQ	0.345	12 : 55 : 22.5	+01 : 43 : 46.2	15.48	−26.29	May 16 2000	EQS−B1252+020
1001+291	RQQ	0.330	10 : 04 : 06.1	+28 : 55 : 19.2	15.50	−26.16	May 21 2000	TON0028
1230+097	RQQ	0.415	12 : 33 : 28.8	+09 : 31 : 04.9	16.15	−26.05	Jul 05 2000	1230+097
0031−707	RLQ	0.363	00 : 33 : 57.2	−70 : 25 : 24.5	15.50	−26.39	Aug 07 2000	MC4
1208+322	RLQ	0.388	12 : 10 : 39.8	+31 : 56 : 26.0	16.00	−26.04	May 07 2000	B2−1208+32
1313+705	Star	0	13 : 38 : 54.1	+70 : 16 : 21.2	12.77	–	May 01 2000	PSF-STAR

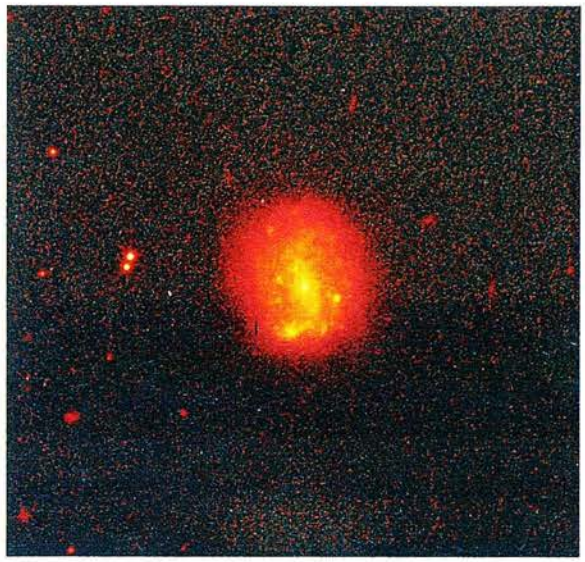

Figure 2.2: **The inactive spiral galaxy, 1404−049**, at $z = 0.04$ mistakenly identified as a quasar at $z = 0.4$, due to a typographical error, and its blue colour.

Table 2.2: V**-band magnitudes and 5 GHz radio flux densities** for the quasars in our sample. At the time of writing the majority of the RQQs have only upper limits to their radio fluxes, but these are sufficient to place them safely below the accepted radio-loud/radio-quiet boundary of $L_{5GHz} < 10^{-24}$ W Hz^{-1} sr^{-1}. The final column gives the source of the radio data (VCV=Veron-Cetty and Veron (2000); G+99=Goldschmidt et al. (1999); B+96=Blundell et al. (1996)). Upper limits from the NVSS were converted to 5 GHz by assuming a radio spectral index $\alpha = 0.5$ ($f_\nu \propto \nu^{-0.5}$).

Source	Class	z	V	S_{5GHz} (mJy)	L_{5GHz}	Ref.
Low-luminosity						
1237−040	RQQ	0.371	16.96	< 0.3	< 22.14	G+99
1313−014	RQQ	0.406	17.54	< 0.3	< 22.21	G+99
1258−015	RQQ	0.410	17.53	< 0.2	< 22.05	G+99
1357−024	RQQ	0.418	17.43	< 0.3	< 22.24	G+99
1254+021	RQQ	0.421	17.14	< 0.3	< 22.25	G+99
1150+497	RLQ	0.334	17.10	717.0	25.62	VCV
1233−240	RLQ	0.355	17.18	670.0	25.45	VCV
0110+297	RLQ	0.363	17.00	340.0	25.17	VCV
0812+020	RLQ	0.402	17.10	845.0	25.62	VCV
1058+110	RLQ	0.420	17.10	225.0	25.12	VCV
High-luminosity						
0624+691	RQQ	0.370	14.2	< 1.2	< 22.75	NVSS
1821+643	RQQ	0.297	14.1	8.6	23.58	B+96
1252+020	RQQ	0.345	15.48	0.8	22.50	G+99
1001+291	RQQ	0.330	15.5	< 1.2	< 22.65	NVSS
1230+097	RQQ	0.415	16.15	< 1.2	< 22.85	NVSS
0031−707	RLQ	0.363	15.5	95.0	24.62	VCV
1208+322	RLQ	0.388	16.0	91.0	24.90	VCV

2.3 Observing strategy

The HST observations for the entire project, outlined in Dunlop et al. (2003) were carried out as a group, with James Dunlop as the PI. All of our previous HST observations of quasar hosts were carefully designed to maximise the chances of successfully separating the starlight of the host from the point spread function (PSF) of the central quasar. We used the same observing strategy for the current observations and, since some of the quasars in our new sample are significantly more luminous than those in the earlier programmes, these precautions assume even greater importance.

Observing dates for each object are listed in Table 2.1, along with the name under which the dataset is listed in the HST Archive. The observations were carried out in two different HST observing cycles, although in practise the dates overlap. Observations of the low-luminosity subsample were carried out in Cycle 7 whilst the high-luminosity subsample was observed as part of Cycle 9.

2.3.1 Choice of filter

As in previous programmes we selected filters to correspond to V-band in the quasar's restframe. This choice ensures that our images sample the object's restframe spectrum longwards of the 4000Å break, where the starlight from the host is relatively bright, whilst avoiding strong emission lines such as Hα and [OIII]λ5007. Despite being directly associated with the quasar activity, ionised emission line regions can extend over several kiloparsecs. By excluding such emission from the images, we obtain a cleaner picture of the distribution of starlight in the hosts.

For the low-luminosity subsample we used the F814W "broad I" filter which corresponds roughly to the standard cousins I-band. The high-luminosity subsample covers a broader range of redshifts and in order to avoid contamination of the images by emission lines we used the slightly narrower F791W filter.

2.3.2 Choice of detector

Observations were made with the HST's Wide Field & Planetary Camera 2 (WFPC2). We opted to use the WF chips (800×800 pixels, with a scale of 100 mas pixel^{-1}) since their relatively large pixels offer greater sensitivity to low surface brightness emission. Targets were centred on one of the three WF chips, the exact choice depending on the which of the three had performed best over the period immediately prior to the Phase 2 proposal deadline.

2.3.3 Exposure times

High dynamic range is imperative in a study of this kind in which it is necessary to accurately characterise both the central core of the quasar as well as the faint outer wings of the PSF and the underlying host. In order to obtain a deep but unsaturated final image of each quasar we took several exposures of increasing length, with exposure times carefully scaled so that no image would saturate beyond the radius out to which the PSF could be followed in the previous, shorter exposure. The series of exposures could then be spliced together in annuli to construct an unsaturated image of the requisite depth (the pointing stability of HST between successive exposures using the FGS fine tracking mode is $\simeq 0.003$ arcsec).

For the "low-luminosity" subsample a single orbit of HST time was sufficient for each object, with exposures of 5, 26 and 3×600 seconds. For the more luminous quasars in the second subsample we required some shorter exposures to avoid saturation of the central pixels, as well as more long exposures to provide greater depth, since the wings of the quasar PSF encroach further out into the surrounding galaxy. Here we devoted two orbits to each object, with exposures of 2, 26, 2×100 and 3×600 seconds in the first orbit and 3×700 seconds in the second.

2.3.4 PSF determination

Previous host galaxy studies have emphasised the importance of characterising the instrumental point spread function (PSF) over a large range of radii in order to accurately separate the contributions of host galaxy and active nucleus. The structure of HST's PSF is quite variable, especially at large radii, and depends on its position in the instrument field of view, the SED of the target source and the timing of the observations.

We therefore devoted two orbits of our HST time allocation to obtaining deep, unsaturated stellar PSFs through both the F814W and F791W filters. The star used was GRW+70D5824 ($V = 12.77$), the same white dwarf used in our earlier host galaxy studies with HST (McLure et al. 1999, Kukula et al. 2001, Dunlop et al. 2003). This star is an optical standard for WFPC2, and so very accurate photometry is readily available. Its DA3 spectral type and neutral colour ($B - V = 0.09$) mimics well the typical quasar SED at the redshifts typical of our sample. In addition, as there are no comparably bright stars within 30 arcsec, we can be sure that our stellar PSF is not contaminated by light from nearby objects. The star was observed on the same part of the chip as the quasars.

We used an observing strategy similar to that for the quasars in order to obtain final images with high dynamic range. A series of exposures were carried out with durations of 0.23, 2.0, 26.0 and 160.0 seconds. Although the increasing exposure times lead to increasing saturation in the core, they never become saturated outside the radius at which the signal-to-noise of the preceding (shorter) exposure has become unsatisfactory. The *I*-band PSF is chronically undersampled by the 0.1 arcsec pixels of the WF chips, and a 2-point dither pattern was adopted in order to achieve better sampling. Dithering was not used on the quasar images, being unsuited to the 2-dimensional modelling described in section 2.5. Each additional exposure results in extra read-noise, and lowers our overall sensitivity to the low surface-brightness flux of the host galaxy.

2.4 Data reduction

All the images were passed through the standard HST/WFPC2 pipeline software which performs many of the initial image processing and calibration steps such as dark and bias frame subtraction, along with flat fielding. I carried out three additional reduction steps prior to analysing the images: cosmic-ray decontamination, sky subtraction, and reconstruction of the saturated core regions of both quasar and stellar PSFs by splicing in images with shorter exposures. Work was done using the IRAF data reduction software, and in particular, the HST-specific STSDAS package.

2.4.1 Removal of cosmic rays and bad pixels

Cosmic rays were removed using CRREJ, an iterative sigma-clipping algorithm in IRAF.STSDAS, which rejects high pixels from sets of exposures of the same field. The result is a single deep image (with integration time equal to the sum of its parts). This technique however cannot remove the numerous persistent bad or "hot" pixels that appear in the WFPC2 chips. These are listed in a tabular form on the WFPC2 web page and can be incorporated into a mask for modelling purposes.

2.4.2 Background subtraction

In order to remove a smoothly varying sky background from each image I adopted the following procedure. First, the mean and standard deviation of the background in each image were estimated from a subset of pixels excluding obvious sources. A estimate of the sky distribution was then created by fitting a 2nd order polynomial to each image, having replaced 1σ deviations away from the mean background level by the mean value. This smooth sky map was subtracted from each original image to give a final sky-subtracted frame.

2.4.3 Building deep, unsaturated quasar images

After cosmic ray removal from the deep images, the central regions from the shorter exposures were cut out, multiplied by a factor determined by annular photometry, and substituted into the saturated cores. I was careful to avoid regions in which the response of the CCD becomes non-linear, in effect cutting off at 3500 counts per pixel, althought the hard saturation level is somewhat higher than this ($\sim$ 5000 counts). All steps were performed using standard data-reduction task within IRAF. For the brightest quasars in our sample, in which the saturated region was large, I spliced together three images in this way to create the final image.

2.5 2-dimensional modelling of active galaxy images

Here we discuss the techniques used in analysing the quasar images in order to uncover the host galaxy, and determine its morphology and scalelength. This technique forms the core of the work for my PhD and is referred to in each of the following chapters, along with any modifications to the basic methodology laid out here.

2.5.1 History

As was mentioned in the introductory chapter, host galaxy studies really began with the discovery by Kristian (1973) of the low surface-brightness "fuzz" surrounding the bright optical nuclei of quasars. However, quantitative studies did not get underway until the mid-1980's, with 1-dimensional radial profile fits being done by Smith et al. (1986) At its inception, one of the key goals of the Hubble Space

Telescope was to be the investigation of quasar host galaxies, being ideally suited to the task thanks to its atmosphere-free PSF and good sensitivity. Partly as a result of the successes of HST/WFPC2, the fully 2-dimensional modelling approach is now firmly established in the literature, and has been shown to allow distinction between Disc and Elliptical morphologies in quasar host galaxies. The techniques and software used here to perform the 2D modelling are a continued development of those discussed in Dunlop et al. (1993), Taylor et al. (1996), McLure et al. (1999, 2000).

2.5.2 Quasar models

A simple idealised model quasar is constructed in 2 components: a model host galaxy and an unresolved nuclear component in the centre. The model is then convolved with the PSF and compared to the real quasar image. We choose which pixels to incorporate into the fit on an individual basis, eliminate bad pixels and companion objects from the fit, and assign each pixel an error based on its Poisson (shot) noise, assuming independence of adjacent pixels. I initially tested two *a priori* forms for the host galaxy light; an exponential Freeman disc (Freeman 1970):

$$\Sigma(r) = \Sigma_0 \exp\left\{-\frac{r}{R_0}\right\} \tag{2.1}$$

and a De Vaucoulers $r^{1/4}$-law (de Vaucouleurs and Capaccioli 1979):

$$\Sigma(r) = \Sigma_e \exp\left\{-7.67\left((\frac{r}{R_e})^{1/4} - 1\right)\right\} \tag{2.2}$$

These are modelled in terms of Σ, the galaxy surface brightness at radius r, and some "scalelength":

- R_0 is the exponential scalelength.
- $R_e = R_{1/2}$ is the effective scalelength, or half-light radius (within which half of the galaxy's

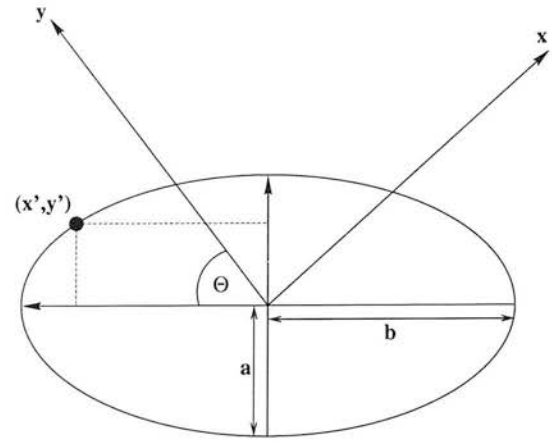

Figure 2.3: **The geometry of an ellipse.** The axes $(x\prime, y\prime)$ are aligned with the axes of the ellipse and are inclined w.r.t. the global or **image axes**, (x, y) by an angle Θ. See equation 2.6.

light falls);

Note that the two are simply related as $R_e = 1.68R_0$. Although it is common to describe disc galaxies in terms of their exponential scalelength, I have adopted the half-light radius, $R_{1/2}$, throughout this work.

It is clear that equations 2.1 and 2.2 can be written in the more general format, first proposed by Sèrsic (Sersic 1968):

$$\Sigma(r) = \Sigma_{1/2} \exp\left\{ -\left(\frac{r}{R_{1/2}}\right)^{\beta} \right\} \tag{2.3}$$

Here $R_{1/2}$ is the half-light radius, and β describes the overall shape of the profile.

I shall refer to the surface brightness in terms of μ, in the conventional astronomer's units of magnitudes per square arcsecond. Magnitudes are defined by Pogson's equation:

$$m_1 - m_2 = -2.5 \log_{10}(F_1/F_2) \tag{2.4}$$

Now, $\mu(r)$ describes an azimuthally-symmetric distribution, which is projected on to a generalised

elliptical coordinate system to allow for different eccentricities and orientations of the host galaxy (see Figure 2.3):

$$r = \sqrt{\frac{a}{b}x\prime^2 + \frac{b}{a}y\prime^2} \tag{2.5}$$

The new coordinates, $x\prime, y\prime$ are related to x, y as:

$$x\prime = i\cos\Theta + j\sin\Theta y\prime = -i\sin\Theta + j\cos\Theta \tag{2.6}$$

Note that the radius r is a geometric average of the semi-major and semi-minor axes. In galaxy modelling it is conventional to attribute the length of the semi-major axis to all points lying on a given ellipse. Such a definition is only really valid when discussing an inclined disc and is not, in general, a satisfactory measure of the true characteristic "size" of an elliptical galaxy. However, to facilitate direct comparison with previously published works, all scalelengths presented in this thesis have been converted to their equivalent semi-major axis (SMA) values, by the simple multiplication:

$$R_{1/2}(\mathrm{SMA}) = R_{1/2} \times \sqrt{\frac{a}{b}} \tag{2.7}$$

Care must be taken in translation from the continuous distribution described by $\mu(r)$ to the discrete regime of CCD pixels. Simply basing the surface brightness of each pixel upon the radius of the centre of that pixel is inaccurate, particularly toward the centre, where $\mu(r)$ varies rapidly over a pixel-width. Galaxy models were calculated on a grid with finer resolution than the pixel scale. The resolution was chosen in order to sufficiently sample the surface brightness, based on the gradient of the distribution, and the pixel size:

- $r < 0.5$"; 676 (26×26) calculations of μ per pixel.

- 0.5" $< r <$ 0.75"; 121 (11×11) calculations per pixel.
- 0.75" $< r <$ 1.0"; 25 (5×5) calculations per pixel.
- $r >$ 1.0"; 9 (3×3) calculations per pixel.

Having constructed the model, I rebinned to match the WFPC2 resolution. Each pixel therefore depends upon at least 9 calculations of its surface brightness, and up to 676 calculations within the central 0.5 arcsec. Flux is now added to the central pixel of the model galaxy, to represent the unresolved nuclear component - the QSO itself.

Free parameters

A given model quasar is thus specified uniquely by a point in the 6-dimensional parameter space $\{\mathbf{X}\} = \{L_n, \mu_{1/2}, R_{1/2}, \beta, \Theta, \frac{a}{b}\}$;

- L_n = luminosity of the nucleus
- $\mu_{1/2}$ = surface brightness of the host galaxy
- $R_{1/2}$ = half-light radius of the host galaxy
- Θ = position angle of the host galaxy.
- $\frac{a}{b}$ = axial ratio of the host galaxy.
- β controlling the shape of the profile (equation 2.3).

We now have a perfect, seeing and telescope free image of a quasar, which is convolved with the appropriate PSF to produce a simulated HST observation.

Modelling procedure

I follow the procedure of McLure et al. (1999) in fitting first to *a priori* disc ($\beta = 1$) and bulge ($beta = 1/4$) models. These fits are compared to determine whether the host galaxy is significantly better fit by an elliptical/bulge model or a disc model. The shape parameter, β is then freed up to test the validity of, and to help detect any deviation from the standard, fixed-β morphologies. Finally, I attempted to fit a 2-component model, which encompasses individual bulge and disc components, each with its own surface brightness, scalelength, position angle and axial ratio. This technique results in a 9-dimensional model (4 for each of the 2 galaxy components, plus one for the nuclear flux).

In addition, and as described below, a three-dimensional grid search was performed on the best-fit simple fixed morphology model. Here the free parameters were the nuclear luminosity, and the scalelength and surface brightness of the host galaxy. The axial ratio and position angle were held fixed in this case to make the grid search computationally viable. Such a grid search enables us to plot χ^2 contours and to explore the nature of any degeneracies in the parameter space.

2.5.3 Modelling the PSF

The Point Spread Function (PSF) of an optical device is its response to an infinitesimally small point of light. The PSF, or its Fourier Transform, known as the Optical Transfer Function (OTF) are commonly used in optics to characterise optical response.

Although the original Spherical Aberration present in the Hubble Space Telescope optics was fixed with the Corrective Optics Space Telescope Axial Replacement (COSTAR) unit aboard servicing mission STS-61 in December 1993, the PSF of the post-refurbishment HST remains complex (see Figure 2.4), sensitive to changes in position, and heavily under-sampled on the WF chips. This defect means that an accurate characterisation of the PSF for each individual quasar observation is essential

if we are to deconvolve host and nucleus.

Many workers in the field have made use of the TINYTIM software (Krist 1999). The TINYTIM calculation depends upon optical path differences within the Optical Telescope Assembly, and can in principle be performed at any sampling rate, and for any pixel on WFPC2. This code has been show to successfully reproduce the PSF for radii < 1.5arcsec. However, an empirical stellar PSF is essential for an accurate characterisation of the extended halo of scattered light at larger radii. The technique adopted here is to use a composite stellar plus TINYTIM PSF. However, the sub-pixel centring was chosen here on the basis of a 2-dimensional minimum χ^2 grid search.

Firstly, the sub-pixel centring of each quasar image was found using the CENTROID routine in IRAF. Accurate $9\times$ oversampled (w.r.t. WFPC2) models of the central PSF regions were then generated with TINYTIM, using the correct central position to provide an accurate model of the central few pixels of each quasar image. These were then shifted, with no need for interpolation, on a 9×9 grid, rebinned to WFPC2 resolution, and compared to the central region of the quasar. The best-fit PSF core was thus found using a 2D, minimum χ^2 grid search. There is no loss of information, assuming that the PSF generated applies across the whole pixel. The final TINYTIM model is then scaled up (by annular photometry) and spliced into the centre of the deep stellar PSF image.

The seeing-free model quasar and PSF are now convolved by taking a Fast Fourier Transform (Press et al. 1992) of each, multiplying in Fourier Space and then inverse Fourier Transforming.

2.5.4 Goodness of fit & Error Analysis

The model quasar can now be compared to the data through the χ^2 figure of merit:

$$\chi^2 = \sum_{i=1}^{n} \left[\frac{y_i - y(\{X\})}{\sigma_i} \right]^2 \tag{2.8}$$

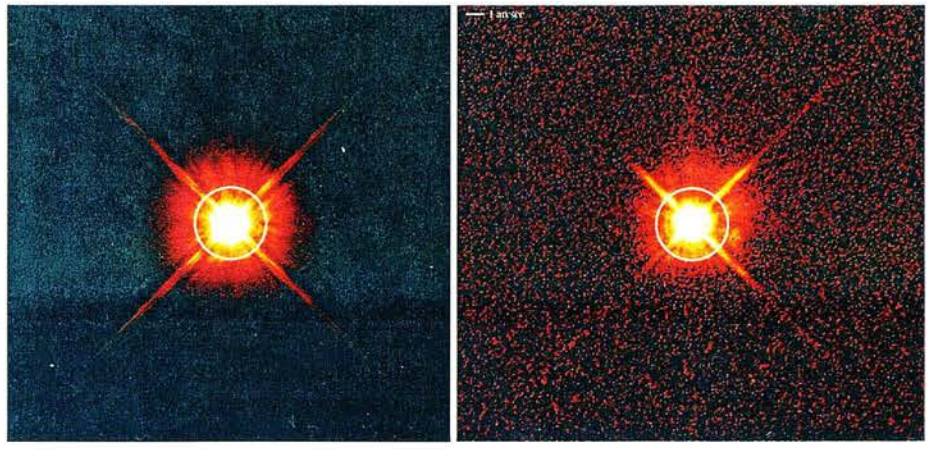

Figure 2.4: **Above:** A TINYTIM idealisation (left) and empirical stellar measure (right) of the HST/WFPC2 point spread function. The white circle indicates the radius of 1.5arcsec at which the TINYTIM model becomes unable to accurately represent the scattered halo of light.
Below: The 1-dimensional radial profiles of the TINYTIM PSF (dashed line) and the empirical stellar PSF (solid line). The fit is extremely tight in the central 0.5arcsec, and acceptable out to about 1.5arcsec. The huge quantity of 2D structure makes a fully 2-dimensional modelling technique well worthwhile.

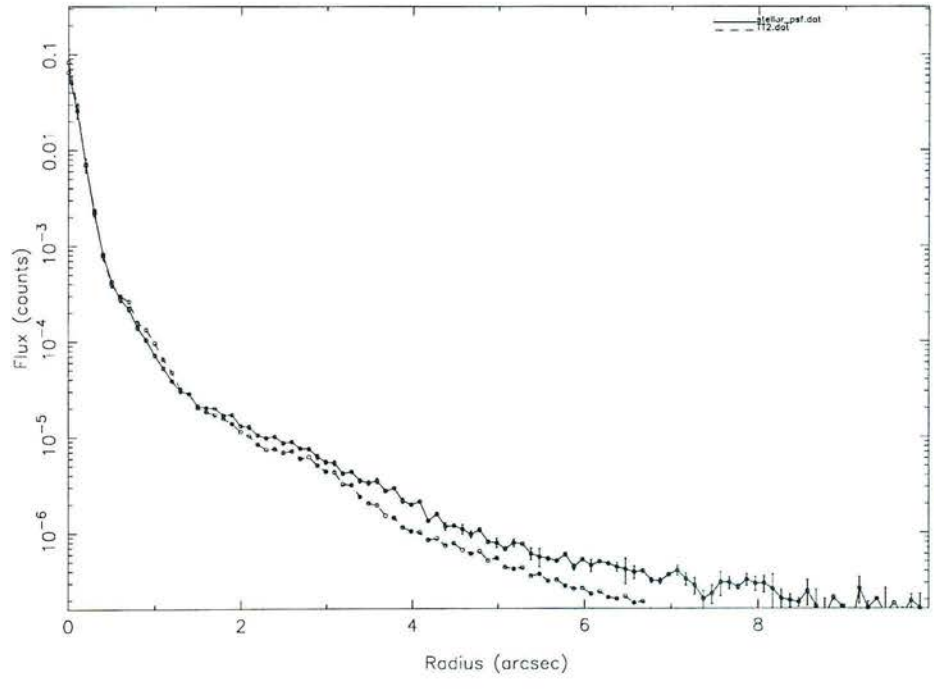

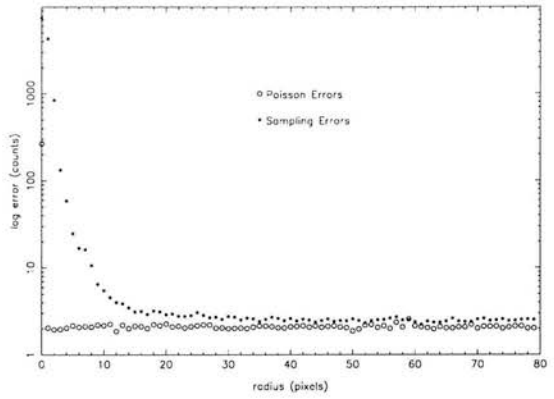

Figure 2.5: **Sampling errors and Poisson errors for 1254+021.** Sampling errors (filled circles) are used in the central regions, where the lack of knowledge of the precise form of the PSF dominates. This drops to the level of the background Poisson error (open circles), typically within about 1.5arcsec. For the 3 most luminous quasars, the sampling error fails to drop to the background Poisson level (see figure 2.6).

where there are n pixels included in the fit, y_i is the value of the i^{th} pixel in the object image, $y(\{X\})$ is the value of the corresponding pixel in the model image, and σ_i is the error on that pixel. The advantage of this 2-dimensional approach is that each pixel can be included in the fit at a weighting assigned on an individual basis: We can choose to completely ignore bad pixels, or companion objects, whilst good pixels can be assigned their individual Poissonian error.

2.5.5 Pixel Error Analysis

The error allocation for such a technique must be done carefully if the χ^2 figure of merit is to have any real meaning. Inaccurate error weighting may lead to the dominance of one region over another in the fitting, and hence biased results. Pixel values were assumed to be independent and to obey Poisson statistics. I used a combination of Poisson and sampling errors, illustrated in Figure 2.5.

Poisson Noise Error

The minimum possible noise in a given pixel is the combination of Poisson error due to photon shot noise (the arrival of photons as random, independent point events), and the read-noise. However,

this simple error calculation severely underestimates the error in the central region, due to the gross under-sampling of the steep PSF.

Sampling Errors

We construct a "PSF residual" frame by scaling up the PSF to match the quasar in the central pixel and subtracting. The residuals give us an idea of how well the PSF models the central region of the quasar. A series of pixel-wide annuli are built up around the centre of this residual frame, and the variance of the distribution of pixel values calculated for each annulus. This variance (σ^2) value is then assigned to each pixel in that annulus, from the centre out, until the value of this sampling error has fallen to approximately the level of the mean Poisson Noise Error discussed above. We call this radius the "sampling error radius", R_{samp}. We could choose to use this approach across the whole image, since it falls to the same level as the Poisson noise by the time we get outside the central arcsecond of the quasar. However, it is preferable to assign each pixel an error based upon its own merit, rather than a blanket error for an entire annulus.

Central pixel

Clearly no sampling error can be computed for the single central pixel. In this case we apply the Poisson error, noting that the central pixel value is an amplified number, from a short snapshot exposure (in order to avoid saturation). The error on the central pixel is typically of the same order as, or a little larger than the sampling error on the innermost annulus.

2.5.6 Minimization

We have now reduced the problem to one of minimisation: We can construct any model quasar we like, with a host galaxy subject to the a priori light distributions described by equation 2.3, and see it

as we would through HST, by convolving it with an HST PSF. Our task is simply to find the point, $\{X\}$, which characterises the model that best describes our image (i.e. minimises χ^2).

Clearly, for such a large number of pixels (each pixel represents one degree of freedom in the fit) and just 5 or 6 free parameters, an exhaustive grid search through the parameter space is not computationally viable. Rather than adopting such a stochastic process, we must resort to some level of selection.

There are a wide range of minimisation techniques available to the computational scientist. The Downhill Simplex technique (Press et al. 1992) has been adopted, due to its robustness, and comparative insensitivity to initial conditions. This technique is not fast, nor elegant, but does the job in a reasonable length of time. It is a highly geometrically appealing technique, with an almost biological aspect, and an important application of the Minimax theorem (Casti 1996).

Finally, once the best-fit (fixed-morphology) model, $\{X\}$, has been found, the Position Angle and Axial Ratios are fixed, and a 3D grid search is performed on the remaining free parameters to ensure that we have found the true minimum χ^2 solution. The $100 \times 100 \times 100$ grid was constructed using even spacings in log space in nuclear luminosity, and host galaxy scalelength and surface brightness. Typically, the grid was performed over the range of the best-fitting parameters $\pm 10\%$ in log space. The grid search yields a useful data-cube of chi^2 values spanning models close to the best-fit. This grid seach acts as a final confirmation that we have isolated the global minimum, and also allows us to explore the nature of any degeneracies in the parameter space.

2.5.7 A note on morphology

It is worth taking a moment to clarify what we mean by "bulge-dominated" or "disc-dominated", as this remains a source of some controversy for two very good reasons.

Firstly there is the purely observational issue: To what extent can we rule out small, or dim discs within bulge-dominated hosts, and vice-versa. Are we missing some additional component? Here we can place limits on the surface brightness of any detectable artifact, but we have the additional problem of the glare of the nucleus. The better defined our PSF is, the more we can reduce this latter problem. Ground-based observations suffer from the dual problems of bright and variable atmospheric background (especially in the infrared). Our modelling software finds the best overall fit to the light from the quasar and its host galaxy. This is dominated by contributions from the point-like nucleus itself, and from the smooth, high SNR host region far from the nucleus. At the depth of our HST images we expect to be able to detect features at least as dim as 27 Vmag.arcsec^{-2}. This surface brightness is roughly equivalent to that of the prominent tidal arm in Mrk1014, placed at a redshift of $\approx 1-1.5$. [1] However, close to the nucleus, this sensitivity is impaired by our lack of knowledge of the PSF, and a small-scale, relatively bright feature can go unnoticed. Such features are exposed by our modelling residual images, which show the best fit model subtracted from the data (see appendices). Thus when we claim to detect bulge or disc-dominated hosts, we mean just that: At the largest scale, the host light is dominated by smooth emission that follows a bulgy or a discy profile.

Secondly there is the issue of what the De Vaucouleurs $r^{1/4}$ power-law profile actually means. If we find a De Vaucouleurs profile to best describe a given host galaxy, does this mean that that host is a genuine "Elliptical" or Early type galaxy? Such a profile has been shown to result from the merger of 2 gas-rich systems (Naab and Burkert 1999), and does not necessarily imply a completely Virialised, or dynamically relaxed system, as is supposed when we speak of "Elliptical" or "Early-type" galaxies. Therefore worries over fuelling of an AGN inside bulge-dominated hosts should not be overplayed, as the galaxy may not be an entirely red, dead elliptical. In addition, several studies have found gas

[1] Markarian 1014 is a well-known disturbed active galaxy at $z = 0.163$, with a prominent tidal arm that is easily detected at surface brightnesses of ≈ 24 V mag. arcsec^{-2} (see images and profiles in McLure et al. 1999).

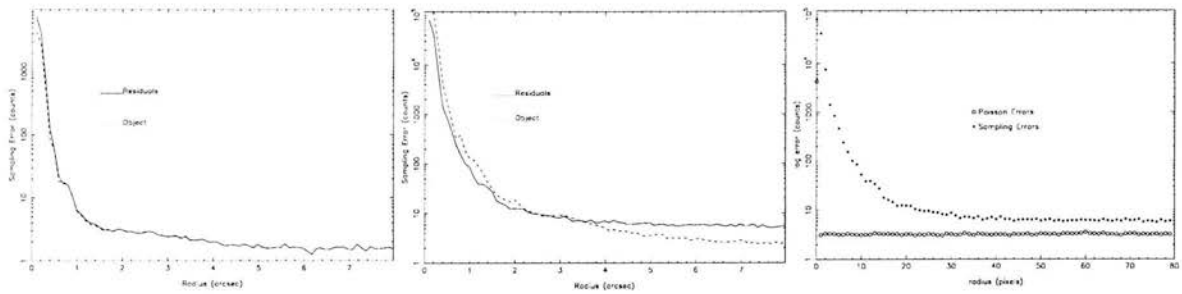

Figure 2.6: **High-luminosity quasar error calculations.** In the case of the highest luminosity quasars, the sampling errors fail to fall to the background Poisson limit, due to insufficient depth in the PSF image. The left hand graph illustrates the Sampling errors and the annular standard deviations in the object frame for a normal quasar image. The middle frame illustrates the situation for the luminous quasar, 0624+6907. The residual errors are larger than the plain object errors in this latter case, due to the additional noise introduced in scaling up the PSF frame before subtraction.

and dust to be present in early-type hosts of radio galaxies (e.g. de Koff et al. (2000), Verdoes Kleijn et al. (1999)).

2.5.8 Modelling High-luminosity quasars

For the two most luminous objects in this study, E1821 and HS0624, the sampling error in the PSF residual image remained above the mean Poisson noise at radii much larger than 1 arcsec (Figure 2.6). This is because, in these two cases the central quasar is so bright that the image actually contains more information on the detailed structure of the PSF at large radii than does our deepest image of the PSF star. Consequently, for these two objects, the errors in our knowledge of the PSF at radii of several arcsec become important, and we had to enhance the adopted errors in the image at large radii (by typically $\sqrt{2}$; in practice we adopted an average of the 'sampling' and Poisson errors at large radius) to achieve an acceptable model fit with a flat distribution of values in the final χ^2 image produced by the model-fitting procedure.

2.5.9 Photometry

For ease of comparison with our earlier work, I have adopted a flat Einstein-de Sitter cosmology with $H_0 = 50$ km s^{-1} Mpc^{-1}. Photometric calibration was performed using the HST headers PHOTFLAM and PHOTZPT, in order to convert counts into physical units of spectroscopic flux density (erg s^{-1} cm^{-2}Å^{-1}). In each case, the rest frame filter band is calculated and compared to standard Johnson V-band.

We have taken the naive assumption of a flat spectrum across the filter bandpass. The internal uncertainty in photometry due to the accuracy of the calibration reference files and the stability of the instrument is 1-2%. The conversion from the HST to the Johnson photometric system also has an uncertainty of a few percent.

2.6 Results

As described in the previous chapter, I used three separate modelling strategies in order to determine the morphology of the hosts and the relative contributions of the nuclear and galaxy components. In the first case I fitted a pure de Vaucouleurs ($r^{1/4}$-law) elliptical galaxy and then a pure (exponential) Freeman disc to the host and used the difference in the χ^2 values for the two models to decide which model gave the best overall fit. Unless otherwise stated in the notes, all objects were modelled out to a radius of 4 arcsec. Table 2.3 lists the results of this strategy.

In the second case, I carried out modelling using a variable-β fit, in which the β parameter (of equation 1) is allowed to vary freely, with $\beta = 0.25$ equivalent to a de Vaucouleurs elliptical profile and $\beta = 1$ an exponential disc. This allows for a more general morphology than the strictly disc or bulge technique. Table 2.4 shows the results of this variable-β fitting, and for the most part this

Table 2.3: **Modelling Results.** Results of model fitting with both de Vaucouleurs spheroid and Freeman disc models. Columns are as follows: object name; best fitting host-galaxy morphology (disc or elliptical); reduced-χ^2 value for the best fit model; $\Delta\chi^2$ between the chosen and alternative-morphology model; half-light radius, $R_{1/2}$, of best fitting galaxy model in kpc; surface brightness of the host at the half-light radius, $\mu_{1/2}$, in units of V mag.arcsec^{-2}; integrated absolute magnitudes of the nucleus and the host galaxy, converted from the appropriate filter band (F814W/F791W) to Johnson V-band; the ratio of integrated nuclear and host galaxy luminosities; position angle of the host (in degrees, anti-clockwise from vertical in the images); the axial ratio of the host.

IAU name	Morphology (best fit)	χ^2_{red}	$\Delta\chi^2$	$R_{1/2}$ (kpc)	$\mu_{1/2}$	M_V^{nuc}	M_V^{host}	L_N/L_H	PA (°)	a/b
Radio-Quiet Quasars										
0624+691	Elliptical	1.488	486.2	9.7 ± 0.7	22.0 ± 0.15	−27.18	−24.01	18.45	140	1.2
1001+291	Elliptical	1.318	326.3	15.4 ± 0.6	23.1 ± 0.10	−25.62	−23.47	7.27	58	1.7
1230+097	Elliptical	1.219	107.7	5.8 ± 0.2	21.7 ± 0.13	−25.24	−23.24	6.26	1	1.3
1237−040	Disc	1.323	334.5	6.7 ± 0.1	22.0 ± 0.05	−23.98	−22.63	3.46	14	1.1
1252+020	Elliptical	1.228	102.0	3.9 ± 0.5	22.1 ± 0.30	−25.26	−22.04	19.47	150	1.1
1254+021	Elliptical	1.356	646.3	14.2 ± 0.3	23.2 ± 0.05	−23.91	−24.00	0.92	30	1.1
1258−015	Elliptical	1.352	14.4	1.5 ± 0.2	19.8 ± 0.25	−23.77	−22.33	3.77	140	1.1
1313−014	Disc	1.254	351.0	5.6 ± 0.1	21.7 ± 0.06	−23.74	−22.68	2.65	174	1.1
1357−024	Disc	1.257	457.1	5.8 ± 0.1	21.9 ± 0.05	−23.66	−22.47	2.99	160	1.2
1821+643	Elliptical	1.828	570.4	18.9 ± 0.2	22.9 ± 0.05	−27.14	−24.33	13.35	113	1.3
Radio-Loud Quasars										
0031−707	Elliptical	1.268	802.8	11.0 ± 0.4	23.1 ± 0.08	−23.84	−23.21	1.80	70	1.2
0110+297	Elliptical	1.327	561.1	12.3 ± 0.8	23.6 ± 0.12	−23.93	−22.99	2.39	31	1.2
0812+020	Elliptical	1.509	904.7	17.4 ± 0.3	23.6 ± 0.05	−24.80	−23.81	2.49	155	1.2
1058+110	Elliptical	1.390	135.5	13.1 ± 1.1	24.1 ± 0.14	−23.58	−22.69	2.28	159	1.3
1150+497	Elliptical	1.360	340.6	8.3 ± 0.3	22.1 ± 0.11	−24.09	−23.28	2.11	174	1.5
1208+322	Elliptical	1.096	49.1	6.5 ± 0.1	22.2 ± 0.05	−25.01	−22.50	10.06	7	1.9
1233−240	Elliptical	1.358	47.7	3.1 ± 0.1	20.6 ± 0.05	−24.78	−22.98	5.23	58	1.1

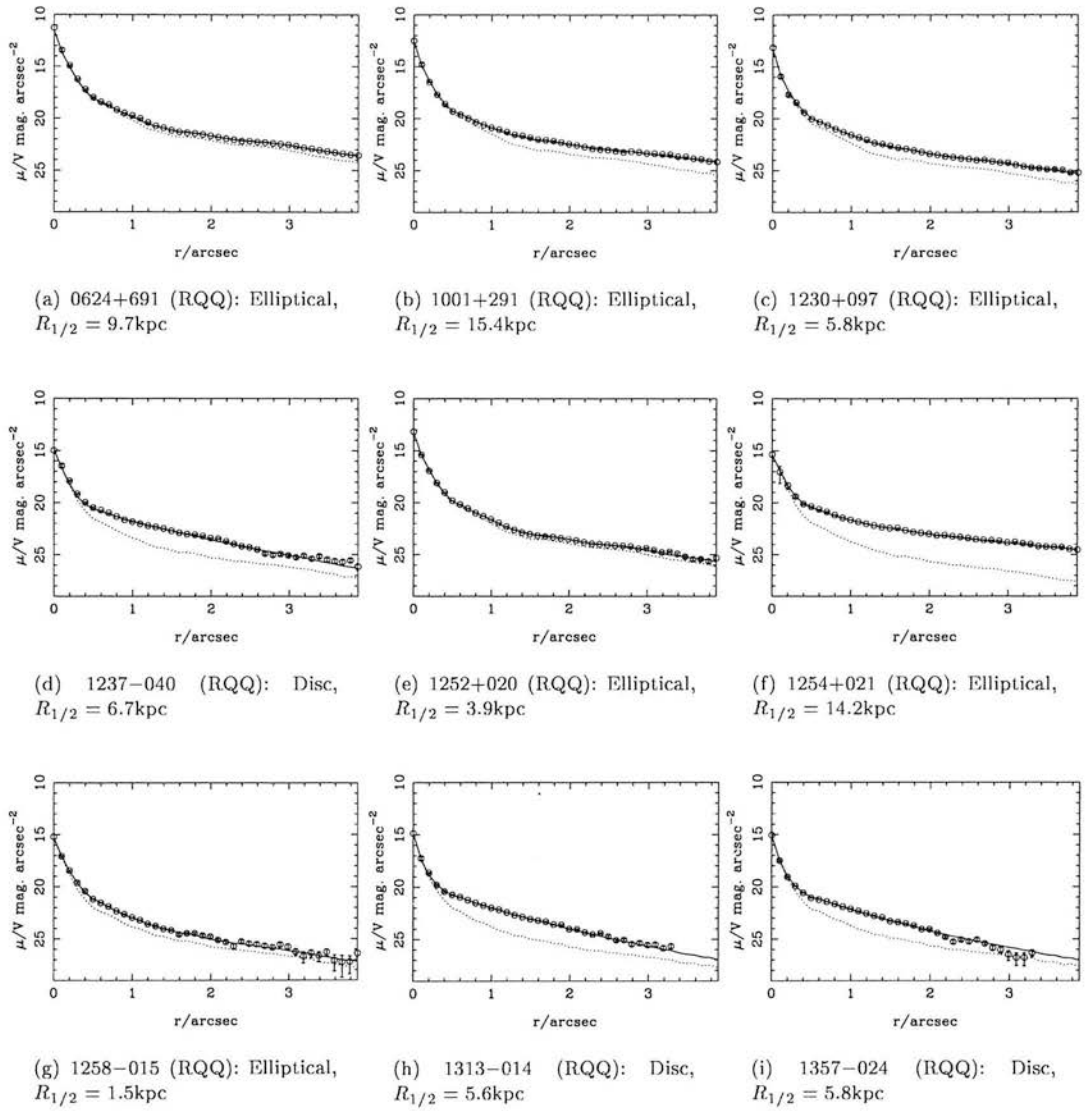

(a) 0624+691 (RQQ): Elliptical, $R_{1/2} = 9.7$kpc

(b) 1001+291 (RQQ): Elliptical, $R_{1/2} = 15.4$kpc

(c) 1230+097 (RQQ): Elliptical, $R_{1/2} = 5.8$kpc

(d) 1237−040 (RQQ): Disc, $R_{1/2} = 6.7$kpc

(e) 1252+020 (RQQ): Elliptical, $R_{1/2} = 3.9$kpc

(f) 1254+021 (RQQ): Elliptical, $R_{1/2} = 14.2$kpc

(g) 1258−015 (RQQ): Elliptical, $R_{1/2} = 1.5$kpc

(h) 1313−014 (RQQ): Disc, $R_{1/2} = 5.6$kpc

(i) 1357−024 (RQQ): Disc, $R_{1/2} = 5.8$kpc

Figure 2.7: **The radial profiles** of the best-fitting bulge or disc models for the 17 quasars in our sample. Each plot shows the azimuthally averaged image data (open circles with 1σ error bars), the azimuthally averaged best-fit model after convolution with the PSF (solid line) and the azimuthally averaged best-fit unresolved nuclear component after convolution with the PSF (dotted line). The form of the fit (disc or elliptical) and the scalelength of the model galaxy are also given beneath each panel.

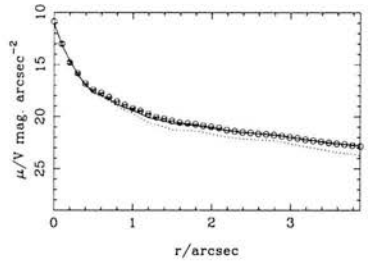

(j) 1821+643 (RQQ): Elliptical, $R_{1/2} = 10.4$kpc

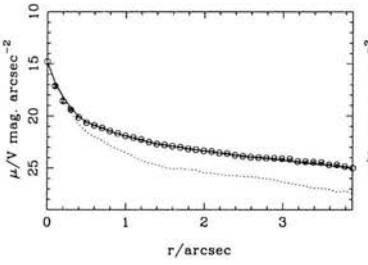

(k) 0031−707 (RLQ): Elliptical, $R_{1/2} = 11.0$kpc

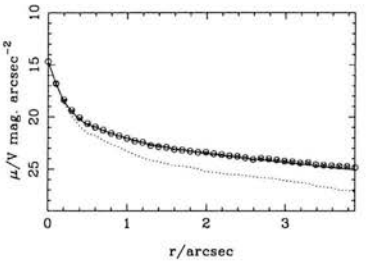

(l) 0110+297 (RLQ): Elliptical, $R_{1/2} = 12.3$kpc

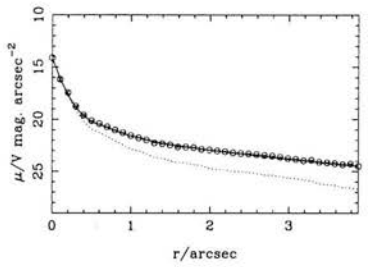

(m) 0812+020 (RLQ): Elliptical, $R_{1/2} = 17.4$kpc

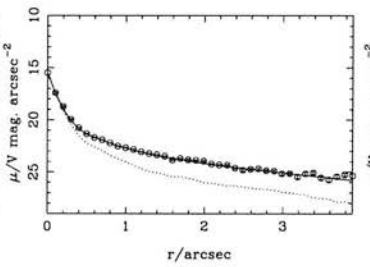

(n) 1058+110 (RLQ): Elliptical, $R_{1/2} = 13.1$kpc

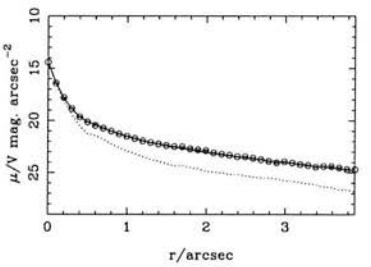

(o) 1150+497 (RLQ): Elliptical, $R_{1/2} = 8.3$kpc

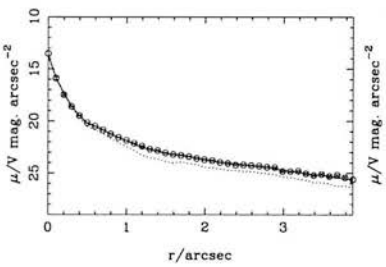

(p) 1208+322 (RLQ): Elliptical, $R_{1/2} = 6.5$kpc

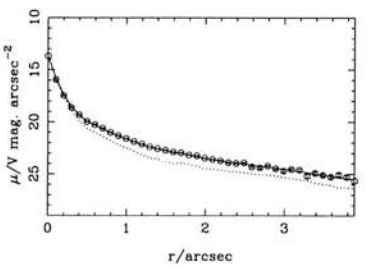

(q) 1233−240 (RLQ): Elliptical, $R_{1/2} = 3.1$kpc

Figure 2.7: ***- continued***

Table 2.4: **Outcome of variable-β modelling.** Columns are as follows: object name; best-fit morphology from pure bulge & disc models (Table 2.3); best-fit β value with no assumed morphology; the value of reduced-χ^2 produced by this best-fit model; improvement in fit, $\Delta\chi^2$ obtained by using the variable-β technique compared to the best-fit fixed morphology model.

IAU name	Morph.	β	χ^2_{red}	$\Delta\chi^2$
Radio-Quiet Quasars				
0624+691	Bulge	0.20	1.485	42.2
1001+291	Bulge	0.26	1.318	0.1
1230+097	Bulge	0.37	1.216	12.0
1237−040	Disc	0.96	1.321	0.6
1252+020	Bulge	0.22	1.227	0.7
1254+021	Bulge	0.24	1.356	2.0
1258−015	Bulge	0.26	1.351	2.0
1313−014	Disc	0.97	1.254	0.2
1357−024	Disc	1.32	1.246	22.8
1821+643	Bulge	0.22	1.771	485.4
Radio-Loud Quasars				
0031−707	Bulge	0.26	1.266	11.9
0110+297	Bulge	0.22	1.323	15.5
0812+020	Bulge	0.23	1.503	9.5
1058+110	Bulge	0.33	1.388	6.9
1150+497	Bulge	0.36	1.356	19.4
1208+322	Bulge	0.32	1.091	19.5
1233−240	Intermediate	0.56	1.361	57.2

reinforces the results of the fixed models. However there are a few objects in which the variable-β technique returned a hybrid value and these are noted in the entry for the relevant object.

Finally, I attempted to fit a 2-component model (bulge + disc), in order to determine whether the best fit morphology could be improved upon by allowing an additional contribution in the form of the other morphology. This modelling was initially done for the three discy objects, in order to see whether any significant bulge, and hence black hole might be present. The modelling was later extended to cover all the objects studied here. Results of the 2-component modelling are presented in Table 2.5.

Greyscale images of the individual objects are presented in Appendix A. For each quasar I show the final reduced *I*-band (F814W/F791W) HST image (top left), the best-fit model (either pure bulge or pure disc) to the quasar image (top right), the model host galaxy only (bottom left) and the model-

Table 2.5: **Outcome of 2-component modelling.**

Source	Morph.	$\Delta\chi^2$	M_K(Nuc)	r_B kpc	M_K(Bulge) kpc	r_D	M_K(Disc)	Bulge/Disc
Radio-Quiet Quasars								
0624+691	B/D	143.9	-27.17	2.5	-24.35	63.6	-23.23	2.8
1001+291	B/D	488.6	-25.62	24.4	-23.38	8.0	-21.69	4.7
1230+097	B/D	88.6	-25.27	8.9	-22.81	6.7	-21.40	3.7
1237−040	D/B	10.8	-23.96	3.8	-21.18	6.5	-22.46	0.31
1252+020	B	0.8	-25.25	5.5	-21.83	5.9	-21.35	1.6
1254+021	B	1.4	-23.92	14.1	-24.00	1.0	-16.13	1400.0
1258−015	B/D	5.4	-23.81	1.3	-21.67	4.0	-20.81	2.2
1313−014	D/B	4.7	-23.72	3.3	-20.28	5.6	-22.62	0.12
1357−024	D	0.3	-23.65	0.4	-18.38	6.3	-22.47	0.023
1821+643	B	0.0	-27.14	19.0	-24.33	0.7	-15.13	4900.0
Radio-Loud Quasars								
0031−707	B/D	70.7	-23.86	50.2	-23.41	5.1	-21.78	4.5
0110+297	B/D	69.6	-23.90	16.8	-23.02	1.3	-21.16	5.6
0812+020	B/D	150.6	-24.78	38.5	-24.00	3.7	-21.71	8.2
1058+110	B/D	16.7	-23.59	16.0	-22.69	2.9	-19.70	16.0
1150+497	B	0.0	-24.09	8.3	-23.27	0.6	-15.18	1700.0
1208+322	B	0.7	-25.01	6.5	-22.5	8.5	-14.59	1500.0
1233−240	B/D	27.9	-24.79	3.1	-22.74	8.2	-20.65	6.9

subtracted residual image (bottom right).

Radial profiles for the best-fit bulge and disc models are presented in Figure 2.7. We can gain some insight into how successful we have been in disentangling the host galaxy from the nucleus through investigation of the χ^2 contours in the $\mu - R$ plane (see Figure 2.9). For any quasar in which we have successfully characterised the host luminosity (i.e. eliminated the degeneracy between host and nuclear contributions), these contours should lie along a slope of 5.0 (see e.g. Abraham et al. 1992, Malkan 1984). In this case, we still have an obvious degeneracy between the host galaxy's size and its surface brightness, and the contours allow us to assess how well constrained these two parameters are.

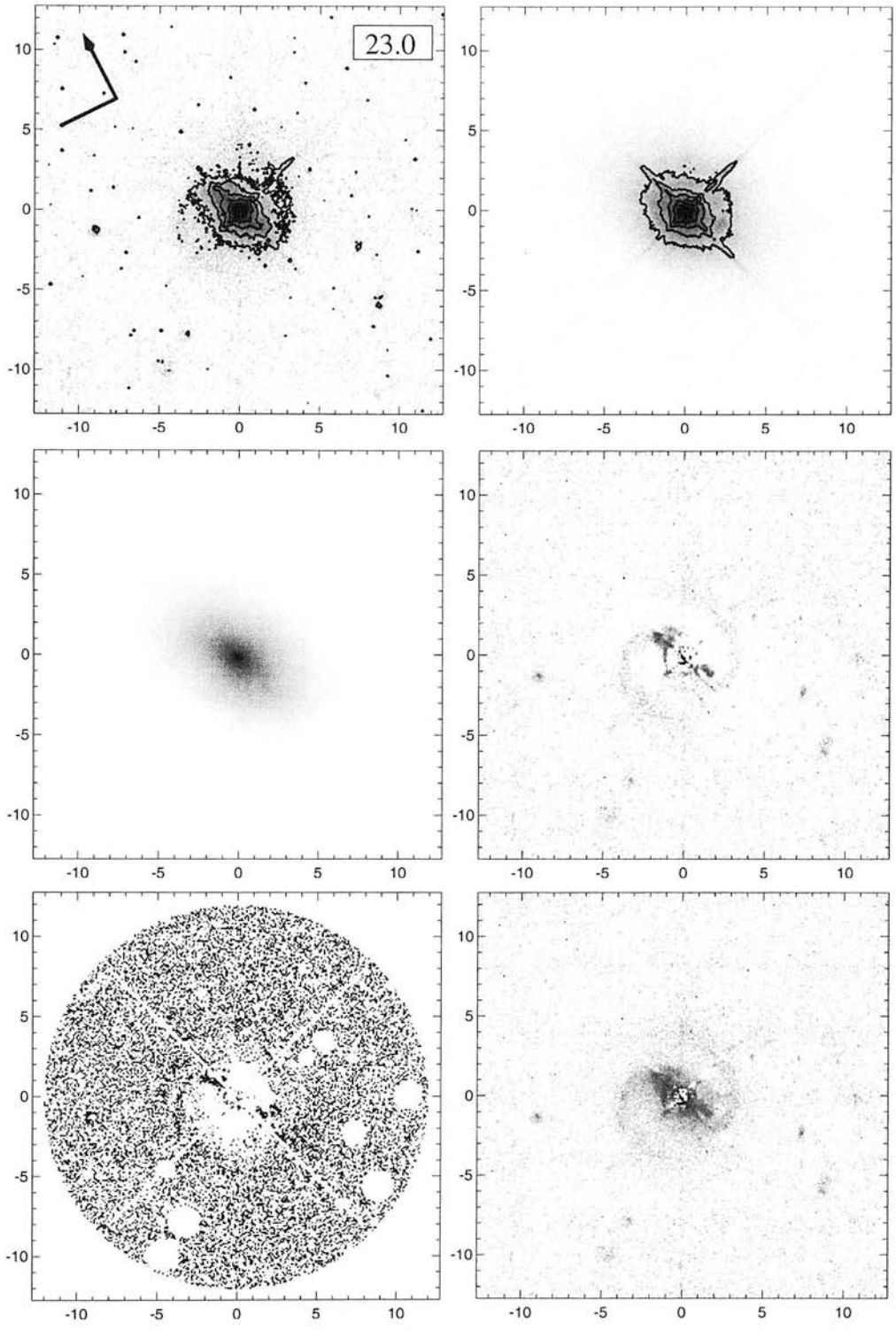

Figure 2.8: **Modelling the RQQ 1001+291:**
A: Here I present the fully-reduced HST image of 1001+291 (TON0028). **B:** The best-fitting model quasar. **C:** The best-fitting host galaxy model. **D:** The modelling residuals. **E:** The χ^2 frame. Similar greyscale figures for all objects are presented in the Appendices.

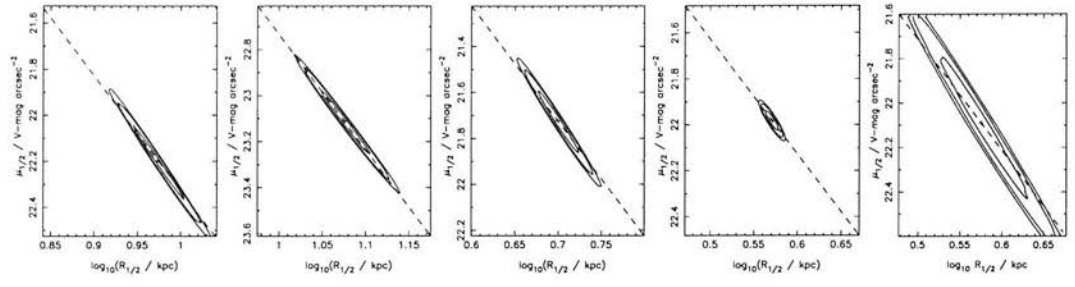

(a) 0624+691 (b) 1001+291 (c) 1230+097 (d) 1237-040 (e) 1252+050

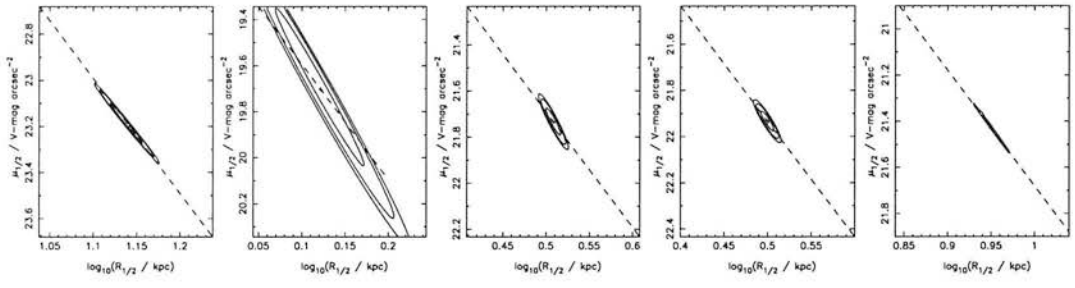

(f) 1254+021 (g) 1258-015 (h) 1313-014 (i) 1357-024 (j) 1821+643

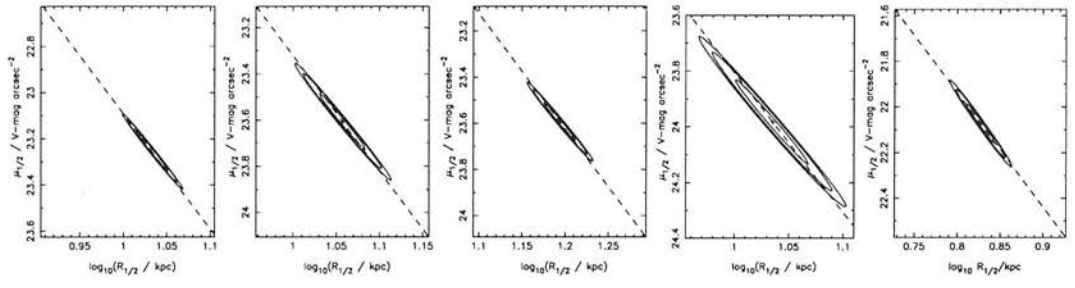

(k) 0031-707 (l) 0110+297 (m) 0812+020 (n) 1058+110 (o) 1150+497

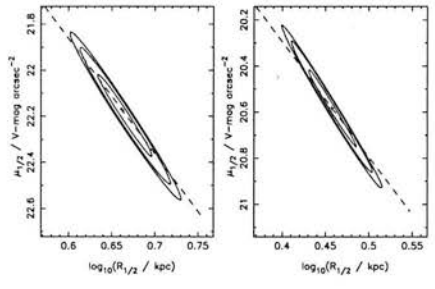

(p) 1208+322 (q) 1233-240

Figure 2.9: χ^2 **contours** (at $1-3\sigma$ levels) in the $\mu - R$ plane for each object. In each case, the best-fit solution is marked by a dot. The figure demonstrates the degeneracy that remains between galaxy size and surface brightness, even when any confusion between host and nuclear light has been eliminated. The former is a typical example of the objects in this study and the contours describe a slope close to 5 (dashed line), as expected if the host galaxy's luminosity has been correctly constrained. Of all the objects in our sample, 1252+020 and 1258-015 have the least robust host galaxy fits. For these objects the contours lie along a somewhat steeper slope, suggesting that we have not constrained the host galaxy luminosity accurately, and that there is some degeneracy remaining between host and nucleus.

2.7 Notes on Individual Objects

2.7.1 Radio-Quiet Quasars

0624+691 (HS0624+6907). One of the brightest quasars in the sky, this object has been the subject of a comprehensive multi-wavelength study (Reimers et al. 1995), which classified the host galaxy as a massive elliptical, fitting a de Vaucouleurs profile with a nominal scale length of 1.8kpc to their PSF-subtracted image. The quasar appears to lie in a cluster, with a number of small companion objects visible in the field.

We find the host to be best fit by a giant elliptical galaxy ($R_{1/2} = 10$ kpc), with an extremely strong nuclear component ($L_N/L_H = 18$). The variable-β fit returns a value of $\beta = 0.20$, again consistent with a pure de Vaucouleurs elliptical host. However, the 2-component modelling does reveal a significant, and large-scale discy component (Bulge/Disc = 2.8; r_D=64kpc), with a significant improvement in the fit. The scalelength of the spheroidal component is significantly reduced, but its luminosity is only slightly affected.

Due to the extreme luminosity of this quasar the masking for the diffraction spikes was applied over a much larger area than for the majority of objects in this study. The host galaxy contribution is obvious out to a radius of at least 5 arcsec, and we used a fitting radius of 6 arcsec to ensure that all detectable host light was used to constrain the model parameters.

1001+291 (TON0028, PG 1001+292, 2MASSi J1004025+285535). This object was studied in some detail by Boyce et al. (1999), who claimed two galactic nuclei; one 1.92 arcsec (14.6 kpc) to the south-west of the quasar nucleus, and the other 2.30 arcsec (15.9 kpc) to the north-east. However, this claim appears to be a result of over-subtraction of the nuclear point source, since Márquez et al. (2001)

showed that the host possesses prominent spiral arms and a bar which crosses the nucleus from north east to south west, although they were unable to fit a surface-brightness profile.

In the current data we also find spiral arms and a nuclear bar which is clearly visible in the residual image of this object. However, we find that the surface light profile of the underlying smooth component is very well fitted by a de Vaucouleurs law ($R_{1/2} \simeq 15$ kpc, $\beta = 0.26$), suggesting a bulge-dominated host. 2-component modelling reveals a low-level disc component (Bulge/Disc=4.7) with a significant improvement in the fit, and a 0.1mag decrease in the luminosity of the dominant bulge component.

1230+097 (LBQS 1230+0947). We find the host galaxy of this quasar to be an elliptical with a scale length of $R_{1/2} = 6$ kpc. There are a number of other objects in the same field with possible evidence for a tidal interaction with the nearest object to the north.

Allowing for a variable value of β yields a slightly better fit with $\beta = 0.37$, suggesting a somewhat intermediate morphology. This is borne out by the 2-component modelling which reveals a significant bright disc component (Bulge/Disc=3.7), and requiring a 0.4mag decrease in the luminosity of the dominant bulge.

1237−040 (EQS B1237−0359). This object appears to be interacting with a companion galaxy to the north, and the residual image shows that a tidal tail has been induced in the quasar host itself. The host is best fitted by a large ($R_{1/2} = 4$ kpc) disc galaxy, with the variable-β modelling returns a value of $\beta = 0.96$. The residual image shows some excess nuclear flux which has not been accounted for by the pure disc fit, and the 2-component modelling reveals a luminous spheroidal component (Bulge/Disc=0.31) of moderate size ($R_{1/2} = 3.8$kpc). The luminosity of the dominant disc is reduced by 0.2mag. This is the most luminous of the disc-hosted quasars studied here, and it is interesting to

note that it is also the one with the most significant detection of a spheroidal host galaxy component.

1252+020 (EQS B1252+020, HE 1252+0200). This is a radio-quiet (Goldschmidt et al. 1999), X-ray detected (Voges et al. 1999) quasar with a strong UV excess (Goldschmidt et al. 1992). Of all the objects in the current sample, this quasar proved to be the hardest for which to achieve an unambiguous model fit to the host galaxy. Indeed, as is shown in Fig.3, we were unable to constrain the luminosity of the host to the same extent as for the other quasars: the χ^2 contours in the $\mu - R$ plane have a slope slightly steeper than 5. One nearby companion had to be masked out, along with the diffraction spikes, before modelling could be carried out. In addition, there is a faint region of nebulosity directly to the north of the quasar.

Our best fit model has an elliptical host with $R_{1/2} = 4$ kpc and the highest nuclear-to-host ratio in the sample, $L_N/L_H = 19.5$, although as has been stated, the host and nuclear flux have not been completely disentangled, and there is a large error associated. The β parameter modelling also favours an elliptical host, with $\beta = 0.22$. 2-component modelling prefers a hybrid host galaxy (Bulge/Disc=1.6), with a 0.2mag decrease in the lumniosity of the dominant bulge component. However, the improvement in the quality of the fit is insignificant, and we should label this galaxy as an Elliptical.

1254+021 (EQS B1254+0206). This radio-quiet (Goldschmidt et al. 1999) quasar shows very smooth extended emission, with only weak diffraction spikes, and an absence of nearby companions. We find that the object is best fitted by a large ($R_{1/2} = 14$ kpc) elliptical galaxy and a weak nuclear component. The variable-β fit confirms the host morphology, returning a value of $\beta = 0.24$. No improvement is made with the addition of a discy component.

1258−015 (EQS B1255−0143, 2MASSi J1258152−015918). A highly compact object, with an al-

most stellar appearance in the HST *I*-band image. However, there is sufficient galaxy light to model, and we find that the best-fit host is a small elliptical galaxy with a half-light radius of just 1.5 kpc. This is confirmed by the variable-β model which returns a value of $\beta = 0.26$, with no appreciable improvement to the fit. Little excess flux remains in the residual image suggesting that the model has accurately accounted for all the host galaxy light, and the radial profile is a good fit to the data throughout. However, the χ^2 contours in $R_{1/2} - \mu_{1/2}$ are slightly too steep to be convinced that we have completely resolved host from nucleus. The 2-component modelling revelas a large, and quite luminous disc component (Bulge/Disc=2.2, $R_{1/2} = 4$kpc) with a marginal improvement in the fit.

1313−014 (Q1313−0138, EQS B1313−0138, LBQS 1313−0138). The nuclear component of this quasar is relatively weak, with no prominent diffraction spikes visible in the image. Hence, despite the small angular size of the host, the model fit to the galaxy is robust. A spiral feature is visible in the residual image, with possible evidence for a bar passing through the nucleus. We find the host to be best fitted by a disc model with $R_{1/2} \simeq 3$ kpc, and this is supported by the variable-β model which returns a best-fit value of $\beta = 0.97$. A low-level spheroidal component is detected by the 2-component modelling, although the improvement in the fit is marginal.

1357−024 (EQS B1357−0227, 2MASSi J1400066−024131). There are several fainter objects in the field, suggesting that 1357−024 might lie in a relatively rich cluster environment. Diffraction spikes from a nearby bright star are visible in the southeast quadrant of the image. However, the quasar itself is a compact source with no discernible diffraction spikes. All companion objects, and the majority of the southeast region of the image were masked out of the fit. In addition, we only modelled out to a radius of 2.5 arcsec. The modelling software shows a strong preference for a disc-dominated host, although the variable-β model returns the unusual value of $\beta = 1.32$. Most likely this is due

to the nearby stellar diffraction spike leading to a flatter profile (and hence higher β). The residual image shows a small amount of excess flux in the nucleus. No improvement is obtained with the 2-component modelling.

1821+643 (E1821+643, IRAS 18216+6418, 8C 1821+643). The brightest quasar in the current sample, this object has been extensively studied at many wavelengths. Extremely luminous in the infrared and also with a strong X-ray component, this was one of the first radio-quiet quasars to be studied in detail at radio wavelengths and is known to contain a small radio jet (Blundell and Rawlings 2001).

Although this quasar appears to lie in a rich field, most of the surrounding objects are believed to be part of a background cluster at a redshift $z \simeq 0.6$. A previous study resolved the host galaxy, finding it to be large, featureless and red, but failed to determine its morphology (Hutchings and Neff 1991). In addition, the nucleus itself is unusually red, indicating the presence of large quantities of dust, though no discrete dust lanes have been observed. McLeod and McLeod (2001) separated the host and nucleus in their H-band NICMOS imaging study, finding a luminous elliptical galaxy of magnitude $M_H = -26.7$, with a nuclear component with $M_H = -29.2$, (when converted into our cosmology).

Because of the prominent diffraction spikes a larger than usual region of the image was masked prior to modelling. However, since extended flux is clearly visible in the image out to a radius of at least 6 arcsec we therefore used this as our fitting radius. The quasar is best modelled as a large elliptical host ($R_{1/2} \simeq 10$ kpc), with a strong nuclear component ($L_N/L_H = 11$). The variable-β model is good accord with this decision ($\beta = 0.22$), with a significant improvement in the fit. The 2-component modelling could find no evidence for an underlying disc-component, and the fit is identical to that obtained with the simple de Vaucouleurs model.

The residuals accentuate the nebulous artifact some 4 arcsec east-southeast of the nucleus, and also appear to show a spiral-like feature wrapping around to the northeast. It is unclear whether this is a genuine feature of the host galaxy, or simply a PSF artifact.

2.7.2 Radio-Loud Quasars

0031−707 (MC4, 2MASSi J0034052−702552).

A radio-loud quasar (Gregory et al. 1994) originally identified as a Magellanic object due to its proximity to the galactic plane. There are a number of companion objects, suggesting that the object lies in fairly rich cluster environment, with the potential for interactions with nearby objects. The HST image shows a relatively weak nucleus (the model fit gives a nuclear/host ratio of $L_N/L_H \approx 2$). The host is best fit by an elliptical galaxy model with $R_{1/2} = 11kpc$ (the variable-β model gives a value of $\beta = 0.26$, with only a slight improvement in the quality of the fit). The 2-component model yields a significant improvement with a low-level disc (Bulge/Disc=4.5), but a very large (50kpc) spheroidal component.

0110+297 (B2−0110+29, 4C 29.02, 2MASSi J0113242+295815). Malkan (1984) attempted to resolve the host galaxy of this quasar from the ground but was prevented from doing so by poor seeing. This quasar appears fairly compact in our HST image, with prominent diffraction spikes and a number of other objects nearby on the sky, including a well-resolved spiral galaxy some 4 arcsec to the east. We found the best fitting host to be a large elliptical galaxy with $R_{1/2} \approx 12$ kpc, confirmed by the variable-beta fit, which returns a best-fit value of $\beta = 0.22$. There is a small symmetrical circumnuclear artifact present in the residual image, and the 2-component model results in a significantly

improved fit with the addition of a compact disc component ($R_{1/2}$ =1.3kpc, Bulge/Disc=5.6).

0812+020 (PKS0812+02, 4C +02.23) An early study of this object (Wyckoff et al. 1981) measured the extent of the nebulosity surrounding the quasar and found it to have a diameter of some 88 kpc. Subsequent work was carried out by Hutchings and Neff (1990), who fitted an elliptical galaxy profile to the host and obtained a scale length of around 12 kpc (converted to our cosmology). They also claimed to find evidence for a tidal interaction.

This quasar lies in a crowded region of sky, and consequently a great deal of masking was required before modelling could be carried out. However, the host itself is relatively bright, and the preference is for a large elliptical galaxy with a scale length of $\simeq$ 17 kpc. The variable-β modelling confirms the morphology of the host, returning a best-fit value of $\beta = 0.23$. We find some residual nuclear flux, but no strong evidence for any disturbance or interaction in the host. A major improvement in the fit is obtained by adding a moderate disc component ($R_{1/2}$ =3.7kpc, Bulge/Disc=8.2). There is a 0.2mag drop in the lumn=inosity of the spheroidal component, but the nuclear component is unchanged.

1058+110 (AO1058+11, PKS 1058+11C, 4C 10.30). There are a number of apparent companion objects, and the clustering amplitude was studied by Yee and Green (1987) & Green and Yee (1984). However, Block and Stockton (1991) found these objects to be at a different redshift from the quasar. Hutchings (1987) detected extended nebulosity around this object, but was unable to fit a radial profile.

Although the active nucleus appears to be relatively weak in our image, the host and nuclear components proved quite difficult to separate. However the model did converge on a large elliptical host, with $R_{1/2} = 13$ kpc. The variable-β fit returns a slightly intermediate value of $\beta = 0.33$. No signs of major disturbance are visible, although some circumnuclear flux remains in the residual image. Addition of a low-level disc (Bulge/Disc=16.0) results in a significant improvement in the fit, with no

change in the properties of the dominant bulge model.

1150+497 (LB2136, 4C 49.22). Several previous attempts have been made to detect the host galaxy of this Optically Violent Variable (OVV) quasar. Malkan (1984), using the Palomar 1.5m telescope, and seeing-degraded models of elliptical and disc-like hosts, claimed to find a massive elliptical host of scale length 25 kpc (when converted to our adopted cosmology). However, an exponential disc was found to give a reasonable fit by Hutchings (1987) & Hutchings et al. (1988), after PSF-subtraction, and 1D profile fitting. Finally Wright et al. (1998), by assuming an elliptical galaxy model (the relatively poor sampling in their data meant that no real morphological classification could be performed), detected a host in K-band, with $M_K = -27.3 \pm 0.6$.

The object appears to be elongated along a north-south axis in the current HST image. There are several fainter objects some 10 arcsec to the NE which have previously been conjectured to be associated with the quasar (Hutchings et al. 1988). Our image also shows two objects, roughly 2 arcsec to the north & north west of the quasar which were masked out along with the diffraction spikes prior to modelling.

Our modelling procedure shows a strong preference for an elliptical host galaxy, with the best-fit model having a scale length of $R_{1/2} = 8$ kpc. However, the variable-β modelling returns a best-fit value of $\beta = 0.36$, intermediate between pure bulge and disc morphologies. The reason for this discrepancy may be apparent in the residual image of the object which shows several regions of excess flux to the south of the nucleus. The 2-component model fails to make any improvement with the addition of a disc-like component.

1208+322 (B2−1208+32, 7C 1208+3213). This quasar was detected as a soft X-ray source by Einstein (Puchnarewicz et al. 1992). Optically, it appears to be a compact object with a strong nuclear

component. We find an underlying elliptical host with a scale length $R_{1/2} = 6.5$ kpc. A slight improvement to the quality of the fit is obtained by allowing β to vary freely, giving a best-fit value of $\beta = 0.32$. However, the 2-component modelling reveals no major disc component, with the best-fit model being identical to the simple de Vaucouleurs model.

Although there are no obvious signs of interaction, there do appear to be a number of small, faint companion objects surrounding the quasar. This is the only radio-loud object in the current sample whose accretion efficiency appears to come close to the Eddington limit ($L_N/L_{Edd} = 0.76$).

1233−240 (PKS1233−24, [HB89] 1232−249). Wyckoff et al. (1981) found an extended nebulosity with a diameter of some 166 kpc surrounding this quasar. The object was also imaged by Veron-Cetty and Woltjer (1990), who found an elliptical host with magnitude $M_V = -22.7$, but were not able to provide a scale length.

Despite the prominent diffraction spikes of the strong nuclear component, some galaxy light is clearly visible in our image, and there are also several other objects in the field. The best-fit host is an elliptical with a scale length of about 3kpc. Examination of the radial profile shows some excess flux compared to the pure elliptical model and the variable-β model returns a value of $\beta = 0.56$ suggesting that a significant disc component is also present. This is borne out by the 2-component modelling, which results in a significantly improved fit, with the addition of a large ($R_{1/2} = 8$kpc) and moderately luminous disc (Bulge/Disc=6.9). The luminosity of the dominant bulge is decreased by 0.24mag, with the nucleus unchanged.

2.8 Discussion

The quasars imaged in this study span almost two orders of magnitude in optical luminosity but only a narrow range of redshifts. They therefore allow us to investigate the relationship between galaxies and their central black holes, and the relative roles of black hole mass and fuelling efficiency in determining quasar luminosities.

We have successfully recovered a host galaxy for each one of the 17-strong sample. In general, the host size and central surface brightness have been constrained to within a few kiloparsecs, and half a magnitude, respectively, as is illustrated by the joint confidence regions illustrated in Figure 2.9. However, there are two objects, the RQQ's 1252+020 and 1258-015, for which the fits yield a poorer stability for the host properties, and the resulting confidence regions have noticeably steeper slopes. Overall host and nuclear fluxes are typically constrained to better than 0.1mag by the modelling software, with a similar error due to the conversion from ST mags to standard V-band.

2.8.1 Host galaxy morphologies

With regard to basic host galaxy morphology, the results of this study are quite clear cut, and confirm and extend the findings of Dunlop et al. (2003). For every quasar host the modelling software yielded a clear decision in favour of either a disc-dominated or bulge-dominated host. Moreover, in virtually every case this preference was confirmed by the variable-β model, which returned a value of β very close to either 0.25 (elliptical) or 1 (disc).

At this point it is important to clarify what we mean by "bulge-dominated" or "disc-dominated" galaxies. Our modelling software finds the best overall fit to the light from the quasar and its host galaxy. This light is dominated by contributions from the point-like nucleus itself, and from the smooth, high SNR host region far from the nucleus. Our HST images are of sufficient depth that we

expect to be able to detect large features at least as dim as $V = 27$ mag.arcsec^{-2}. To place this number in some context, this is a sufficient depth that the prominent tidal arm in Mrk1014, could be detected if it were placed at a redshift of $\approx 1 - 1.5$. [2] However, close to the nucleus, this sensitivity is impaired by our lack of knowledge of the form of the PSF, and here a small-scale, relatively bright feature might go unnoticed by the model. Such features can be exposed in our residual images, which show the best fit model subtracted from the data. Thus when we claim to detect bulge or disc-dominated hosts, we mean just that: on large scales of a few Kpc, the host light is dominated by smooth emission that follows a spheroidal ($r^{1/4}$-law) or a disc-like (exponential) profile.

There obviously remains the possibility of a small and/or dim bulge component, and it is worth noting that the 2-component modelling uncovered a significant secondary component in the majority of cases (Table 2.5). A spheroid is found in two of the three disc-dominated hosts, (1237−040 and 1313−014), and a disc in 9 of the 14 bulge-dominated galaxies. The most significant case is 1001+291, for which we find that the host flux is dominated overall by a de Vaucouleurs $R^{1/4}$ law profile, yet we find clear evidence for a large spiral disc feature at low surface brightness. This bulge-dominated host is most likely an early spiral galaxy.

As illustrated in Figure 2.10, the three quasars in the current sample for which we find disc-dominated hosts are, i) radio-quiet, and ii) in the low-luminosity sub-sample with $M_V > -25$. In fact, reference to Table 2.3 reveals that the three disc-dominated hosts house nuclei with $M_V > -24$. Furthermore, the brightest such object is found to have a significant spheroid. This result therefore meshes well with the luminosity-dependence of host-galaxy morphology illustrated in Figure 10 of Dunlop et al. (2003); disc-dominated host galaxies are not found for nuclei with $M_V < -24$. There is still a problem in rationalising the large nuclear luminosity for the other two disc-hosted objects.

[2] Markarian 1014 is a well-known disturbed active galaxy at $z = 0.163$, with a prominent tidal arm that is easily detected at surface brightnesses of ≈ 24 V mag. arcsec^{-2} (see images and profiles in McLure et al. 1999).

In one case (1313-014) we detect a spheroidal component at low luminosity, and in the final object (1357−024) we detect no bulge component at all.

As discussed by Dunlop et al. (2003), this result can now be viewed as a natural consequence of the now well-established proportionality of black-hole and spheroid mass. However there remains a significant problem in understanding the nuclear luminosity in two of the disc-dominated objects.

2.8.2 Host galaxy scalelengths and luminosities

Table 2.3 lists the scalelengths and luminosities for the best-fit fixed-morphology models. Once again, the results are broadly consistent with those of McLure et al. (1999) and Dunlop et al. (2003); the hosts are generally large, luminous galaxies.

Three of the five smallest galaxies are the disc-dominated hosts.

There is a tendency for the hosts of the RLQs to be slightly larger than those of the RQQs, but this is not statistically significant.

$$\langle R_{1/2} \rangle_{(RLQ)} = 10.2 \pm 1.8\text{kpc}$$

$$\langle R_{1/2} \rangle_{(RQQ)} = 8.7 \pm 1.8\text{kpc}$$

On average the more luminous quasars also have slightly larger hosts, but again the mean values for the two subsamples are in agreement given the statistical uncertainty.

$$\langle R_{1/2} \rangle_{(M_N<-25)} = 10.0 \pm 2.4\text{kpc}$$

$$\langle R_{1/2} \rangle_{(M_N>-25)} = 9.0 \pm 1.5\text{kpc}$$

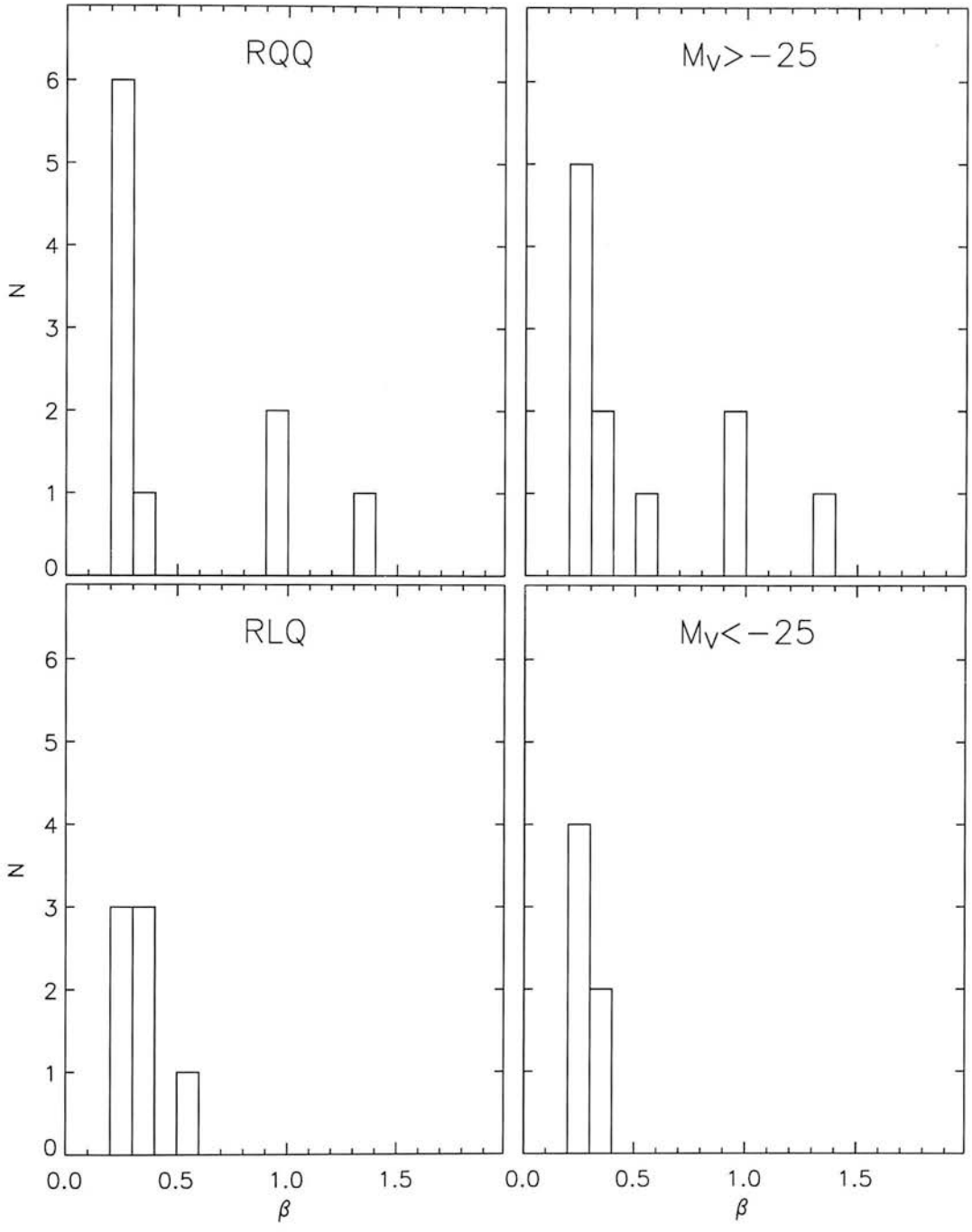

Figure 2.10: **Histograms of the best-fit β values** from the variable-β models. $\beta = 0.25$ is equivalent to an $r^{1/4}$ de Vaucouleurs law, $\beta = 1$ is an exponential Freeman disc. In the panel to the left we divide the sample in terms of radio luminosity. On the right, the sample is divided according to optical absolute magnitude. Clearly all optically-luminous, and all radio-loud objects lie in bulge-dominated hosts, confirming and extending the trends deduced by Dunlop et al. (2003).

I find that that all the hosts are more luminous than $L^{\star}$ ($M_V^{\star} = -21.0$; Efstathiou et al. 1988). There is no statistically significant difference between the average values for each subsample, but these basic statistics should not obscure the fact that the two quasars in the sample with $M_V(Nuc) < -27$ are also the only two objects for which I find $M_V(Host) < -24$.

$$\langle M_V(Host)\rangle_{(RLQ)} = -23.06 \pm 0.16$$

$$\langle M_V(Host)\rangle_{(RQQ)} = -23.12 \pm 0.25$$

$$\langle M_V(Host)\rangle_{(M_N<-25)} = -23.27 \pm 0.36$$

$$\langle M_V(Host)\rangle_{(M_N>-25)} = -23.01 \pm 0.16$$

2.8.3 Kormendy relation

The Kormendy relation is the photometric projection of the fundamental plane exhibited by elliptical galaxies. The host galaxies of the quasars in our sample follow a Kormendy relation of the form

$$\mu_{1/2} = (19.2 \pm 0.6) + (3.33 \pm 0.7) \log_{10} R_{1/2} \tag{2.9}$$

shown in Figure 2.8.3 (where I have plotted and fitted only those with bulge-dominated hosts). A galaxy with a well-constrained luminosity but unknown scalelength will lie along a locus with a slope of 5, illustrated by the error ellipse in the top right corner of this figure (c.f. Figure 2.9). The slope of 3.33 is in excellent agreement with that determined recently for 9000 early-type galaxies (3.33±0.09) drawn from the SDSS by Bernardi et al. (2003) and is sufficiently different to a slope of 5 to convince us that the surface brightnesses and scalelengths of the hosts have been well constrained.

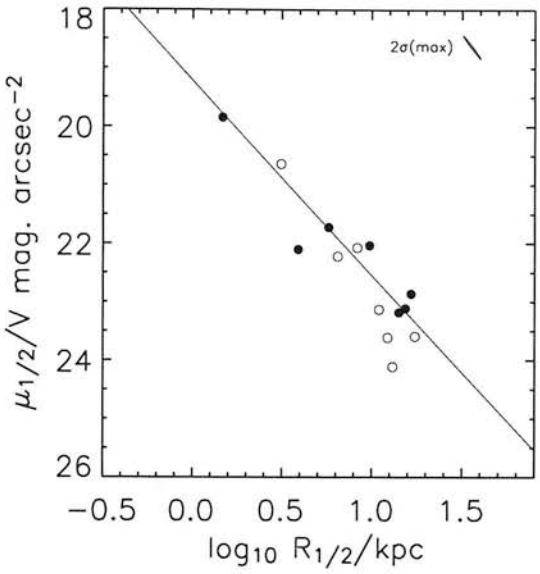

Figure 2.11: **The scalelength ($R_{1/2}$) vs surface brightness** ($\mu_{1/2}$) projection of the fundamental plane. Filled circles represent RQQ hosts, open circles RLQ hosts. The solid line shows the best fit Kormendy relation to the sample and has the form $\mu_{1/2} = (19.2 \pm 0.6) + (3.33 \pm 0.7) log_{10} R_{1/2}$. The narrow ellipse in the top right corner of the plot shows the 2σ error contours for 1258−015; its slope of 5 is due to the remaining degeneracy between size and surface brightness when host luminosity has been well constrained.

2.8.4 The role of galaxy mergers and interactions

Interactions and merging events between galaxies have long been suggested as the triggering events for the activation of quasars, especially at low redshifts where some mechanism is required to initiate fuelling of the black holes in otherwise stable, gas-depleted ellipticals. Indeed, most host galaxy studies to date have found that indications of disturbance such as tidal tails, multiple nuclei and close companions are present in around 50% of quasar hosts (e.g. Smith et al. 1986, Hutchings and Neff 1992, Bahcall et al. 1997). However Dunlop et al. (2003) point out that this is also true of inactive massive ellipticals, so that it is not clear whether mergers are genuinely a defining feature of quasar hosts or merely the legacy of their parent population. Certainly many quasar hosts appear to be entirely undisturbed, so clearly a large-scale disruption of the host is not always necessary to trigger fuelling of the central engine (or at least the timescales for relaxation after the merger event and of fuel reaching

the central engine may sometimes be vastly different).

The residual images of the quasars in the current study (see Appendix), provide a means of identifying signs of galaxy interactions which might not be obvious in the raw HST images. They are produced by subtracting the best-fitting axially-symmetric quasar model from the HST image. Since the model only attempts to fit the smooth underlying distribution of galaxy light, any additional structures (spiral arms, bars, tidal tails, double nuclei etc) will be made more obvious in the residual image.

In this sample I find unambiguous evidence for an ongoing galaxy interaction in only one object, the RQQ 1237−040. Several other objects are candidates for some form of disturbance having taken place (for instance the RQQ 1001+291 with its prominent spiral arms and large-scale de Vaucouleurs profile), or have other objects within a few arcsec on the sky which might conceivably be interacting if they lie at the same redshift. In fact the majority of our quasars appear to have some companions nearby on the sky, which is at least suggestive of a cluster environment.

However I find no correlation between the luminosity of the quasar and the presence of any morphological disturbance in the host. In our small sample, at least, the most luminous quasars seem no more likely to be interacting systems than their less luminous counterparts.

2.8.5 Black hole masses

Reliable black hole masses are available for at least 37 nearby galaxies (Kormendy and Gebhardt 2001), highlighting the correlations which exist between spheroid luminosity and black hole mass (e.g. Magorrian et al. 1998), and between spheroid velocity-dispersion and black hole mass (Gebhardt et al. 2000, Ferrarese and Merritt 2000). As discussed by McLure and Dunlop (2002), both these relations for inactive ellipticals, and the results of Hβ-derived virial black hole estimates in active objects, are consistent with a direct proportionality of black hole and spheroid mass of the form

$M_{BH} = 0.0012 M_{sph}$, with a typical scatter of 0.3 dex.

I used the luminosities from our best-fit galaxy models to estimate host-galaxy masses, given an estimate of the mass-to light ratio of an early-type galaxy (Jørgensen et al. 1996); $(M/L)_{R-band} \propto L^{0.31}$. I then used the black hole/galaxy mass relation above to estimate black hole masses for the quasars, independent of their observed nuclear output.

The results of this calculation are given in column 3 of Table 2.6. I find that all of the host galaxies are sufficiently massive ($M_{sph} > 10^{11} M_{\odot}$) to contain a black hole in excess of $10^8 M_{\odot}$, but the difference in mass between the black holes in optically powerful and optically weak quasars is not large enough to account for the factor ~ 10 increase in luminosity, implying that increased fuelling efficiency must also play a role in the most luminous objects. The median black hole masses for the high and low-luminosity subsamples are:

$$med(M_{BH})_{(M_N<-25)} = 7.7 \times 10^8$$

$$med(M_{BH})_{(M_N>-25)} = 5.9 \times 10^8$$

2.8.6 Fuelling efficiencies

We can now calculate the predicted luminosity of each object if the black hole were to radiate at its Eddington limit ($L_{Edd}^{Bol} = 1.26 \times 10^{31} \frac{M_{BH}}{M_{\odot}}$ Watts) and compare this with the actual luminosity of the quasar nucleus obtained from our model fitting. The results of this procedure are listed in columns 5 and 6 of Table 2.6. I have plotted these efficiencies against black hole mass in Figure 2.12 It is clear that there is no correlation: A given black hole may be found to radiate at any fraction of its Eddington Luminosity, and therefore a quasar's luminosity is set by both its black hole mass, and its fuelling rate. However, there is now a clear distinction between our high and low-luminosity subsamples in terms

of fuelling efficiency:

$$med\left(\frac{L_n}{L_{Edd}}\right)_{(M_N<-25)} = 0.62$$

$$med\left(\frac{L_n}{L_{Edd}}\right)_{(M_N>-25)} = 0.13$$

If we exclude the relatively poorly constrained luminous RQQ 1252+020 (which appears, from our modelling, to exceed the Eddington limit), the median Eddington ratio for the luminous subsample drops to 0.47, but this is clearly still significantly higher than for the low-luminosity sample.

Thus, within our $z = 0.4$ sample, increasing quasar luminosity appears, on average, to reflect a mix of both larger black hole mass, and increased fuelling efficiency. Not surprisingly, the only two quasars in the present sample with $M_V < -27$ have the two most massive black holes.

A number of other features of the results summarised in Table 2.6 are worthy of comment. First, while inferred fuelling efficiencies range over an order of magnitude, I find no evidence for super-Eddington accretion. If one excludes the poorly constrained RQQ 1252+020, the most efficient emitter is 0624+691, with $L_{nuc}/L_{edd} \simeq 1$. Second, the most massive central black hole found in our sample has a mass of $3 \times 10^9 M_\odot$, comparable to the inferred mass of the super-massive black holes at the centres of M87 (Marconi et al. 1997) and Cygnus A (Tadhunter et al. 2003). Thus, the basic physical quantities derived for the quasars in our sample appear to be entirely reasonable, requiring neither unorthodox methods of accretion, nor surprisingly massive black holes.

Due to the large scatter in inferred nuclear fuelling efficiency, the nature of the link between quasar luminosity and black hole mass is more easily explored by plotting host versus nuclear luminosity, shown in Figure 2.13 where I have plotted the absolute magnitudes of the hosts against those of the nuclei in our sample (circles), with 100%, 10% and 1% of the Eddington limit shown as solid,

Object	M_{sph} $(10^{11}M_{\odot})$	M_{BH} $(10^{9}M_{\odot})$	M_V^{Edd}	L_{nuc}/L_{Edd}
Radio-Quiet Quasars				
0624+691	13.90	1.67	−27.28	0.90
1001+291	7.23	0.87	−26.57	0.42
1230+097	5.54	0.66	−26.28	0.38
1252+020	1.27	0.15	−24.68	1.72
1254+021	13.70	1.64	−27.26	0.05
1258−015	1.83	0.22	−25.08	0.30
1821+643	24.70	2.96	−27.90	0.47
Radio-Loud Quasars				
0031−707	5.29	0.64	−26.23	0.11
0110+297	4.04	0.48	−25.94	0.16
0812+020	10.40	1.25	−26.96	0.14
1058+110	2.82	0.34	−25.54	0.16
1150+497	5.74	0.69	−26.32	0.13
1208+322	2.27	0.27	−25.31	0.76
1233−240	4.16	0.50	−25.97	0.33

Table 2.6: **Galaxy spheroid and black hole mass estimates** for each of the quasars in our sample with bulge-dominated hosts. The table also lists the theoretical Eddington luminosity, M_V^{Edd}, of each black hole, and the efficiency at which the black hole is accreting expressed as the ratio of the luminosity ascribed by our model to the nuclear point source to the Eddington luminosity predicted by the model of the host galaxy (L_{nuc}/L_{Edd}). Note that the RQQ 1252+020 appears to be accreting at a super-Eddington rate. This object has the least robust model fit of the entire sample and it is likely that the nuclear flux has been overestimated.

dashed and dotted lines respectively. Shown also are points from Dunlop et al. (2003) (diamonds) and McLeod et al. (1999) (triangles), converted to rest-frame V-band, and our adopted cosmology. I have also included 3 objects from the sample of Percival et al. (2001) (stars), for which archival HST images are now available (0043+039, 0316−346 and 1216+069). It now seems likely that seeing limitations in this ground-based study effectively prevented successful disentanglement of host and nuclear fluxes, and accurate morphological distinctions. The replacement images from the HST archive have been analysed in precisely the same way as has been described for the present sample, and converted into rest-frame V-band.

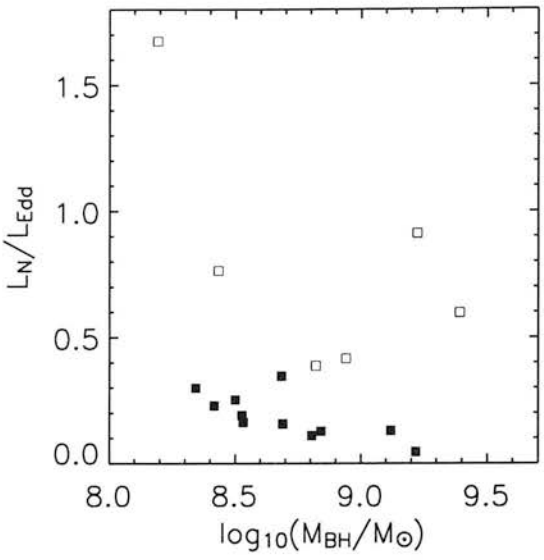

Figure 2.12: **Quasar accretion efficiency as a function of the Eddington luminosity versus black-hole mass** (as determined from the host galaxy luminosity). The sample is divided into optically luminous (open squares) and optically dim (solid squares) subsamples at $M_V(Nuc) = -25$, as discussed in the text. Our model fit to the RQQ 1252+020 implies that the object has a small host with an extremely luminous nucleus, yielding a super-Eddington luminosity. However, the quality of the model fit is poor, and this value is almost certainly erroneous. Overall there is no obvious tendency for fuelling efficiency to vary as a function of black-hole mass.

2.8.7 Black hole mass versus fuelling rate

The top panel of Figure 2.13 shows that, while central black holes appear to accrete with a wide range of efficiencies, the objects we term quasars are generally produced by black holes emitting at $> 10\%$ of their Eddington limit, residing in host galaxies with $L > L^\star$. However, perhaps the most impressive feature of this plot is that, for a given host galaxy luminosity, the most luminous nuclear source has a luminosity essentially exactly as would be predicted from the Eddington limit corresponding to the mass of the central black hole as deduced from the relationship $M_{BH} = 0.0012 M_{sph}$. In other words, while the statistical correlation between host-galaxy and nuclear luminosity within these samples may not be very strong, the relationship between host-galaxy and *maximum* nuclear luminosity appears extremely tight, and completely consistent with Eddington limited accretion. Indeed, so clean is this relation over two orders of magnitude in L_{nuc} that it has the potential to constrain the size of the scatter

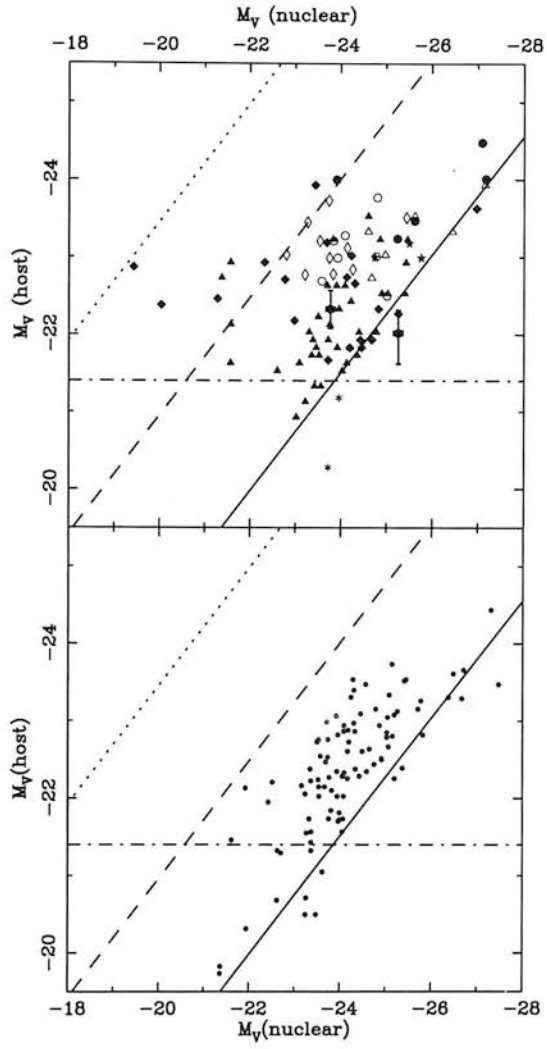

Figure 2.13: **Upper panel:** Host versus nuclear luminosity for the bulge-dominated quasars in the current sample (circles). The spheroidal components of the two disc-dominated quasars, 1258−015 and 1237−040 are shown by asterisks. The samples of McLeod et al. (1999) (triangles), and Dunlop et al. 2003 (diamonds), plus three objects from Percival et al. 2001 re-imaged with the HST (stars - see main text) are also presented. Filled symbols once again denote radio-quiet objects, and open symbols radio-loud objects. The solid, dashed and dotted lines represent objects radiating at 100%, 10% and 1% of the Eddington luminosity respectively on the assumption of a fixed black-hole to bulge mass ratio of $M_{BH} = 0.0012 M_{sph}$. The majority of the quasars in our sample appear to be radiating at $> 10\%$ of their Eddington limit (the single super-Eddington object is the poorly constrained 1252+020 - Figure 2.9 and main text). Error bars are smaller than the symbols for all objects except 1252+020 and 1258−015.
Lower panel: The predicted distribution on the host versus nucleus luminosity plane for a sample of quasars radiating at 50% of the Eddington limit, given an adopted scatter of 0.3 dex in the black hole:spheroid mass relation, and including the effect of the exponential cutoff in the luminosity function above L^* (dot-dashed line). The random sample has been re-sampled in order to reflect the the same distribution of nuclear luminosities as is displayed by the combined data in the upper panel. This scenario re-produces much (but not all of) the observed scatter in apparent fuelling efficiency without in fact requiring a range of Eddington ratios. However, at the same an assumed scatter of 0.3 dex or lower is required to avoid too many objects apparently breaching the rather solid Eddington limit displayed by the data.

in the underlying black-hole:spheroid relation for massive galaxies. In turn, such constraints can then illuminate the extent to which the apparent 1 dex scatter in fuelling efficiency can also be explained by intrinsic scatter in the underlying black-hole:spheroid mass relationship.

The lower panel of Figure 2.13 illustrates a simple model in which a sample of quasars is generated from a parent spheroidal galaxy population defined by a Schechter function (equation 2.10) with $\alpha = 1.25$ and $log_{10}(\frac{M^{\star}_{tot}}{M_{\odot}}) = 11.5$ (where $M^{\star}_{tot}$ denotes the turnover in the distribution of total mass, stellar and dark matter - see next section for further details). Here I assume a fixed accretion rate, the scatter being a reflection of the underlying scatter in the black-hole:spheroid mass ratio. The figure presented illustrates the situation for a sample of quasars radiating at 50% of the Eddington limit, with an assumed scatter in the underlying black hole:spheroid mass relation of 0.3 dex. These values were chosen for this illustration as the combination which best reproduces both the apparently tight Eddington limit, and level of scatter displayed by the data in the upper panel of Figure 2.13. Adoption of a scatter larger than 0.3 dex produces significantly more apparently super-Eddington objects than are observed. Conversely, adoption of a scatter substantially smaller than 0.3 dex reproduces the apparent Eddington limit more closely, but seriously under-predicts the apparent scatter in fuelling efficiency. This of course may not be a serious problem because even in the illustrated example some admixture of varying fuelling efficiency appears to be required to explain the full extent of the observed scatter in nuclear luminosity for a given host luminosity. The model is discussed in greater detail in the next section.

2.9 Monte-Carlo simulation of quasar population luminosity

I decided to follow up this latter section of the work, as it appears to be showing us something very interesting. We have found that the "Eddington" line forms quite a tight bound on the nuclear: host distribution of the quasar population. However, it is also clear that given any realistic scatter in the black hole:spheroid mass relation, we can get quite a large amount of scatter without the need for a range of fuelling efficiencies. This also means that if we do have any number of objects radiating at or close to L_{Edd}, we should expect to see a number of apparently super-Eddington objects on the plot.

I conducted Monte-Carlo simulations by generating random samples of black holes, drawn from a population of spheroidal galaxies. This population is defined by a Schechter function (an idealised luminosity function - equation 2.10), but with a fixed quantity of scatter on the $M_{BH} - M_{sph}$ relation.

$$\frac{dN(L)}{dL} = C(\frac{L}{L^{\star}})^{-5/4} e^{-L/L^{\star}} \tag{2.10}$$

Thus the mass of a black-hole is not fixed uniquely by the mass of its host spheroid, but the black-hole mass function will follow that of the host population. A fixed accretion rate is then assumed for the black hole sample, giving us a nuclear luminosity in direct proportion to the black-hole mass. I fixed the turnover at $log_{10}(\frac{M^{\star}_{tot}}{M_{\odot}}) = 11.5$ (where $M^{\star}_{tot}$ denotes the turnover in the distribution of total mass, stellar and dark matter). For validity of comparison, and to eliminate the effect of any selection effects, the simulated sample is forced to match the observed sample in terms of its nuclear luminosity distribution (which closely approximates the total luminosity distribution, under the assumption of fixed accretion rate).

Monte-carlo simulations are generated from the resulting probability distribution, and compared

to the observed dataset (top panel of Figure 2.13) through the 2-dimensional Kolmogorov-Smirnov test (Table 2.7). Figure 2.14 shows a small selection of my simulated datasets, illustrating the effect of increased $M_{BH} - M_{sph}$ scatter on the observed $L_{Nuc} - L_{Host}$ distribution in a simple quasar population, modelled as described above. Results are also shown for different values of the accretion efficiency (across the page).

2.9.1 The 2D Kolmogorov-Smirnov test

The Kolmogorov-Smirnov (KS) test is a useful way of comparing two 1-dimensional unbinned populations (see Press et al. 1992 for more detail). A useful generalisation to two-dimensional distributions was first proposed by Peacock (1983), and developed by Fasano and Franceschini (1987). Instead of comparing the cumulative difference between the distributions (which is not well defined in more than one dimension), we look at the integrated probability in each of the four quadrants defined by a given point. So for the point (x_i, y_i), we look at the total fraction of the data that is found in each of the four quadrants: $(x > x_i, y > y_i), (x < x_i, y > y_i), (x < x_i, y < y_i), (x > x_i, y < y_i)$. The two-dimensional KS statistic, D is defined by the maximum difference of the corresponding integrated probabilities (Press et al. 1992), in a manner that is analogous to the statistic calculated in the 1D KS test.

The results of comparison using the 2D KS test are presented in Table 2.7. Here I have marginalised over the accretion efficiency in each case, in order to obtain the overall probability p that the quasar sample is consistent with a fixed efficiency, and a given scatter. The only prior is that the fuelling efficiency is bound between 1% and 100% of the Eddington rate.

I find that for a 0.4dex scatter, the quasar sample is marginally consistent with a population in which there is a fixed fuelling efficiency (p=0.157). However, if the scatter is found to be any smaller, we are able to exclude this hypothesis quite strongly: For 0.3dex scatter, p=0.012; and for 0.2dex

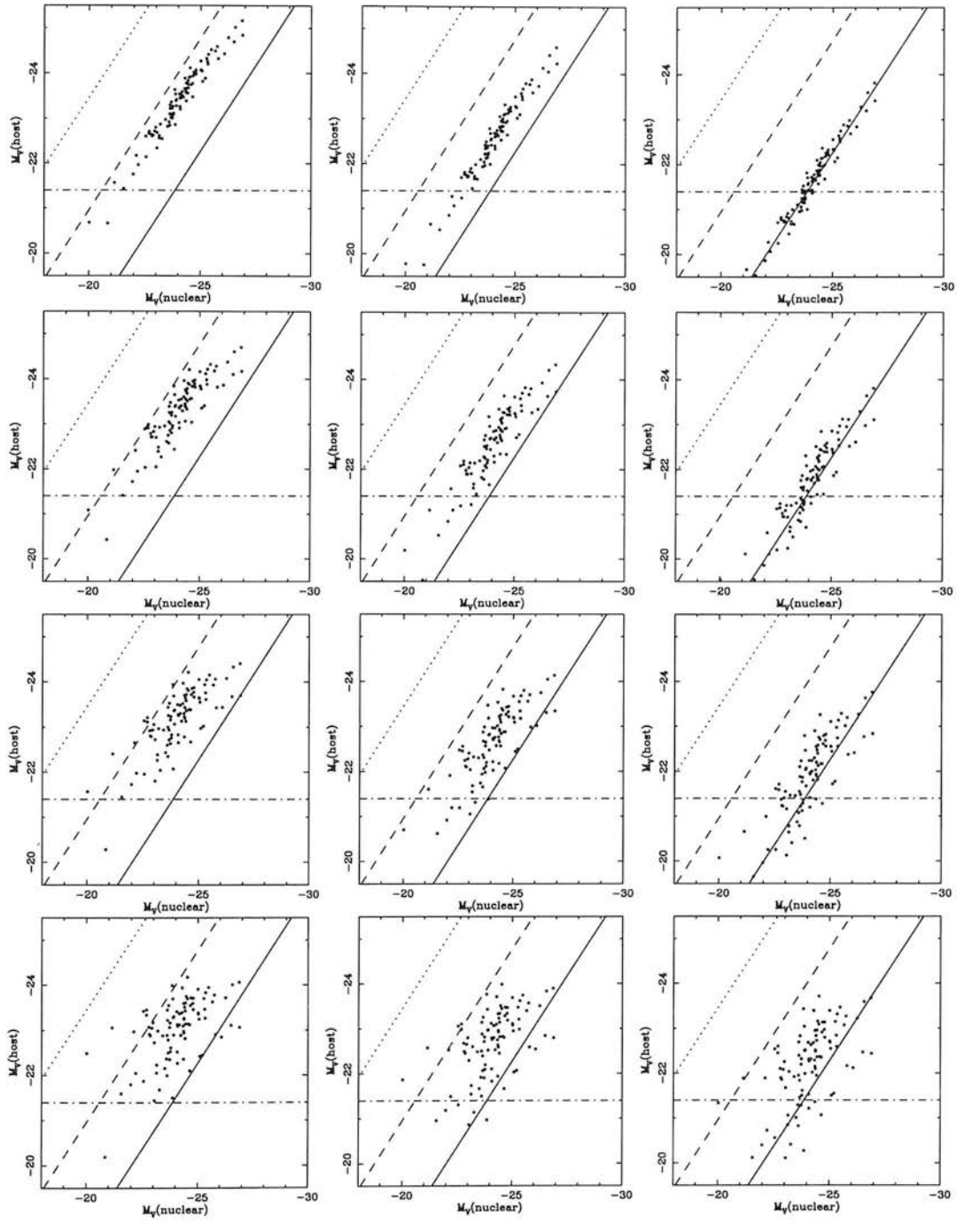

Figure 2.14: **Simulated quasar samples** illustrating the effect of increased efficiency (with respect to Eddington) across the page, and scatter on the Black Hole-Spheroid mass relation of the underlying galaxy population down the page. Figures are shown with 0.1, 0.2, 0.3 and 0.5dex scatter, and at efficiencies of 0.1, 0.3 and 0.5. Note that, due to the effects of the scatter, an efficiency of 0.1 does *not* coincide with the $10\%L_{Edd}$ line.

Table 2.7: **Constraining the scatter on the $M_{BH} - Msph$ relation** using the 2D KS test, marginalised over the fuelling efficiency for a given scatter. The table shows the KS statistic, D, and the significance level, p.

Scatter on $M_{BH} - Msph$ (dex)	D	p
0.1	0.172	0.005
0.15	0.151	0.022
0.2	0.150	0.022
0.25	0.156	0.015
0.3	0.161	0.012
0.35	0.154	0.018
0.4	0.100	0.157
0.45	0.152	0.198
0.5	0.190	0.002

scatter, p=0.022.

2.9.2 Discussion

From simulations of the sort described above, the observed apparent tight upper (Eddington) limit on fueling efficiency can be used to set an upper limit of 0.3 dex on the scatter in the underlying black-hole:spheroid mass relation, consistent with other recently derived values (McLure and Dunlop 2002, Marconi and Hunt 2003). A significant fraction of the scatter observed in the upper panel of Figure 2.13 can then still be attributed to the scatter in the underlying mass relationship, but some variation in assumed efficiency would still seem to be required to reproduce the most underluminous objects.

We can use the tightness of the bound placed by the Eddington line to place constraints on the hosts of higher redshift quasars, where direct imaging of the host is not possible. A quick inspection of Figure 2.13 reveals that any quasar brighter than $M_V = -27$ must be found in, or at least end up within, a spheroidal galaxy brighter than $M_V = -24$, and must be radiating at a rate close to its Eddington limit. The turnover in the Schechter function places a natural limit on the abundance of

such large galaxies, and the data appear to show just such a cutoff at a host luminosity of $M_V \simeq -24.5$, the first time that such an effect has been observed.

2.10 Summary

Through the careful analysis of deep HST images, I have succeeded in determining the basic properties of the host galaxies of quasars spanning a factor of $\simeq 20$ in luminosity, but within a narrow redshift range at $z \simeq 0.4$. The sample under study contains both radio-loud and radio-quiet quasars, and includes some of the most luminous quasars known in the low-redshift universe.

Our results confirm and extend the trends uncovered in our previous HST-based studies of lower luminosity objects (McLure et al. 1999, Dunlop et al. 2003). Specifically we find that the hosts of all the radio-loud quasars, and all the radio-quiet quasars with $M_V < -24$ are giant elliptical galaxies, with luminosities $L > L^{\star}$, and scalelengths $R_e \simeq 10$ kpc. Moreover, the Kormendy relation displayed by these host galaxies is indistinguishable from that displayed by nearby, inactive ellipticals.

From the luminosities of their hosts I have estimated the masses of the black holes which power the quasars using the relationship $M_{BH} = 0.0012 M_{sph}$ and hence, via comparison with the quasar nuclear luminosities, also the efficiency with which each black hole is emitting relative to the Eddington limit. We find that the order-of-magnitude increase in nuclear luminosity across our sample is the result of an increase in characteristic black hole mass by a factor $\simeq 3$, coupled with a comparable increase in typical black hole fuelling efficiency. However, we find no evidence for super-Eddington accretion, and the largest inferred black hole mass in our sample is $M_{BH} \simeq 3 \times 10^9 \mathrm{M}_{\odot}$, comparable to the mass of the black holes at the centres of M87 and Cygnus A.

We explore whether intrinsic scatter in the underlying $M_{BH} : M_{sph}$ relation (rather than a wide range in fuelling efficiency) can explain the observed scatter in the $M_V(host) : M_V(nuc)$ plane occu-

pied by quasars. We find that the observed tight upper limit on the relation between $M_V(host)$ and maximum $M_V(nuc)$, (consistent with the Eddington limit inferred from a single constant of proportionality in the $M_{BH} : M_{sph}$) constrains the scatter in the underlying black-hole:spheroid mass relation to be 0.3 dex or smaller, but that this mass-relation scatter can indeed explain a substantial fraction of the apparent range in fuelling efficiency displayed by the quasars.

Finally, our results imply that any quasar more luminous than $M_V = -27$ must be destined to end up in a present-day massive elliptical with $M_V < -24$, but capped by the Schechter cutoff at $M_V \approx -24.5$.

2.11 Concluding Remarks

I have successfully deconvolved HST V-band images of a sample quasars, spanning $-23 < M_V < -28$ at $z \sim 0.4$, and recovered host galaxy morphological details in each case. The sample pushes the study of quasar host galaxies into hitherto uncharted regions, including objects that are comparable with the brightest quasars known. The majority of hosts are found to be giant ellipticals, with only three of the dimmest five AGN being hosted by discs. All radio loud objects in the sample are found to be hosted by giant ellipticals.

We find that the spread in nuclear luminosity cannot be explained purely by a simple increase in black hole mass: fuelling must play a key role. The sample spans approximately a decade in nuclear luminosity, but we find only an increase by a factor of ~ 3 in host luminosity, and hence in projected black hole mass. The scatter in the Magorrian relation clearly plays a role too, but cannot describe this variation on its own, in the absence of significant numbers of apparently super-Eddington objects. The precise role of engine size vs fuelling can only be unravelled through accurate independent measures of Black Hole Mass,and at present the only truly reliable method is reverberation mapping, with BLR

linewidth techniques improving.

We appear to see a turnover in the M_{Nuc}/M_{Host} distribution at high host luminosity. This is attributed to the exponential tail in the galaxy luminosity (Schechter) function. However, we do not see a glut of super-Eddington objects at high Luminosity, and we must suppose that the Eddington limit imposes a natural barrier to quasar luminosity. Furthermore, there is emerging evidence that the Magorrian relation continues to hold at the most massive extremes, entwining the galaxy and black hole mass functions, and offering a tantalising glimpse of the intimacy between black hole and galaxy evolution.

There is still some discrepancy between the hosts of these luminous quasars, and the better-studied, lower-luminosity, disc-dominated Seyferts. Three of the hosts studied here were found to be disc-dominated, with one of these showing no detectable sign of a bulge. These three are all hosts of lower-luminosity quasars, close to the Seyfert dividing line. It is possible that the luminous nuclei in quasars are masking a small-scale disc component, but it is now clear that all luminous quasar hosts are, at the very least, bulge-dominated.

It is important to bear in mind that the Hubble tuning fork represents a continuum in galaxy properties, and not simply a bimodal (Bulge / Disc) distribution. The observed increase in AGN luminosity may turn out to be a simple reflection of this. As we progress to larger and larger bulges, and hence larger and larger black holes, we are progressing to larger and larger central engines. Seyferts and Quasars are not disconnected phenomena, but perhaps two extremes of a spectrum which is reflected also in the host galaxy properties, as we appear to see in this sample.

Further work must seek to address the fuelling issue, both its relevance to overall quasar luminosity (as discussed above), and mechanisms by which it might proceed in giant elliptical galaxies. In particular, we must investigate further whether these hosts are genuine old red, dead ellipticals, or whether they contain significant young stellar populations, and large quantities of dust.

It seems that in the optical, we do not have the same dichotomy as in the radio: The cutoff between radio-loud and radio-quiet quasars was once defined by the ratio of radio to optical luminosities. This definition was dropped when it became clear that there was no correlation, and hence no physical meaning in the cutoff (Miller et al. 1990). In the optical case, we do not see a bimodal distribution. It would appear that the apparently bimodal distribution in morphological type has blinded us to this fact, and we therefore end up talking about Quasars and Seyferts almost as though they were disconnected phenomena. Although this field is hardly cut and dried, this terminology appears to be misleading, as more and more signs point in the direction of a continuum in nuclear luminosity, which runs alongside a continuum in host type.

Studies such as this one continue to have relevance in the days of massive datasets, such as SDSS. Clearly there is a number issue. Nearby objects offer us the chance to probe directly the physics in specific instances, and laboratories in which to run theories of accretion through their paces. Large datasets will provide us with powerful statistical information, but no individual detail. Quasar host studies span the yawning gap, and will continue to offer an ever deeper insight into the connection between galaxies and their black holes, by spanning the range of AGN phenomenology, and providing details on significant numbers of differently behaved objects.

CHAPTER 3

Evolution of quasar hosts out to redshift 2

In recent years the Hubble Space Telescope has played a major role in establishing the close link between black-hole mass and spheroid mass in both quiescent and active galaxies in the local universe. Consequently black-hole and spheroid formation and growth are now viewed as intimately related processes, and establishing the mass of quasar host galaxies as a function of redshift is now seen as a key measurement in observational cosmology (e.g. Kauffmann and Haehnelt 2000).

In Kukula et al. (2001), NICMOS imaging was used to derive the best estimate to date of the mass evolution of the hosts of both radio-quiet and radio-loud quasars out to $z \sim 2$. Under the assumption of passive stellar-population evolution their results are consistent with the black-hole/spheroid population being unchanged out to this distance. However, the crucial assumption of passive evolution needs to be tested, because discovery of any substantial star-formation activity would yield a reduction in luminosity-estimated host masses at $z \sim 1-2$, potentially bringing these results into line with the order-of-magnitude mass reduction predicted by the hierarchical models of Kauffmann & Haenhelt

2000.

3.1 Introduction

In this chapter we re-visit the luminosity-matched Kukula et al. quasar sub-samples at $z \sim 1$ and $z \sim 2$, using WFPC2 to obtain rest-frame near-UV images. When coupled with the NICMOS data, this data yields the first reliable rest-frame $U - V$ colours for high-z quasar hosts, and hence the first unbiased measurement of host-galaxy masses out to $z \sim 2$. This work enables us to test evolutionary scenarios, in particular the crucial assumption in Kukula et al., of passive evolution, and is of central importance to quasar host galaxy studies. We saw in the introductory chapter that the quasar number density appears to peak at about the same time as the star formation rate. However we do not yet understand the nature of the link between this phase of massive black hole growth and the formation or evolution of galaxies. Determining accurate host-galaxy masses at cosmologically significant redshifts will go some way to solving this problem.

Colours straddling the 4000Åbreak provide sensitive measurement of the age of a stellar population (e.g. Chiosi et al. 1997). We require rest-frame near-UV observations, which are particularly difficult for quasar host galaxies, given the domination of the nucleus at such wavelengths. We attempt to alleviate this problem as far as possible through careful filter selection (figure 3.1).

3.2 Observations

As before (both in this thesis and in Kukula et al. 2001), we carefully choreographed our observations in order to give us the best chance of recovering information about the host galaxy. However, since in this case the aim is to measure the rest-frame U-band flux (necessarily dominated by the nuclear

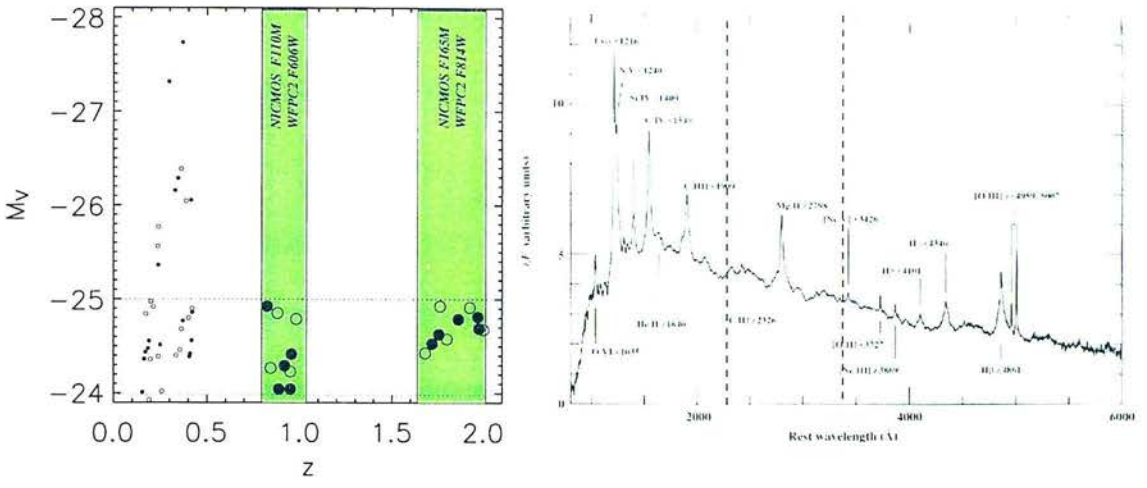

Figure 3.1: **Left:** Absolute V-band magnitudes versus redshift for the RQQ's (filled circles) and RLQ's (open circles) in the current study, and illustrating the optical matching of the RQ/RL subsamples (see text). These objects were studied by Kukula et al. 2001, using NICMOS data, and are revisited here using WFPC2. Also shown for comparison are the samples of Dunlop et al. 2003, at $z \approx 0.2$, and chapter 2 / Floyd et al. 2004 at $z \approx 0.4$. Note in particular the comparison subsamples of those papers, in the same luminosity range, and selected in the same manner as the present sample.
Right: A composite quasar spectrum illustrating the rest-frame wavelength range of the WFPC2 observations. Due to the rapid falloff of galaxy flux, it is futile pushing further into the UV to avoid the MgII line. However, we do avoid the [NeV], [OII] and CIII] lines.

component), minimisation of the nuclear-to-host ratio obviously has to suffer somewhat at the expense of achieving our goals. We were careful to ensure observations of the required sensitivity (much higher than required previously), and to select filters that avoid the main nuclear emission lines where possible.

3.2.1 Sample design

The sample is divided into 2 subsamples, at $z \approx 1$ and $z \approx 2$. Each subsample contains an even mix of RLQ's and RQQ's. The selection criteria and matching are discussed in some detail in Kukula et al. (2001).

Radio and optical luminosities

The sample is confined to the same $-24 > M_V > -25$ absolute magnitude range as the comparison low-redshift "baseline" sample of McLure et al. (1999) and Dunlop et al. (2003), and the "low-luminosity" comparison sample of chapter 2 and Floyd et al. (2004). It is necessary to limit such high-redshift samples to quasars of moderate luminosity if we are too have any chance of detecting the host galaxy. However, we are still clearly above the $M_V = -23.5$ Quasar / Seyfert dividing line.

The radio-quiet and loud subsamples were originally selected in such a way as to avoid intrinsic bias in comparison of the host properties (Kukula et al. 2001), by ensuring that their distributions in the $M_V - z$ plane are indistinguishable. This technique results in samples that are optically matched, and differ *a priori* only in terms of their radio properties. This task is a difficult one, requiring:

- That all RQQ's have been observed on the VLA with high sensitivity, but remain undetected.
- That the RLQ sample is confined to steep-spectrum objects, thus avoiding any in which the radio luminosity might be boosted artificially by relativistic beaming.

These two criteria almost uniquely define each of the four samples selected (Kukula et al. 2001).

The radio properties are listed in table 3.1. For the RQQ's only VLA upper limits are presently available, but these are sufficient to place the objects well below the RLQ/RQQ cutoff at $L_{5GHz} = 10^{-24}$ W Hz^{-1} sr^{-1}.

I searched the available radio archives (FIRST/NVSS) for detections of these objects. The archives simply look for 5-σ source detections. However, if we are to take a specific region of sky, and find an object at a location that we know is occupied by a quasar, then an even-lower significance detection can be useful in placing flux limits on that object. Unfortunately, all of the regions occupied by these RQQ's were found to be blank.

Table 3.1: V-band magnitudes and 5 GHz radio flux densities for the quasars in the present sample. At the time of writing the majority of the RQQ's have only upper limits to their radio fluxes, but these are sufficient to place them safely below the accepted radio-loud/radio-quiet boundary of $L_{5GHz} < 10^{-24}$ W Hz^{-1} sr^{-1}.

Source	Class	z	V	S_{5GHz} (mJy)
		$z \approx 1$		
1302+361	RQQ	0.890	18.73	
1301+358	RQQ	0.910	18.54	
0049−277	RQQ	0.955	18.88	
1303+360	RQQ	0.970	18.57	
0440−003	RLQ	0.844	18.41	1084
2112+172	RLQ	0.878	17.89	159
2044−027	RLQ	0.942	18.69	870
0938+185	RLQ	0.943	18.49	158
2207+020	RLQ	0.976	18.19	260
		$z \approx 2$		
0056−281	RQQ	1.716	19.64	
0048−293	RQQ	1.756	19.62	
0049−295	RQQ	1.868	19.55	
0053−286	RQQ	1.964	19.65	
0050−291	RQQ	1.976	19.77	
1524−136	RLQ	1.687	19.69	1338
2351+456	RLQ	1.992	19.79	1145
2156+297	RLQ	1.759	19.29	432
2204−205	RLQ	1.923	19.49	155

3.2.2 Filter Selection

In order to sample the host galaxy light we used the F606W filter (equivalent to a wide-V band) at redshift 1, and the F814W (standard HST I-band) at redshift 2. In each case, this filter equates in the rest-frame to wavelengths in the range $2300\mathring{A} < \lambda < 3400\mathring{A}$; roughly rest-frame U-band. These filter choices neatly avoid certain strong nuclear emission lines such as [OII]λ3727] and CIII]λ1909. Unfortunately, we cannot avoid straddling the prominent MgII line at λ =2798.

3.2.3 Sensitivity limits

The sample was previously observed in J-band ($z \approx 1$) and H-band ($z \approx 2$) using NICMOS (Kukula et al. 2001), corresponding approximately to rest-frame V-band at the respective redshifts of the 2 subsamples. The new observations were performed using WFPC2, during the Hubble Space Telescope's cycle 10. The shift to UV requires a large increase in sensitivity. Although the nuclear flux is fairly flat in the optical-UV ($f_\nu \propto \nu^{-0.2}$), the host galaxy flux is reduced by a factor of ~ 3 in crossing the 4000Åbreak (see the normal galaxy spectrum, figure 1.3 in the introduction). Furthermore, we are sampling a part of the spectrum where the presence of some nuclear emission lines is unavoidable. This extra flux means that the nuclear to host ratio could be an order of magnitude larger at λ_r =2800Å than was the case at rest-frame V. This is somewhat offset thanks to WFPC2's far smaller PSF and higher-throughput wide filters (relative to NICMOS), but we still need to roughly double our sensitivity.

At J-band (F110M), Kukula et al. achieved 3σ surface brightness sensitivity limit of 19.5 mag arcsec^{-2} per NICMOS pixel. At H-band this limit was 18.75 mag arcsec^{-2} per NICMOS pixel. At a radius of 0.8arcsec, a pixel-wide annulus with NICMOS 0.043 arcsec pixels contains roughly $\sim$ 100 pixels. Azimuthal averaging over this annulus yields a surface brightness limit of $\mu_J \sim 22$mag

arcsec^{-2}.

Assuming passively evolving elliptical hosts, we would expect to find colours:

- $V_{606} - J \approx 4$ at $z \approx 1$.
- $I - H \approx 4$ at $z \approx 2$.

We therefore need to follow the rest-frame UV luminosity profile of the hosts right down to $\mu_V \sim 26$ and $\mu_I \sim 25.25$, at the 6σ level. With the larger 0.1arcsec pixels of the WF chips, this level corresponds to 6σ sensitivity limits per WF pixel at levels of $\mu_V \sim 23.75$ and $\mu_I \sim 23$.

Integration Times

Two whole orbits were devoted to each member of the lower redshift sample, and four orbits to each redshift ~ 2 object. Each orbit is sufficient to fit in 3 long (600 or 700s) exposures, plus a few short snapshots to provide a good characterisation of the bright nuclear region, in the event that the longer integrations saturated. This strategy resulted in a total on-source integration time of at least 3600s for the $z \approx 1$ objects, and 7800s for those at $z \approx 2$. Details of the observations are summarised in table 3.2.

Detector

The WF3 detector was selected for use throughout, due to its performance relative to WF2, and WF4 during the 12 month period preceding the phase 2 proposal deadline. It suffered fewer faulty pixels than the other 2 Wide Field chips.

3.2.4 PSF determination

As before, the key to recovering the host galaxies is in accurate characterisation of the PSF, and hence successful modelling and removal of the highly dominant active nuclear component. This issue

Table 3.2: **Summary of observations** J2000 co-ordinates were obtained from the Digitised Sky Survey plates maintained by the Space Telescope Science Institute. Redshifts and apparent V magnitudes are from the quasar catalogue of Veron-Cetty and Veron (2000). For consistency I use a B1950 IAU format to refer to the quasars in this thesis; the name under which each object appears in the HST Archive is given in the final column and additional names are given in the description of each object in Section 3.6. Observations were carried out as part of HST cycle 10 (2001), using the f606w filter for the low-redshift objects, and f814w at high-redshift. These correspond fairly closely to the rest-frame U band in each case.

Name (B1950)	Type	z	RA (J2000)	Dec (J2000)	V	M_V	Observing date	HST archive name
Wide-V-band (f606w) sample ($z \approx 1$)								
1302+361	RQQ	0.890	13 : 05 : 05.04	+35 : 51 : 20.58	18.73	−24.0	Jun 08 2001	BVF247
1301+358	RQQ	0.910	13 : 04 : 10.47	+35 : 36 : 50.83	18.54	−24.3	Jun 10 2001	BVF225
0049−277	RQQ	0.955	00 : 52 : 22.76	−27 : 30 : 02.80	18.88	−24.0	Aug 11 2001	SGP5:46
1303+360	RQQ	0.970	13 : 05 : 30.91	+35 : 17 : 13.48	18.57	−24.4	May 23 2001	BVF262
0440−003	RLQ	0.844	04 : 42 : 38.64	−00 : 17 : 43.43	18.41	−24.2	Jul 17 2001	PKS0440−00
2112+172	RLQ	0.878	21 : 14 : 56.68	+17 : 29 : 22.66	17.89	−24.8	Jun 05 2001	MC2112+172
2044−027	RLQ	0.942	20 : 47 : 10.39	−02 : 36 : 22.48	18.69	−24.2	Jun 08 2001	3C422
0938+185	RLQ	0.943	09 : 41 : 23.17	+18 : 21 : 06.00	18.49	−24.4	Jun 07 2001	PKS0938+18
2207+020	RLQ	0.976	22 : 09 : 32.82	+02 : 18 : 40.85	18.19	−24.8	Jun 06 2001	4C02.54
1313+705	Star	0	13 : 38 : 59.49	+70 : 16 : 39.51	12.80		Jun 15 2001	PSF-STAR
I-band (f814w) sample ($z \approx 2$)								
0056−281	RQQ	1.716	00 : 59 : 08.88	−27 : 51 : 24.7	19.64	−24.55	Oct 22 2001	SGP4:39
0048−293	RQQ	1.756	00 : 51 : 14.32	−29 : 05 : 19.7	19.62	−24.61	Jun 13 2001	SGP2:36
0049−295	RQQ	1.868	00 : 52 : 07.60	−29 : 17 : 50.2	19.55	−24.81	Jun 14 2001	SGP2:25
0053−286	RQQ	1.964	00 : 55 : 43.41	−28 : 24 : 09.7	19.65	−24.82	Jun 15 2001	SGP3:39
0050−291	RQQ	1.976	00 : 52 : 38.47	−28 : 51 : 12.9	19.77	−24.71	Jul 11 2001	SGP2:11
1524−136	RLQ	1.687	15 : 26 : 59.44	−13 : 51 : 01.3	19.69	−24.46	Jun 06 2001	PKS1524−13
2351+456	RLQ	1.992	23 : 54 : 22.27	+45 : 53 : 05.19	19.79	−24.71	Jun 09 2001	4C45.51
2156+297	RLQ	1.759	21 : 58 : 42.0	+29 : 59 : 08.0	19.29	−24.95	Jun 10 2001	B2−2156+29
2204−205	RLQ	1.923	22 : 07 : 33.94	−20 : 38 : 34.9	19.49	−24.93	Jun 22 2001	PKS2204−20
1313+705	Star	0	13 : 38 : 59.49	+70 : 16 : 39.51	12.80		Jun 16 2001	PSF-STAR

assumes even more critical importance in the present study than in the previous one for two reasons:

- We are dealing with more distant objects in which the flux of the host appears less extended.
- We are observing in the rest-frame U-band of the object, in which we expect less galaxy light, and a more nuclear-dominated image.

We therefore dedicated two whole orbits to the observation of GRW+70D5824, the same PSF star as used in the previous study. The star was observed through each filter used in the observations, for one orbit, to give an accurate representation of the PSF at each wavelength. However, this empirical PSF cannot accurately reproduce the sub-pixel centring of each object.

3.3 Data reduction

Data reduction was performed basically as before, using the standard HST/WFPC2 pipeline for the most of the basic steps, and IRAF for the more detailed work. Briefly, the data reduction steps were as follows:

- **Cosmic Ray Removal** using CRREJ (iterative sigma clipping algorithm) to generate a single deep CR-free image from the individual .
- **Background subtraction:** Fitting and subtraction of a smooth surface to the background of each image. The sky frame is preserved for the calculation of Poisson statistics at the modelling stage.
- **Building deep, unsaturated quasar images** where necessary, by replacing the saturated central regions of the deep CR-free image with an unsaturated "snapshot" of the quasar.

The final step was only necessary for the $z \approx 1$ sample and 0049-295 (SGP2:25).

3.4 Modelling

I applied the same 2D modelling technique as is discussed in detail in the previous chapter. This code simultaneously models host galaxy and active galactic nucleus through the convolution of a simple model quasar (galaxy + unresolved nucleus) with an accurate representation of the instrumental PSF, *positioned at the precise location of the nucleus.* We assume that the central region is dominated by nuclear flux, and that the shape of the PSF at large radius in insensitive to sub-pixel shifts in the position of the nucleus. A TINYTIM model is used to accurately represent the PSF close to the nucleus, and this can be substituted into a stellar PSF which better models the flux at large radii.

For the $z \approx 2$ objects we found that the images were so compact ($r < 2''$)that the stellar PSF was unnecessary, and the TINYTIM model was used alone.

The changeover from PSF sampling errors to Poisson was calculated by the modelling code, by finding the radius at which the sampling error drops to 1.5 times the mean background Poisson noise. The noise on the central pixel was fixed by the Poisson statistic.

Fits using both spheroidal and disk host galaxy morphologies were attempted in all cases, to discover whether there was any significance in the quality of fit.

As explained earlier, a downhill simplex method was adopted for its combination of robust reliability and relative speed. I started with 6 common starting simplexes for each object, running the code to find the best fit. A more refined fit was then performed using simplexes that took the best-fit values from the first round and adding $\pm 25\%$, $\pm 10\%$ and $\pm 5\%$. Finally, I used a 3D grid search centred on the best-fitting model yielded by the iterative simplex searches. For this final grid, I locked the position angle and axial ratio of the hosts, as they have the least impact on the overall quality of the fit, and this results in a grid in the remaining three parameters (nuclear flux, host flux, and host size) that could be implemented with reasonable resolution and remained computationally viable. The 2-D

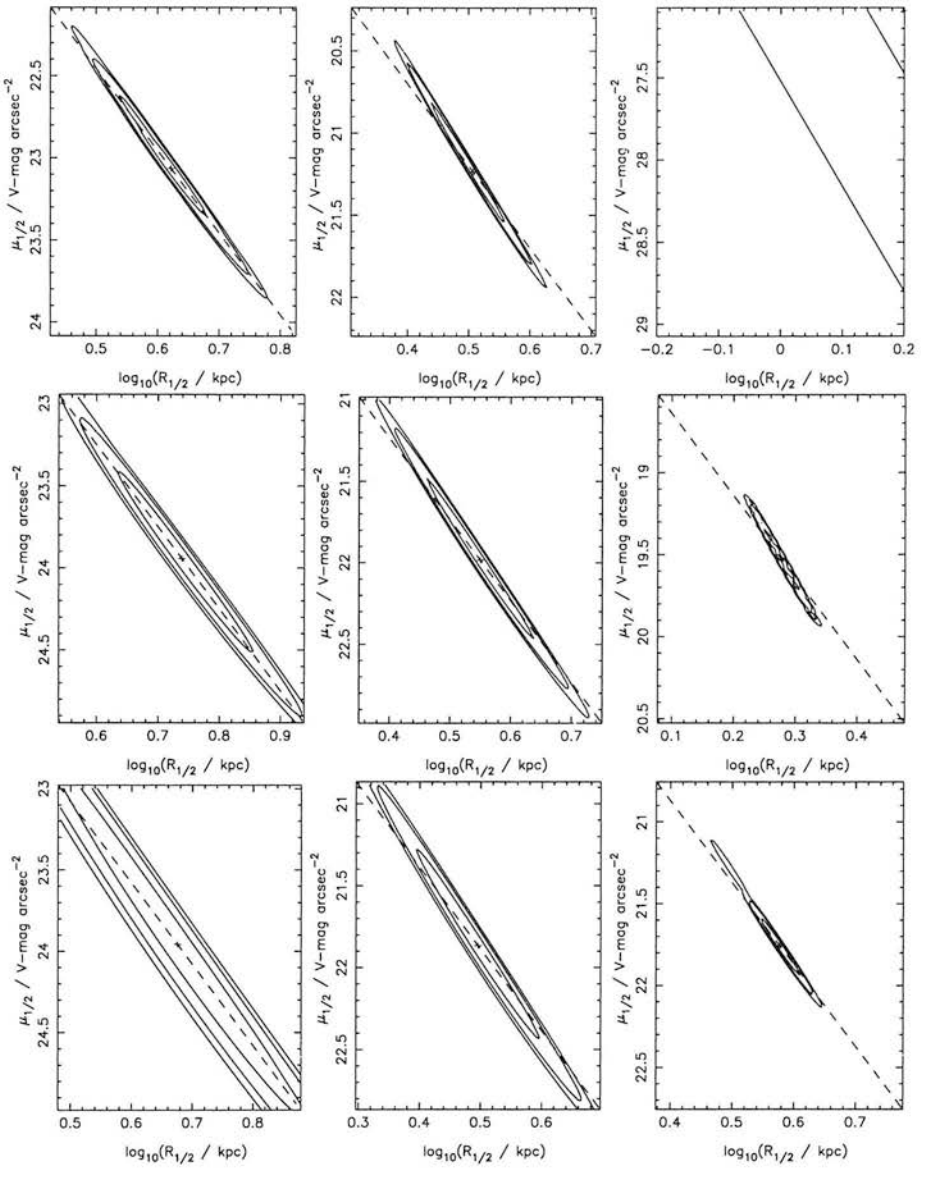

Figure 3.2: χ^2 **contours in the** $\mu - R$ **plane** for the $z \approx 1$ sample. Note that the slope of 5 (dashed line) implies a constrained host galaxy luminosity, even where the scalelength and surface brightness are poorly constrained.

projection onto the $\mu - R$ plane is shown in figures 3.2 and 3.2.

3.4.1 Fixed scalelength models

Since one of the aims of this work is to directly compare the host galaxies in U band with those detected in V band by Kukula et al. (2001), it is important to be certain that we are comparing

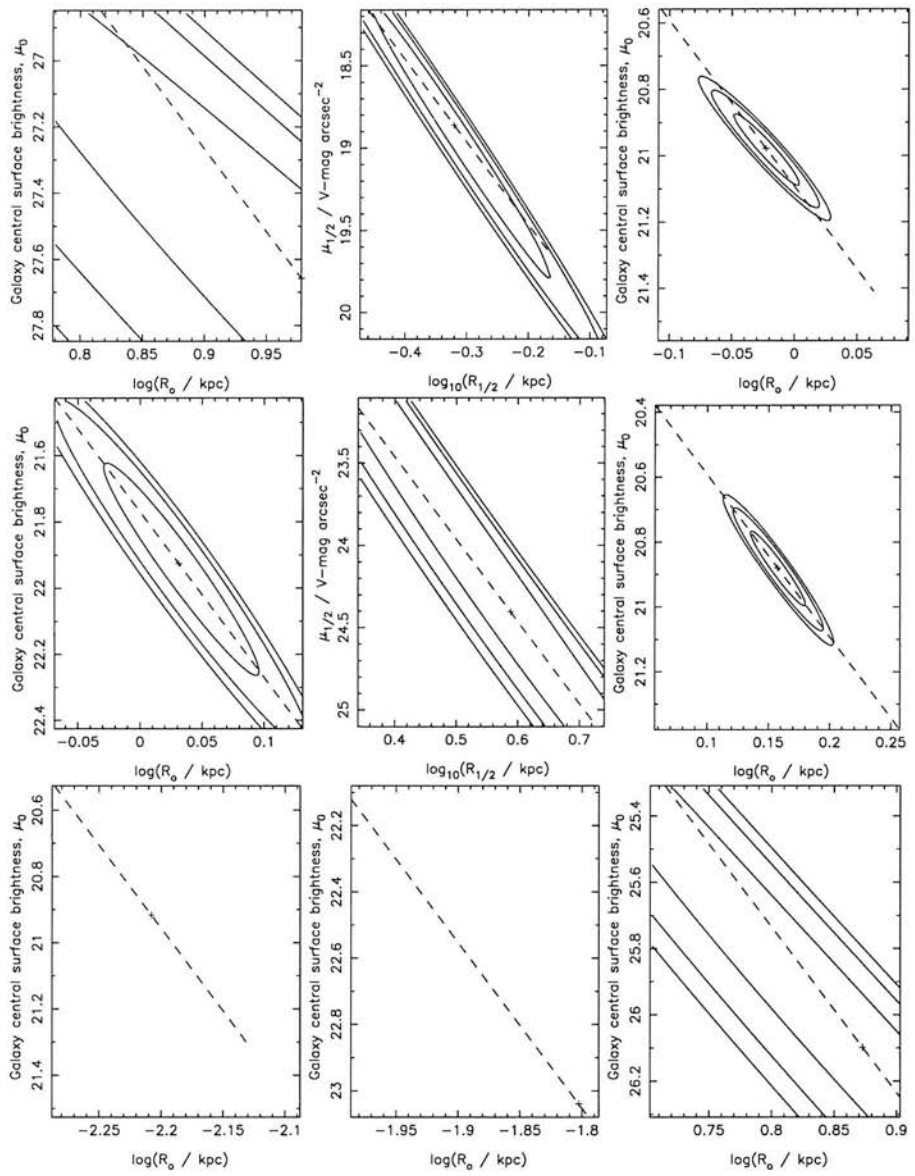

Figure 3.3: χ^2 **contours in the** $\mu - R$ **plane** for the $z \approx 2$ sample. Note that the slope of 5 (dashed line) implies a constrained host galaxy luminosity, even where the scalelength and surface brightness are poorly constrained.

comparable galaxies. Therefore in addition to the conventional modelling, I decided to fit each object using a series of fixed scalelength models. In this case we have a 4-dimensional search, but the modelling is identical in all other respects. This technique was adopted by Kukula et al. for many of their $z \approx 2$ objects, since they were unable to recover reliable measures of the scalelength at this redshift. I obtained the original data and the results of all the fits from the Kukula et al. NICMOS imaging of the high-redshift bin, so that a direct comparison could be made between the host galaxy fits with identical scalelengths. They did not follow the same approach for the lower redshift bin, as they were able to accurately determine all the scalelengths. However, I chose to apply the technique across the board in an effort to demonstrate the stability of the host galaxy luminosities recovered by the modelling, and in order to compare host models of similar sizes at different wavelengths.

3.5 Results

Here I present results for the best fitting models, as arrived at through the iterative method explained above, alongside the fixed scalelength models. For the lower redshift ($z \approx 1$) sample, the code successfully fit both elliptical and disc galaxy components to the objects, but in all cases found a preference for the de-Vaucouleurs morphology (table 3.3). At the higher redshift bin ($z \approx 2$), no significant morphological distinctions could be made. The results presented therefore all assume a de-Vaucouleurs type host (table 3.3). Note the consistency of the host and nuclear luminosities obtained using host galaxies of different fixed scalelength, which vindicates the use of the our recovered host galaxy luminosities in calculating colours.

Radial profiles for the best-fit models are presented in figures 3.4 and 3.5. In the lower redshift bin we are generally able to trace the host out to radii of about 3 arcsec. For the higher redshift objects, the limit is approximately 2 arcsec. In three of the $z \approx 2$ objects we have a significant deficit in nuclear

Table 3.3: Results of model fitting with both de Vaucouleurs spheroid and Freeman disc models. Columns are as follows: object name; best fitting host-galaxy morphology (disc or elliptical); reduced-χ^2 value for the best fit model; $\Delta\chi^2$ between the chosen and alternative-morphology model; half-light radius, $R_{1/2}$, of best fitting galaxy model in kpc; surface brightness of the host at the half-light radius, $\mu_{1/2}$, in units of I mag.arcsec^{-2}; Integrated apparent V-band magnitudes of the nucleus and the host galaxy; integrated absolute magnitudes of the nucleus and the host galaxy, converted to Johnson U-band ($h = 0.5$); the ratio of integrated nuclear and host galaxy luminosities; position angle of the host (in degrees, anti-clockwise from vertical in the images); the axial ratio of the host.

IAU name	Morphology (best fit)	χ^2_{red}	$\Delta\chi^2$	$R_{1/2}$ (kpc)	$\mu_{1/2}$	V_{Nuc}	V_{Host}	M_V^{nuc}	M_V^{host}	L_N/L_H	PA (°)	a/b
Radio-Quiet Quasars												
1302+361	E	1.198	0.044	4.5 ± 0.7	23.9 ± 0.4	20.83	22.11	-23.1	-21.9	3.3	172	1.229
1301+358	E	1.125	0.109	3.4 ± 0.5	22.2 ± 0.4	18.94	20.87	-25.1	-23.1	5.9	9	1.141
1303+360	E	1.123	0.010	6.5 ± 1.5	24.9 ± 0.6	20.03	22.44	-24.1	-21.7	9.2	10	1.405
Radio-Loud Quasars												
0440−003	E	1.152	0.053	3.7 ± 0.9	22.9 ± 0.5	19.29	21.37	-24.5	-22.5	6.8	126	1.058
2112+172	E	1.039	0.040	2.4 ± 0.2	20.5 ± 0.2	20.37	20.30	-23.6	-23.6	0.9	176	1.649
2044−027	E	1.160	0.0002	8.2 ± 2.5	24.7 ± 1.1	18.91	22.74	-25.2	-21.4	35.7	167	3.696
0938+185	E	1.091	0.015	3.6 ± 0.8	22.8 ± 0.6	19.46	21.57	-24.6	-22.5	6.9	164	1.311
2207+020	E	1.340	0.193	4.2 ± 0.4	22.7 ± 0.2	19.38	21.06	-24.8	-23.1	4.7	173	1.235

Table 3.4: Results of model fitting with a de Vaucouleurs spheroid model. Columns are as follows: object name; reduced-χ^2 value for the best fit model; number of degrees of freedom in fit; half-light radius, $R_{1/2}$, of best fitting galaxy model in kpc; surface brightness of the host at the half-light radius, $\mu_{1/2}$, in units of V mag.arcsec^{-2}; integrated absolute magnitudes of the nucleus and the host galaxy, converted from the appropriate filter band (F814W/F791W) to Johnson V-band; the ratio of integrated nuclear and host galaxy luminosities; position angle of the host (in degrees, anti-clockwise from vertical in the images); the axial ratio of the host.

IAU name	Morphology (best fit)	χ^2_{red}	$\Delta\chi^2$	$R_{1/2}$ (kpc)	$\mu_{1/2}$	I_{Nuc}	I_{Host}	M_V^{nuc}	M_V^{host}	L_N/L_H	PA (°)	a/b
Radio-Quiet Quasars												
0056−281	E	1.135		3.7±	25.0±	21.31	23.71	-24.2	-21.8	9.1	142	1.33
0048−293	E	1.156		0.8 ± 0.2	20.6 ± 0.9	23.26	23.16	-22.3	-22.4	0.9	24	2.08
0049−295	E	1.332		0.5 ± 0.1	19.6 ± 0.1	22.30	22.47	-23.4	-23.3	1.2	2	1.15
0053−286	E	1.396		1.0 ± 0.2	21.5 ± 0.4	21.58	22.78	-24.3	-23.1	3.0	179	1.09
0050−291	E	1.262		3.6±	25.5±	21.46	23.98	-24.4	-21.9	10.2	94	1.11
Radio-Loud Quasars												
1524−136	E	1.256		2.6 ± 0.1	22.8 ± 0.1	20.42	22.26	-25.0	-23.2	5.5	2	1.31
2351+456	E	1.799		2.9 ± 1.0	23.8 ± 0.8	21.81	22.71	-24.1	-23.2	2.3	137	1.11
2156+297	E	0.986		3.8 ± 1.0	23.2 ± 0.7	20.95	21.77	-24.6	-23.8	2.1	84	1.20
2204−205	E	1.198		2.8±	22.7±	22.53	22.24	-23.3	-23.6	0.8	21	1.72

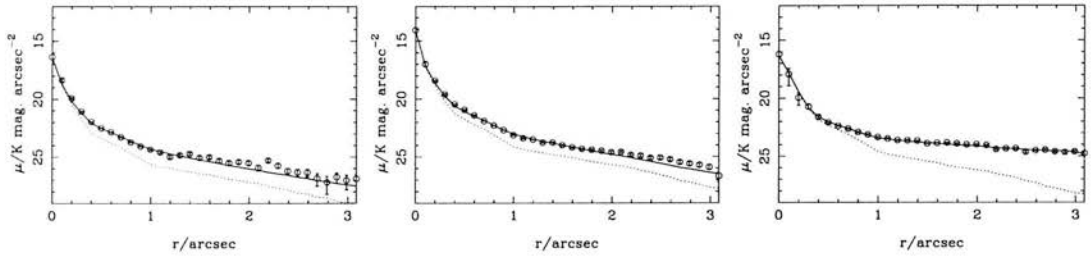

(a) 1302+361 (RQQ); $R_{1/2} = 4.5$kpc

(b) 1301+358 (RQQ); $R_{1/2} = 3.4$kpc

(c) 0049−277 (RQQ); $R_{1/2} =$

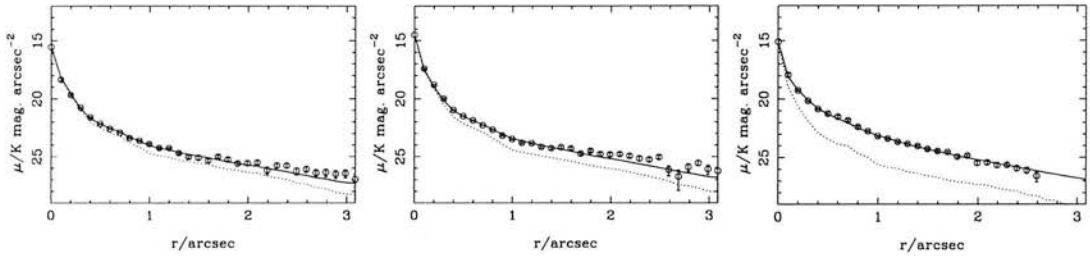

(d) 1303+360 (RQQ); $R_{1/2} = 6.5$kpc

(e) 0440−003 (RLQ); $R_{1/2} = 3.7$kpc

(f) 2112+172 (RLQ); $R_{1/2} = 2.4$kpc

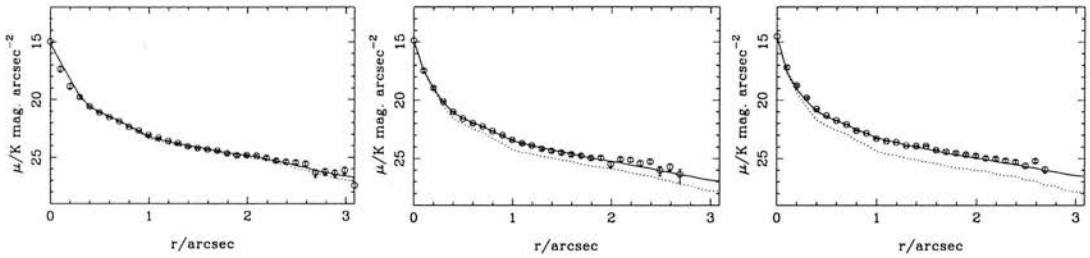

(g) 2044−027 (RLQ); $R_{1/2} = 8.2$kpc

(h) 0938+185 (RLQ); $R_{1/2} = 3.6$kpc

(i) 2207+020 (RLQ); $R_{1/2} = 4.2$kpc

Figure 3.4: **Radial profiles of the $z \approx 1$ sample.**

flux, which shows up in the model/qso flux ratio.

3.5.1 Fixed scalelength fits

It can be seen from the results tables that in many cases, we find a quite different host galaxy to that found by Kukula et al. (2001). I therefore attempted a series of fits using host galaxies of fixed

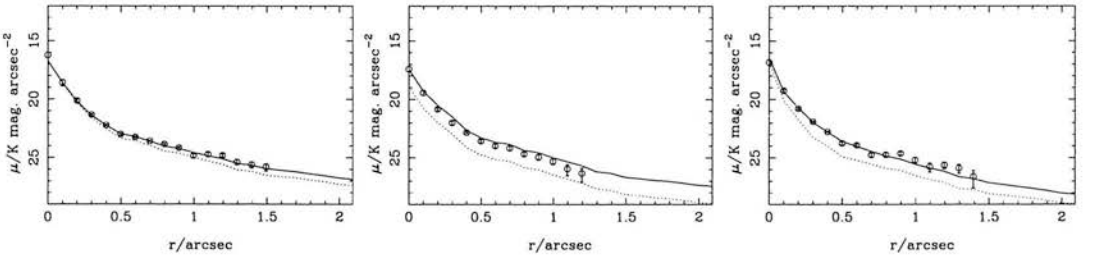

(a) 0056−281 (RQQ); $R_{1/2} = 3.7$kpc

(b) 0048−293 (RQQ); $R_{1/2} = 0.8$kpc

(c) 0049−295 (RQQ); $R_{1/2} = 0.5$kpc

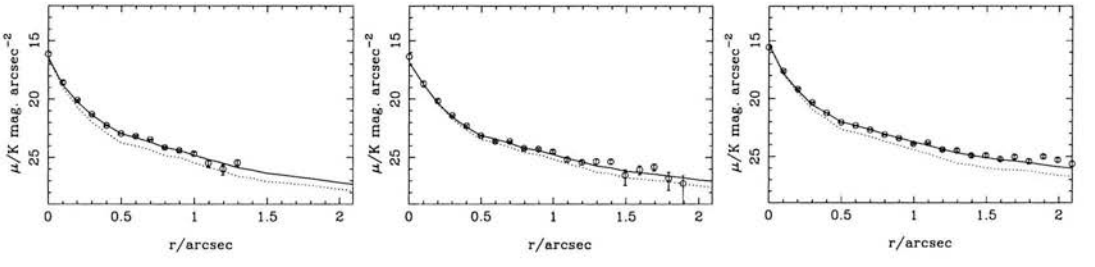

(d) 0053−286 (RQQ); $R_{1/2} = 1.0$kpc

(e) 0050−291 (RQQ); $R_{1/2} = 3.6$kpc

(f) 1524−136 (RLQ); $R_{1/2} = 2.6$kpc

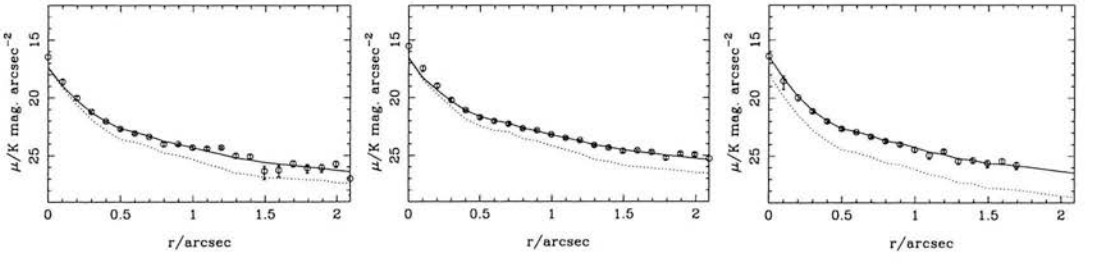

(g) 2351+456 (RLQ); $R_{1/2} = 2.9$kpc

(h) 2156+297 (RLQ); $R_{1/2} = 3.8$kpc

(i) 2204−205 (RLQ); $R_{1/2} = 2.8$kpc

Figure 3.5: **Radial profiles of the $z \approx 2$ sample.**

standard scalelengths (1, 2, 5, and 10kpc), in an effort to determine the effect of the overall best-fit host galaxy luminosity. In cases where we find a very different scalelength to Kukula et al., it is then possible to make a fairer comparison using similar shaped galaxies.

This technique was also employed by Kukula et al. for their high-redshift ($z \approx 2$) data, where they struggled to obtain fits in many cases

It is clear that in the majority of cases, a stable host-nuclear separation has been attained, and the fixed scalelengths make little or no difference to the luminosity of the best-fit host.

3.6 Notes on Individual Objects

3.6.1 $z \approx 1$

The RQQ BVF247 (1302+361) at $z = 0.890$

A number of candidate companions are visible, most noticeably a small, possible interacting object some 2 arcsec to the North.

Found by Kukula et al. to be hosted by a giant ($R_{1/2} = 11.9kpc$) elliptical host. In R-band (rest-frame UV) we again find the host is best fit by a smooth giant elliptical, although at about half the scalelength, $R_{1/2} = 4.5kpc$.

Whilst the host is quite prominent in rest-frame V, it is heavily nuclear dominated in the UV:

$$[L_{nuc}/L_{host}]_V = 0.3$$

$$[L_{nuc}/L_{host}]_U = 3.3$$

In both cases, we obtain very similar ellipticities for the host, at around $a/b = 1.2$. Kukula et al. do

Table 3.5: **Fixed scalelength results** for the $z \approx 1$ sample.

IAU name	χ^2_{red}	$R_{1/2}$	$\mu_{1/2}$	θ	$\frac{a}{b}$	I_{Nuc}	I_{Host}
Radio-Quiet Quasars							
1302+361	1.20	4.05	22.99	172	1.23	19.90	21.29
	1.21	2.0	21.32	171	1.24	19.94	21.04
	1.20	5.0	23.46	173	1.23	19.89	21.19
	1.22	10.0	24.89	174	1.24	19.87	21.12
J-band		11.9				20.14	18.88
1301+358	1.13	3.22	21.24	9	1.14	18.00	19.94
	1.14	2.0	19.95	12	1.13	18.03	19.68
	1.13	5.0	22.35	5	1.15	17.99	20.09
	1.18	10.0	23.93	0	1.20	17.96	20.17
J-band		17.1				17.91	20.11
1303+360	1.12	5.48	23.94	10	1.41	19.10	21.50
	1.13	2.0	21.54	5	1.33	19.11	21.29
	1.12	5.0	23.74	10	1.40	19.10	21.50
	1.13	10.0	25.21	13	1.48	19.09	21.47
J-band		4.6				19.85	19.24
Radio-Loud Quasars							
0440−003	1.15	3.55	21.98	126	1.06	18.36	20.44
	1.16	2.0	20.54	124	1.04	18.39	20.24
	1.15	5.0	22.79	126	1.07	18.35	20.50
	1.17	10.0	24.29	123	1.10	18.32	20.50
J-band		13.0				18.47	18.84
2112+172	1.04	1.89	19.53	176	1.65	19.44	19.37
	1.04	2.0	19.68	176	1.65	19.42	19.40
	1.15	5.0	22.18	176	1.69	19.28	19.91
	1.27	10.0	23.85	177	1.81	19.25	20.07
J-band		17.4				18.97	18.18
2044−027	1.16	4.29	23.72	167	3.70	17.98	21.81
	1.16	2.0	21.85	167	3.80	17.98	21.59
	1.16	5.0	24.08	167	3.80	17.98	21.83
	1.16	10.0	25.61	167	4.27	17.99	21.86
J-band		17.0				17.90	18.29
0938+185	1.09	3.15	21.88	164	1.31	18.53	20.64
	1.09	2.0	20.72	162	1.30	18.55	20.46
	1.09	5.0	22.99	166	1.34	18.51	20.75
	1.11	10.0	24.53	168	1.40	18.48	20.78
J-band		4.3				19.81	19.49
2207+020	1.34	3.77	21.75	173	1.24	18.45	20.13
	1.36	2.0	20.10	173	1.21	18.49	19.85
	1.34	5.0	22.43	173	1.25	18.44	20.19
	1.38	10.0	23.96	174	1.28	18.43	20.22
J-band		10.4				17.61	19.32

Table 3.6: **Fixed scalelength results** for the $z \approx 2$ sample.

IAU name	χ^2_{red}	$R_{1/2}$	$\mu_{1/2}$	I_{Nuc}			
Radio-Quiet Quasars							
0056−281	1.135	3.22	23.6	142	1.33	19.9	22.3
	1.344	2.0	22.3	146	1.21	20.0	22.0
	1.347	5.0	24.7	146	1.32	19.9	22.4
	1.352	10.0	26.3	145	1.44	19.8	22.6
K-band		< 10				18.9	21.6
0048−293	1.156	5.79	24.47	24	2.08	21.86	21.75
	1.162	1.00	24.52	21	1.77	21.61	22.06
	1.186	5.00	25.62	20	4.23	20.98	23.36
	1.189	10.0	27.27	22	16.0	20.90	23.50
K-band		~ 5				19.98	19.74
0049−295	1.332	0.47	18.2	2	1.15	20.9	21.1
	1.617	2.0	22.6	19	1.11	20.3	22.3
	1.635	5.0	25.1	51	1.24	20.2	22.8
	1.643	10.0	26.7	61	1.79	20.1	22.9
K-band		< 10				19.6	19.9
0053−286	1.396	0.94	20.1	179	1.09	20.2	21.4
	1.403	2.0	22.2	15	1.15	20.0	21.9
	1.423	5.0	24.6	7	1.26	19.9	22.3
	1.436	10.0	26.3	3	1.50	19.8	22.4
K-band		< 10				19.6	19.8
0050−291	1.262	3.47	24.1	94	1.11	20.1	22.6
	1.262	2.0	22.7	82	1.13	20.1	22.4
	1.262	5.0	25.0	80	1.12	20.0	22.7
	1.263	10.0	26.5	77	1.10	20.0	22.7
K-band		< 10				19.0	20.7
Radio-Loud Quasars							
1524−136	1.256	2.24	21.4	2	1.31	19.0	20.9
	1.256	2.0	21.1	2	1.30	19.0	20.8
	1.266	5.0	23.5	1	1.46	18.9	21.2
	1.281	10.0	25.1	1	1.70	18.8	21.3
K-band		~ 5				18.1	19.4
2351+456	1.799	2.78	22.36	137	1.11	20.41	21.32
	1.801	2.0	21.49	137	1.11	20.53	21.17
	1.803	5.0	23.84	141	1.15	20.23	21.52
	1.812	10.0	25.43	142	1.21	20.07	21.61
K-band		17.9				17.48	17.86
2156+297	0.986	3.44	21.83	84	1.20	19.56	20.38
	0.995	2.0	20.34	84	1.19	19.77	20.06
	0.988	5.0	22.82	84	1.22	19.44	20.55
	0.999	10.0	24.48	84	1.28	19.28	20.70
K-band		16.0				17.97	17.87
2204−205	1.198	2.12	21.29	21	1.72	21.14	20.84
	1.198	2.0	21.12	21	1.70	21.20	20.81
	1.208	5.0	23.51	21	2.11	20.49	21.21
	1.223	10.0	25.07	20	2.59	20.24	21.27
K-band		~ 5				18.57	20.66

not publish position angles, so we can't determine whether we are measuring the same alignment.

The RQQ BVF225 (1301+358) at $z = 0.910$

A prominent nucleus, with a single interacting companion are the most noticeable features of this object. The field contains a number of other small, possible associated galaxies, at radii greater than 5 arcsec. This quasar has been detected in the X-ray by the Einstein satellite (Wilkes et al. 1994), but I was unable to find any reliable photometric measurements.

Kukula et al. found the largest host in their sample ($R_{1/2} = 17.1$ kpc) but heavily drowned out by the powerful $J = 17.91$ nucleus

$$[L_{nuc}/L_{host}]_V = 7.6$$

In rest-frame U, rather surprisingly, we find a slightly less nuclear-dominated object:

$$[L_{nuc}/L_{host}]_U = 5.9$$

The host in U is significantly smaller, at $R_{1/2} = 3.4$kpc. Our axial ratio of 1.14 is noticeably different to that of Kukula et al. ($a/b = 3.2$).

The RQQ SGP5:46 (0049-277) at $z = 0.955$

A UV-excess quasar (Boyle et al. 1990), this object has just 2 photometric points in NED; U and B. It was studied as part of the Hook et al. (1994) 16-year quasar variability survey. It has a mean B-band magnitude of $\bar{B}_J = 19.52$, and a variability $\sigma v = 0.15$.

This quasar is in a crowded region, being very close on the sky to SGP 5:49, at $z = 0.059$, as well as the bright (11th magnitude) star CD-28 268, which contaminates our image with a very prominent diffraction spike in the southern half. This spike made it impossible to obtain any morphological in-

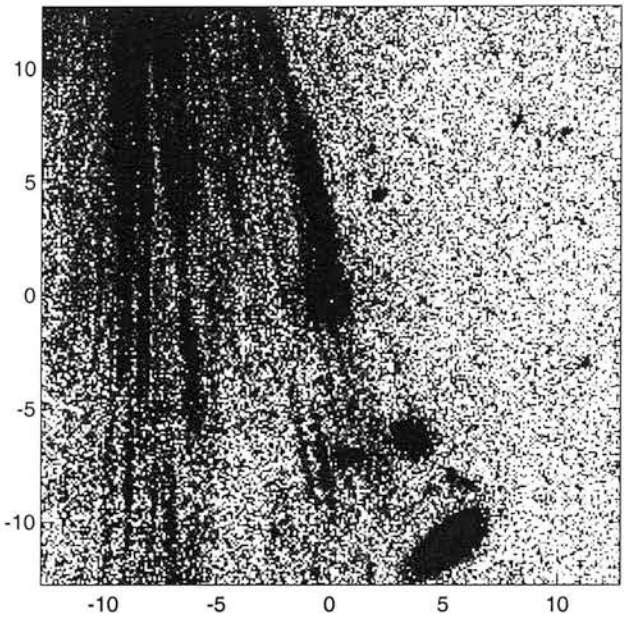

Figure 3.6: **The RQQ SGP5:46** featuring a prominent stellar diffraction spike which prevented modelling of this object.

formation for this image. I attempted fixed-radius fits, and obtained a fixed host luminosity. However, due to the contaminating flux from the spike we cannot place any real confidence in such a model.

A large whirlpool spiral is visible in the foreground, and approximately 12 arcsec due north. In addition, there are a number of smaller potential companions some 8 arcsec north.

Kukula et al found a slightly nuclear-dominated 3.9kpc Elliptical in V-band, with $L_{nuc}/L_{host} = 1.79$, and an axial ratio of 1.14.

The RQQ BVF262 (1303+360) at $z = 0.970$

Detected in the X-ray by the Einstein satellite (Wilkes et al. 1994), but no reliable photometry is available. We find similar sized and shaped elliptical hosts at both U and V bands, with ellipticities around 1.4, and scale lengths of 4.6kpc in V and 6.5kpc in U. Nuclear domination is more extreme in

U, as expected.

$$[L_{nuc}/L_{host}]_V = 1.76$$

$$[L_{nuc}/L_{host}]_U = 9.19$$

The RLQ PKS0440-00 (0440-003) at $z = 0.844$

A high-powered radio quasar (p_{max}=12.5% Stickel et al. 1994), exhibiting a Gigahertz-peaked spectrum, with a turnover at ν_T=0.3GHz (Stanghellini et al. 1998). See figure 3.8).

We note a number of very compact candidate companions in the field, but there are no obvious mergers or interactions. We find quite different hosts at U and V Kukula et al. found a giant 13kpc host, whereas we find a more modest scalelength of 3.7kpc. The object is more nuclear-dominated at U, as expected:

$$[L_{nuc}/L_{host}]_V = 1.41$$

$$[L_{nuc}/L_{host}]_U = 6.8$$

The RLQ MC2112+172 (2112+172) at $z = 0.878$

A steep spectrum radio source like all the RLQ's in this sample (see figure 3.8).

A curiously elongated object in our WFPC2 image, suggesting the possibility of an ongoing minor merger with a smaller object to the East. The usual congregation of small candidate companions are observed.

Curiously, Kukula et al. find a giant 17.4kpc host, whereas we only uncover a small 2.4kpc galaxy. In each case the galaxy dominates the nucleus, although the nuclear contribution is stronger in U.

$$[L_{nuc}/L_{host}]_V = 0.48$$

$$[L_{nuc}/L_{host}]_U = 0.9$$

The RLQ 3C422 (=PKS2044-027, 4C-02.80) at $z = 0.942$

A typical compact steep-spectrum object, with a spectral peak of about 10 Jy at about 200 MHz (Dallacasa et al. 1998). The radio emission is resolved with the VLA (Price et al. 1993) at 6 cm, but it is still dominated by a compact component with 0.5 Jy. With VLBI in S-band, Dallacasa et al. (1998) show well resolved emission with a lobe-like morphology, which accounts for about $\approx$25% of the total flux density. In the X band the source is barely detected, and the weak component (probably the hot-spot of the lobe) contains only about $\approx$ 5% of the flux density of the source at this frequency.

The optical counterpart to this 3C radio source was first identified by Veron (1971), and confirmed by Brandie and Bridle (1974) (who identified the same object as part of the Michigan 8GHz equatorial survey). Both studies classified this object as a distant galaxy due to its reddish colour, and slightly diffuse appearance on the Palomar Sky Survey plates. Smith and Spinrad (1980) present a deep red photograph of the object taken with the KPNO 4m telescope, clearly showing a stellar appearance and thus suggesting a QSO. They followed up with spectroscopy on the 3m Shane telescope at the Lick observatory to produce the spectrum reproduced on the left hand side of figure 3.7. Notable are the broad bump near λ5400, identified by Smith and Spinrad (1980) as the MgII doublet, and a second strong line identified as [OII]λ3727 at $z = 0.942$. Other tentative identifications are marked on the figure. Aldcroft et al. (1994) present higher-resolution Palomar 200-inch spectroscopy, reproduced on the right of figure 3.7, in which we can see that the MgII emission feature has a number of associated absorption features at a redshift very close to that of the quasar. The nucleus is found to be moderately variable in the near-infrared by Stickel et al. (1996). They also find further evidence for strong reddening in the change of spectral index from $\alpha \sim -1.3$ (0.65-2.2μm) to $\alpha \sim -2.5$ in the optical.

There is one obvious, comparably large companion 6 arcsec to the south, as well as a number

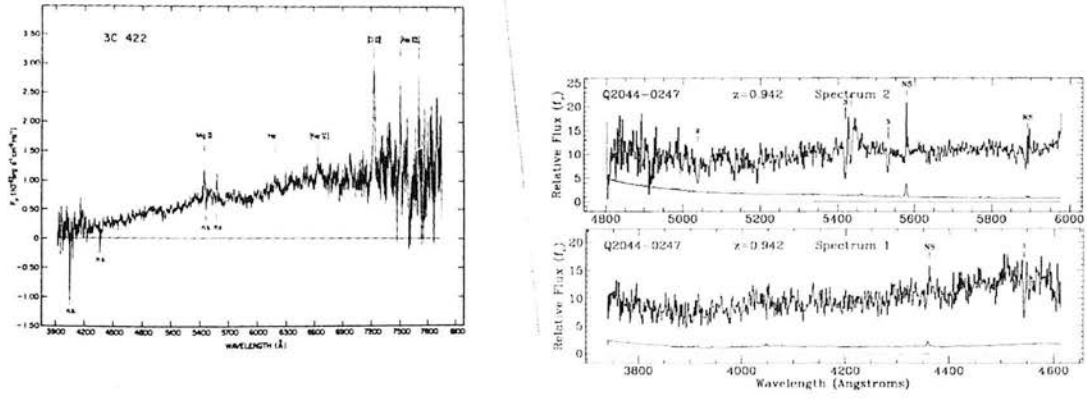

Figure 3.7: **Spectra of 3C422.** There are narrow lines, and weak broad ones at $z = 0.943$. **Left:** From Smith & Spinrad (1980) showing the MgII doublet at 5400Å.
Right: From Aldcroft et al. (1994). Here we can see the MgII feature in more detail, including a complicated absorption feature in MgI, MgII and FeII, at a redshift close to that of the quasar itself.

of smaller objects dotted around the field, an concentrated in particular in the southern corner. The diffraction spikes seem relatively weak, yet this is the only $z = 1$ object for which we get no clear-cut morphological preference.

Kukula et al. find a giant 17kpc host, against our more moderate scalelength of 8.2kpc. The quasar appears to be heavily nuclear-dominated at U.

$$[L_{nuc}/L_{host}]_V = 1.43$$

$$[L_{nuc}/L_{host}]_U = 34.7$$

Given the lack of morphological preference, the large errors on the scalelength, and the unusually large ellipticity of 3.8, we should probably not trust the morphological fit to this host. However, we obtain very stable host and nuclear luminosities with all the fixed scale-length models, and appear to have disentangled host and nucleus reasonably well, judging by the $\mu - R\,\chi^2$ contours.

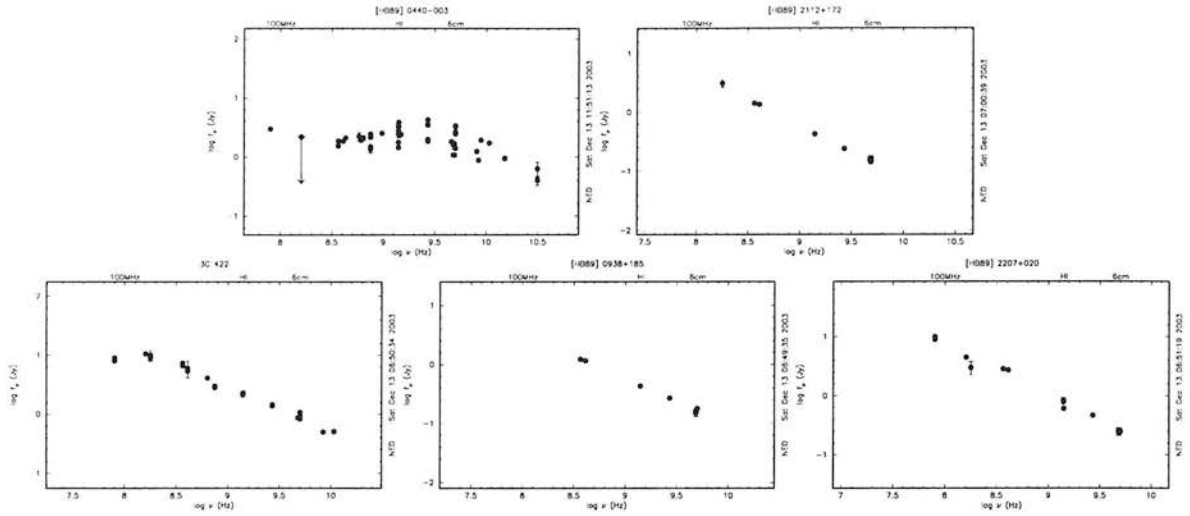

Figure 3.8: **The radio SED's of the 5 RLQ's at $z \approx 1$.** From left to right we have PKS0440-00, MC2112+172, 3C422, PKS0938+18, and 4C02.54. All clearly exhibit steep spectra, but only PKS0440-00 has an observed turnover.

PKS0938+18 (0938+185) at $z = 0.943$

One of the first radio sources to have an optical counterpart identified (Cohen and Kundu 1966), using the Arecibo 1000 foot dish to monitor the object's occultation by the moon. It is clearly a Steep-spectrum object(figure 3.8), although there have been insufficient measurements made to determine its turnover.

Very similar hosts are found at U and V bands: In V Kukula et al. find $R_{1/2} = 4.3$kpc, $a/b = 1.33$. In U we have $R_{1/2} = 3.6$kpc and $a/b = 1.31$ We see the expected increase in nuclear domination from

$$[L_{nuc}/L_{host}]_V = 2.29$$

in V to triple that in U:

$$[L_{nuc}/L_{host}]_U = 6.9$$

There is a loose collection of small candidate companions out to a radius of around 20 arcsec. In

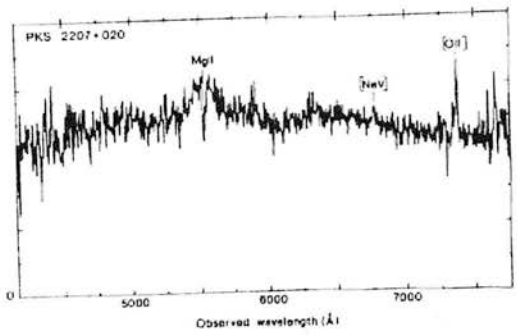

Figure 3.9: **Optical spectrum of 4C02.54 (2207+020)** taken from Veron-Cetty and Veron (1993b). Note the extreme width of the MgII line. Its strength shows that this object truly is a quasar and not a BL Lac object, as it had been previously identified. A strong, narrow Mg II absorption line is also seen at the same redshift.

addition, there is some very low-surface brightness "fuzz", 3 arcsec NW of the nucleus, which is left over in the modelling residuals and may indicate an ongoing minor merger.

The RLQ 4C02.54 (PKS2207+020) at $z = 0.976$

Previously identified as a BL Lac object by Burbidge and Hewitt (1987) due to its compact ($<$ 0.05arcsec) radio core. However, three pieces of evidence have overturned this belief: Firstly, high-resolution VLBI radio imaging failed to detect structure on small scales which would be expected in a BL Lac object (Booth et al. 1979). Secondly, Altschuler (1982) detected no variability at 2380MHz. And finally the radio spectrum was found to be steep, with a spectral index $\alpha \sim 1$ between 178MHz and 5000MHz (Veron-Cetty and Veron 1993b) - see figure 3.8.

Veron-Cetty and Veron (1993b) present a spectrum, reproduced in figure 3.9 showing several emission lines: Mg II λ2800, [Ne V] λ3426, [O II] λ3727 at $z = 0.976$.

In our image there is clear evidence for a merging companion 3 arcsec to the northwest, in addition to a number of other potential candidates in close proximity to the quasar. If the large object 5 arcsec to the southeast is found to be at the same redshift as the quasar, then it too is a large elliptical galaxy.

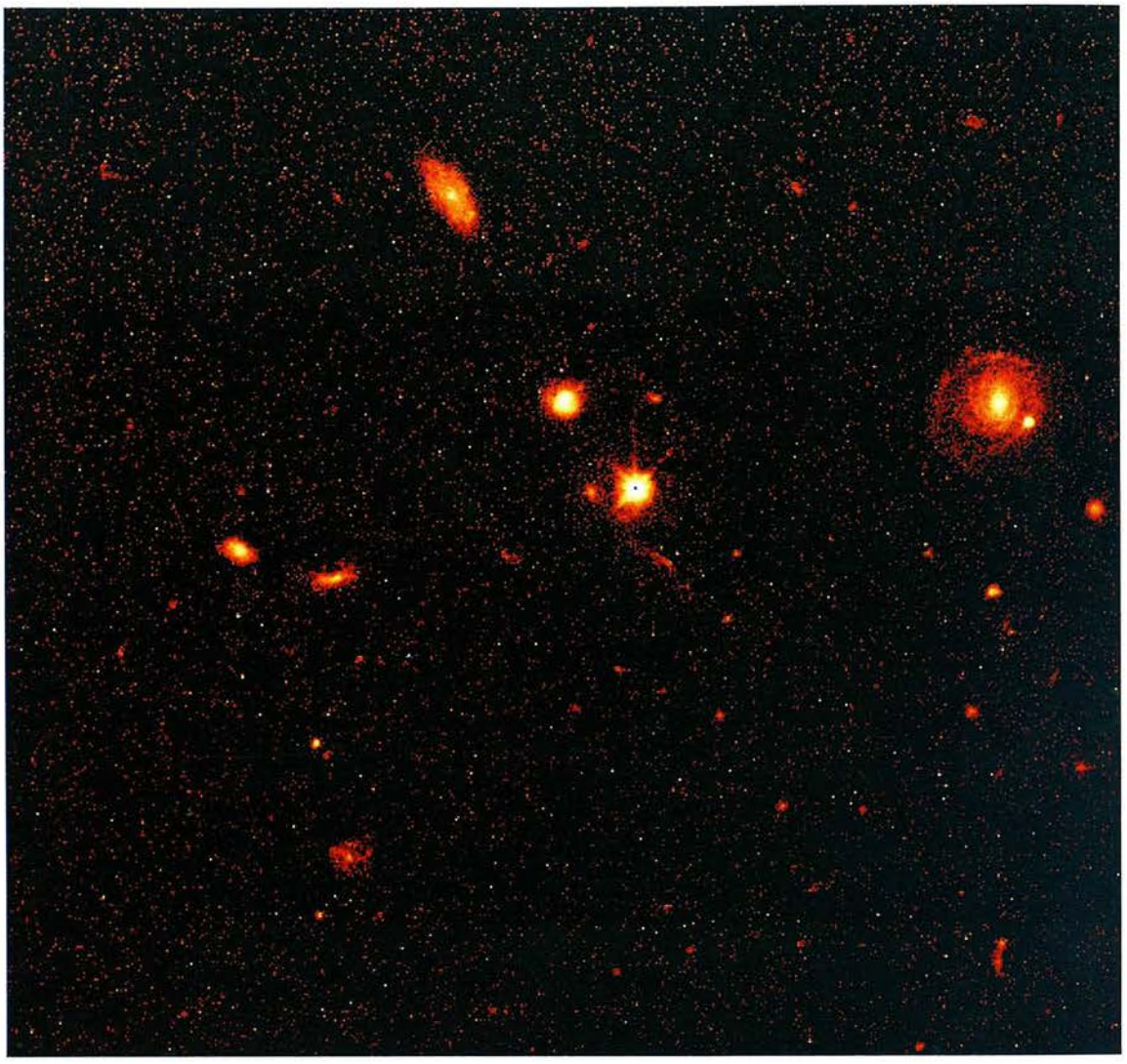

Figure 3.10: **The full WF3 image of 4C02.54** ($z = 0.976$)

There is an impressive grand design spiral some 15 arcsec to the southeast, and cut off in the 256×256 pixel "postage stamp" presented in the appendix. In the full image (figure 3.10) there is a second such object at a similar distance to the north/northwest, as well as a smattering of smaller objects across the field.

Kukula et al. find a large, nuclear-dominated, 10.4kpc V-band host, although their claimed axial ratio of 4.08 is rather curious! We find a more moderate 4.2kpc, round ($a/b = 1.2$) host galaxy, with

roughly the same level of nuclear dominance.

$$[L_{nuc}/L_{host}]_V = 4.8$$

$$[L_{nuc}/L_{host}]_U = 4.7$$

3.6.2 $z \approx 2$

The RQQ SGP4:39 (0056-281) at $z = 1.716$

A UV excess quasar (Boyle et al. 1990), with little photometry or information available. It was included in Hook et al.'s (1994) variability survey of South Galactic Pole objects, and found to have a mean B-band magnitude of $\bar{B}_J = 20.19$, with a variability index of $\sigma_V = 0.26$.

The field of our image is dominated by a single object some 10arcsec SW of the quasar. This object looks stellar, so I decided to attempt a fit to it too. The code found 2 possible solutions: Pure PSF, or PSF plus an extremely compact host galaxy, confirming the stellar nature of this source. Notice also the trail of smaller objects apparently joining the 2 bright ones.

Kukula et al. were unable to fit a fixed radius host galaxy, but found it to be a heavily nuclear-dominated quasar in V,

$$[L_{nuc}/L_{host}]_V = 12.43$$

with a host presumed to be smaller than 10kpc.

In U we detect a less nuclear-dominated $\sim$ 4kpc host:

$$[L_{nuc}/L_{host}]_U = 9.1$$

The RQQ SGP2:36 (0048-293) at $z = 1.756$

A UVX (Boyle et al. 1990) quasar. Mean B-band magnitude $\bar{B}_J = 20.65$, and a variability index $\sigma_V = 0.19$ (Hook et al. 1994).

Kukula et al. found a $\sim$ 5kpc host, with a relatively weak nucleus in V:

$$[L_{nuc}/L_{host}]_V = 0.80$$

In U we were unable to fit a model of fixed radius, obtaining our best fit with a fixed scalelength of 1kpc. Again we find a relatively weak nucleus, with

$$[L_{nuc}/L_{host}]_U = 0.91$$

A large number of small objects are visible in the field.

The RQQ SGP2:25 0049-295 at $z = 1.868$

This UVX quasar (Boyle et al. 1990) is quite close on the sky to the quasar SGP2:27 at $z = 1.93$. Its variability studied in Hook et al 1994: $\bar{B}_J = 20.81$, $\sigma_V = 0.33$.

Kukula et al. found a host with a scalelength $<$ 10kpc and a moderate nuclear component.

$$[L_{nuc}/L_{host}]_V = 1.31$$

We also were unable to determine the scalelength of the host, and getting our best fit with a fixed 1kpc host galaxy. We again find a moderate nuclear component;

$$[L_{nuc}/L_{host}]_U = 1.16$$

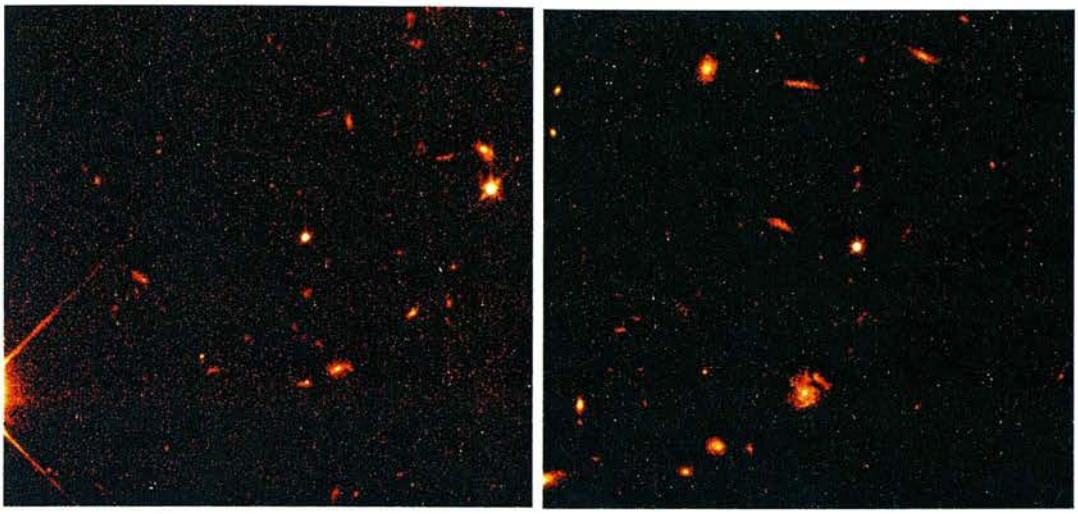

Figure 3.11: **The full WF3 images** of SGP3:39 ($z = 1.868$) and SGP2:25 ($z = 1.868$).

A large number of faint objects are observed in the field, but they do not appear to be associated with SGP2:25.

The RQQ SGP3:39 (0053-286) at $z = 1.964$

Very nearby another quasar, SGP3:35 at $z = 1.498$. UVX (Boyle et al. 1990), slightly variable (Hook et al 1990): $\bar{B}_J = 20.53$, $\sigma_V = 0.21$. The quasar appears to be at the centre of a loose cluster of faint objects (see figure 3.11).

The quasar has a fairly weak nuclear component in V, but moderate in U:

$$[L_{nuc}/L_{host}]_V = 1.16$$

$$[L_{nuc}/L_{host}]_U = 3.01$$

Neither I nor Kukula et al. could accurately obtain the host scalelength of this object.

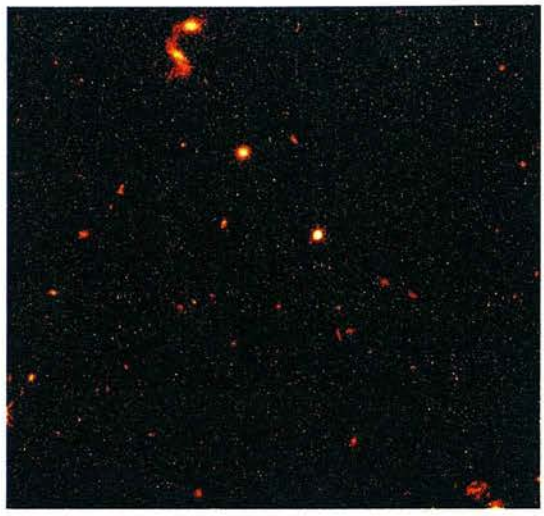

Figure 3.12: **The full WF3 image of SGP2:11**

The RQQ SGP2:11 (0050-291) at $z = 1.976$

A UVX quasar (Boyle et al. 1990). Variability studied in Hook et al 1990: $\bar{B}_J = 20.74$, $\sigma_V = 0.15$. An impressive pair of interacting galaxies are seen to the far south of the full WF3 image (figure 3.12).

Kukula et al. limit the host as being smaller than 10kpc in size. We obtain a fit with a 3.6kpc fit in U. The quasar is heavily nuclear-dominated at U, only moderately at V.

$$[L_{nuc}/L_{host}]_V = 4.70$$

$$[L_{nuc}/L_{host}]_U = 10.2$$

PKS1524-13 (1524-136) at $z = 1.687$

This quasar is the fastest varying source at 408 MHz found by Fanti et al. (1983). A high resolution VLBI radio image is published in Fomalont et al. (2000), showing elongated structure in the northeast-southwest direction.

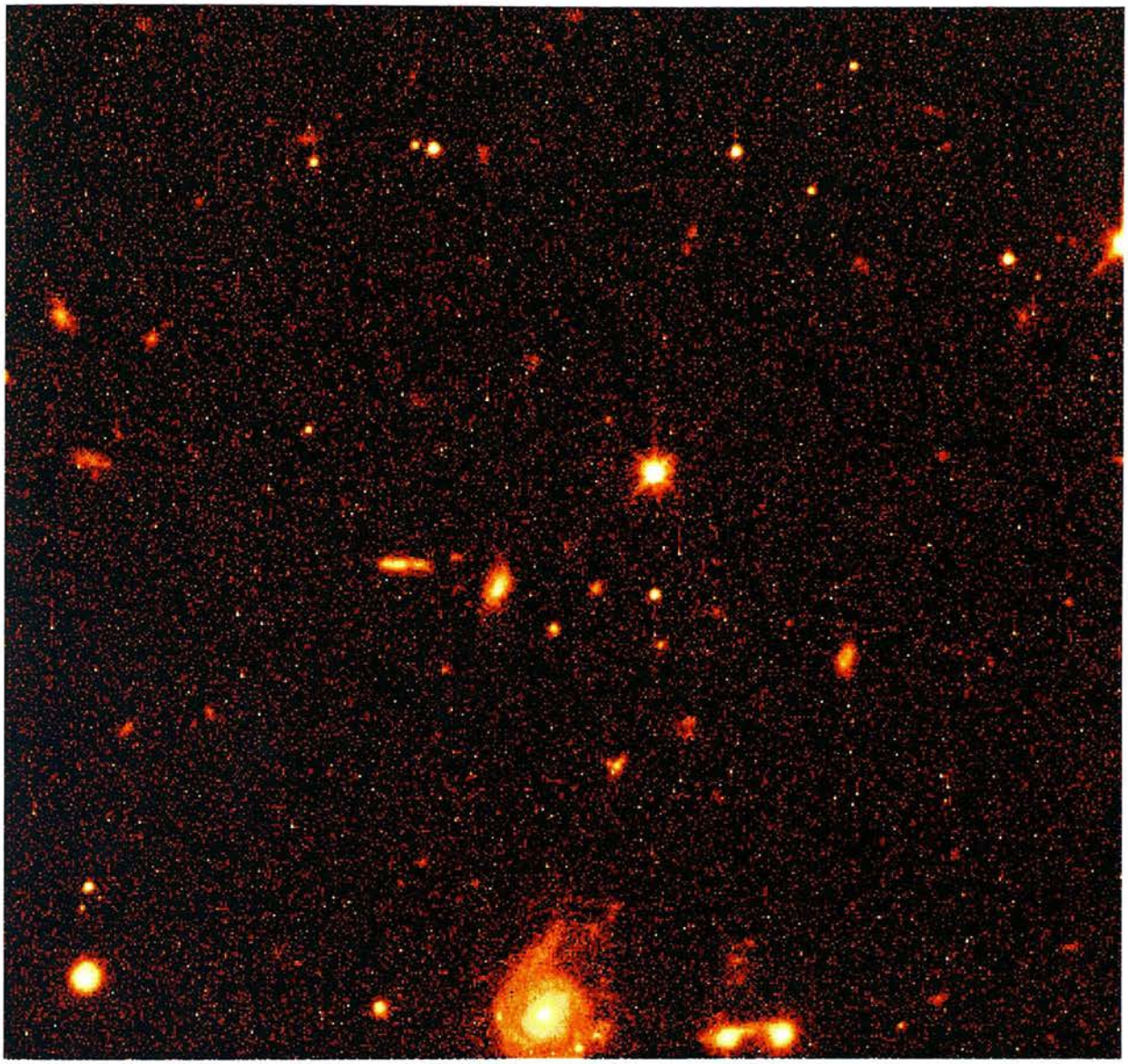

Figure 3.13: **The full WF3 image of PKS1524-13** ($z = 1.687$)**.**

We see a large number of foreground / companion objects in the field, particularly to the south (see figure 3.13).

A scalelength of around 5kpc in V and 2.6kpc in U.

$$[L_{nuc}/L_{host}]_V = 3.22$$

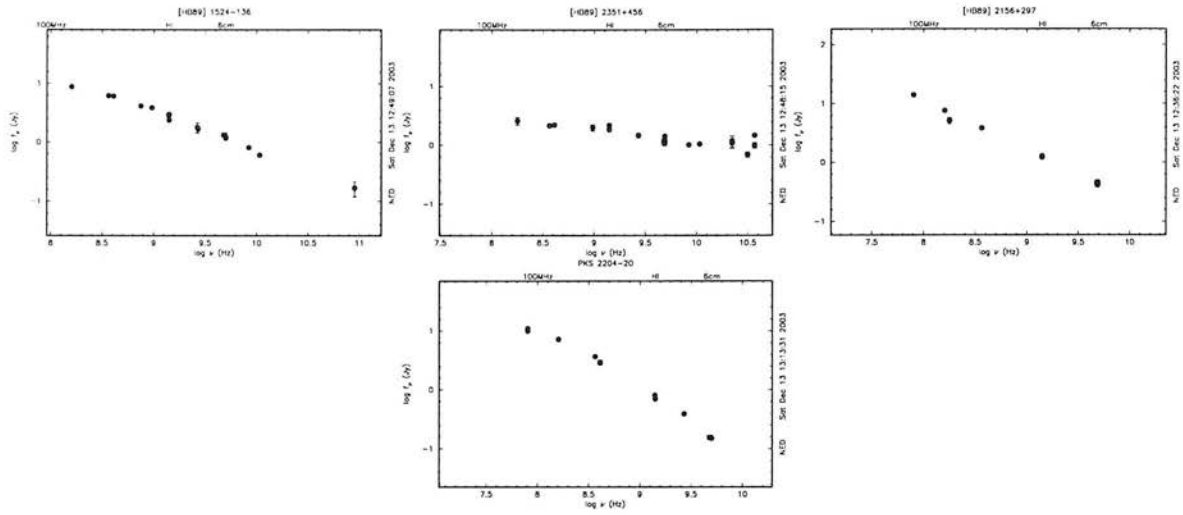

Figure 3.14: **The radio SED's of the 4 RLQ's at $z \approx 1$.** From left to right we have MC2112+172, 3C422, PKS0938+18, and 4C02.54. All clearly exhibit steep spectra.

$$[L_{nuc}/L_{host}]_U = 5.48$$

The RLQ 4C45.51 2351+456 at $z = 1.992$

Originally given the wrong optical ID by Peterson et al. (1978). Their suggestion turned out to be a galactic star showing absorption lines at rest wavelengths rather than an object with a continuous optical spectrum. This quasar exhibits a rather complex optical spectrum (figure 3.15) due to an associated absorption line system at $z = 1.991$ (Stickel and Kuhr 1993).

Kukula et al. fitted a giant 17.9kpc host galaxy. We find a small 3kpc host in U.

$$[L_{nuc}/L_{host}]_V = 1.42$$

$$[L_{nuc}/L_{host}]_U = 2.30$$

We see diffraction spikes from a nearby star at the top (southeast) of the image. There are 4 noticeable foreground / companion objects within 10arcsec.

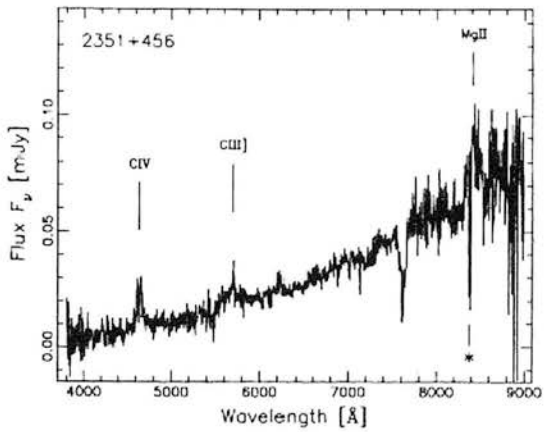

Figure 3.15: **Optical spectrum of 4C45.51 at** $z = 1.992$, with its associated absorption line spectrum at $z = 1.991$ (from Stickel & Kuhr 1993).

The RLQ B2-2156+29 (2156+297) at $z = 1.759$

B2-2156+29 has a number of nearby galaxies (Thomas et al. 1995) visible in the image in the appendix. They do not explicitly associate these galaxies with the quasar, using them instead within a broader statistical study of quasar - galaxy associations.

Kukula et al. find a giant 16kpc host in V against our more moderate 4kpc one in U. The nucleus dominates in U.

$$[L_{nuc}/L_{host}]_V = 0.91$$

$$[L_{nuc}/L_{host}]_U = 2.13$$

The RLQ PKS2204-20 (2204-205) at $z = 1.923$

There are 2 quasars with this basic identifier, this one being the more distant one. The other, at $z = 1.62$ is some way off our field of view. This quasar has a crowded field (figure 3.16), tempting us to believe that we are seeing structure on a grand scale.

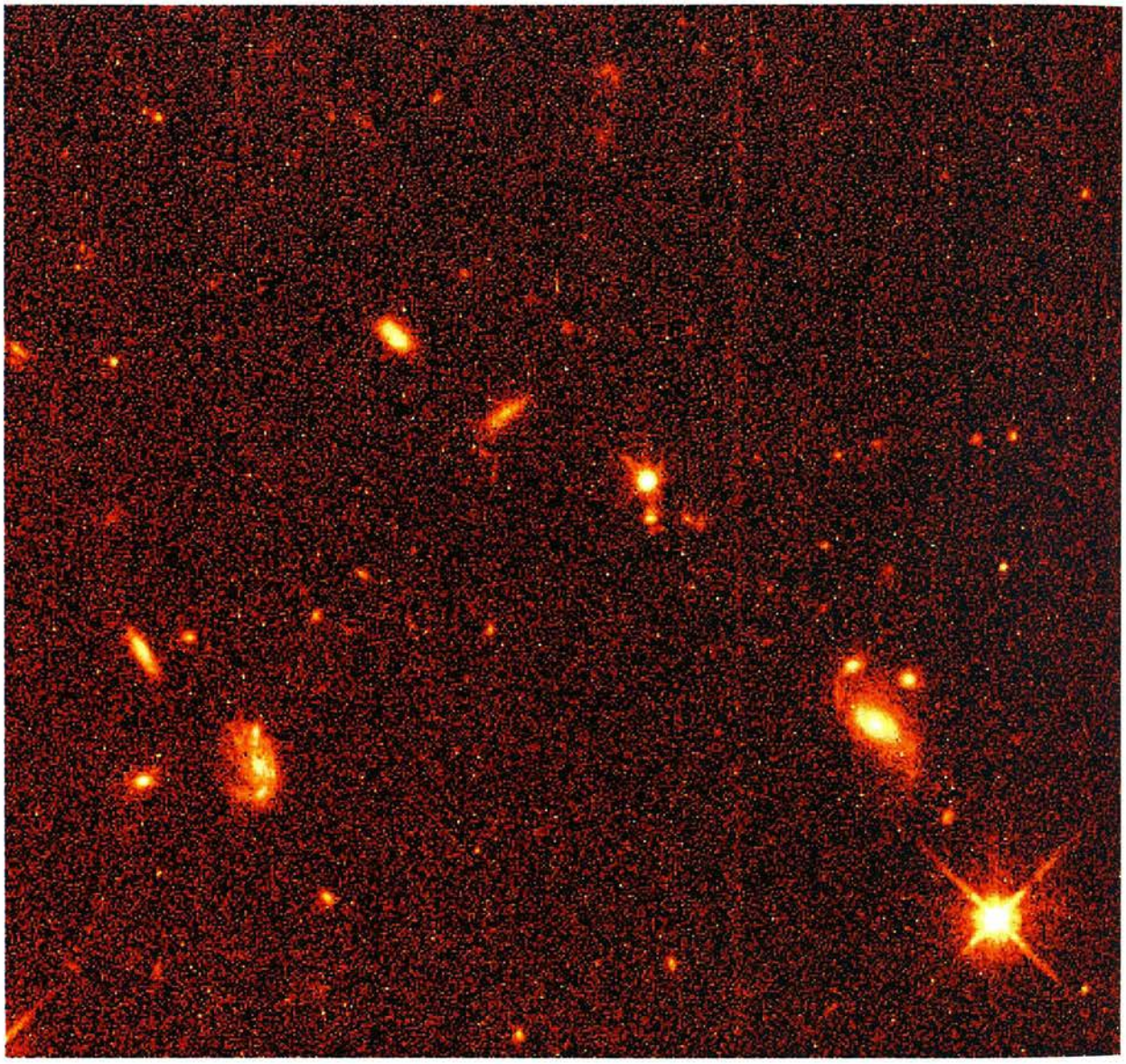

Figure 3.16: **The full WF3 image of PKS2204-20** ($z = 1.923$)

Kukula et al. find a $\sim$ 5kpc host galaxy. I find a small 3kpc host, with a weak nucleus.

$$[L_{nuc}/L_{host}]_V = 3.22$$

$$[L_{nuc}/L_{host}]_U = 0.76$$

3.7 Discussion

The results are broadly found to be in line with those of Kukula et al. (2001), and underline the need for a giant elliptical host galaxy in order to host a quasar (Floyd et al. 2004, Dunlop et al. 2003, McLure et al. 1999). In general we find somewhat smaller hosts in the U band than was found in V by Kukula et al. However, the similarity of many of the axial ratios is a comforting finding.

3.7.1 Host galaxy colours

The host colours are calculated for each individual object in the observer's frame (see tables 3.7 and 3.8).

We find the mean $V-J$ colours at $z \approx 1$ for the radio-loud and radio-quiet subsamples to be (with associated standard errors):

$$\langle V-J \rangle_{RLQ} = 2.6 \pm 0.2$$

$$\langle V-J \rangle_{RQQ} = 2.2 \pm 0.3$$

Whilst at $z \approx 2$, the mean $I-H$ colours are

$$\langle I-H \rangle_{RLQ} = 3.1 \pm 0.2$$

$$\langle I - H \rangle_{RQQ} = 2.9 \pm 0.1$$

We immediately note that the RQQ hosts are significantly bluer than their RLQ counterparts, at both epochs. This result is to be expected based on previous results (e.g. Kukula et al. 2001) which suggest that RLQ's exhibit evolution that is somewhat closer to passive than is the case for RQQ's, based simply upon a mass estimate from single-band photometry. The next step is to compare with different evolutionary predictions.

3.7.2 Simple Stellar Populations

The study of stellar population models has been an active field since the early 1960's when Crampin and Hoyle (1961) realised that integrated colours of stellar populations could be used to date extra-galactic systems. Things have moved on enormously in the intervening three decades, and today huge simulations of stellar populations are run on some of the world's largest supercomputers in order to predict colours of simple stellar populations (SSP's). There are always going to be problems in such a complicated field, and it is still developing today.

There are 2 main techniques: The fuel consumption theorem, and the isochrone technique. The first is highly elegant, recognising simply that the net contribution of a given phase of stellar evolution to the flux of a population is proportional to the amount of fuel burned during that phase. The second uses "isochrones" computed for individual stellar populations. This technique really owes its success to the work of Bruzual A. and Charlot (1993) who synthesised isochrones for specifically solar metallicity, and a wide range of ages. Subsequent releases have introduced a wider metallicity range, and really defined the standard in the literature. The method has come into its own with the huge growth of cheap computer power, and it is now a major field of its own.

Particular early problems existed in accurately accounting for relatively short-lived, yet energeti-

cally important phases, such as how to integrate along the Red Giant Branch of a given population:

> *"...very slight departures from equal spacing in the stellar lifetimes lead to unacceptable regularities in colour because of the short-lived but energetically-important points"*
>
> (Tinsley and Gunn 1976)

Similar problems are faced today in accounting for the Thermally Pulsing Assymptotic Giant (TP-AGB) Branch. Mass loss and nuclear burning in the envelope are very important for such objects, yet the laws that govern these processes are still poorly understood, or highly non-linear. It is important to take heed of the first "S" in SSP, and keep things as "Simple" as possible. In a SSP, the stars are coeval and chemically homogeneous.

3.7.3 Testing evolution in quasar hosts

Since in all other respects, quasar host galaxies appear to be normal giant elliptical galaxies, it seems sensible to test the null hypothesis of passive evolution for such a population. I have adopted the models of Jimenez et al. (2004), which are based on a library of spectra from the new 8-10m class of telescopes. These SSP models are based on the isochrone technique, employing a new algorithm to model post main-sequence evolutionary phases, which in particular includes a proper modelling of the Horizontal Branch. This method results in improved accuracy in modelling of post-Main Sequence evolution (Jorgensen and Thejll 1993, Jimenez et al. 1996, Jorgensen and Jimenez 1997).

Predictions for a simple passively evolving elliptical galaxy formed in an instantaneous starburst at $z = 5$ are illustrated in figure 3.17 (solid lines). Predictions of this model are presented for each individual band (J, H, I and V) for which I present data in table 3.7 and 3.8, as well as the 2 colours, $V - J$, and $I - H$. It is immediately obvious that we can make a far clearer distinction with the 2-

Table 3.7: **Host galaxy $V-J$ colours at $z \approx 1$**

Source	z	V_{Nuc}	V_{Host}	J_{Nuc}	J_{Host}	$V-J$(Nuc)	$V-J$(Host)
				RQQ's			
1302+361	0.890	20.8261	22.1109	20.1387	18.8810	0.69	3.23
1301+358	0.910	18.9362	20.8681	17.9111	20.1140	1.03	0.75
0049−277	0.955	20.0883	21.7258	19.4639	20.0961	0.62	1.63
1303+360	0.970	20.0274	22.4354	19.2399	19.8533	0.79	2.58
				RLQ's			
0440−003	0.844	19.2940	21.3747	18.4713	18.8530	0.82	2.52
2112+172	0.878	20.3739	20.2976	18.9708	18.1767	1.40	2.12
2044−027	0.942	18.9095	22.7411	17.9014	18.2859	1.01	4.46
0938+185	0.943	19.4615	21.5668	18.5865	19.4884	0.88	2.08
2207+020	0.976	19.3836	21.0589	17.6131	19.3210	1.77	1.74

Table 3.8: **$I-H$ colours at $z \approx 2$**

Source	z	I_{Nuc}	I_{Host}	H_{Nuc}	H_{Host}	$I-H$(Nuc)	$I-H$(Host)
				RQQ's			
0056−281	1.716	21.31	23.71	18.86	21.60	2.45	2.11
0048−293	1.756	23.26	23.16	19.98	19.74	3.28	3.42
0049−295	1.868	22.30	22.47	19.60	19.89	2.70	2.58
0053−286	1.964	21.58	22.78	19.55	19.77	2.03	3.01
0050−291	1.976	21.46	23.98	18.97	20.65	2.49	3.33
				RLQ's			
1524−136	1.687	20.42	22.26	18.10	19.36	2.32	2.90
2351+456	1.992	21.81	22.71	17.48	17.86	4.33	4.85
2156+297	1.759	20.95	21.77	17.97	17.87	2.98	3.90
2204−205	1.923	22.53	22.24	18.57	20.66	3.96	1.58

band colours than was possible from the simple 1-band photometric mass estimate of Kukula et al. (2001). For comparison, the dotted line illustrates passive evolution plus an ongoing 1% by mass of star forming activity (i.e. 1% of the galaxy's luminosity is generated by an ongoing starburst). Other lines show the best-fitting models (passive evolution plus constant star-formation rate) to each of the sub-samples in each redshift bin.

Remarkably we find that each subsample is consistent with the same evolutionary model in each redshift bin, although the models plotted are for the absolute best fit in each case:

- • **At $z \approx 1$:**

For the RLQ's we find that the host galaxies are consistent with a passively evolving model which has an additional 0.2% of its mass is involved in ongoing star-formation. By contrast, the RQQ hosts require an extra 0.48% of star-formation over and above the passive model.

- • **At $z \approx 2$:**

  For the RLQ's we require just an additional 0.08% mass provided by ongoing star-formation, relative to the passive model. The RQQ hosts again require more than double this; an extra 0.23% of star-formation over and above the passive model.

This crucial test has shown that both populations are broadly consistent with the null hypothesis of a passively evolving population of Giant Elliptical galaxies. The RLQ hosts are typically slightly closer to this than their RQQ counterparts, suggesting that the RQQ's undergo somewhat more rapid evolution, or are formed somewhat later - perhaps fitting in better with hierarchical models of galaxy formation (Kotilainen and Falomo 2000). However, note that at present, these results are not statistically significant, due to the necessary smallness of the samples. Using a 2-sample Kolmogorv-Smirnov test (Press et al. 1992), we find that the probability of the 2 populations arising from the same underlying distribution is $p = 0.48$, whilst at $z = 2$ it is as high as $p = 0.96$. Thus whilst it appears that there is some difference, we must wait for larger samples in order to confirm this finding.

3.8 Conclusions

I find that quasar host galaxies can be detected and modelled in the (rest-frame) UV at cosmologically significant redshifts. I have successfully fitted de Vaucouleurs profiles to all 20 objects examined at redshifts 1 and 2. At redshift 1 it is possible to distinguish basic morphological data; scale length, central surface brightness and ellipticity of the host. Once we reach redshift 2, we can generally no

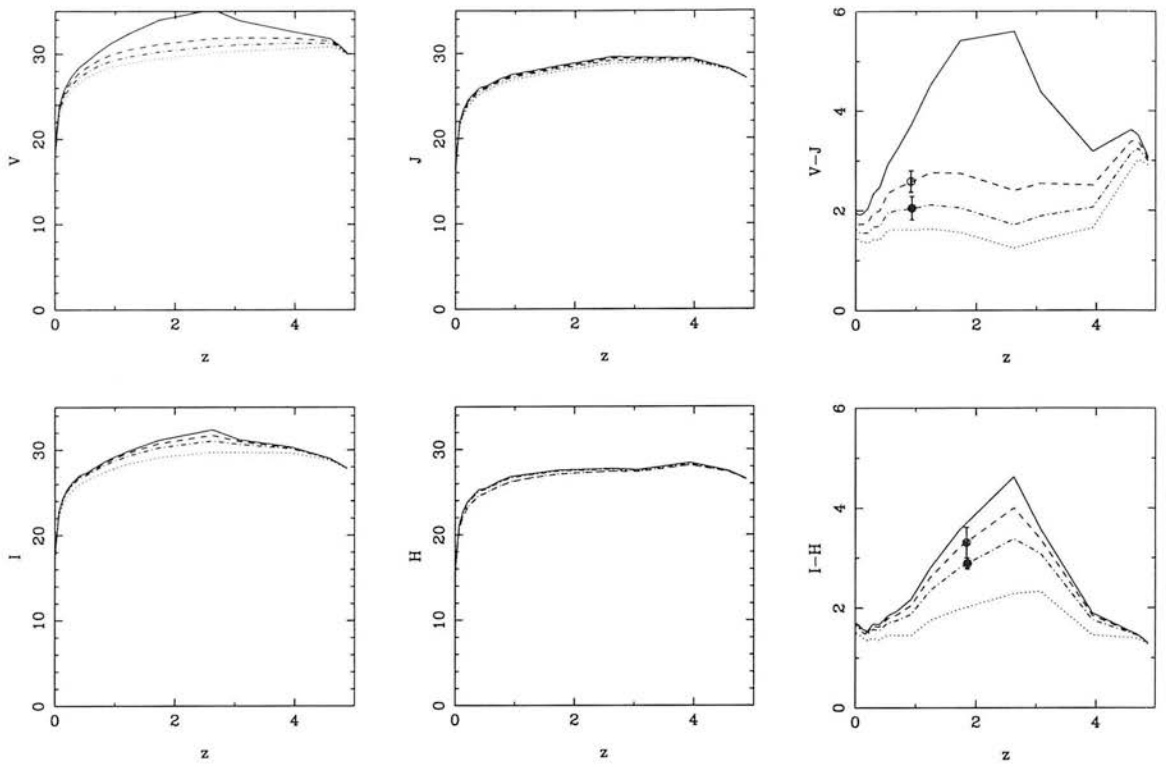

Figure 3.17: **Colour evolution in RLQ and RQQ host galaxies.** Models are shown for: passive evolution (solid line), 1% ongoing star formation (dotted line), and the best-fitting models to the RQQ (filled circles; dot-dashed line) and RLQ (open circles; dashed line) samples, as described in the text. Clearly the host galaxies are evolving at close to the passive rate. We appear to have a more rapid evolution in the RQQ's than in the RLQ's.

longer determine a host galaxy's size to any reasonable degree of accuracy, but can still accurately constrain its overall luminosity.

I find that the host galaxies are broadly consistent with the null hypothesis of a population of passively evolving giant (L^*) elliptical galaxies, in terms of the evolution of their colours from $z \approx 2$ to $z \approx 1$. However, there is found to be a small deviation from this model. This deviation can be attributed to a small ($< 1\%$ by mass) ongoing starburst. Perhaps the most interesting finding is that this additional component is slightly larger in the RQQ's than in the RLQ's, although this difference remains statistically insignificant, due to the small sample size. This finding supports, but does not prove the hypothesis that the RQQ's are evolving more rapidly than the RLQ's, and have possibly

formed more recently, more in keeping with the traditional hierarchical view of galaxy evolution. The RLQ's as a class however clearly do not fit into such a picture, and must have finished forming far earlier.

CHAPTER 4

ULIRG's: an evolutionary link with Quasars?

4.1 Introduction

In this chapter I present the scientific background and preliminary results from a UKIRT K-band imaging study to investigate the connection between ULIRG's and Quasars. Only half of the full sample has so far been observed, so the results and discussion remain tentative.

Ultra-luminous infrared galaxies (ULIRG's) have been intensively studied in recent years through a combination of ground-based and optical HST imaging (e.g. Lawrence et al. 1989, Scoville et al. 2000, Farrah et al. 2001, 2002, Genzel et al. 2001, Bushouse et al. 2002). As a result it is now generally accepted that a combination of both starbursts and AGN are powering the infrared emission in many ULIRG's, and that a large fraction (70 to 100%) of ULIRG's are interacting or merging systems.

However, because of the large uncertainties involved in estimating the lifetimes of starbursts, AGN and merger remnants, a consensus has yet to be reached on the crucial question of whether ULIRG's are an essential step in QSO formation, or simply one way in which to trigger an existing supermassive black-hole into activity.

Based on our results concerning the host galaxies and central black-hole masses of quasars we decided to combine K-band UFTI imaging with existing HST data to directly test whether a link between ULIRG's and QSO's (as proposed by Sanders et al. 1988), is viable. The evidence from our earlier studies (this thesis, Floyd et al. 2004, Dunlop et al. 2003, McLure, Dunlop & Kukula 2000, McLure et al. 1999) is that all optically powerful quasars are located in old (~ 9 Gyr), luminous ($L > L^{\star}$) elliptical host galaxies, regardless of radio power. Furthermore, using the width of broad emission lines to estimate the central black-hole masses, McLure and Dunlop (2002) have demonstrated that quasar hosts display the same correlation between bulge mass and black-hole mass as seen in inactive ellipticals (e.g. Merritt and Ferrarese 2001).

We shall assume as a null hypothesis that all ULIRG's are on the evolutionary path toward becoming fully-fledged optical quasars. They are therefore powered by quasar-like activity (accretion on to black holes of mass $\approx 10^9 M_{\odot}$), buried within a very dusty host that we would expect to contain a very large mass ($\sim 10^{12} M_{\odot}$) of evolved stellar population. ULIRG's are, in general, extremely messy disturbed systems, at least in the optical. One might wonder, therefore, how one could ever hope to fit a simple de Vaucouleurs, Freeman, or Sèrsic profile to these objects. The answer here is K-band imaging, where we obtain a relatively undistorted view of the dynamically relaxed stellar population. We therefore look for host galaxies brighter than $M_K^{\star} = -25.1$ (Mobasher et al. 1993) as evidence of a "quasar capable" host galaxy.

4.1.1 Aims

In this work, I aim first of all to determine whether or not there is sufficient mass in the well-evolved population to conceivably host a quasar-capable SMBH. Secondly I aim to compare the hosts of the ULIRG's with those of a sample of IR-bright (IRAS-detected) QSO's, and with a sample of normal, optically-selected (IRAS-undetected) QSO's. Finally, I use our K-band images in combination with archived HST V-band images to look at the colours of the dominant stellar population, and to examine the 2D distribution of star-forming regions.

4.1.2 Comparison with other studies

This study provides two crucial advantages over existing imaging studies:

- Using the 2D modelling technique described elsewhere in this thesis, any regions of star formation and obscuration can be masked to allow 2D modelling of any underlying old-stellar population without being biased by high surface brightness features.

- Age-dating of the areas of current star formation will provide much needed information about the relative timescales of the starbursts and the interaction features.

Although two major samples of ULIRG's have recently been imaged with NICMOS (Scoville et al. 2000, Bushouse et al. 2002), the 19.2×19.2 arcsec field-of-view of the NIC2 camera means this data is not suitable for detecting the existence of large-scale bulges. At $z = 0.1$ for example, this field-of-view corresponds to a diameter of $\approx$ 45kpc. By $z = 0.2$ NICMOS fits in a diameter of 80kpc, but this is still insufficient to view the whole of a large galaxy, including background. UFTI, with its 92arcsec field-of-view, can easily fit in an entire giant elliptical even at $z = 0.1$, and thus allow complete and accurate modelling right down to the low surface brightness wings. Such work

complements the largely spectral study of Genzel et al. (2001) which examines the position of the ULIRG's on the Fundamental Plane. Note however that their study focuses purely on ULIRG's, with just one QSO, Mrk1014 (also studied here) meaning that the plausibility of a connection between the two populations could not be properly investigated. Together with the high-resolution imaging of HST by Farrah et al. (2001), we have a powerful combination in constraining the role of AGN and starbursts within the ULIRG population.

4.2 Sample Selection

The sample for this study was chosen in order to test the viability of ULIRG-QSO evolution as cleanly as possible, and consists of 16 objects in total,[1] 7 ULIRG's, 7 IRQSO's and 2 hybrid objects (that have been previously classified as both ULIRG's and as QSO's). We selected only objects for which there are existing HST WFPC2 images in the optical, allowing us to obtain population colours, and to permit a two-dimensional study of the on-going star formation. The ULIRG's are all drawn ultimately from the QDOT IRAS galaxy survey Lawrence et al. (1989), but were studied more recently in V and I by Farrah et al. (2001).

The ULIRG and IRQSO sub-samples are matched in terms of their 60μm luminosity and redshift range, whilst it is inevitable that the IRQSO's will be more optically luminous than the ULIRG's (figure 4.1, left and centre). In addition, we already have a suitable comparison sample of 23 optically selected QSO's (undetected by IRAS at 60 μm), in the same redshift range, and with complete WFPC2+UKIRT imaging data from the recent $z \approx 0.2$ quasar host-galaxy study of Dunlop et al. (2003) and McLure et al. (1999). The IRQSO sample was selected in such a way that it optically matches this "normal" QSO sample (figure 4.1, right), allowing for a meaningful comparison to be

[1] Only 9 of which have been successfully observed so far

made.

This method of sample selection will allow us to test the Sanders et al. (1988) model, in which IR-bright QSO's represent an intermediate stage in the evolution of ULIRG's to QSO's, where the active nucleus is still partially shrouded by dust from the initial merger/starburst event.

4.2.1 Classification and morphology

The ULIRG's studied here were classified by Farrah et al. (2001) using three descriptors of their morphology, and presence of companions. These descriptors are included in table 4.1. The first is a 7-band system (a number from 0 to 6) as a quantitative morphological description of the source and its environment used by Lawrence et al. (1989). Broadly, the larger the number, the greater the likelihood of a merger. Zero corresponds to no nearby companions nor signs of merger:

- **0:** Source has no companions within 200kpc and shows no signs of interaction nor merger.
- **1:** Source has a faint companion (between 4 and 2 magnitudes fainter than the source) between 40 and 200kpc away.
- **2:** Source has a bright companion (less than 2 magnitudes fainter than the source) between 40 and 200kpc away.
- **3:** Source has a faint companion less than 40Kpc away, yet shows no sign of interaction.
- **4:** Source has a bright companion less than 40kpc away, yet shows no sign of interaction.
- **5:** Source is interacting with companion, sand there are signs of loops, tails or bridges.
- **6:** Source is merging; either there is obvious disturbance and/or there are multiple nuclei in a common envelope.

This system was added to by Farrah et al. (2001), who noted that for some purposes, it is informative to classify ULIRG's into broader categories, based solely on qualitative descriptions of their optical morphology:

- **Class A:** 2 separate, physically distinguishable objects, close enough to reasonably assume that they are interacting.
- **Class B:** Not distinguishable into separate sources. No QSO activity. However there are clear signs of interaction such as tails, bridges or multiple nuclei.
- **Class C:** The source contains an optical QSO with or without signs of ongoing interaction.

In addition, the "Asymmetry" is given, which is based on the 180° statistic, A (Brinchmann et al. 1998), i.e. how symmetric a given object is under a 180° rotation. In the form adopted by Farrah et al. (2001), this statistic is normalised between 0 (perfect 180° symmetry) and 1 (perfect 180° antisymmetry).

4.2.2 IRAS data

The IRAS satellite which is responsible for the discovery of ULIRG's as a class of objects, made measurements in the Infrared, including at 25 and 60 μm. These two measurements have been used by many to classify the ULIRG population in terms of its "warmth":

$$S_{25\mu m}/S_{60\mu m}$$

If this quantity is greater than 0.2, then the ULIRG is classed as being warm.

Note that the extremely low resolution of the satellite (0.5 degrees even at 25μm) means that the IR fluxes may be contributed to by neighbouring or companion sources.

Table 4.1: **The full ULIRG sample** Names and basic observing data for the 18-strong sample. The final column gives alternative names. Observing dates for the 9 objects observed are given in the penultimate column. Note that $L_{60} = log_{10}(\nu L_\nu(60\mu m)/L_\odot)$, is calculated for our adopted cosmology, $h = 0.5, \Omega = 1$. S_{25}/S_{60} is the ratio of 25μm to 60μm flux, as measured by IRAS. The classification scheme in column 9 is that of Lawrence et al. 1989, and discussed in the main text (section 4.2).

Name	Type	z	RA (J2000)	Dec (J2000)	V	L_{60}	S_{25}/S_{60}	Class	Asymm.	Observing date	Notes
					IRQSO's						
0027−289[a]	QSO	0.280	00:30:04.20	-28:42:25.4	16.6	12.30	0.25	6/C			00275−2859
0157+001	QSO	0.163	01:59:50.21	+00:23:40.6	15.7	12.35	0.23			20020115,20020116	Mrk1014
0316−346	QSO	0.265	03:18:06.51	-34:26:37.1	15.2	11.73	<0.51				
0450−299	QSO	0.286	04:52:30.09	-29:53:35.3	16.0	12.30	0.29				
0759+651	QSO	0.149	08:04:30.49	+64:59:52.4	14.5	12.11	0.33				
0829+046	QSO	0.180	08:31:48.88	+04:29:39.1	16.2	11.69	0.60			20020116	
0923+201	QSO	0.190	09:25:54.81	+19:54:06.8	16.0	11.67	<0.49			20020116	
1003+437[b]	QSO	0.178	10:05:41.89	+43:32:40.5	16.3	11.85	0.33	0/C		20020114,20020115	10026+4347
1226+023	QSO	0.158	12:29:06.70	+02:03:08.6	12.9	12.26	0.43			20020115,20020116	3C273
					ULIRG's						
02054+0835	Sy1	0.345	02:08:06.80	+08:50:02.0	17.7	12.48	<0.417	1/C	0.242	20020114,20020116	
06268+3509	Sb	0.170	06:30:13.20	+35:07:49.0	17.3	12.00	<0.27	6/A	0.414	20020116	
06561+1902	Sb	0.188	06:59:06.52	+18:58:16.7	17.9	12.11	<0.27	5/A	0.252	20020114,20020115	
07381+3215	Sb	0.170	07:41:24.20	+32:08:02.0	18.6	11.90	<0.20	6/B	0.333	20020115	
10579+0438	Sb	0.173	11:00:34.33	+04:21:58.9	18.5	11.84	<0.44	6/B	0.272	20020114,20020115	
23140+0438	BLRG	0.220	23:16:35.23	+04:05:18.1	17.3	12.02	<0.31	0/B	0.215		
23220+2919	HX	0.240	23:24:27.03	+29:35:36.9	18.8	12.27	<0.15	6/B	0.307		

[a] Also classified as a ULIRG; IRAS00275−2859

[b] Also classified as a ULIRG; IRAS 10026+4347

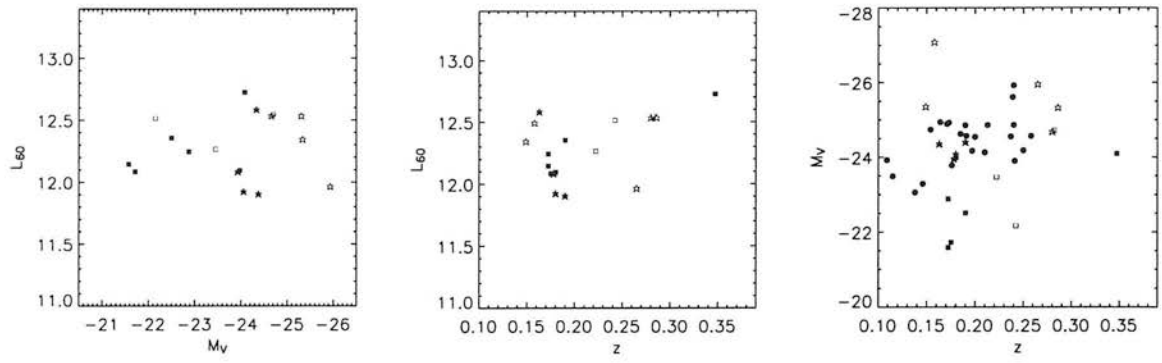

Figure 4.1: **Quasar & ULIRG sample matching.** The left-hand panel shows the matching of the ULIRG's (squares) and IR-bright QSO's (stars) in the $L_{60} - M_V$ plane. Filled symbols denote the objects for which we have obtained imaging. As should be expected, the QSO's are systematically brighter than the ULIRG's because of their bright optical nuclei. The central panel shows the matching of the ULIRG's and IRQSO's in terms of their redshift distributions. The right-hand panel illustrates the matching of the IR-bright QSO's with the existing comparison sample of "ordinary" quasars (filled circles) which are undetected by IRAS at 60μm, and for which complete HST WFPC2 and K-band UKIRT imaging data exist (Dunlop et al. 2003, McLure et al. 1999).

4.3 Observations & Data Reduction

The observations were carried out on the United Kingdom Infrared Telescope (UKIRT), Mauna Kea, Hawaii, over 3 successive nights, (20020114-20020116). We used UFTI, the 0.8-2.5μm UKIRT Fast Track Imager, a basic Near-Infrared Imager with a proven track record of sensitive, robust reliability. It has a field of view of 92 arcsec, and onboard UKIRT, it routinely delivers images with a FWHM less than 0.5 arcsec (Roche 2002), essential for our needs. To date, we have only been awarded sufficient observing time to image half of these objects, for which observing dates are also given in table 4.1.

We adopted a standard NIR observational technique, using the QUADRANT_JITTER observing mode. The source is observed on four different parts (quadrants) of the 1028×1028 Rockwell Hawaii detector. The resulting images are registered using bright sources in the field, or the World Coordinate System (WCS), and averaged in the standard way to produce a final science frame. Such a pattern of observations allows for accurate measurement of the background to a slightly extended source, and can be repeated several times until the required sensitivity is attained. Our programme of observations

allowed for regular measurements of the instrumental / atmospheric PSF, and the same observing technique was utilised for both science targets and the PSF stars. In addition to these observations, we observed one calibrated UKIRT faint standard per science target, for photometric calibration purposes. This observation was typically carried out in between science target observations, just before moving the telescope to a new position on the sky.

For the science objects, we performed 2 on-source iterations of the QUADRANT_JITTER routine, using exposure times of 35 seconds per quadrant. This jitter was typically performed 4 times in succession, before moving to a suitable nearby PSF star. For the PSF stars, we typically performed 5 iterations of the jitter pattern, using integration times of 5 seconds per quadrant. This was also done 4 times in succession. We alternated between object and PSF star in this way several times, before moving on to the next target. Before and after changing target, the PSF star was always quickly checked, going just twice around the jitter pattern. The resulting images yield a total on-source integration time of 35 sec$\times$4 per jitter, but these are averaged to produce a 35 sec frame made up of 4 different observing positions. Bad pixels are flagged in each case.

4.3.1 Observing Notes

Figure 4.2 pictorially summarises the variation in the PSF from observation to observation, on a night-by-night basis. The figure illustrates the χ^2 distribution resulting from an attempt to fit one PSF to the next, normalising over total flux. Each figure is normalised in the same way in χ^2.

On the first night, our images were basically unusable due to instability in the PSF, whose shape changed from oval, to almost circular, with a prominent spur. As a precaution, we ignored the data from this night, and the telescope was refocused. The middle of the second night, 20020115, saw strong winds, gusting close to 50 knots. A number of the PSF's exhibit defects due to wind-shear.

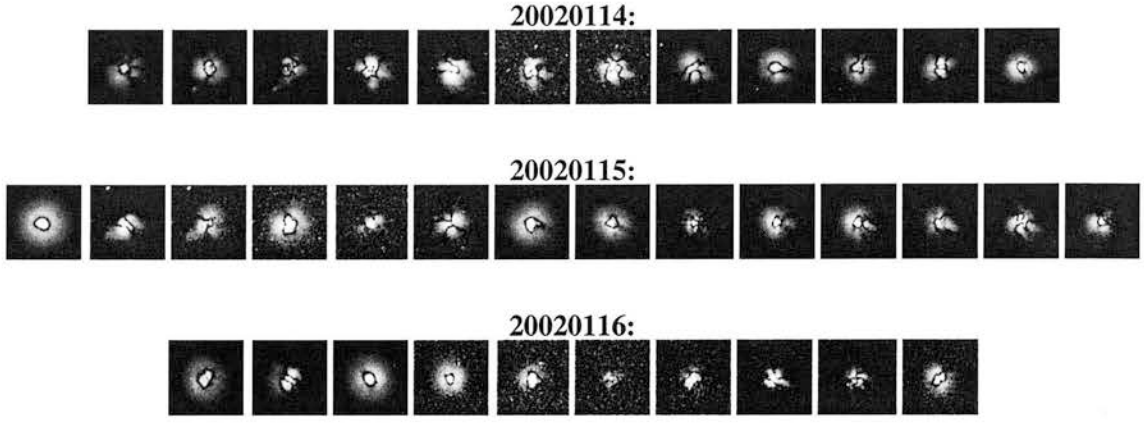

Figure 4.2: **Variation in the UKIRT PSF** on the 3 nights of observing (top to bottom) and from observation to observation (left to right). The thumbnails show the distribution in χ^2 when attempting to fit one PSF to the next, and are all normalised to the same greyscaling. Note the curious unstable defect which made most of our first night's observations redundant. The excellent seeing on the other 2 nights shows up in the far stabler shape of the residuals.

20020116 saw stable, sub-arcsecond seeing throughout the night.

On both attempts to observe 1226+023 (3C273) we ended up with saturated images, due to the large flux. The data is un-modellable without any information on the nuclear spike.

4.3.2 PSF stars

Although the form of the UKIRT PSF is somewhat simpler than that of HST, it is also far more variable, and no theoretical model exists to model it in its entirety. As a result, we must depend entirely upon observed stellar PSF's for our modelling. Thus as much work went into getting accurate PSF measurements, as went into observing the science targets themselves. Over the course of the 3-night observing run, we therefore built up a library of observed stellar PSF's for use in our modelling, discussed further in section 4.4.1

4.3.3 Standard Stars

Several UKIRT faint standards Hawarden et al. (2001) were used throughout the observing run to provide accurate night-by-night, and object-by-object photometry. These stars were observed using the same jitter pattern, but performed once around only.

4.3.4 Data Reduction

The basic data reduction steps (flat-fielding, bias subtraction) were performed using the standard ORAC_DR pipeline data reduction for the QUADRANT_JITTER observing mode. Within an individual jitter pattern we generally found the registration and co-addition to be accurate. However, for the co-addition of subsequent jitter frames, we found many cases in which the automatic registration went somewhat awry, and had to be performed by hand. In all cases, centroiding was performed on the individual frames. Because in this case we are oversampled, we can perform an interpolated shift so that each individual jitter frame shares the same centroid. All images - object and PSF - were re-centred at (128.00, 128.00) using a cubic spline interpolation within IRAF.

4.4 Modelling

The basic modelling technique is essentially identical to that described for the HST data in Chapter 2. The only significant difference was in the generation of an error frame for the ULIRG's. Since we cannot assume that the central pixel of the ULIRG observations is purely nuclear flux (nor even necessarily nuclear-dominated), we cannot generate the statistical sampling errors that were used for our HST QSO programme. Instead, for the central regions of the ULIRG's, we calculate statistical errors, in annuli, upon the object itself. When these fall away to roughly the background Poisson level,

we revert to the individual pixel-by-pixel Poisson noise calculation.

In one case (06561+1902), there are two clearly distinct separable sources, and here I have attempted to model each one individually. In addition there are two objects (06268+3509, 10579+0438) that are clearly undergoing ongoing merger. In the former case, I have attempted fits to each individual object, as there is a clear separation, and distinguishable nucleus in each. For 10579+0438, however, the secondary object is small and indistinct, and is left as a modelling residual.

4.4.1 PSF's

In the case of UKIRT, or indeed any ground-based telescope, the PSF is going to be affected by seeing, and there is no simple way of generating a theoretical one, in the way that we could for HST using TINYTIM. Instead, we must rely solely on observed stellar PSF's.

During the 3-night observing run, we built up a library of 39 PSF observations for use in our modelling. The key, as before is to match the central region (especially in the IRQSO's where the centre is still dominated by a "star-like" unresolved nucleus) to the central region of the PSF. Thus each object was compared in its central 3×3 pixels to each of the library PSF's to obtain the best match using the χ^2 figure of merit. Fitting was attempted using each of the 5 best fit PSF's for each ULIRG.

It is reassuring to note that one of the five best fits was in each case one of the PSF's taken closest in time to the object. However, the best-fitting one was as likely to be from another night altogether, underlining the significance of variability in the PSF. The variability of the PSF over the course of the three nights is summarised in figure 4.2, which shows the chi^2 frame obtained in fitting consecutive PSF images to each other, by matching their total sky-subtracted flux.

4.5 Results

4.5.1 Fixed Morphology Models

Results of the modelling are presented in table 4.2, with radial profiles of the best-fit models presented in figure 4.3. Grey-scale images are found in the appendices. For each object you will see the final UFTI K-band image, along with an image of the best-fit model. These are contoured and grey-scaled at the same levels (see notes in Appendix). In addition, there are images of the best-fit host on its own, the modelling residuals, and the χ^2 frame. χ^2 contours in $\mu - R$ were calculated for all objects in order to examine the stability of the fit (figure 4.4).

Where fits were performed to more than one object, I have presented the two models separately in the table, beginning with the more luminous (centred in the images). The images show the sum of the two models in these cases, although the modelling for each case was performed separately, and the χ^2 frames for each fit are presented in separate frames.

Note the immediate distinction between the Quasar and ULIRG samples. Whereas all the quasars were found to be best-fit with an elliptical host, the ULIRG's are a far more mixed bag. This issue is discussed in detail in the next section.

4.5.2 Variable-β modelling

In the second case, I carried out modelling using a variable-β fit, in which the β parameter (of equation 1) is allowed to vary freely, with $\beta = 0.25$ equivalent to a de Vaucouleurs elliptical profile and $\beta = 1$ an exponential disc. This model allows for a more general morphology than the strictly disc or bulge technique. Table 4.3 shows the results of this variable-β fitting. In many cases, little or no improvement was made with the addition of this extra parameter. In 5 cases there is a significant

Table 4.2: **Modelling results** from fits with both de Vaucouleurs spheroid and Freeman disc models. Columns are as follows: object name; best fitting host-galaxy morphology (disc or elliptical); reduced-χ^2 value for the best fit model; $\Delta\chi^2$ between the chosen and alternative-morphology model; half-light radius, $r_{1/2}$, of best fitting galaxy model in kpc; surface brightness of the host at the half-light radius, $\mu_{1/2}$, in units of I mag.arcsec^{-2}; Integrated apparent K-band magnitudes of the nucleus and the host galaxy; integrated absolute magnitudes of the nucleus and the host galaxy; the ratio of integrated nuclear and host galaxy luminosities; position angle of the host (in degrees, anti-clockwise from vertical in the images); the axial ratio of the host.

IAU name	Morphology (best fit)	χ^2_{red}	$\Delta\chi^2$	$r_{1/2}$ (kpc)	$\mu_{1/2}$	K_{Nuc}	K_{Host}	M_K^{nuc}	M_K^{host}	L_N/L_H	PA (°)	a/b
IRQSO's												
0157+001	E	1.291	10100.0	8.8 ± 0.2	17.9 ± 0.1	12.17	12.76	-27.86	-27.27	1.7	166	1.221
0829+046	E	0.778	24.9	11.7 ± 0.5	19.6 ± 0.1	12.07	14.20	-28.18	-26.06	7.0	127	1.420
0923+201	E	1.025	501.0	110.5 ± 11.0	24.4 ± 0.3	11.92	14.29	-28.46	-26.09	8.9	126	1.543
1003+437	E	0.796	1780.0	1.4 ± 0.1	15.3 ± 0.1	13.31	14.16	-26.92	-26.07	2.2	81	1.025
ULIRG's												
06268+3509	D	1.175	680.0	4.9 ± 0.1	18.6 ± 0.1	15.11	14.53	-25.01	-25.59	0.59	172	1.414
06268+3509	D	0.884	748.0	2.8 ± 0.1	17.8 ± 0.1	16.43	14.82	-23.69	-25.31	0.22	180	1.230
02054+0835	E	0.909	406.0	$.83\pm0.1$	14.0 ± 0.2	14.87	15.11	-26.87	-26.62	1.3	64	1.239
07381+3215	E	0.447	2400.0	1.7 ± 0.1	15.4 ± 0.1	20.84	14.08	-19.29	-26.05	0.002	73	1.385
10579+0438	D	0.652	22.7	1.9 ± 0.1	16.5 ± 0.1	15.63	15.86	-24.53	-24.30	1.2	55	4.672
06561+1902	D	0.810	116.0	6.5 ± 0.6	20.8 ± 0.2	15.32	16.22	-25.04	-24.13	2.3	13	1.301
06561+1902	E	0.628	135.0	20.9 ± 7.0	22.0 ± 0.5	17.03	15.78	-23.33	-24.57	0.32	24	1.908

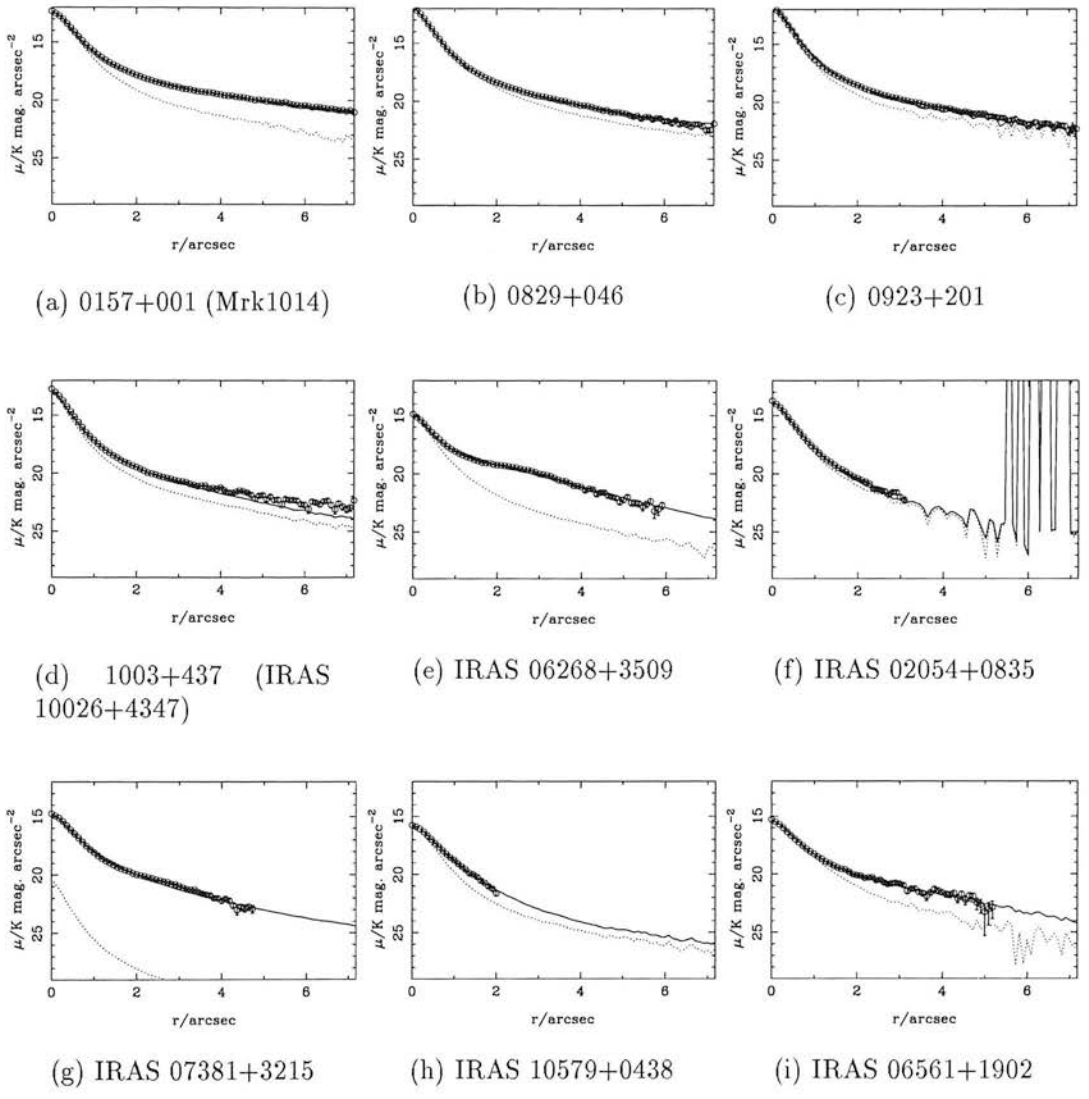

(a) 0157+001 (Mrk1014) (b) 0829+046 (c) 0923+201

(d) 1003+437 (IRAS 10026+4347) (e) IRAS 06268+3509 (f) IRAS 02054+0835

(g) IRAS 07381+3215 (h) IRAS 10579+0438 (i) IRAS 06561+1902

Figure 4.3: **Radial profiles of the ULIRQ/QSO sample.** The dotted line shows the underlying nuclear component.

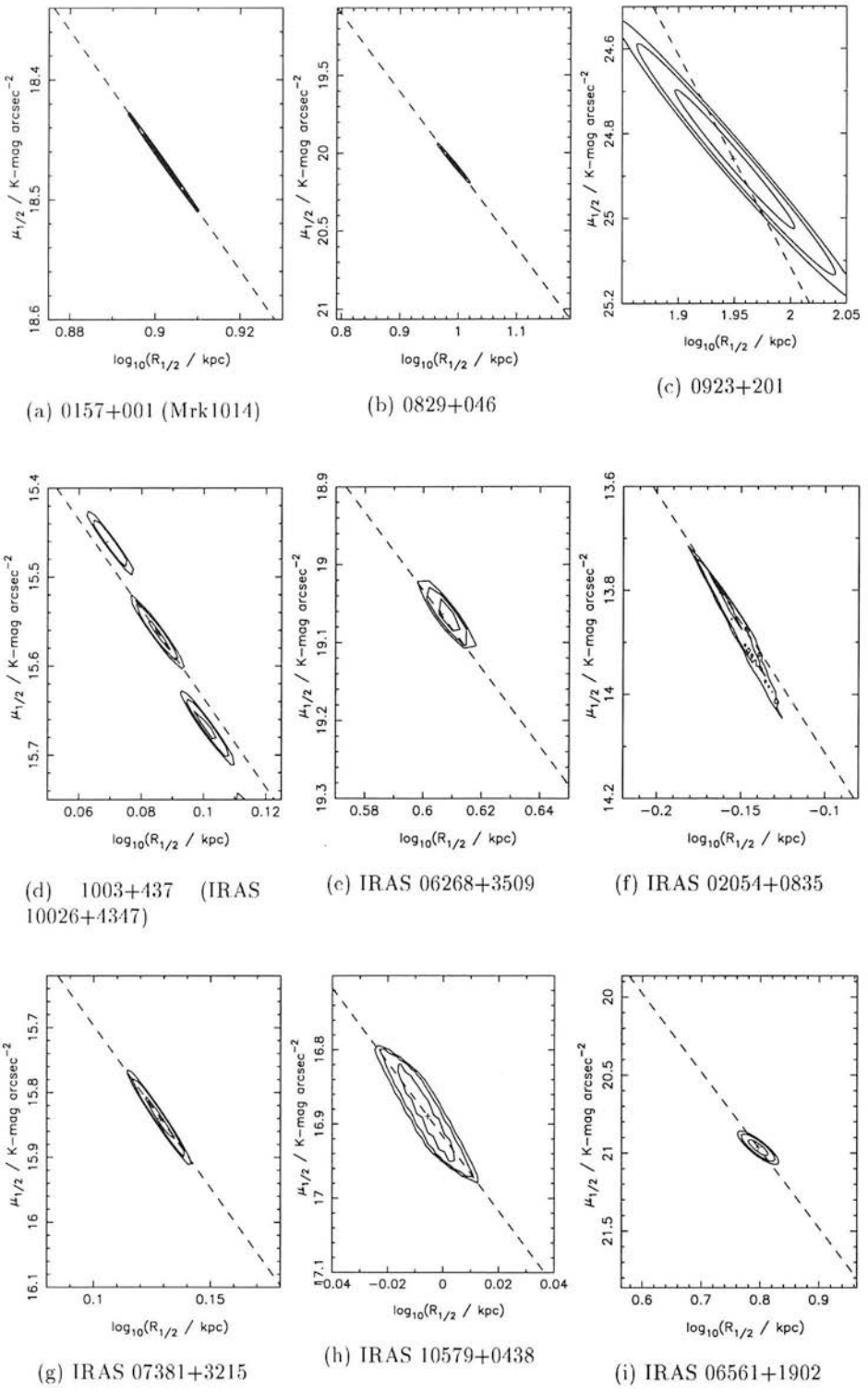

(a) 0157+001 (Mrk1014) (b) 0829+046 (c) 0923+201

(d) 1003+437 (IRAS 10026+4347) (e) IRAS 06268+3509 (f) IRAS 02054+0835

(g) IRAS 07381+3215 (h) IRAS 10579+0438 (i) IRAS 06561+1902

Figure 4.4: χ^2 **contours in the** $\mu - R$ **plane** for the $z \approx 1$ sample. Note that the slope of 5 (dashed line) implies a tightly constrained host galaxy luminosity, even where the scalelength and surface brightness are poorly constrained. The strange multiple minima seen in the contours for IRAS02054+0835 are the minima corresponding to adjacent values of L_{nuc} in the grid used to compute the contours. The contours for 0157+001 are almost too small to see.

Table 4.3: **Outcome of variable-β modelling.** Columns are as follows: object name; best-fit morphology from pure bulge & disc models (Table 2.3); best-fit β value with no assumed morphology; the value of reduced-χ^2 produced by this best-fit model; improvement in fit, $\Delta\chi^2$ obtained by using the variable-β technique compared to the best-fit fixed morphology model.

IAU name	Morph.	β	χ^2_{red}	$\Delta\chi^2$
IRQSO's				
0157+001	E	0.53	1.291	2.3
0829+046	E	0.22	0.778	11.2
0923+201	E	0.25	1.025	0.0
1003+437	E	0.68	0.827	219.8
ULIRG's				
06268+3509	D	1.05	1.175	0.0
	D	0.83	0.877	50.0
02054+0835	E	0.25	0.909	0.0
07381+3215	E	0.25	0.447	0.0
10579+0438	D	1.00	0.652	0.0
06561+1902	D	1.31	0.809	16.0
	E	0.25	0.628	0.0

change most natably in the quasars 0829+046 and 1003+437. 0157+001 also exhibits some change, but the improvement in the fit is insignificant.

4.5.3 2-component modelling

In the light of results obtained using the standard modelling technique (see section 4.5), I decided to attempt to fit a 2-component (Bulge + Disc) model. This modelling was in order to see whether we could pick up on any low surface brightness bulge components in the discy ULIRG's, or any discy component in the QSO's. Generally, the fit was improved slightly using this method, although more often than not this was thanks to one or other of the components being relegated to a very compact, bright source - substituting for some of the nuclear flux. In a couple of notable cases, however, the modelling successfully uncovered an underlying component of differing morphology to the dominant population. The host of 0157+001 in particular, is found to be significantly brighter than that obtained using the simple single-morphology case. The other objects, however, remained fixed in

Table 4.4: **2-component modelling results.** The second column gives the best description of the host morphology. The improvement in the fit over the best-fitting simple morphology model is given in terms of its effect on χ^2_{red}. The overall host magnitude is given, followed by bulge and disc scale-lengths, bulge and disc magnitudes, and finally the bulge-to-disc ratio.

Source	Morph.	$\Delta\chi^2_{red}$	M_K(Host)	r_B kpc	r_D kpc	M_K(Bulge)	M_K(Disc)	Bulge/Disc
IRQSO's								
0157+001	E/D	0.03	-27.2	1.6	29.0	-27.0	-26.4	1.6
0829+046	E	0.001	-25.5	9.9	0.3	-25.5	-22.0	24.0
0923+201	E	0.02	-25.3293					
1003+437	E/D	0.001	-25.6	1.4	14.8	-25.5	-23.7	5.0
ULIRG's								
06268+3509	D/B	0.003	-25.0	14.3	3.8	-23.2	-24.9	0.2
02054+0835	E/D	0.1	-25.5	4.4	0.4	-25.4	-23.2	7.3
07381+3215	E/D	0.006	-23.9	0.9	0.4	-23.7	-22.5	3.0
10579+0438	D	0.000	-23.7	500.0	0.9	-16.9	-23.7	0.0
06561+1902	D	0.07	-23.6	17.6	5.7	-14.6	-23.6	0.0

host luminosity, and table 4.4 shows the relative contributions of the bulge and disc in each case.

4.6 Colour Maps

In this section I present the $V-K$ colour maps generated using my UKIRT data along with the HST V-band data of Farrah et al. (2001). It was found that using the modelling residuals led to heavily artifacted and messy maps. Instead I adopted the Lucy-Richardson deconvolution technique. Using a weighting frame generated as an inverse of the error frames created for the 2-dimensional modelling I obtained excellent results, with the nuclear-dominated objects being well-fit after 1-2 iterations.

However, I found that for the non-nuclear-dominated sources, it is quite possible to create a colour map using the raw image, because the noise in the image outweighs the sampling noise, due to lack of knowledge of the PSF. Thus colour maps for the ULIRG's without a strong nuclear source are created from the raw frame.

In both cases there are issues with unresolved PSF artifacts in the central regions, and thus these

areas should be treated with suitable mistrust.

4.7 Notes on individual objects

4.7.1 The IRQSO PG0157+001 (Mrk1014; IRAS01572+0009) at $z = 0.163$

Mrk1014 is a complex and well-studied object. A "warm" ($S_{25\mu m}/S_{60\mu m} > 0.2$) IRAS object and a QSO, there remains a debate over its radio nature. It is the "loudest" of the radio-quiet sample in McLure et al. 1999, with $log_{10}(L_{5GHz}/\mathrm{WHz^{-1}sr^{-1}}) = 22.87$, making it a candidate Radio-Intermediate Quasar (RIQ, Falcke et al. (1995)) with a morphology similar to that found in several radio-loud quasars. The two radio components lie on either side of the optical nucleus, with the same PA as the large tidal arm, and thus perpendicular to the asymmetric feature visible in our modelling residuals.

Along with 0923+201, this object is a member of the Dunlop et al. (2003) comparison sample of quasars at $z \approx 0.2$. These were originally imaged in K-band (using IRCAM) by Dunlop et al. (1993) and Taylor et al. (1996). These papers were followed up in R-band by McLure et al. (1999). In addition, Hughes et al. (2000) publish 2 optical spectra which are modelled by Nolan et al. (2001), as part of their spectral study to determine the ages of quasar host galaxies. Nolan et al. find a host with an age of 12Gyr from their spectral study. In spite of its appearance, McLure et al. show the host to be best fit by a large 8kpc elliptical in the R-band which is highly consistent with our finding of $r_{1/2} = 8.8 \pm 0.3$kpc. Taylor et al. found a gigantic K-band host with a scalelength of 19.5kpc, but this can be put down to poorer seeing conditions, and the far cruder resolution of IRCAM1.

The 2-component modelling yielded a significantly boosted host luminosity, at the expense of

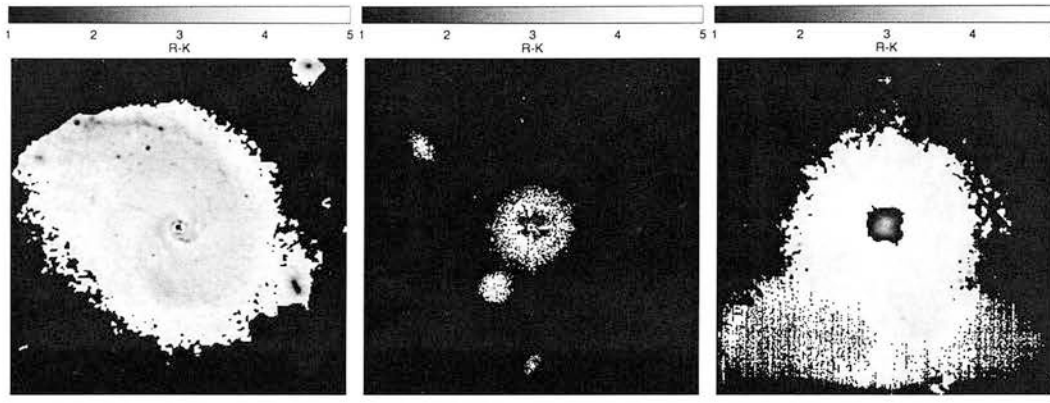

(a) 0157+001 (b) 0829+046 (c) 0923+201

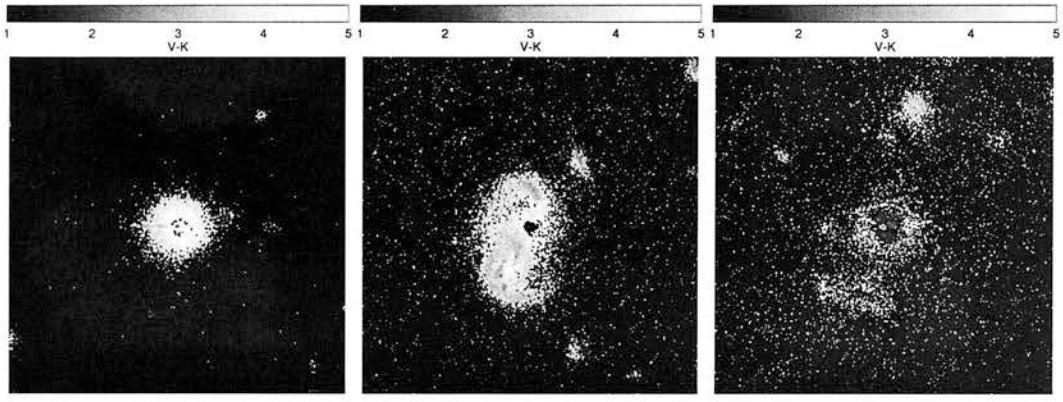

(d) 1003+437 (e) 06268+3509 (f) 02054+0835

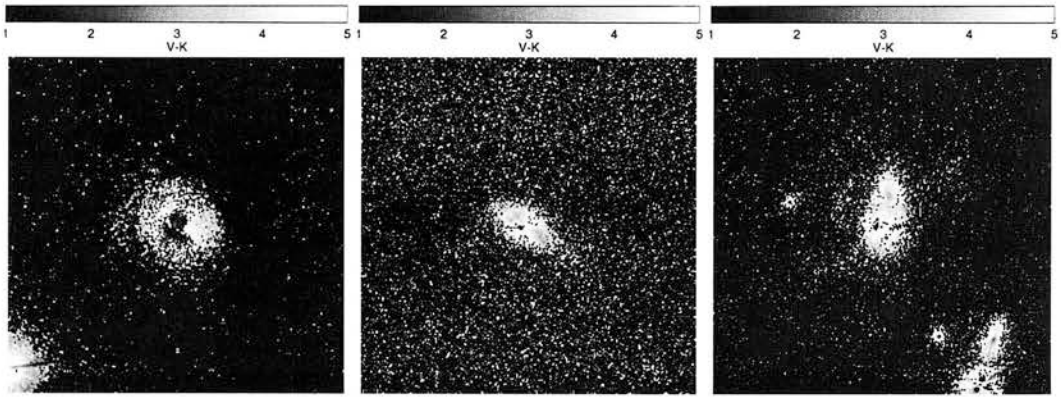

(g) 07381+3215 (h) 10579+0438 (i) 06561+1902

Figure 4.5: $V-K$ **colour-maps for the 9-strong sample.** These have been generated from the present UKIRT data along with archived HST V-band images taken from the samples of Farrah et al. (2001), McLure et al. (1999) and Falomo (1996). For the nuclear-dominated IRQSO's, each image has been de-convolved with the PSF, using the Lucy-Richardson technique. For the more galaxy-dominated ULIRG's, the colour map is produced from the raw V and K-band images (see main text).

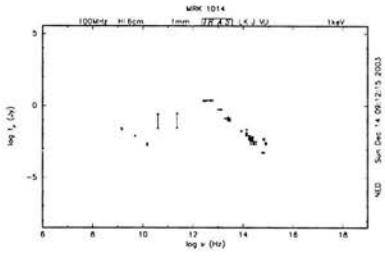

(a) 0157+001 (Mrk1014)

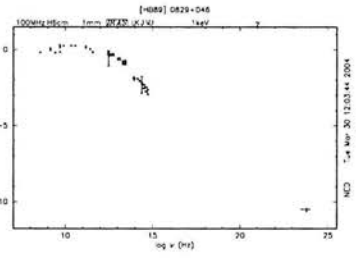

(b) 0829+046

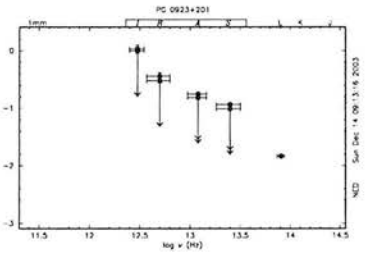

(c) 0923+201

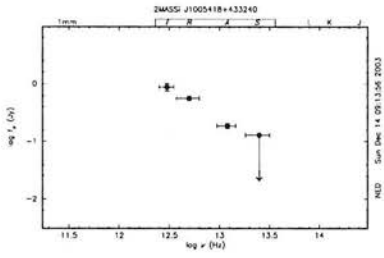

(d) 1003+437 (IRAS 10026+4347)

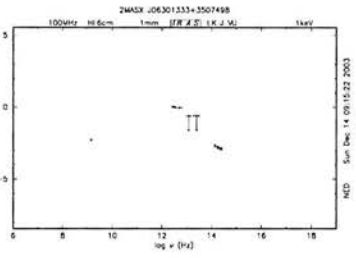

(e) IRAS 06268+3509

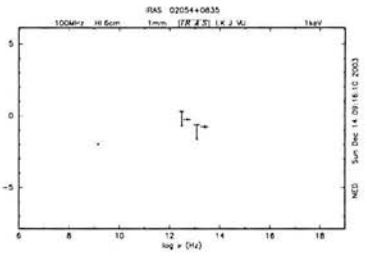

(f) IRAS 02054+0835

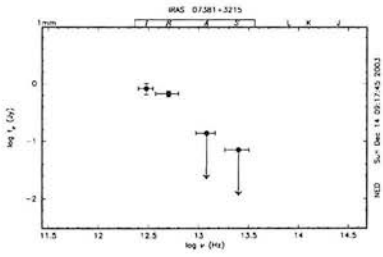

(g) IRAS 07381+3215

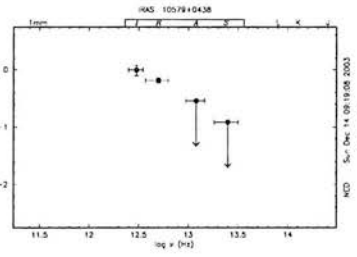

(h) IRAS 10579+0438

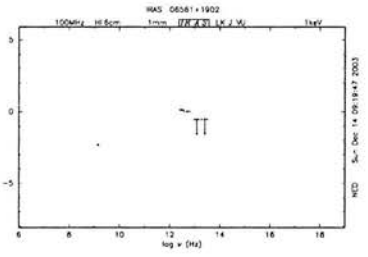

(i) IRAS 06561+1902

Figure 4.6: **Spectral energy distributions** of the ULIRG's and IRQSO's in the present study. We can see the typical broad IR "hump" in several cases, although 0829+046 has a fairly flat spectrum in the radio, and is classified as a BL Lac object.

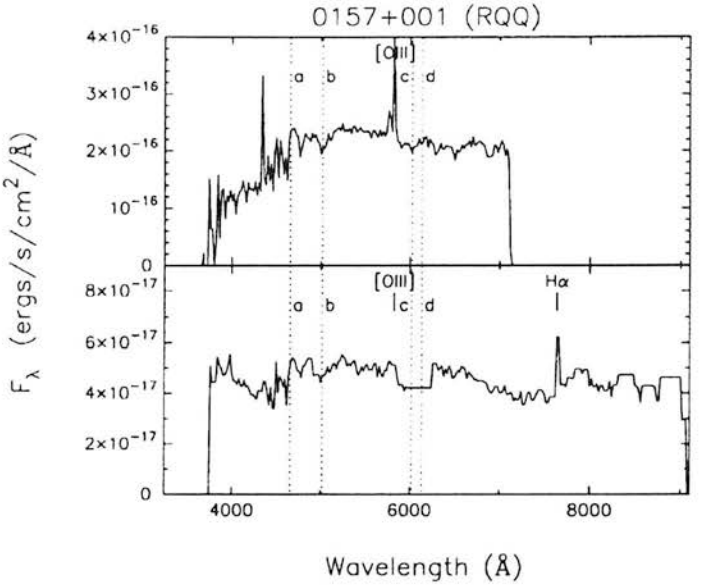

Figure 4.7: **Optical off-nuclear spectra of Mrk1014:** With the Mayall 4m Telescope at Kitt Peak (upper panel) and the 4.2m WHT (lower panel). Taken from Hughes et al. (2000). The [OIII] emission line prominent in the northeastern tidal arm is apparent in the top spectrum. Otherwise, emission lines are not strongly evident from these spectra.

the nucleus. This model fits a large (13kpc) bright ($M_K = -26.4$) disc component to the flux of the tidal arm, though the bulge component is virtually unchanged. The bulge dominates the host with $L_{\rm Bulge}/L_{\rm Disc} = 1.6$.

The colourmap (figure 4.5a) picks out the knots of intense star-formation in the broad tidal arm, as well as spiralling regions of enhanced star-formation. The host colours are consistent with a mature stellar population ($R - K = 3.0$ - see table 4.6 and figure 4.20).

4.7.2 The IRQSO 0829+046 (PKS 0829+046) at $z = 0.180$

A BL Lac object exhibiting strong intra-day variability of polarisation and total flux density at optical and near-IR wavelengths (Sitko et al. 1985, Smith et al. 1987). Previous images obtained at sub-arcsec resolution showed that the host galaxy (z = 0.18) has $M_R \sim -23$ (Falomo 1996). However, inspection of the HST-archive images revealed that the guide star tracking had failed, meaning that successive

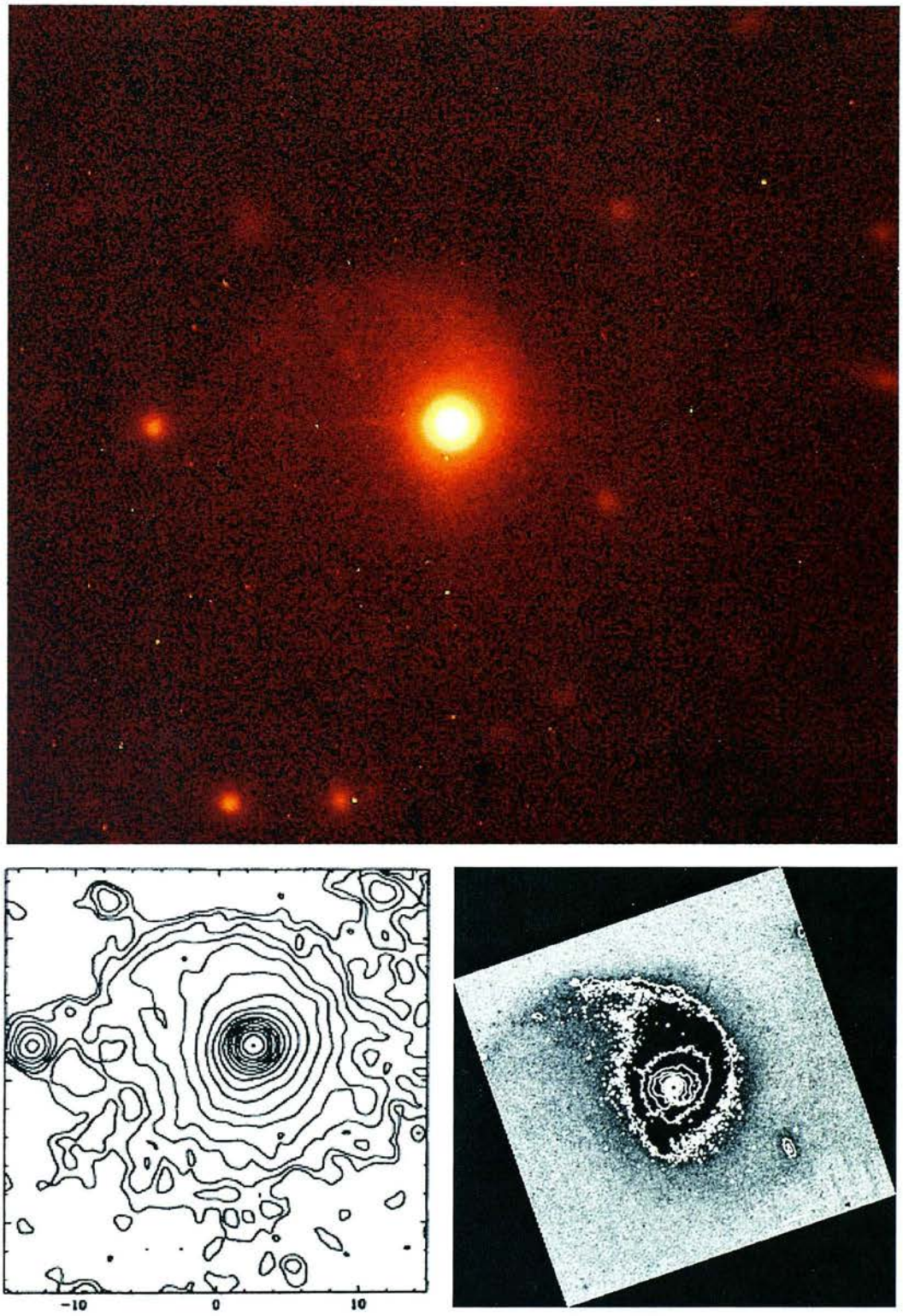

Figure 4.8: **Top:** Full UFTI K-band image of Mrk1014 beautifully illustrating the tidal feature, and nearby companion to the east. There are a number of other nearby objects, but the tidal arm appears to reach out to this eastern one in particular.
Bottom Left: As detected by Taylor et al. (1996), using IRCAM (also in K-band).
Bottom Right: The R-band HST/WFPC2 image of McLure et al. (1999) rotated to have the same orientation. The companion object is slightly out of shot.

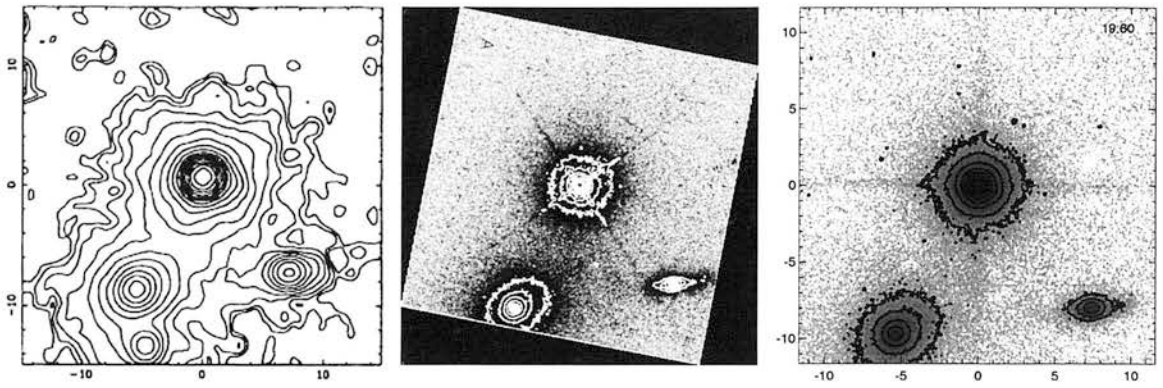

Figure 4.9: **Images of 0923+201:** IRCAM K-band (Taylor et al. 1996), WFPC2 R-band (McLure et al. 1999) and UFTI K-band imaging.

images showed slight drift across the chip. Given the under-sampling of the PSF this failure makes registration and accurate stacking impossible, and thus the R-band data is neglected in the following discussion.

There is an excess density of galaxies around this object although the nearest one, some 5.5arcsec southeast of the quasar, is known to be at significantly higher redshift ($z = 0.24$ Pesce et al. 1994).

I find a luminous 12kpc K-band bulge ($M_K(\mathrm{Host}) = -26.1$). No real improvement is seen with the addition of a low-luminosity disc. The modelling residuals exhibit significant circumnuclear flux, although this appears to be elongated SE-NW, with a flux deficit to the NE and SW of the nucleus. It seems likely that this artifact is a PSF defect, especially when we compare it with the PSF distortions for the night of observations (20020116) shown in figure 4.2.

4.7.3 The IRQSO 0923+201 (PG 0923+201, TON 1057) at $z = 0.190$

A member of the "normal" quasar comparison sample of Dunlop et al. (2003). Nolan et al. (2001) fit an age of 12Gyr to the host, though there is a significant nuclear contribution that has to be modelled. McLure et al. (1999) find an elliptical host with a half-light radius of $r_{1/2} = 8$kpc in R-band. It is

located in a small group of galaxies, with two very bright galaxies, at the same redshift (Heckman et al. 1984), within 11arcsec (45kpc in our adopted cosmology).

I was unable to obtain a stable fit for this galaxy (the steep contours in figure 4.4 imply that the host luminosity is still poorly constrained), with no significant difference found between the 2 morphologies, and an unrealistic 100kpc best-fitting elliptical. Clements (2000) found a normal, quiescent, E2 galaxy, which is consistent with the axial ratio deduced here, of $a/b = 1.356$.

4.7.4 The IRQSO 1003+437 (IRAS 10026+4347) at $z = 0.178$

See Xia et al. (1999) for a detailed optical and X-ray study of this object. In K-band it appears rather ordinary, with no obvious ongoing mergers or interactions (ranked 0/C in the Farrah et al. scheme - table 4.1). However, there are a number of low surface brightness companions in the field, and on closer inspection it appears that the closest object, some 3 arcsec to the west, may be showing low-level signs of an interaction with the quasar, which exhibits slightly elongated isophotes in this direction. Xia et al. conclude that this object is a post-merger system on the basis of its $r^{1/4}$ power-law radial profile, and its strong FeII emission and soft X-ray properties.

I also find a de Vaucouleur's profile, with a scale-length of 1.4 kpc. 2-component modelling yields only a slight improvement with an additional low-level disc component. The modelling residuals are hard to interpret. We can see a low-level tail curving from the SW of the nucleus, up to the western companion object. However, the excess nuclear flux appears to represent a lack of knowledge of the PSF, rather than any genuine artifact (cf. PSF variations for 20020115 in figure 4.2).

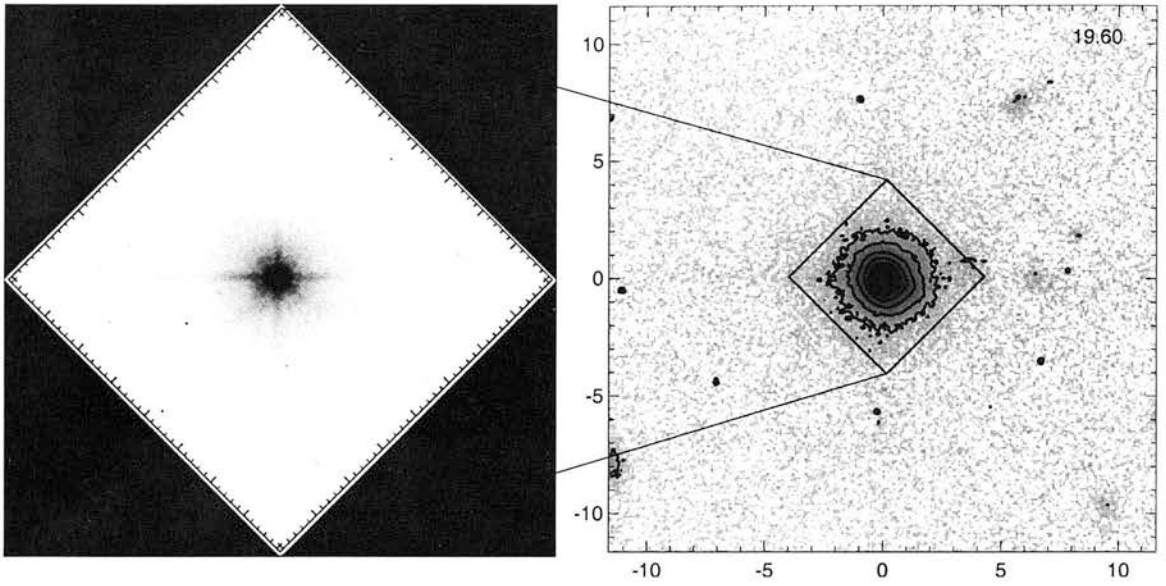

Figure 4.10: **Images of 1003+437 (IRAS 10026+4347):**

4.7.5 The ULIRG 06268+3509 (IRAS 06268+3509) at $z = 0.170$

A beautiful pair of merging spirals - classed as 6/A in the Farrah et al. (2001) scheme. The northern spiral contains several compact bright "knots" at V. There are four further small sources within 12 arcsec. This object is the most galaxy-dominated system studied here ($L_{nuc}/L_{host} = 0.3$), with each component's host galaxy found to be brighter than $L^{\star}$.

The discy primary host of this ULIRG was improved upon very slightly ($\Delta\chi^2 = 0.003$) with the addition of a significant bulge component. However, the bulge:disc ratio is less than 1/5, meaning any bulge component has a luminosity of $\sim= \frac{1}{5}L^{\star}$. This fact, along with the lack of a strong nucleus suggests that any AGN activity in this source is not quasar-like, and the FIR luminosity presumably arises from the immense and very obvious ongoing starburst. The high luminosity of these two galaxies implies that the resulting post-merger object could be a massive, quasar-capable elliptical.

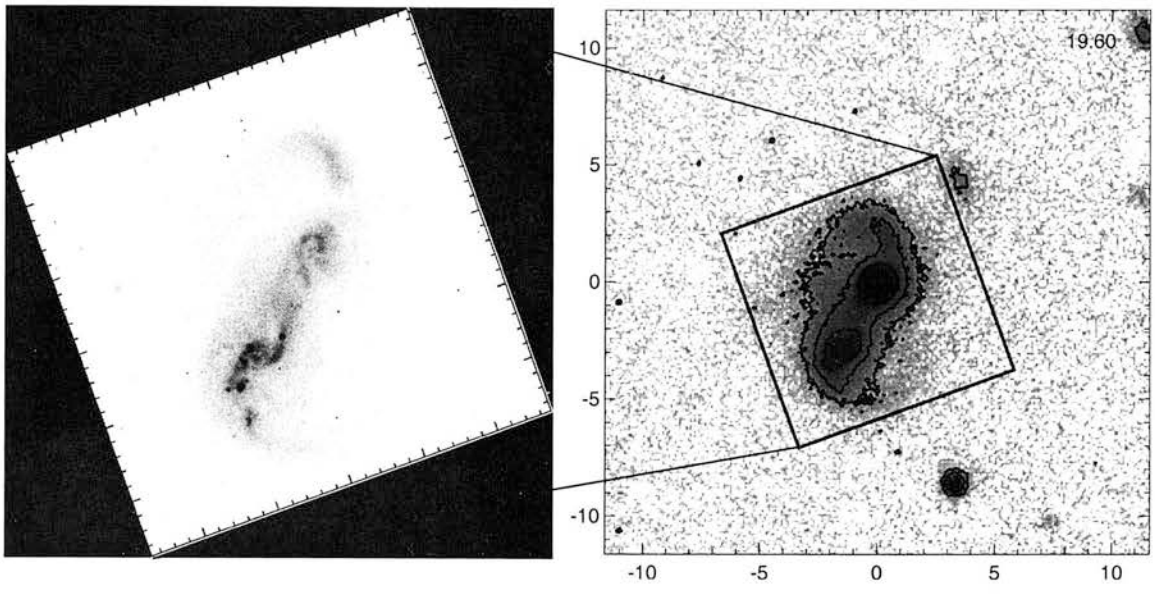

Figure 4.11: **Images of IRAS 06268+3509:**

4.7.6 The ULIRG 02054+0835 at $z = 0.345$

The most 60μm-luminous object in our sample, and the one with the most luminous elliptical host. This object is one of two ULIRGs here that is found to have an elliptical host with a luminosity in excess of $L^{\star}$; $M_K(\mathrm{Host}) = -26.6$. However, with its significant nuclear contribution ($M_K(\mathrm{Nuc}) = -26.7$), this ULIRG could certainly be classed as a QSO. The only sign of interaction is a slight extension to the west of the source, also detected by Zheng et al. (1999). There are, however, five small, faint sources within 10 arcsec, which appear to be companions.

The modelling residuals reveal an interesting ring-like artifact surrounding the nucleus, at a radius of ~ 0.5arcsec, corresponding to a distance of ~ 3kpc. It is impossible to tell whether this is a genuine feature of the ULIRG, or simply a PSF artifact.

The 2-component modelling yielded a modest improvement with the addition of a compact (0.4kpc) low-level ($L_{\mathrm{bulge}}/L_{\mathrm{disc}}$=7.3) disc.

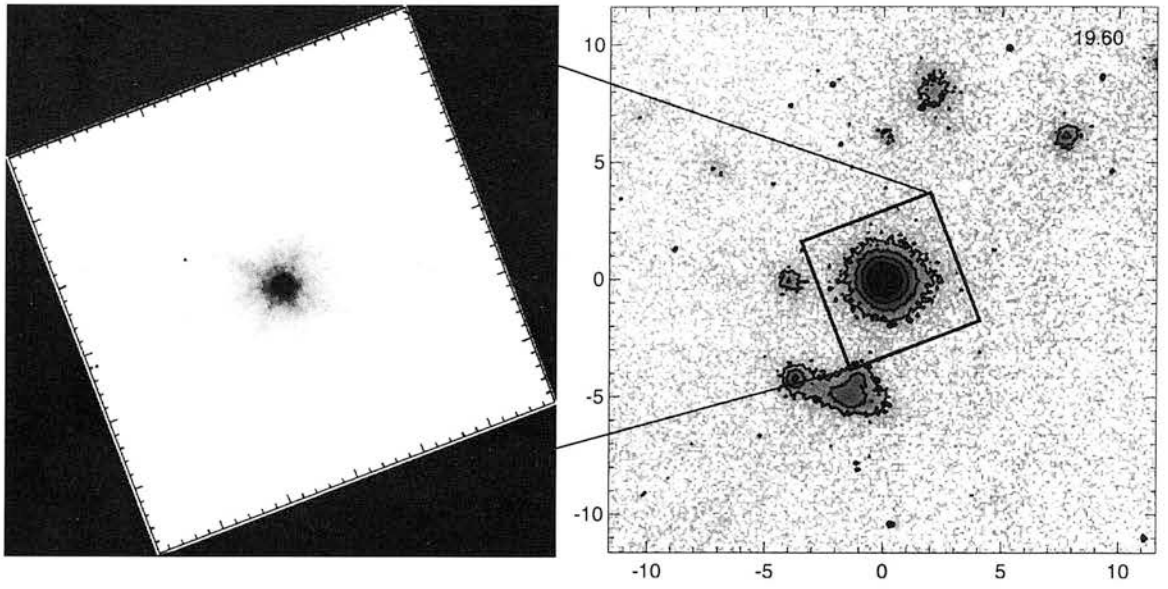

Figure 4.12: **Images of IRAS 02054+0835:**

4.7.7 The ULIRG 07381+3215 at $z = 0.170$

A small, peculiar galaxy with some bright star-forming regions visible in the (Farrah et al. 2001) V-band image (figure 4.13; left). It is classed as 6/B, meaning a merger in which there are no 2 distinguishable sources. From the K-band it appears that any merger must be dynamically finished, with a relatively clean and undisturbed elliptical host galaxy and an extremely weak nuclear component. The host is however found to be luminous, and capable of hosting a quasar.

4.7.8 The ULIRG 10579+0438 at $z = 0.173$

Also classed 6/B in the optical, the K-band image provides direct evidence for 2 separate sources, though the smaller eastern one was too small and faint to be modelled,and was masked out and left as a residual instead. The western object is brighter, larger and more disturbed. The two nuclei are separated by about 1.5 arcsec ($\approx$ 6kpc at the redshift of this object), and are linked by a small tail. The only bright object within 30 arcsec is a foreground star.

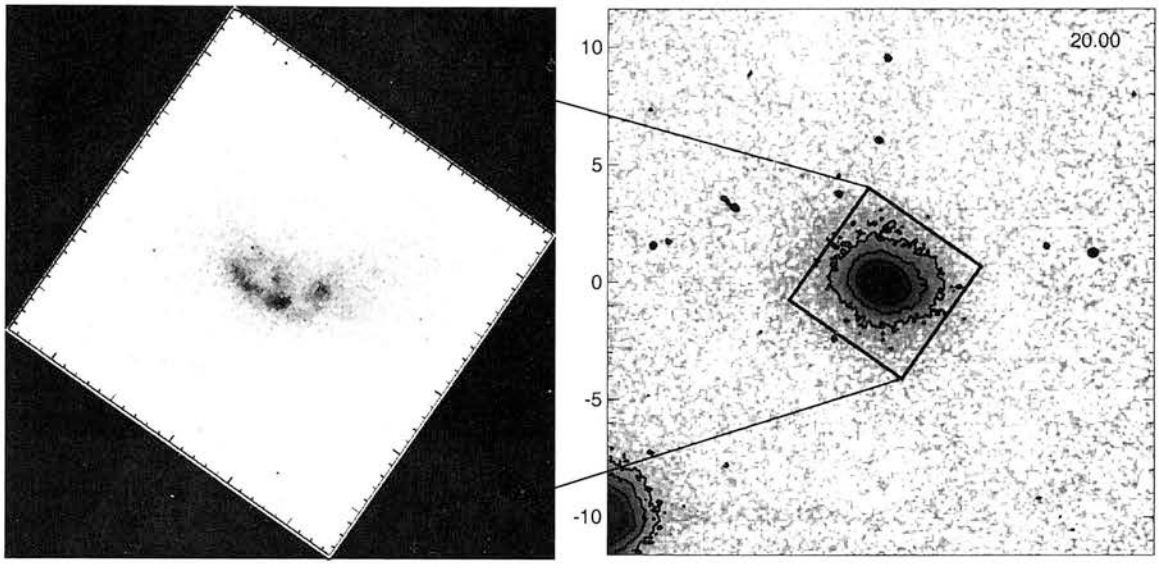

Figure 4.13: **Images of IRAS 07381+3215:**The K-band image (right) is almost unrecognisable from the V-band (Farrah et al. 2001; left), and shows a luminous elliptical with only a very weak unresolved nuclear component.

I fitted a disc galaxy centred on the brighter, western source. The system is clearly undergoing a merger, and there is a significant apparent nuclear component ($L_{nuc}/L_{host} = 1.2$).

4.7.9 The ULIRG 06561+1902 at $z = 0.188$

An interacting pair of galaxies, which although still physically distinct, are connected by a faint bridge (classed 5/A). This source is striking in that there is a similar group of three objects 10 arcsec to the south-west, one of which is a QSO (Farrah et al. 2001).

I find the brighter southern object to be best fit by a disk with a strong nuclear component. The northern object, although apparently dimmer, has a slightly brighter (but sub-$L^{\star}$) elliptical host with a much weaker nucleus.

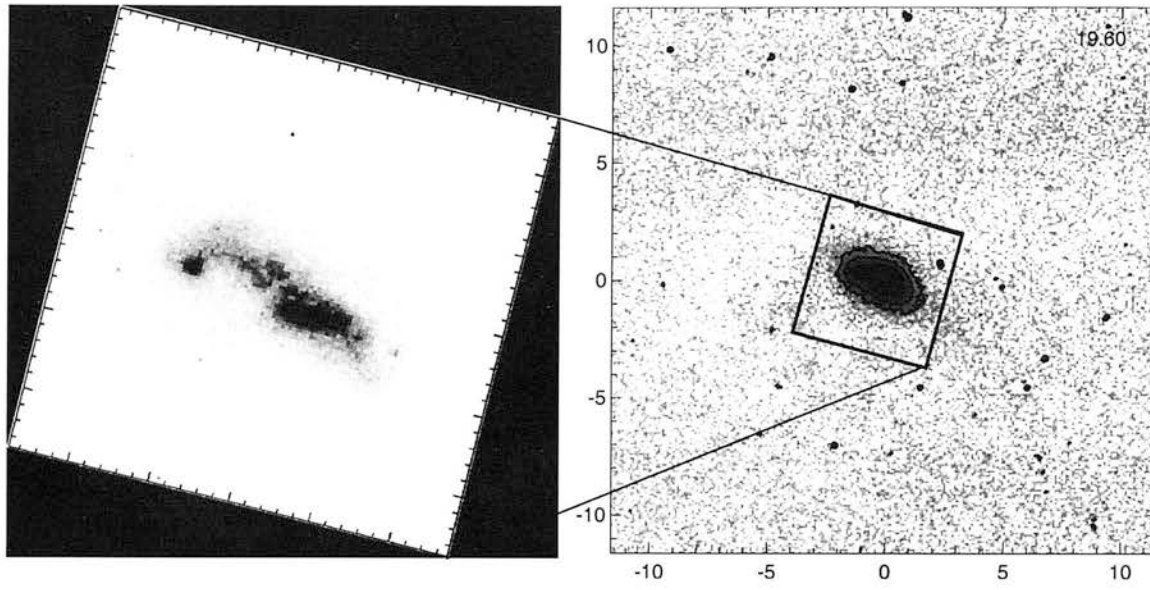

Figure 4.14: **Images of IRAS 10579+0438:**

4.8 Discussion

It should first of all be stressed that atmospheric problems mar the stability of the fits to the nuclear-dominated sources (most clearly in the case of 0923+201, where no clear morphological distinction was made, and we have evidently not completely disentangled host from nucleus. For most of the ULIRGs, the modelling has produced satisfactory fits to the bulk of the host flux, but it is clear that these are disturbed systems, and numerous peculiarities are visible in the residual frames. It should be stressed that the sample is small and still incomplete. In spite of this fact, some clear trends are already apparent from the results of the modelling.

It is quite clear that there is a distinction between the hosts of the quasars and the ULIRG's studied here, and that it is quite possible that they represent different populations of parent object. However, it is also clear that there is significant overlap in the properties of these parent populations. This field is one in which highly detailed multi-wavelength studies of individual objects will pay dividends, as there is a complicated interplay between galaxy, nucleus and environment in each individual case.

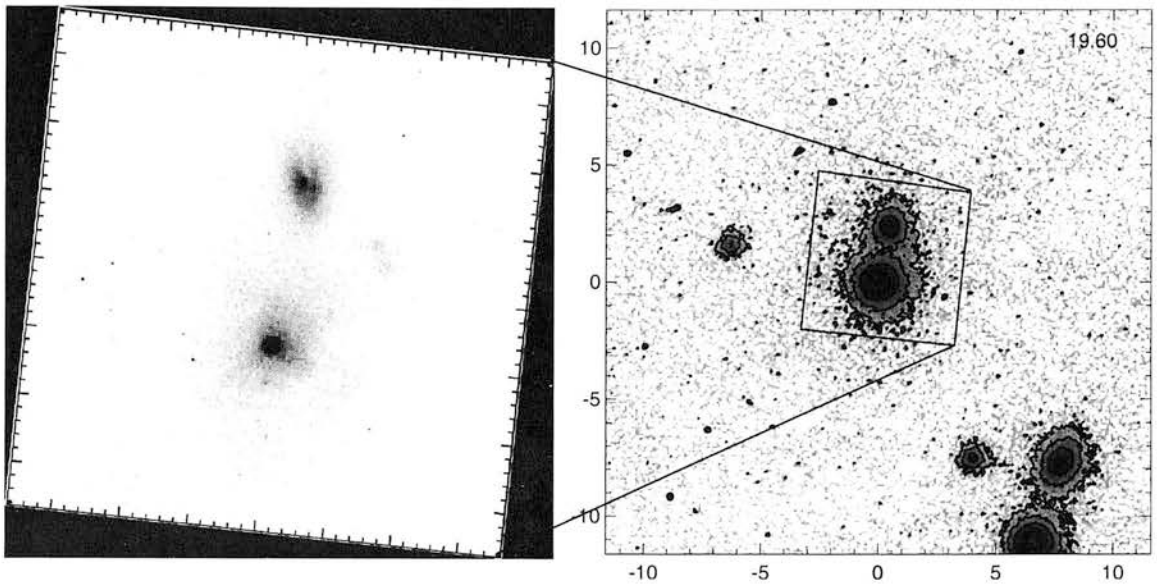

Figure 4.15: **Images of IRAS 06561+1902:**

The following is a brief discussion of the key findings of this study, in which I highlight the key differences and similarities found across the sample observed so far.

4.8.1 Morphology

I have succeeded in uncovering K-band host galaxies for all 9 objects for which we obtained suitable imaging. Of these, three of the ULIRGS are found to contain Freeman disc-like systems, with 3 exhibiting de Vaucouleurs elliptical hosts. One of the major interacting systems was found to contain both a bulge and a disc, with the other one best fit by a pair of merging spirals. This is in stark contrast to the quasar host galaxies, all of which are found to be massive, $> L^{\star}$ ellipticals, consistent with the regular QSO sample of Dunlop et al. 2003, and the work in the rest of this thesis. Two ULIRGs have hosts this luminous; IRAS02054+0835, and IRAS07381+3215 with $M_K = -26.6$, and $M_K = -26.0$ respectively. It is notable from table 4.1 that IRAS02054+0835 is the most 60μm luminous object in our sample, and it is therefore somewhat reassuring that it is found to be hosted by such a massive

elliptical.

Each member of the interacting pair of spirals, IRAS06268+3509 also appear to be $\sim L^{\star}$, but it is possible that each model is contaminated by light from the other galaxies halo, and I have not yet performed a combined joint-galaxy model search, but this would be a useful next step. It seems plausible that this system may end up as a massive and quasar-capable elliptical in its post-merger state.

However, the remaining sources are found to be in sub-$L^{\star}$ hosts, demonstrating that not all ULIRG's can have their enormous power generated by a *quasar-like* supermassive black hole. It remains possible however that there is a contribution from an AGN at a lower level, perhaps more akin to a Seyfert nucleus.

4.8.2 Host scalelength and luminosity

There is a significant difference in the scale-lengths of the QSO's and ULIRG's within our sample:

$$\langle r_{1/2} \rangle_{IRQSO} = 7.0 \pm 2.0\text{kpc}$$

$$\langle r_{1/2} \rangle_{ULIRG} = 3.0 \pm 2.0\text{kpc}$$

Comparing with the results of Scoville et al. we notice a marked difference, their mean ULIRG scale-length being just 2.2 ± 0.1kpc. The one object that the present sample has in common with Scoville et al. is Mrk 1014, for which they found a discy host with $R_{1/2} = 3.3$kpc, compared with our elliptical with $R_{1/2} = 8.8kpc$. I reiterate that the most likely cause of this discrepancy is the small field-of-view on NIC2, which is unsuitable for the detection of large-scale galaxies so nearby.

The mean surface brightnesses of our QSO and ULIRG hosts are also found to differ correspond-

ingly:

$$\langle \mu_K \rangle_{IRQSO} = 17.6 \pm 1.0$$

$$\langle \mu_K \rangle_{ULIRG} = 17.2 \pm 1.0$$

4.8.3 Kormendy relation

The results of attempting to fit a Kormendy relation to the sample are summarised in figure 4.16. Each subsample was independently fit, obtaining a slope of ~ 5 in each case, as well as the full sample together.

$$\text{IRQSO} : \mu_{1/2} = (14.2 \pm 0.7) + (4.9 \pm 0.6) \log r_{1/2}$$

$$\text{ULIRG} : \mu_{1/2} = (14.3 \pm 0.2) + (5.8 \pm 0.3) \log r_{1/2}$$

$$\text{Both} : \mu_{1/2} = (14.3 \pm 0.4) + (5.0 \pm 0.4) \log r_{1/2}$$

However, we find that the sample is *consistent* with an overall slope of 3.0. The best-fitting relation of slope 3 has the form (illustrated in the bottom panel of the figure):

$$\mu_{1/2} = 16.3 + 3.0 \log r_{1/2}$$

Projecting each object onto this relation, along the isophotal projection of the FP, we find an alternative model with the same luminosity. As a quick experiment, this fixed $R - \mu$ model was fitted using the same code as before to find out what difference it would make to the quality of the individual fits. Results are shown in table 4.5, and it is clear that the entire sample is consistent with being drawn from the same host population.

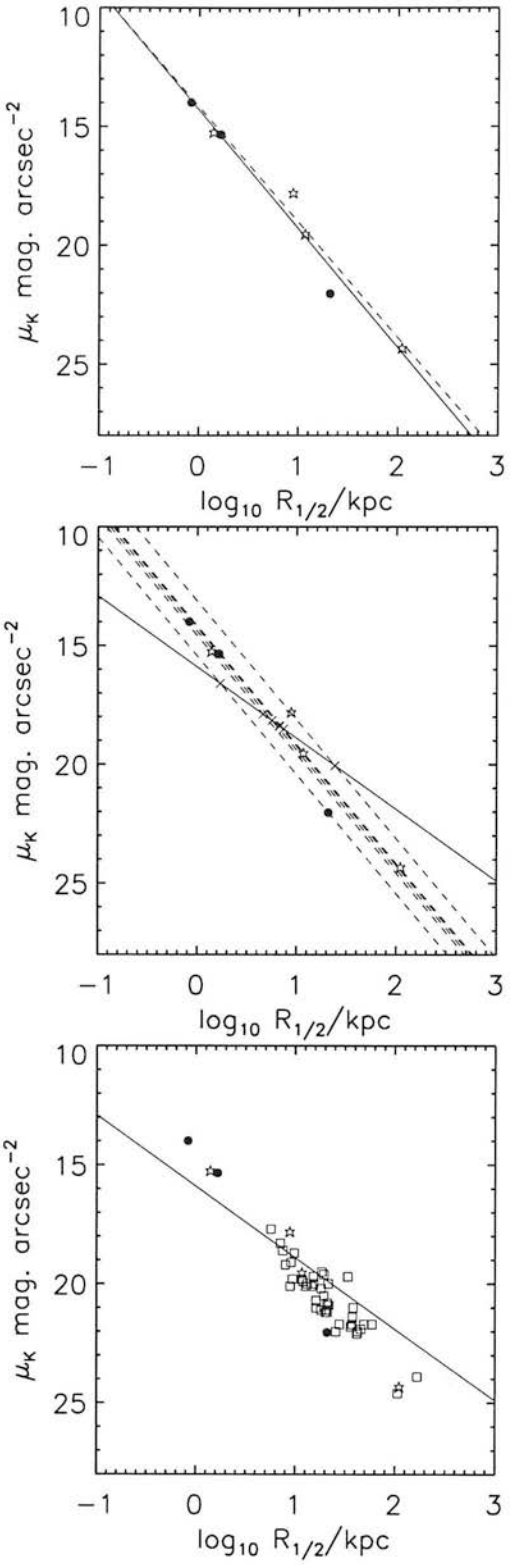

Figure 4.16: **Kormendy relation**
Top: Best-fit Kormendy relations to; the ULIRG's (circles; dashed line); the IRQSO's (stars; dotted line) and the whole sample (solid line, $\chi^2 = 1.15$).
Middle: The best-fitting Kormendy relation with slope 3 is shown (solid line, $\chi^2 = 2.37$), along with the projection of each object onto this relation, along the isophotes (slope 5).
Bottom: The current sample, with its best-fit Kormendy relation of slope 3, along with the sample of Taylor et al 1996.

Table 4.5: **The best-fit models projected onto the Kormendy relation.** The on-Kormendy projections are clearly incompatible with the best-fit models in all cases. However, given the small size of the sample, it is statistically consistent with a Kormendy relation of slope 3 ($\chi^2 = 2.37$).

Source	χ^2	$R_{1/2}$/kpc	$\mu_{1/2}$	$R_{1/2}$/kpc	$\mu_{1/2}$	χ^2	$\Delta\chi^2$
			IRQSO's				
0157+001	1.291	8.8 ± 0.2	17.9 ± 0.1	24.3	20.1	10200.0	
0829+046	0.778	11.7 ± 0.5	19.6 ± 0.1	6.7	18.4	9.7	
0923+201	1.025	110.5 ± 11.0	24.4 ± 0.3	7.4	18.5	2300.0	
1003+437	0.796	1.4 ± 0.1	15.3 ± 0.1	4.6	17.9	1560.0	
			ULIRG's				
02054+0835	0.909	$.83 \pm 0.1$	14.0 ± 0.2	5.6	18.2	980.0	
07381+3215	0.395	1.7 ± 0.1	15.4 ± 0.1	6.7	18.4	5990.0	
06561+1902	0.628	20.9 ± 7.0	22.0 ± 0.5	1.7	16.6	3050.0	

4.8.4 Unresolved Nuclear Flux

A significant unresolved component is detected in the flux from all objects bar IRAS07381+3215, suggesting the presence of an AGN is common, but not ubiquitous. IRAS07381+3215 is however found to be hosted by a massive, and quasar-capable nucleus, and it seems plausible that an AGN is present even within this object. This is certainly an interesting object that demands detailed follow-up work at other wavelengths.

The nuclear luminosity is plotted against host galaxy luminosity in figure 4.17. A clear correlation is seen (the outlier being the aforementioned IRAS07381+3215). This correlation is found to be highly statistically significant ($\rho = 0.68$, $p = 0.03$); The nuclear and host luminosities are positively correlated across the full sample. Interestingly, however, we observe no correlation with the overall 60μm luminosity (see figure 4.18).

This finding should be treated with some caution for the time being. Whilst it *suggests* a connection between the hosts and nuclei of ULIRGS, it remains possible that there is still a degeneracy between host and nuclear luminosity. In the majority of cases, and certainly for all of the ULIRG's, though, we can be confident that such a degeneracy has been overcome (see contours in figure 4.4).

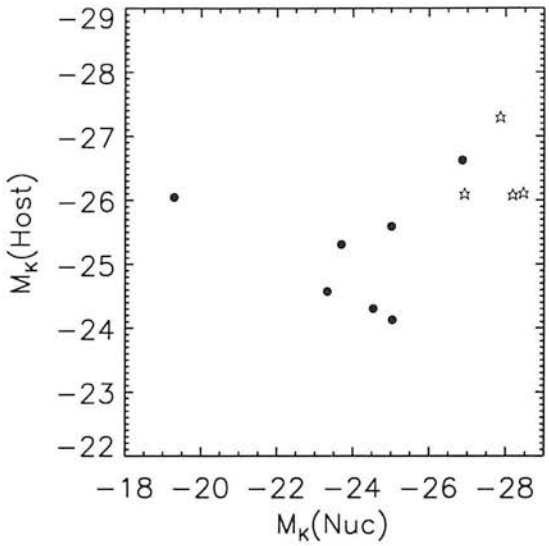

Figure 4.17: **ULIRG/IRQSO nuclear vs host magnitudes.** The nuclear and host luminosities of the full sample are positively correlated ($\rho = 0.67$) at the $p = 0.05$ level.

If we take this correlation at face value, then it shows us that AGN activity is not the full story behind the immense bolometric luminosity of the ULIRG's. It seems clear, even in this small sample, that not all of these objects will end up as luminous quasars. IRAS07381+3215 is of particular interest, as it is one of two objects studied here (IRAS02054+0835 is the other) that almost certainly *will* spend some of its later life as a quasar, and yet currently shows almost *no* sign of an optical nucleus. It seems quite plausible that for these two objects, some of the bolometric luminosity is supplied by a central supermassive black hole, but in the case of IRAS07381+3215 this black-hole is heavily obscured by the gas and dust of a vigorous ongoing, merger-induced starburst. Indeed, for all objects, it is clear that at least some of the bolometric luminosity is supplied by an AGN, but for the majority of the ULIRG's this activity is not the precursor to a quasar phase - rather it is an ongoing lower-level activity, like that observed in the Seyferts. And the host galaxies of these objects are consistent with the more normal galaxy population at large.

In figure 4.18 I present a series of plots which help to shed some light on the situation. The top

panel illustrates the overall distinction between the ULIRG and QSO samples at K. This K-band flux is split into its nuclear and host galaxy components in the other two panels, all plotted against the 60μm luminosity, L_{60}.

We see clearly that the IRQSO's are distinguished by their bright optical-IR luminosity, even though on average they have the same bolometric luminosity as the ULIRG's. This extra optical flux is contributed to both by the quasar nucleus, and also by the host galaxy flux, which correlate together, but fail to produce an increase in bolometric luminosity.

It seems that the extent of AGN activity is set by the mass of the host galaxy, but that the bolometric luminosity is not affected overall by this constraint. It evidently can be contributed to significantly through other means.

4.8.5 Colours

Here I present preliminary colour results for the sample. I have only modelled the UKIRT K-band images presented in this thesis, and not the HST V-band images of Farrah et al. (2001). They present host properties only for the 4 objects that are found to be nuclear dominated. These include 02054+0835 and 1003+437 from this study. For the time being, and until I have remodelled all of the HST images, we presume that the published V-band objects for the other objects is sufficiently close to the host galaxy value to allow for a comparison to be made. The gross host galaxy colours deduced in this naive fashion are presented in table 4.6.

For comparison, the SSP models of Jimenez et al. (2004) have been used in figure 4.20 to generate the anticipated $(V-K)$ colours for a passively evolving stellar population, with varying degrees of ongoing star formation.

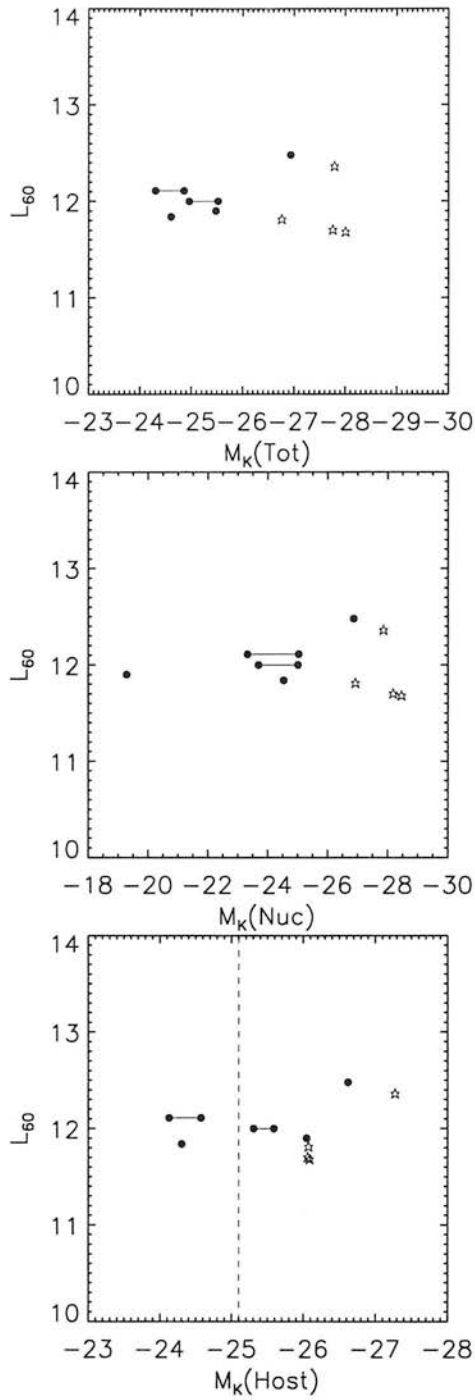

Figure 4.18: **Distinguishing ULIRG's from IRQSO's** using the 60μm luminosity, and the K-band luminosities of the resolved Hosts and Nuclei. The quasars clearly have a higher total K-band luminosities in general, and this excess is reflected most strongly in the nuclear component. Whilst the overlap in host properties is not large, it is far more significant than that in the global and nuclear properties. Two ULIRG hosts (IRAS 07381+3215 and IRAS 02054+0835) are found to be brighter than $M_K^\star = -25.1$ (dashed line). The two components of IRAS 06268+3509 fall just short of the dividing line, the bright disc at $M_K = -25.0$, the spheroidal companion at $M_K = -24.7$. Of course we do not know how the 60μm luminosity is distributed between these two sources, so the object is shown as a linked pair, as is IRAS 06561+1902. However, the most interesting object from the perspective of this study is IRAS 07381+3215. This object alone admits to no strong nuclear source, the flux being heavily dominated by a massive elliptical with $M_K = -25.5$.

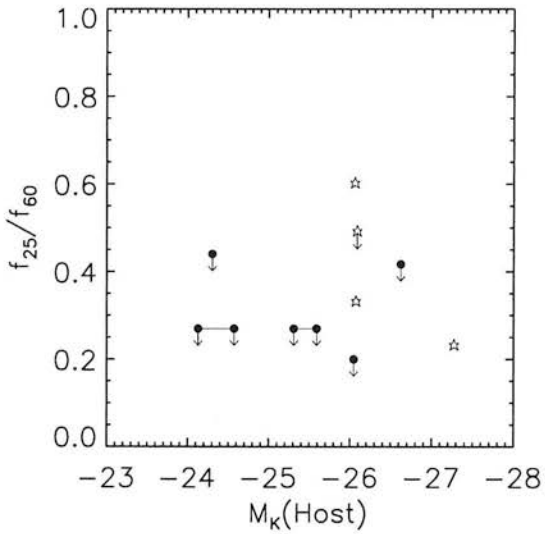

Figure 4.19: **Host galaxy luminosity against FIR "warmth".** The warmest ULIRG, IRAS02054+0835 is found to be closest to the quasars in terms of its general properties. The other warm ULIRG, IRAS10579+0438, however is found to be a lower-luminosity disc-hosted system undergoing a major merger. The quasar-capable IRAS07381+3215 is the coolest object in the sample ($f_{25}/f_{60} < 0.2$), although the quasar 0157+001 has ($f_{25}/f_{60} = 0.23$).

Table 4.6: **Bulk colours for the ULIRG hosts.** R-band data is from Dunlop et al. (2003). V-band data is from Farrah et al. (2001) and from Falomo et al (1996). Note that they only publish specific host galaxy magnitudes for 2 of the objects presented here (IRAS02054+0835 and 1003+437). For the remainder, it has been assumed that the object is host-dominated in the optical.

Source	z	$V_{\rm Host}$	$R_{\rm Host}$	$K_{\rm Host}$	$(V-K)_{\rm Host}$	$(R-K)_{\rm Host}$
	IRQSO's					
0157+001	0.163		15.8	12.8		3.0
0829+046	0.180		17.0	14.2		2.8
0923+201	0.190		17.2	14.5		2.7
1003+437	0.178	18.5		14.1	4.4	
	ULIRG's					
06268+3509	0.170	17.3		14.5	2.8	
02054+0835	0.345	18.5		15.7	2.9	
07381+3215	0.170	18.6		15.7	2.9	
10579+0438	0.173	18.5		15.9	2.7	
06561+1902	0.188	17.9		16.2	1.7	

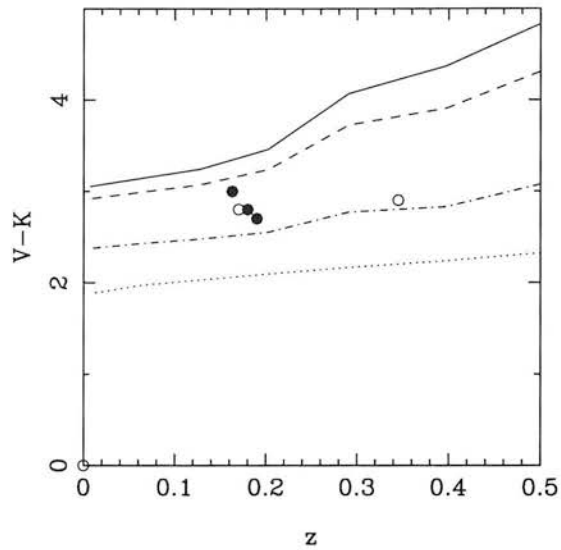

Figure 4.20: $V-K$ **colours** predicted by the models of Jimenez et al. (2004) for passive evolution (solid line), with 1% (dashes), 10% (dot-dash), and 100% (dots) lines also given.

4.9 Conclusions

I have succeeded in uncovering luminous K-band bulges in all of the IRQSO's, but only two of the ULIRG's (IRAS07381+3215, IRAS02054+0835) studied here. It should be noted that one of the IRQSO's, 1003+437 (IRAS10026+4347), is also identified as a ULIRG, and IRAS02054+0835 exhibits a quasar-like nucleus. It is clear therefore, that there is some overlap in these two populations.

An unresolved component is detected in every object except IRAS07381+3215, and furthermore the strength of this component appears to correlate with the luminosity of the host galaxy. However, the systematic increase in nuclear and host luminosity across the sample do *not* correlate with an increase in bolometric luminosity. In objects that lack a large host and powerful nucleus, there is a significant source of additional FIR luminosity. In this light, we should note that the most 60μm luminous object, IRAS02054+0835, is the one ULIRG found in a massive, quasar-capable bulge, and having a bright quasar-like nucleus. It seems plausible (likely?) that IRAS07381+3215 will also end up as a quasar at some point, and that it already channels significant quantities of energy from a

central nucleus into its 60μ flux through dust absorption. Its colour map and V-band image indicates significant ongoing star-formation, and perhaps it is just a little behind IRAS02054+0835 in a standard evolutionary sequence.

However, such a scenario does not fit many of the remaining objects, which tend to be found in less luminous, or discy systems. IRAS06268+3509 is an interesting case, containing two very luminous spirals undergoing a major merger. It seems clear that in this instance, the enormous amounts of gas and dust make for fertile ground for star-formation, although there is also a contribution from a Seyfert-like nucleus within each. Post-merger, this object may end up with an elliptical profile, but it one of the massive "boxy" ellipticals which we now tend to associate with quasars. Thus in general, the ULIRG's do *not* appear to be on their way to becoming fully-fledged quasars, nor the first-ranked massive Ellipticals that we have come to expect to find quasars situated in. They do appear to have a common power-source, and while some may end up as quite large ($\lesssim L^{\star}$) ellipticals, many have more in common with the disk galaxy population.

I conclude that the general ULIRG population is a low-redshift, and thus by necessity, scaled-down version of the SCUBA galaxies at higher redshift. Whilst it is the SCUBA galaxies that evolve to form the massive "boxy" ellipticals that we find hosting luminous QSO's, and in cD galaxies in dense cluster environments, the ULIRG's are the lower-luminosity equivalent currently going through merger and evolution toward the intermediate-mass galaxies. At the extremes these populations overlap, and we see this trend most clearly in the warm ULIRGs which are more clearly quasar-powered.

Thus there is a tumble-down; An anti-hierarchical process in which the biggest blobs evolve most rapidly, and first, so that they are complete by the present epoch. The smaller mass halos evolve more slowly, and later on, as might be supposed in an anti-hierarchical scenario.

CHAPTER 5

Conclusions and further work

During the course of my PhD I have focused on 3 distinct but related projects, which together form a coherent study of the evolution of quasar host galaxies, whilst also shedding some light on the connected issue of galaxy formation and evolution, and the role of quasar activity in shaping this process. In this final chapter I draw together the conclusions of the individual chapters to look at what has been achieved, what questions have been left unanswered, and what new questions have been posed. I then proceed to look at how these new issues can be tackled, and present a brief survey of work planned and already underway.

5.1 Conclusions

As part of a major HST study of quasar environments from redshift 0.2 to 2, I have explored the host galaxies of some of the most luminous quasars in the nearby universe ($z < 0.4$), using a 2-dimensional modelling technique developed by Dunlop et al. (1993), Taylor et al. (1996), McLure et al. (1999). I

have shown that there is no requirement for super-Eddington accretion rates in even the most extreme nearby quasars ($M_V < -27; z < 0.4$), and begun to explore the physical effects behind the nuclear-host luminosity distribution (Floyd et al. 2004). In particular I have worked to constrain the relative roles of Black Hole Mass and Fuelling efficiency in determining quasar luminosity.

Using the same techniques, I have recovered host galaxies from rest-frame U band images of matched samples of Radio Loud and Radio Quiet Quasar hosts. In concert with the V-band study of the same sample by Kukula et al. (2001) this work has given us cross-4000Å-break colour information ($U - V$), and allowed us to place accurate and unbiased constraints on the ages of quasar hosts at cosmologically significant distances.

In the final strand of work I have taken UKIRT observations designed to probe the galactic environments of a sample of Ultra-Luminous Infrared Galaxies (ULIRG's) and Infrared-bright Quasars (IRQSO's) in order to investigate the possibility of an evolutionary link between Quasars, and the ULIRG's. I have been able to recover stable host galaxy model fits for all of the ULIRG's as well as the QSO's.

5.1.1 Host galaxy demographics

It appears now quite certain that the host galaxies of quasars are simply the high-end of the luminosity function of the elliptical galaxies. The extensive body of circumstantial evidence to this effect (e.g. Dunlop et al. 2003, Nolan et al. 2001, Kukula et al. 2001, McLure et al. 1999) has been added to by this work with the first unbiased age measurement of quasar host galaxies at high redshift, through cross-lyman break ($U - V$) colours. The remarkably clear-cut conclusion from chapter 3 is that the host galaxies of all quasars are massive, passively evolving ellipticals, formed at $z \gtrsim 5$. There is a slight discrepancy, which is more significant for the RQQ's than for the RLQ's. In either case we

require less than 1% of the mass of the galaxies to be involved in ongoing star formation. However, at both $z \approx 1$ and $z \approx 2$ we find slightly bluer colours in the RQQ hosts, requiring a slightly higher rate of evolution than for the RLQ's. Further work is required in this area to enlarge the sample and place proper constraints on models of galaxy evolution, but the emerging picture is one in which the RLQ's form in only the most luminous ancient, boxy ellipticals that formed at early epochs. Quasar activity in the RQQ's can perhaps be triggered in lower-mass objects, or ones that form at lower redshift, from mergers fitting in with hierarchical models galaxy evolution. The ULIRGs also appear to fit into this picture, and are not in general *en route* to becoming quasars, nor the most massive giant ellipticals. Thus much of the powerful 60μm luminosity must arise from star-formation, although it is clear that there is a substantial contribution from AGN, but this is generally at a lower level than that expected of a quasar. Whilst a small subset are quasar capable, the majority have more in common with the Seyfert and normal galaxy population in today's Universe.

5.1.2 Quasar luminosity

In chapter 2, I demonstrated that the *maximum* luminosity of a quasar is fixed quite tightly by the host galaxy luminosity. Selecting for luminous quasars automatically picks out from amongst the most massive black holes in the universe. These in turn can only be hosted by the most massive of giant ellipticals. It was noted that such black-hole mass estimates are extremely crude, relying on an extrapolation of the black-hole / spheroid mass relation to very large masses, and great distances. However, I showed at the end of chapter 2 that the variability in the nuclear-to-host ratio, even among the most luminous quasars, is unlikely to be caused by the scatter in the black-hole / spheroid mass relation alone. It appears that the rate of fuelling, even amongst the most luminous quasars, must be a variable. It is not yet known what factors, environmental or specific to the black hole, affect this

fuelling rate, and this will be a key area in both observational and theoretical research in the coming decade.

5.1.3 The ULIRG connection

In chapter 4, I demonstrated that there was a significant unresolved nuclear component present in K-band for all the ULIRG's as well as the QSO's. This could be attributed to a small region of intense star-formation in the circum-nuclear region. However, we find that the nuclear flux is significantly correlated with that of the host bulk, across the 9-object ULIRG-IRQSO sample. This is an interesting result, suggesting that whilst the ULIRG's as a population do not seem to have the same requirement for massive spheroidal hosts as the quasars, they do share a common fuel source: accretion onto supermassive black-holes.

Any black hole (and hence any galaxy) is, in principle, capable of generating AGN activity at some level. The fact that, as a class, the ULIRG's were found to be hosted by such different galaxies to the QSO's forces us to conclude that the ULIRG's are not an evolutionary stepping-stone on the road to becoming quasars, but rather are scaled-down versions, perhaps more akin to the Seyferts. From these morphological results, I conclude that the activity in the ULIRG's studied here must be from somewhat smaller black holes than is the case for a typical quasar. We still need to explain the relatively flat distribution in $L_{60\mu m} - M_V$. It is possible that in the dusty environment of a ULIRG we have an extremely efficient fuelling mechanism, allowing us to generate the maximum possible energy output from the central black hole.

5.1.4 Galaxy Evolution

The quasar hosts, and especially those of the RLQ's appear to originate from one major ancient and short-lived starburst, potentially expelling the remaining gas and dust of the ISM through galactic superwinds. We might therefore expect to find that such galaxies, if and when they later become active, have relatively unobscured active nuclei. The RQQ hosts appear to undergo somewhat more rapid evolution, and are perhaps unable to generate such powerful winds. This would be true of smaller galaxies, galaxies that form later, or that take a longer time to form. However, there appears to be no significant difference in the luminosities of RLQ and RQQ hosts.

The ULIRG's are still undergoing major evolutionary change at the epoch of observation. The bulk colours appear to be somewhat bluer than those of an ancient well-evolved population, and show significant active regions of star-formation over and above this. At the high-mass extreme, the population overlaps the QSO and massive elliptical population, and by association, with the SCUBA sources.

5.2 Outstanding Questions

There is now strong evidence that AGN activity plays a key role in the evolution of most galaxies. By studying the host galaxies of the quasars, we can obtain crucial insight into the evolution of the upper end of the galaxy luminosity function, and investigate whether environment plays any role in determining nuclear activity. Furthermore, it allows us to probe the evolution of a population of objects through most of the history of the Universe, and is therefore a valuable observational tool in refining our cosmological world view.

Key questions that follow on directly from this work include:

- Do the black-hole and host galaxy form and grow in tandem or do they have different origins and mechanisms? Exploring whether the relationship between black-hole mass and host galaxy luminosity evolves with redshift.

- What is the impact of powerful radio sources on galaxy evolution? Do powerful radio sources simply form earlier than other galaxies, or does the host galaxy environment in some way affect the growth of radio lobes?

- Are the ULIRGs on their way to forming fully-fledged quasars, or do they represent a separate epoch of galaxy - black-hole co-evolution?

An important step in galaxy studies will be the establishment of accurate, independent measures of black hole mass. Through this we can more realistically constrain the physics of accretion onto supermassive black holes. Work has been done with Hβ, MgII, and other BLR linewidths, and although these are a good next step, little cross-correlation has been performed, and we must remain a little sceptical about the accuracy of quoted black-hole masses.

Is there a dense circum-nuclear disc, feeding and obscuring the black hole, or is it simply the combined effect of an extremely dusty ISM? In almost all of the modelling residual images for the ULIRG's we see an excess of circum-nuclear flux. More often than not this is attributable to variability in the PSF. Improved observations will help us tell whether this is a genuine artifact, or simply "flies in our eyes".

To confirm the firm link between the ULIRG, QSO and SCUBA source population would be an important result. In addition, the discovery of large volumes of dust in quasar hosts would solve any fuelling issues, and establish an explicit link between these objects and a more dusty, enshrouded past.

5.3 Future and ongoing work

In combination with observations at different wavelengths, the 2D deconvolution of host galaxy from nucleus offers a powerful tool in exploring the evolution of host galaxies, and shedding light upon the evolution of galaxies in general. In the coming years, I plan to develop my studies of quasar hosts, but also to broaden my focus to encompass galaxy evolution in general.

At present I have work planned or in progress in four directions:

- Expansion of the quasar host galaxy dataset.
- Investigation of the reasons behind the radio-loudness dichotomy.
- Independent measurements of black-hole masses to better understand the process of accretion.
- More detailed examination of the host galaxies, in order to constrain models of galaxy evolution.

5.3.1 Ongoing work: Mining the HST archive.

Developing a large sample of Quasar Host Galaxies is an essential step toward resolving once and for all the relative roles of fuelling and black hole mass in determining quasar luminosity. This work requires amassed HST data, and will allow us to tighten constraints on host galaxy parameters, and will help to resolve discrepancies between the work of different groups, of which a small number still exist The 2-dimensional modelling code developed during my PhD places me in an ideal position for this, as it is already optimised for HST data. I have started this work with a 6-month funded archival project at STScI, starting January 2004. In the process, I plan to generate a more complete sample of nearby luminous quasar host galaxies ($z < 0.5, M_V < -25$), using additional observations to fill in the gaps. For luminous quasars at least, HST data is essential for this work, as the seeing problems encountered in ground-based studies have been demonstrated to bias the results.

5.3.2 Origins of radio-loudness in quasars.

The radio-loudness dichotomy remains one of the most intriguing puzzles in AGN astrophysics. As yet, there is no well-understood mechanism for driving radio-loudness. Furthermore, results from the FIRST survey have triggered debate as to whether the dichotomy even exists. The controversy arises from the sensitivity of different surveys to extended as opposed to core radio emission.

We now have a well-defined set of radio-loud and radio-quiet objects at a range of redshifts, which offer a baseline for the continued study of the origins of radio-loudness. These are some of the best-studied samples of quasars in existence, imaging and spectroscopy together giving information on host galaxy, quasar and black hole properties. We are now embarked on a project to obtain radio fluxes and radio source structure for each quasar (both RL and RQ) to take a fresh look at the factors underlying radio loudness. This project makes use of the VLA, VLBA and MERLIN.

Radio detection of RQQ's:

Franceschini et al. (1998) have shown that there is a correlation between black hole mass and the bulk radio luminosity in nearby inactive galaxies. There has been limited work that suggests that this trend is also seen in active galaxies (for example Kukula et al. 1997, 1998, Dunlop et al. 2003). We now need to push out to the most luminous active galaxies, and search for correlations between black hole mass and radio emission. The first stage is to get detections for all of our radio-quiet objects. We were awarded limited time on the VLA in 2003 to begin a high-sensitivity study to detect all of the RQQ's in our sample. This data awaits reduction.

VLBI

The next stage is to resolve the radio flux into that associated with the nuclear region and jets, and that associated with ongoing star formation in the host galaxy. We have very recently obtained VLBI

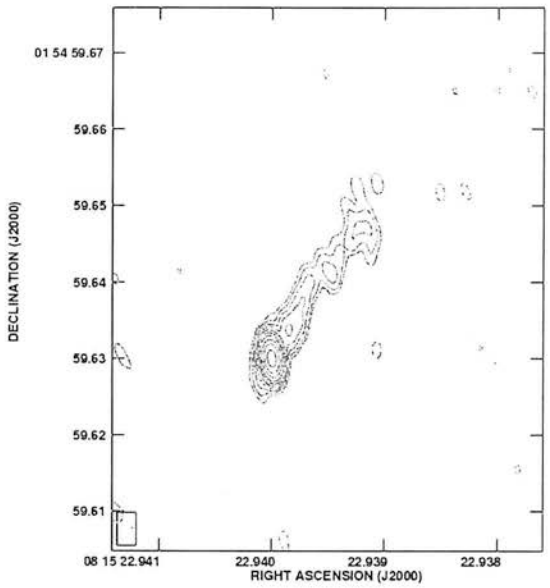

Figure 5.1: **VLBI radio imaging** of the RLQ PKS0812+020 at $z = 0.402$.

imaging of some of the Radio Loud objects in our intermediate and low redshift ($z = 0.2$ and 0.4) HST samples. This data has been partially reduced, and an example of the resulting images is presented in figure 5.1. This work has been carried out by Ignas Snellen, and is included here for completeness. We will determine the influence of Doppler boosting on the correlation between black hole mass and radio power, and for the first time investigate the dependence of the properties of the inner parsec-scale jets on M_{BH}. As the sample of VLBI and host-galaxy-imaged quasars grows, this will shed new light on the physics of jet production.

5.3.3 Black hole mass

It is essential to the continued study of quasar hosts, and quasars more generally, that we obtain accurate estimates of black hole mass independently from host galaxy studies. Much work has been done already by for example McLure & Dunlop (2002) in measuring the linewidths of emission lines in the broad line region (e.g. Hβ). I intend to perform similar observations on the $z \approx 0.4$ sample

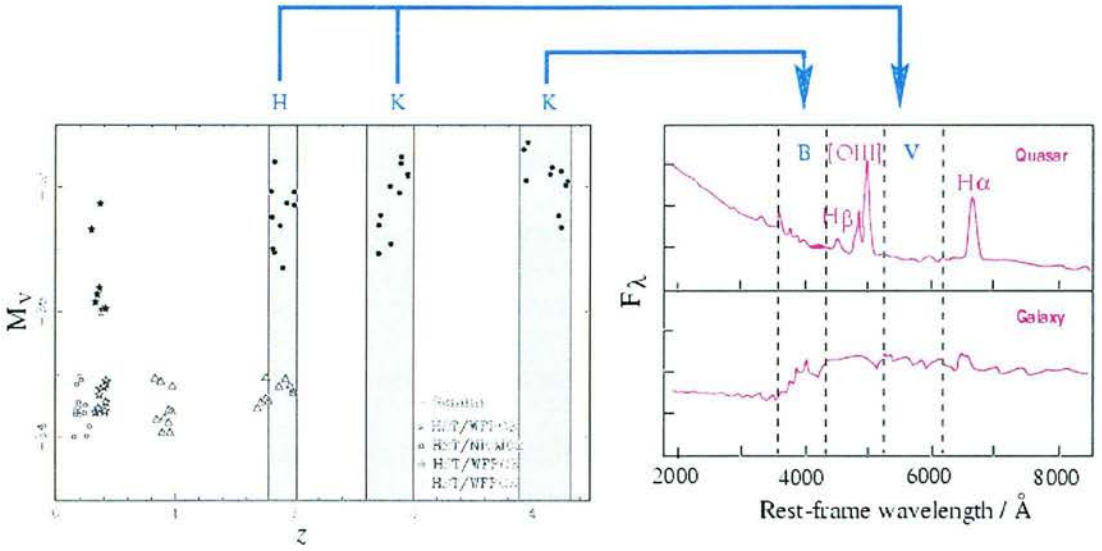

Figure 5.2: **Out to** $z \approx 4$ illustrating the filter selection and samples to be observed, in the context of our completed HST imaging studies at lower redshift. The filled stars show the comparison sample of low-redshift luminous quasars, studied in chapter 2. The open symbols show the lower-luminosity samples, including those at $z \approx 1$ and 2, studied in chapter 3 (triangles).

studied in my thesis.

5.3.4 Nature of the host galaxy.

One of the concerns that have been raised from the finding that quasars are hosted by giant ellipticals is the issue of fuelling. There is a popular conception that giant ellipticals are red, dead, and largely dust-free. Thus how can there be a fuel supply for the central black-hole? We know that radio galaxies are extremely dusty objects, yet they are found to be hosted by the same population of ellipticals as the RLQ's.

Molecular radio emission:

I intend to test whether there exists a significant difference between the molecular CO and HII emission from the host galaxies of quasars at $z \approx 0.2$ and 0.4 and a control sample of inactive ellipticals,

chosen to match the quasar hosts in terms of their optical properties. This work will require sensitive single-dish observations (e.g. IRAM).

Stellar Populations and Host Galaxy ages.

We have obtained a substantial allocation of Gemini North to perform K-band imaging of quasars at $z > 2$ (figure 5.2). We intend to follow up with HST/ACS observations in cycle 13 to obtain multi-band colours for the hosts and thus investigate their stellar composition. In addition, I intend to carry out U-band observations of the high-luminosity sample at $z = 0.4$ from my thesis, allowing $U - V$ host galaxy colours to be measured, and compared with galaxy evolution models. This is vital for making full sense of the imaging studies and relating host galaxies to the general galaxy population.

APPENDIX A

Quasars Images at z=0.4

For each quasar we show the final reduced *I*-band (F814W/F791W) HST image (top left), the best-fit model (either pure bulge or pure disc) to the quasar image (top right), the model host galaxy only (centre left) and the model-subtracted residuals (centre right). The bottom figures represent the χ^2 distribution (left) and the object with the best-fitting nuclear component removed, in order to illustrate the underlying host light.

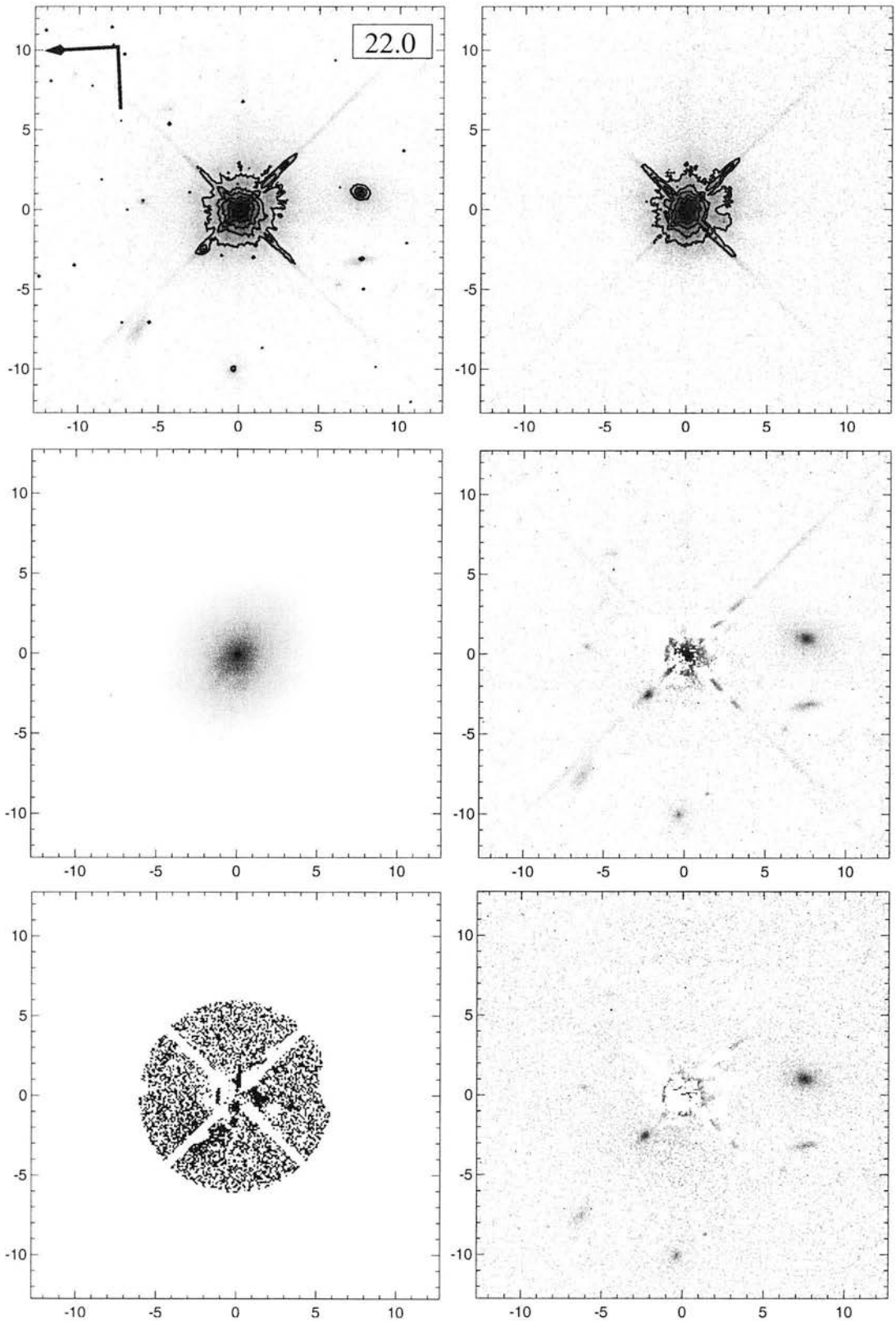

Figure A.1:
The Radio-Quiet Quasar 0624+691

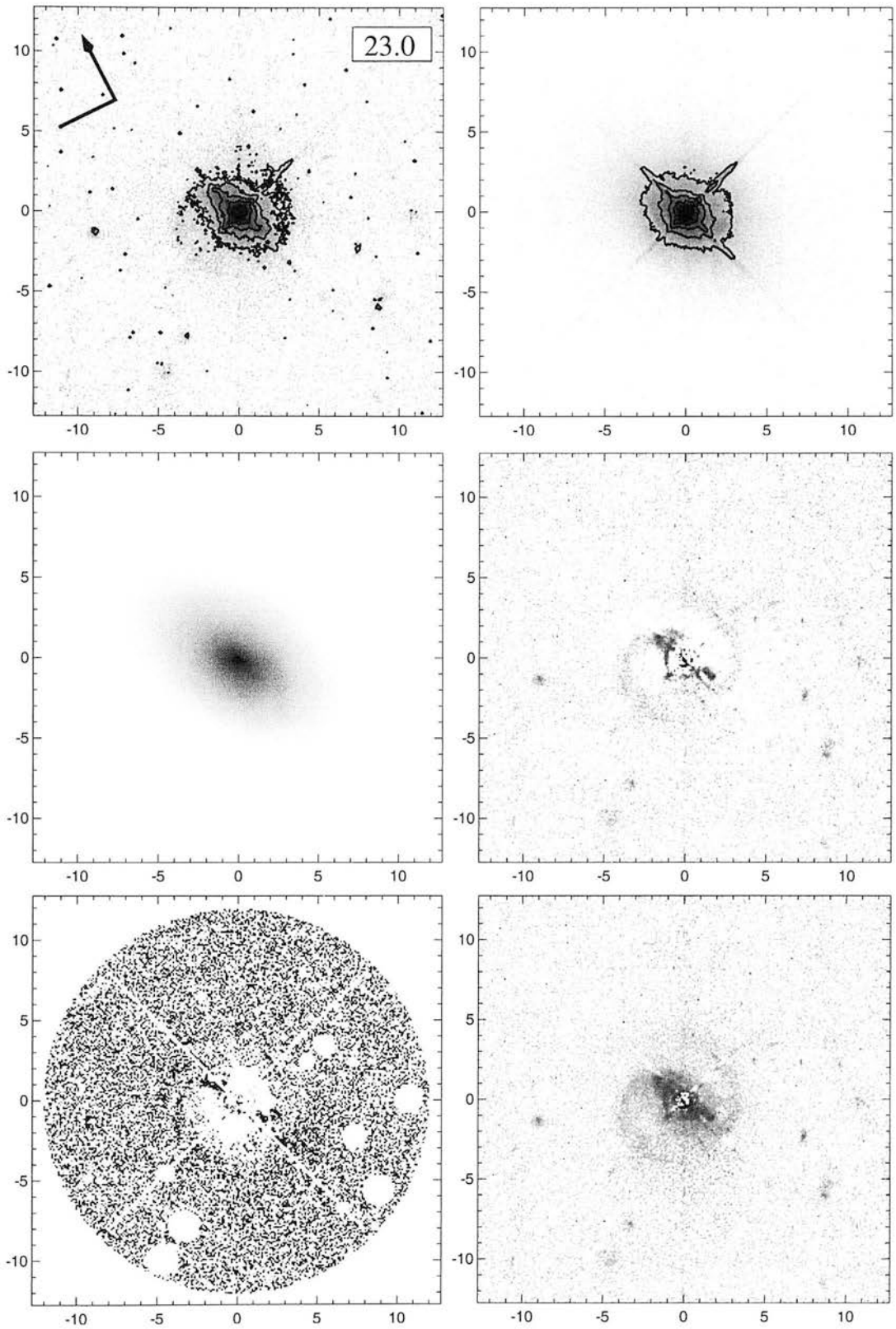

Figure A.2:
The Radio-Quiet Quasar 1001+291

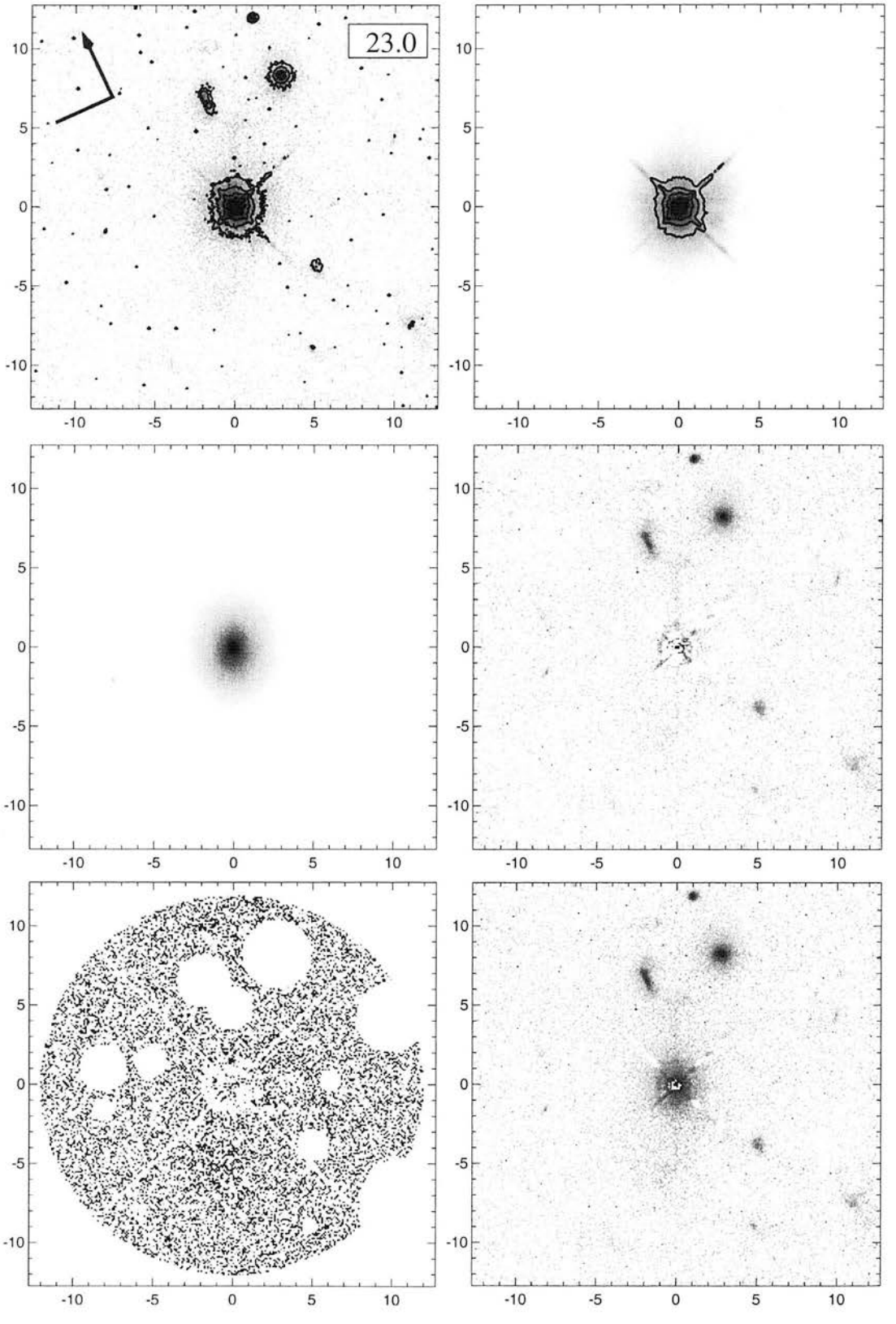

Figure A.3:
The Radio-Quiet Quasar 1230+097

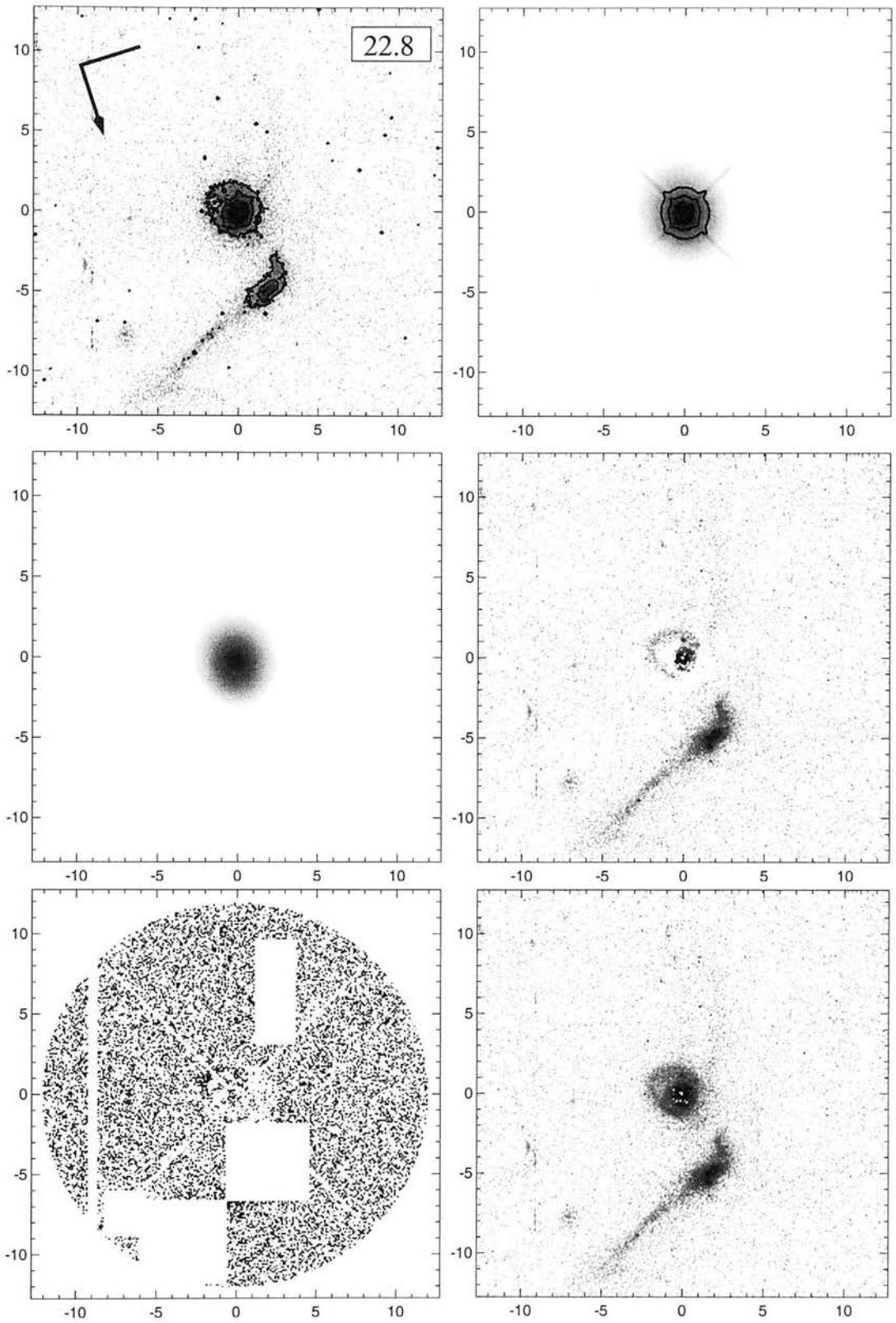

Figure A.4:
The Radio-Quiet Quasar 1239−041

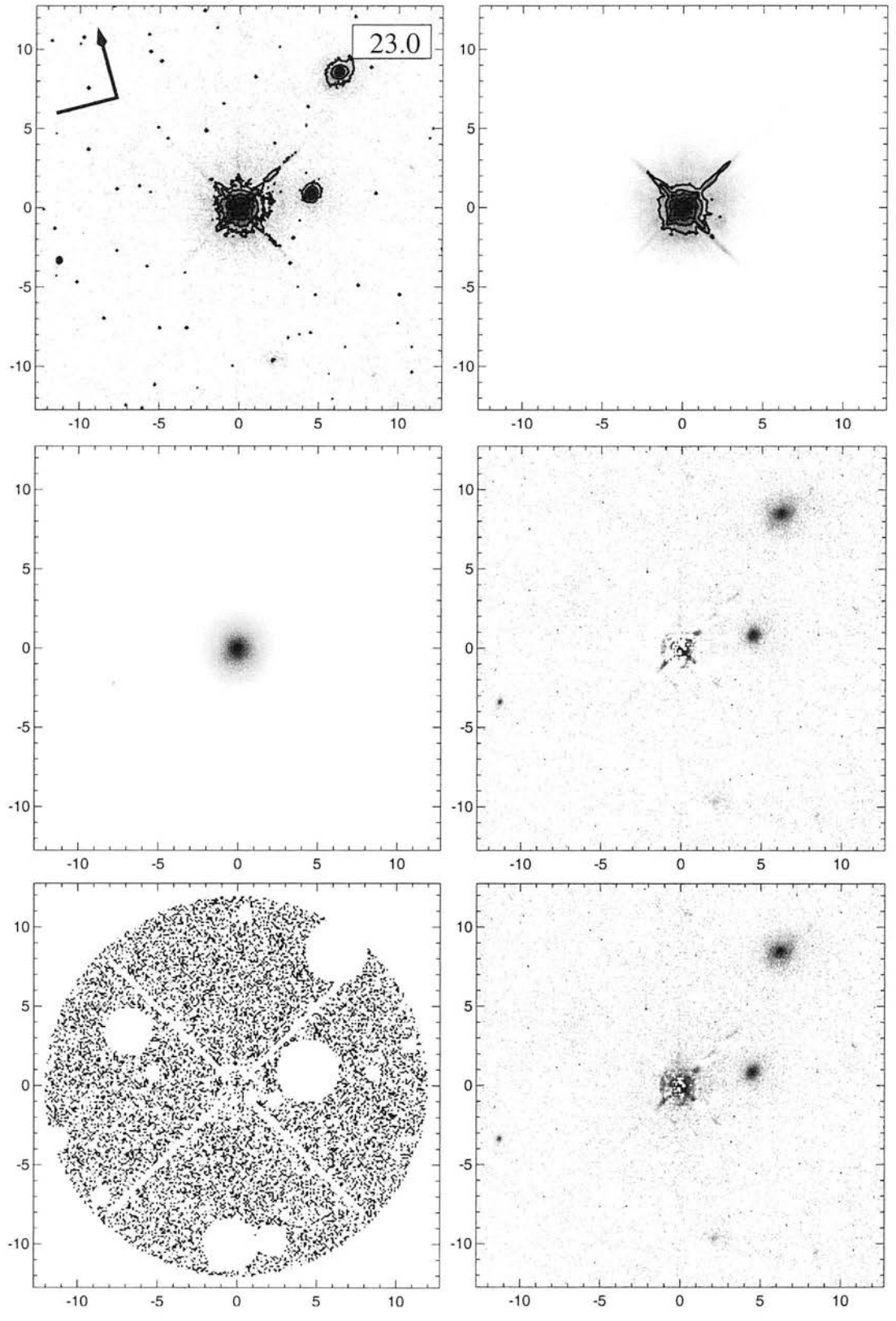

Figure A.5:
The Radio-Quiet Quasar 1252+020

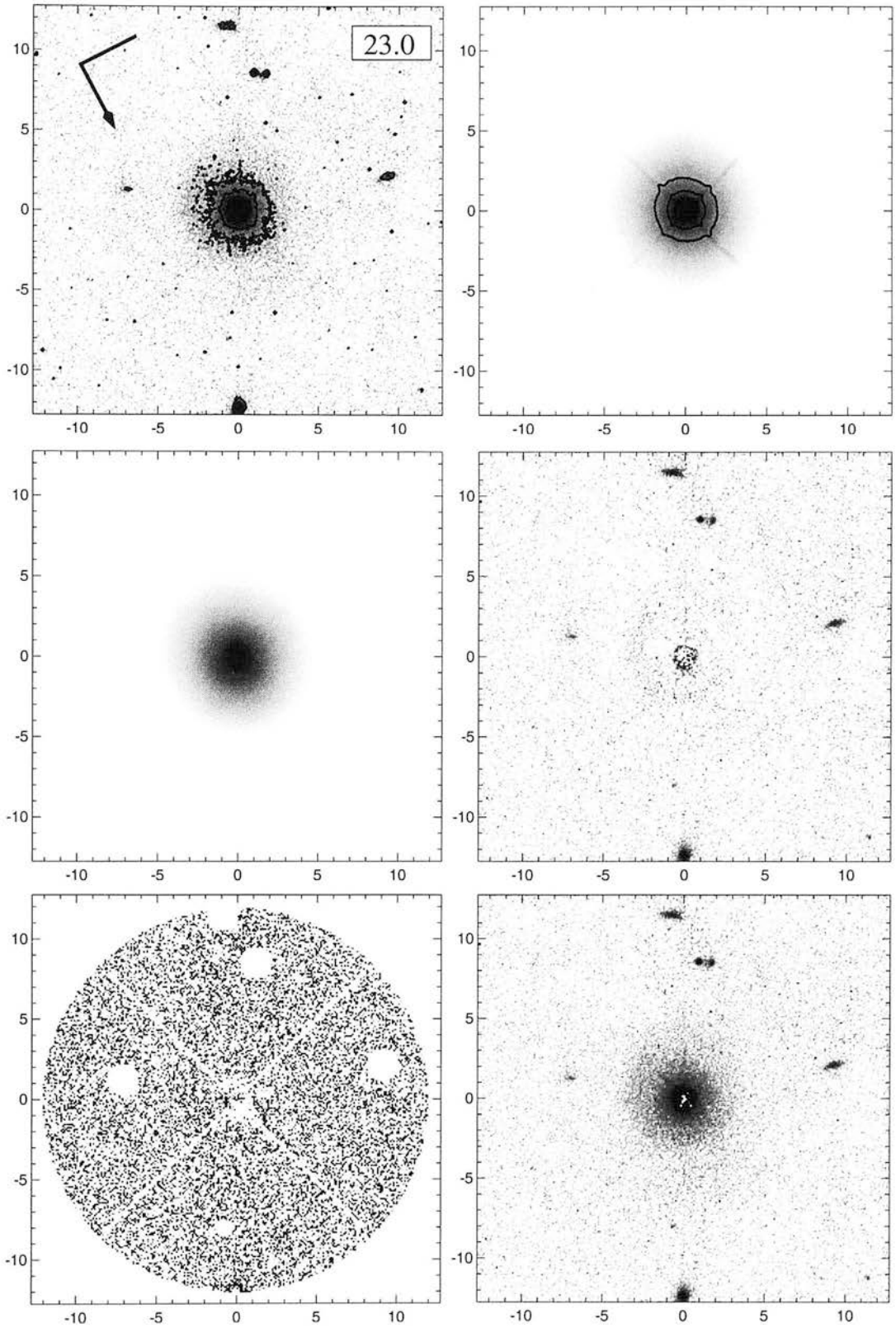

Figure A.6:
The Radio-Quiet Quasar 1257+015

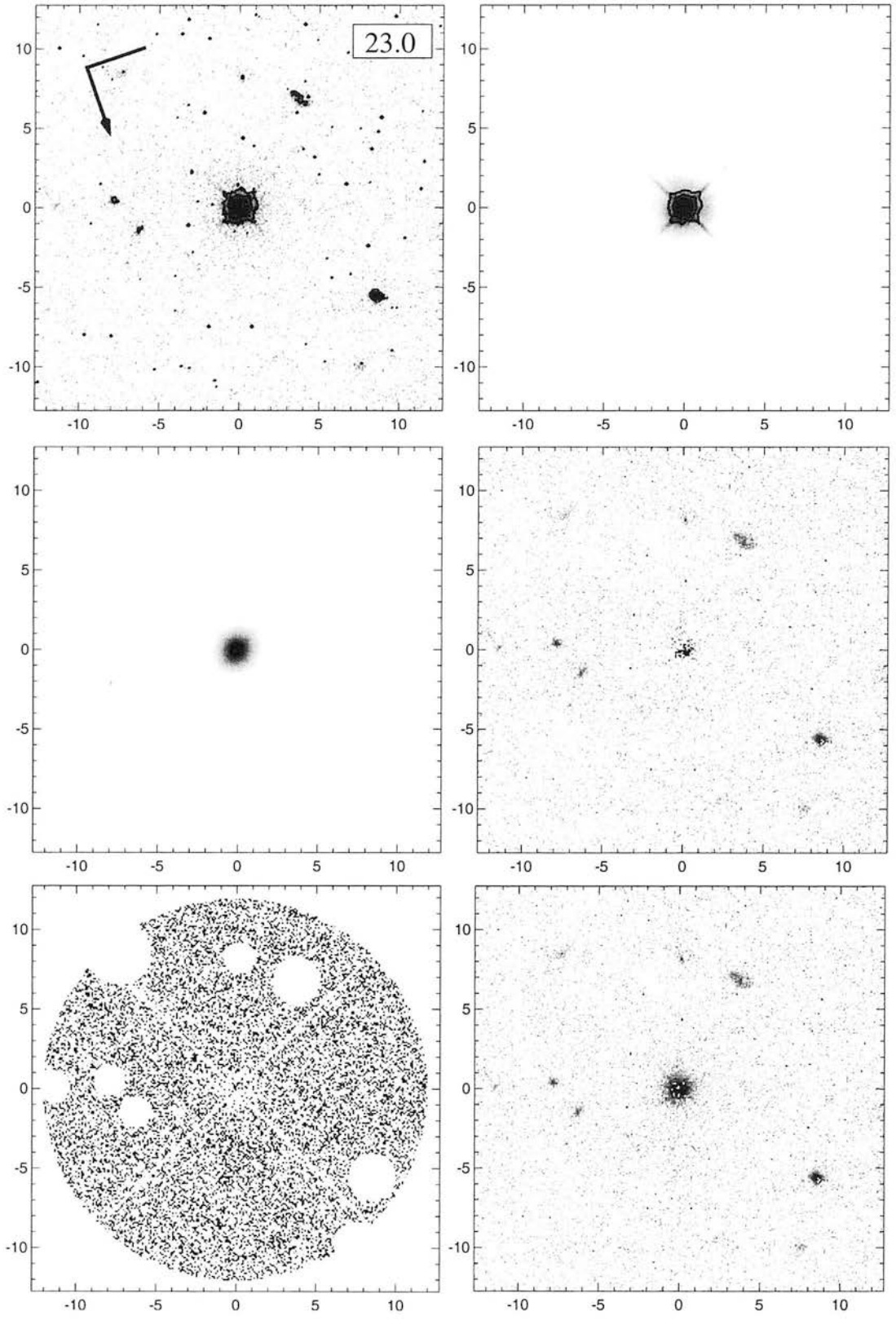

Figure A.7:
The Radio-Quiet Quasar 1258−015

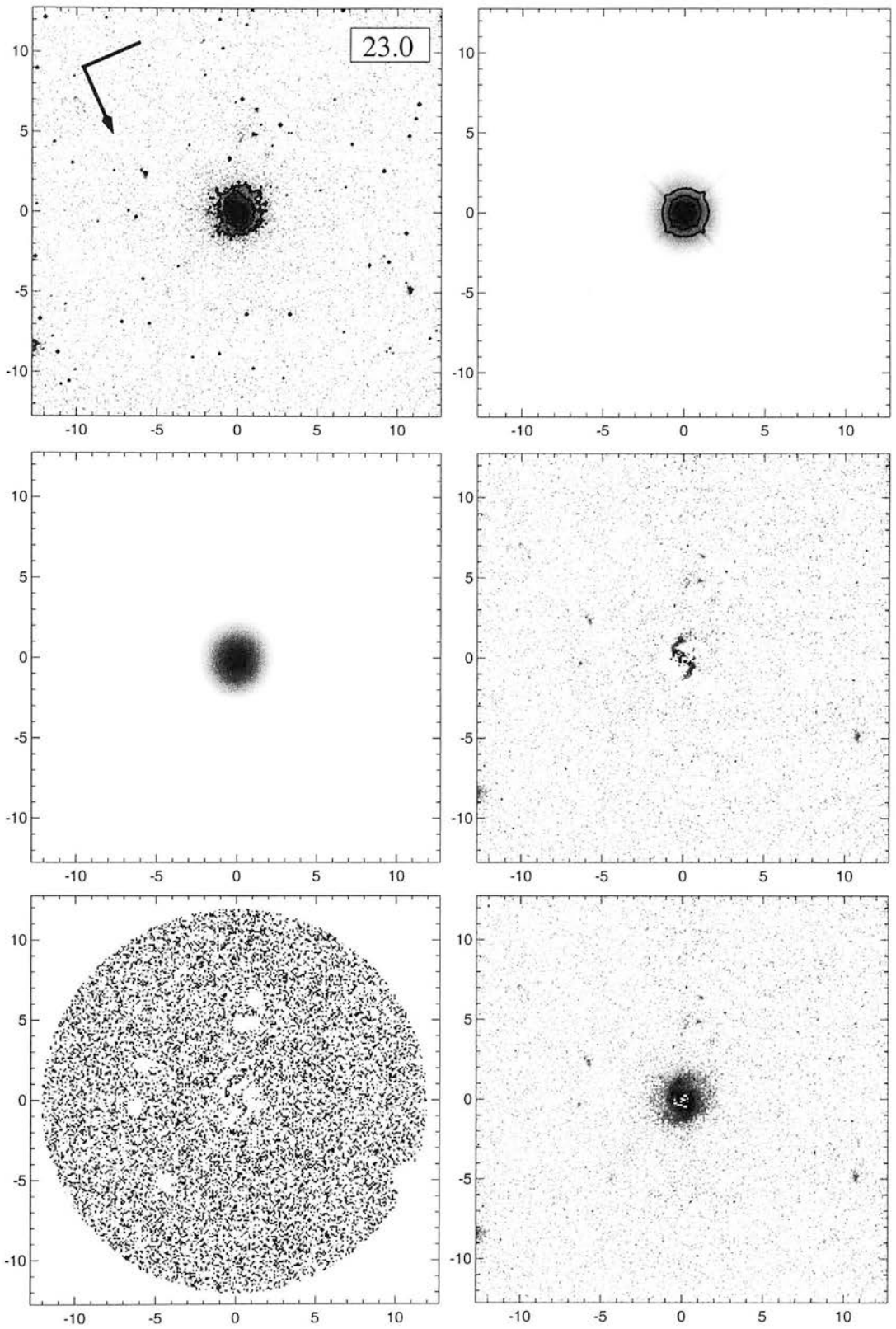

Figure A.8:
The Radio-Quiet Quasar 1313−014

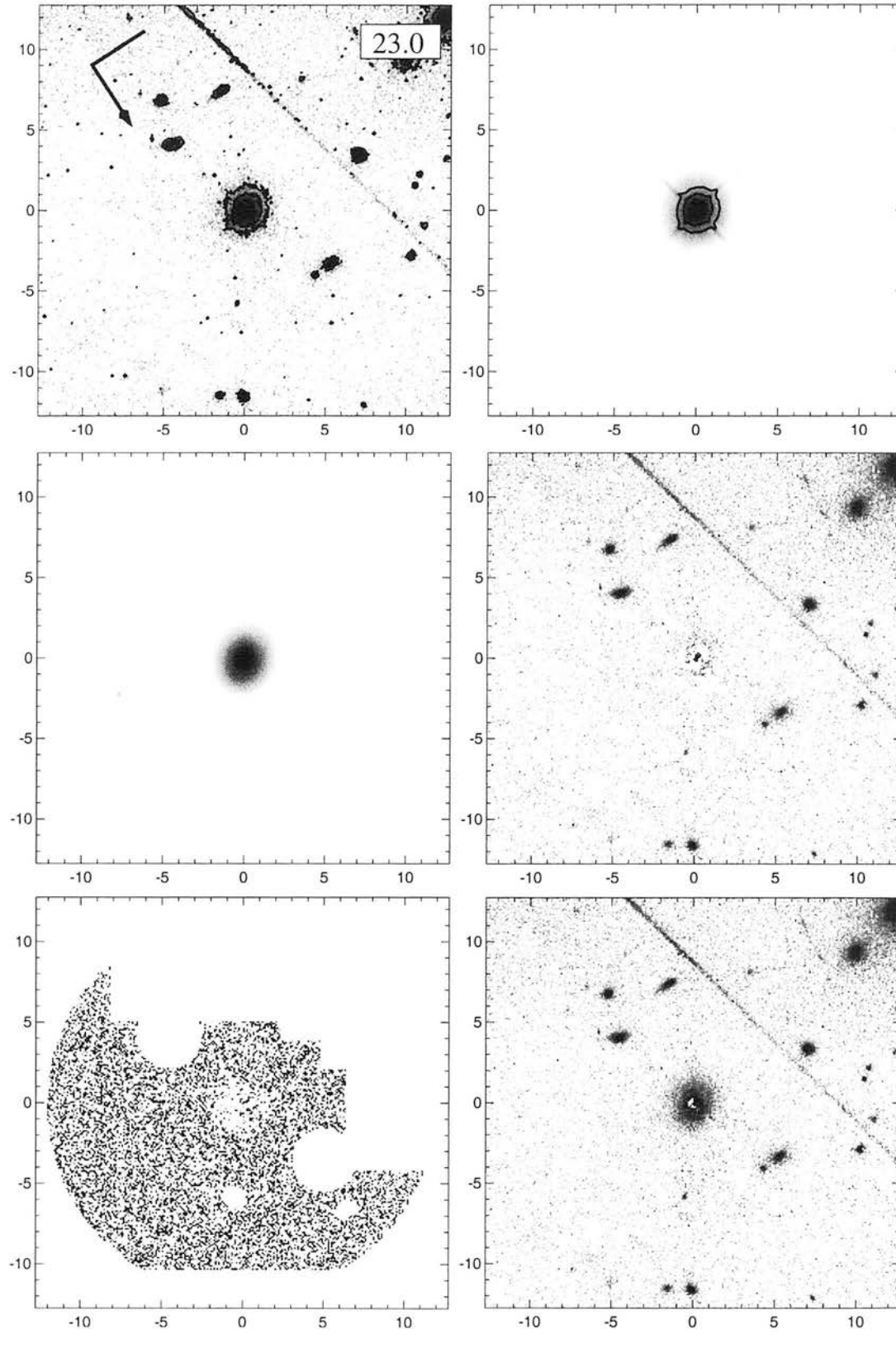

Figure A.9:
The Radio-Quiet Quasar 1400−024

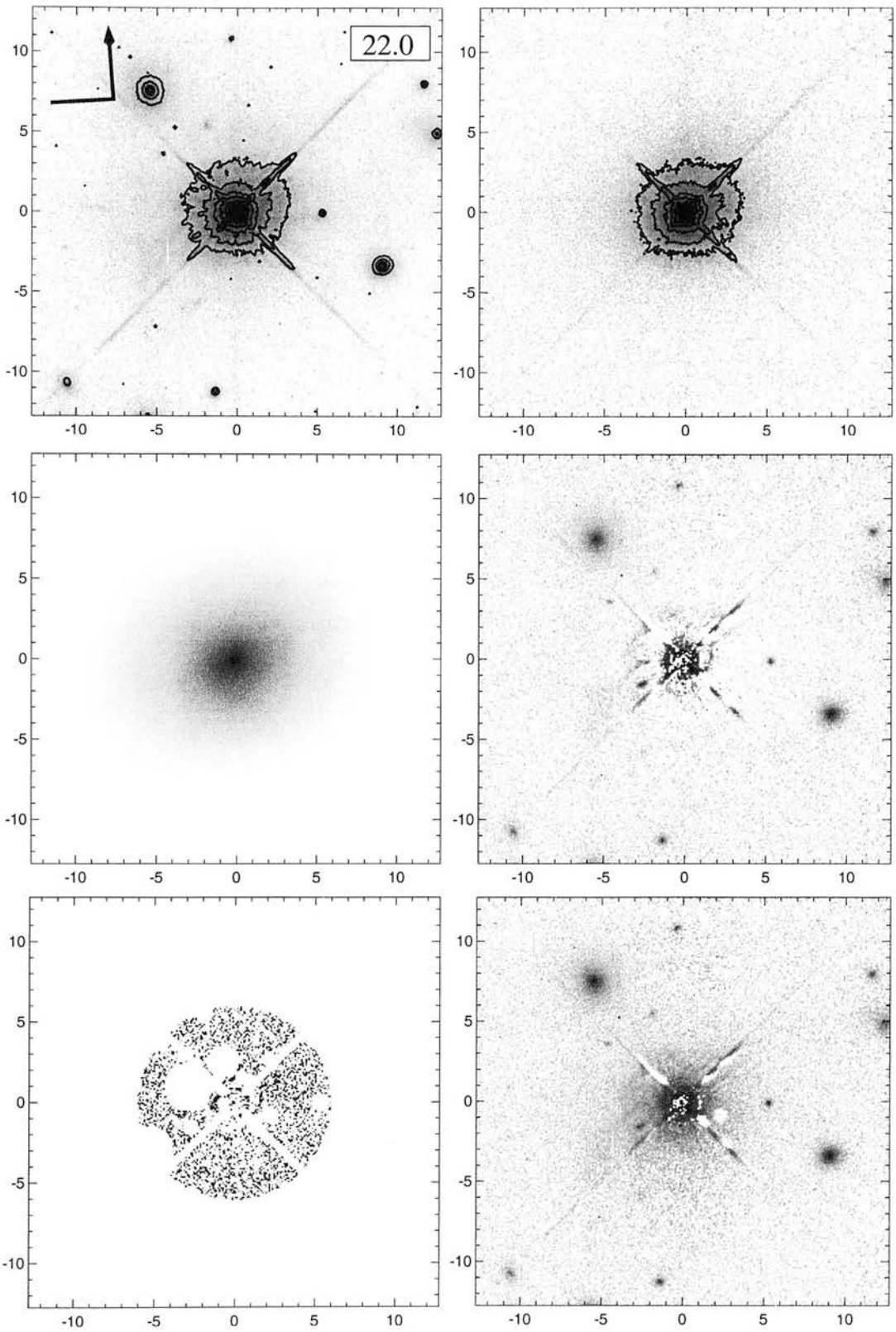

Figure A.10:
The Radio-Quiet Quasar 1821+643

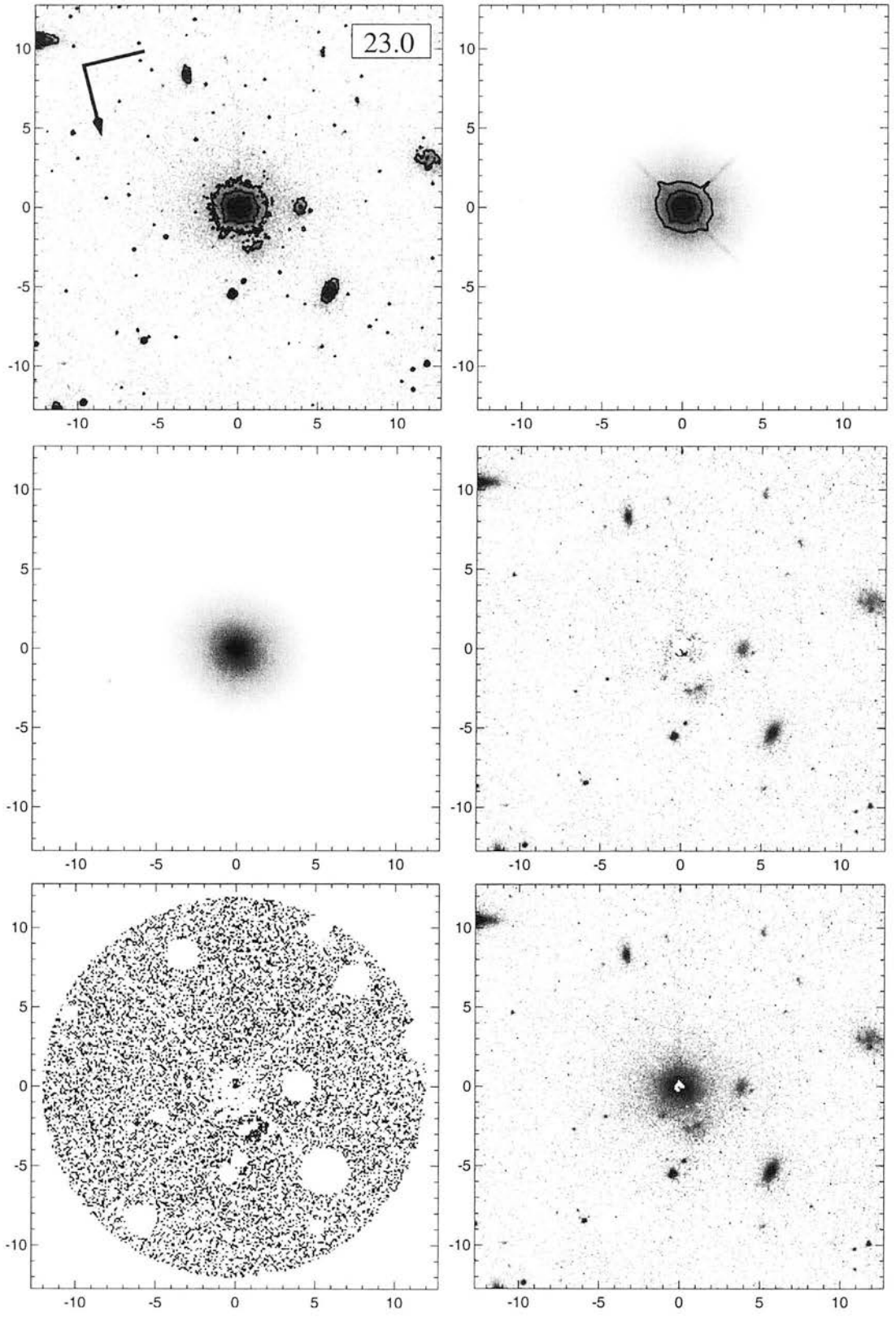

Figure A.11:
The Radio-Loud Quasar 0031−707

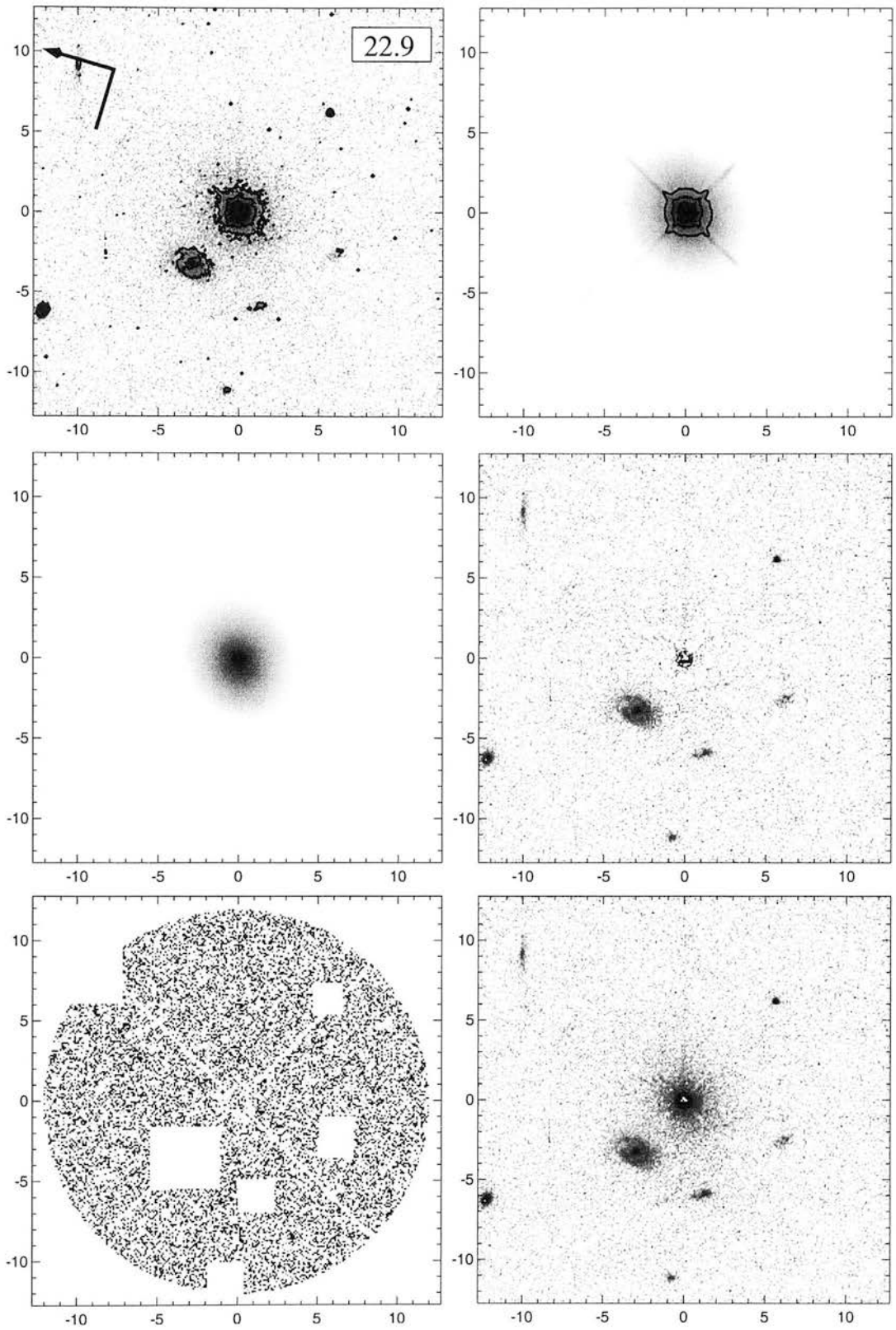

Figure A.12:
The Radio-Loud Quasar 0110+297

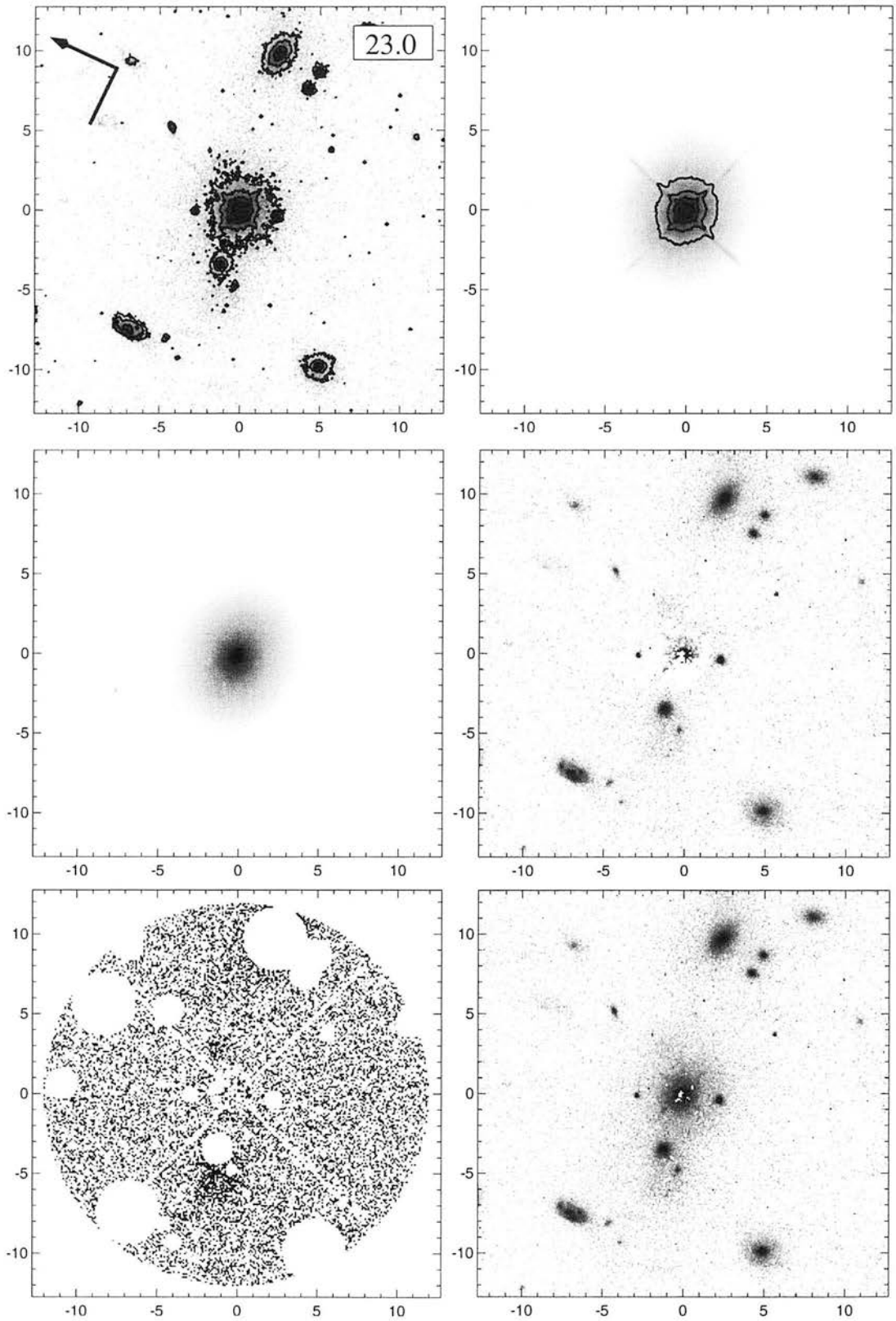

Figure A.13:
The Radio-Loud Quasar 0812+020

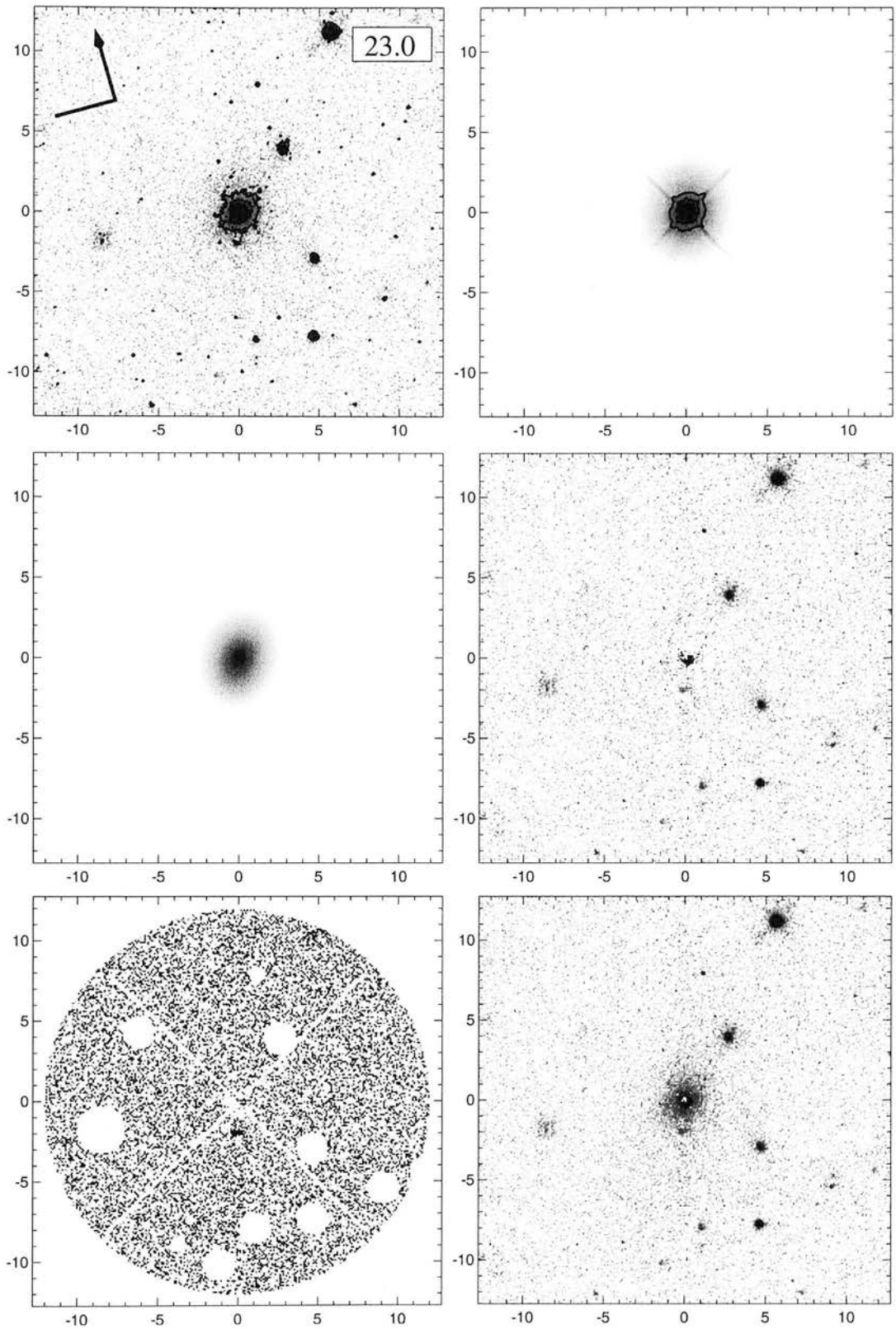

Figure A.14:
The Radio-Loud Quasar 1058+110

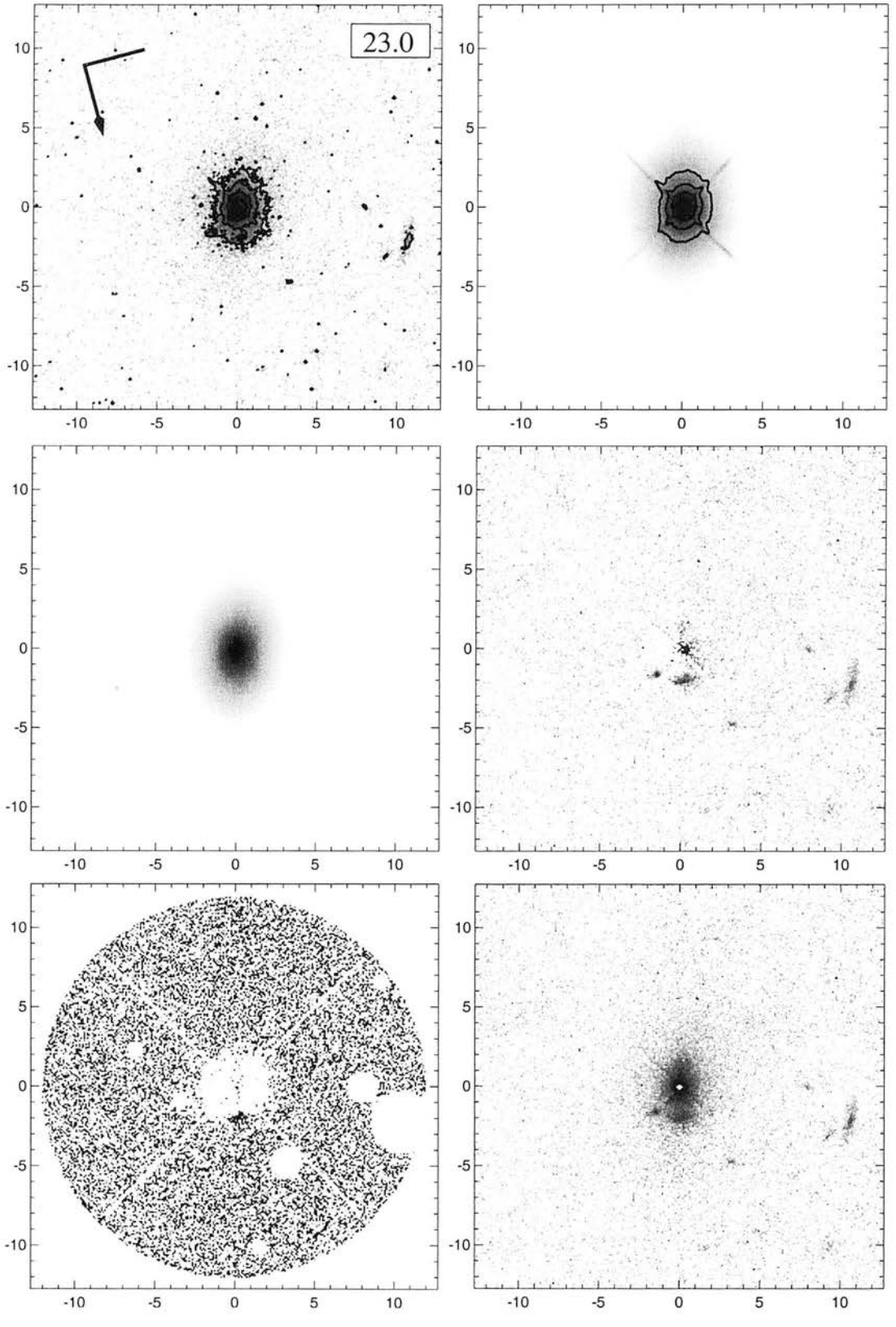

Figure A.15:
The Radio-Loud Quasar 1150+497

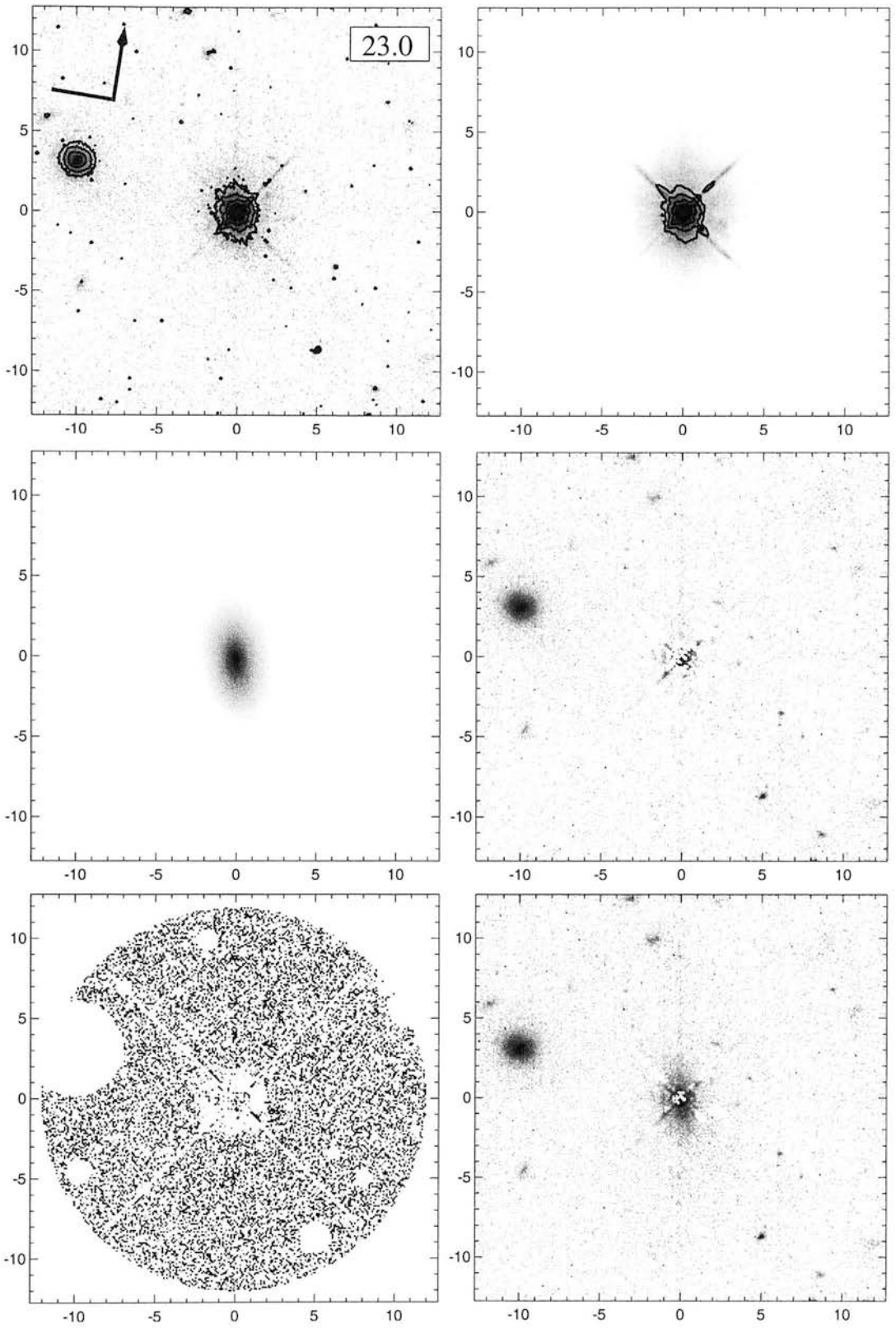

Figure A.16:
The Radio-Loud Quasar 1208+322

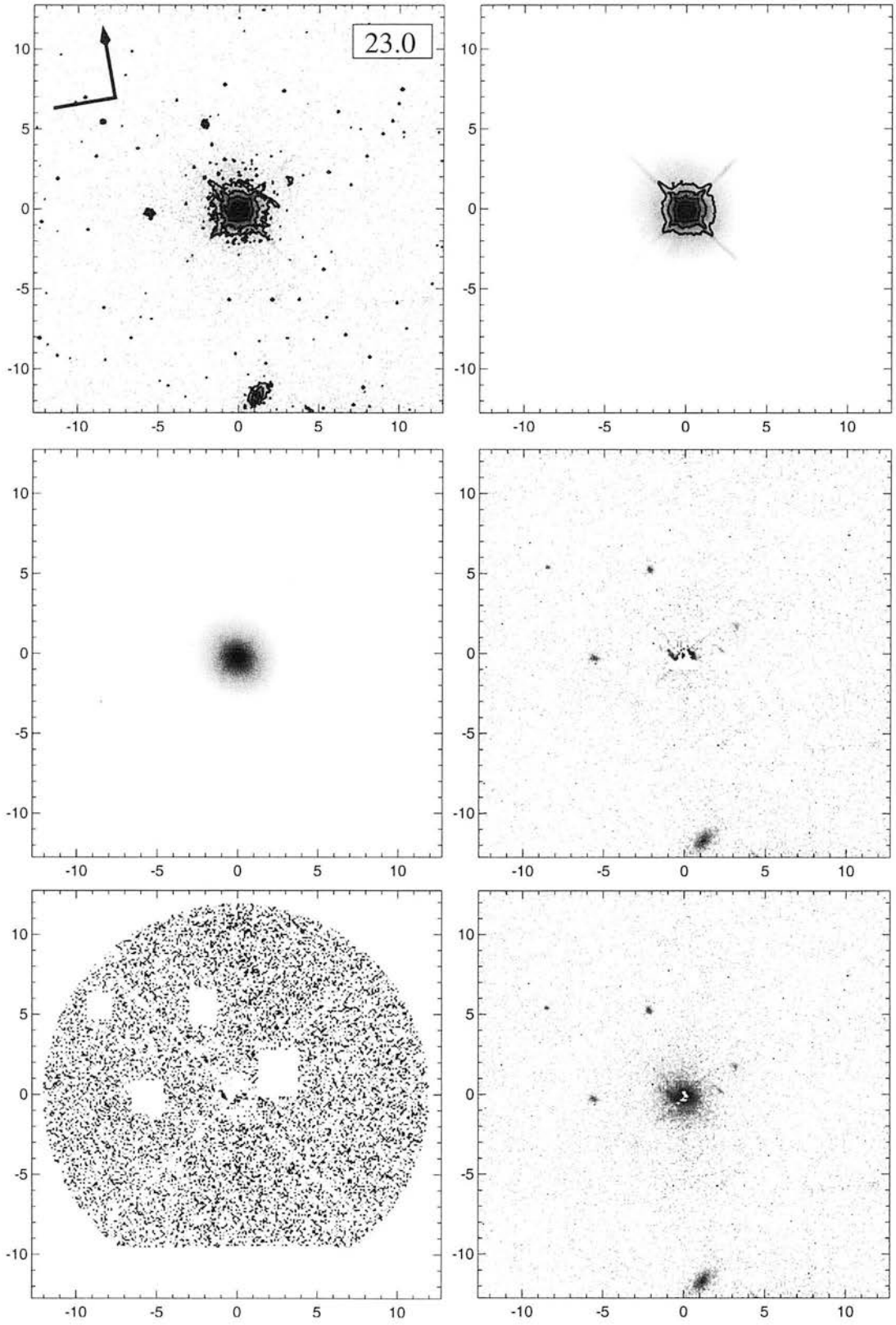

Figure A.17:
The Radio-Loud Quasar 1233−240

APPENDIX B

Quasar images at z=1

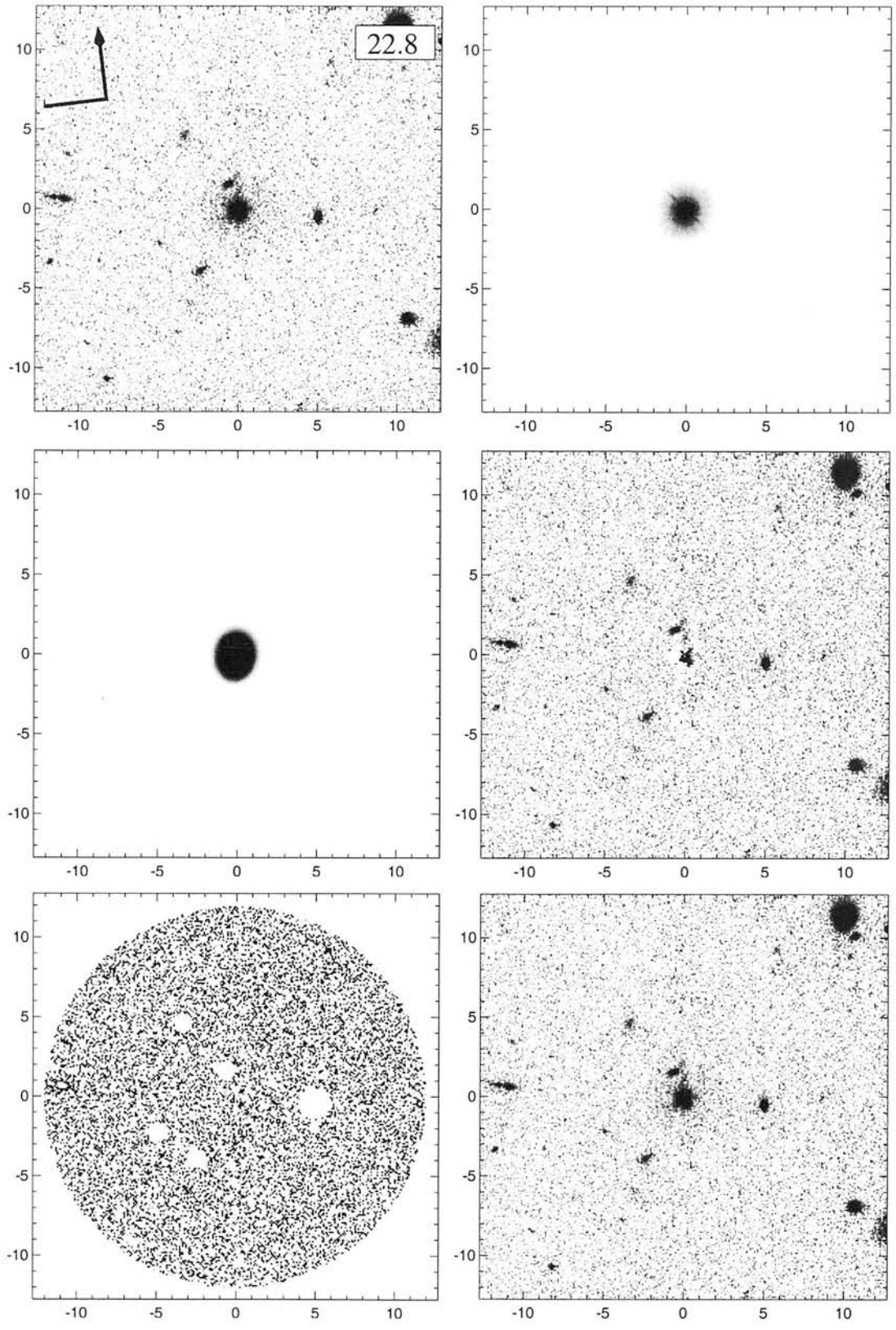

Figure B.1:
The Radio-Quiet Quasar BVF247

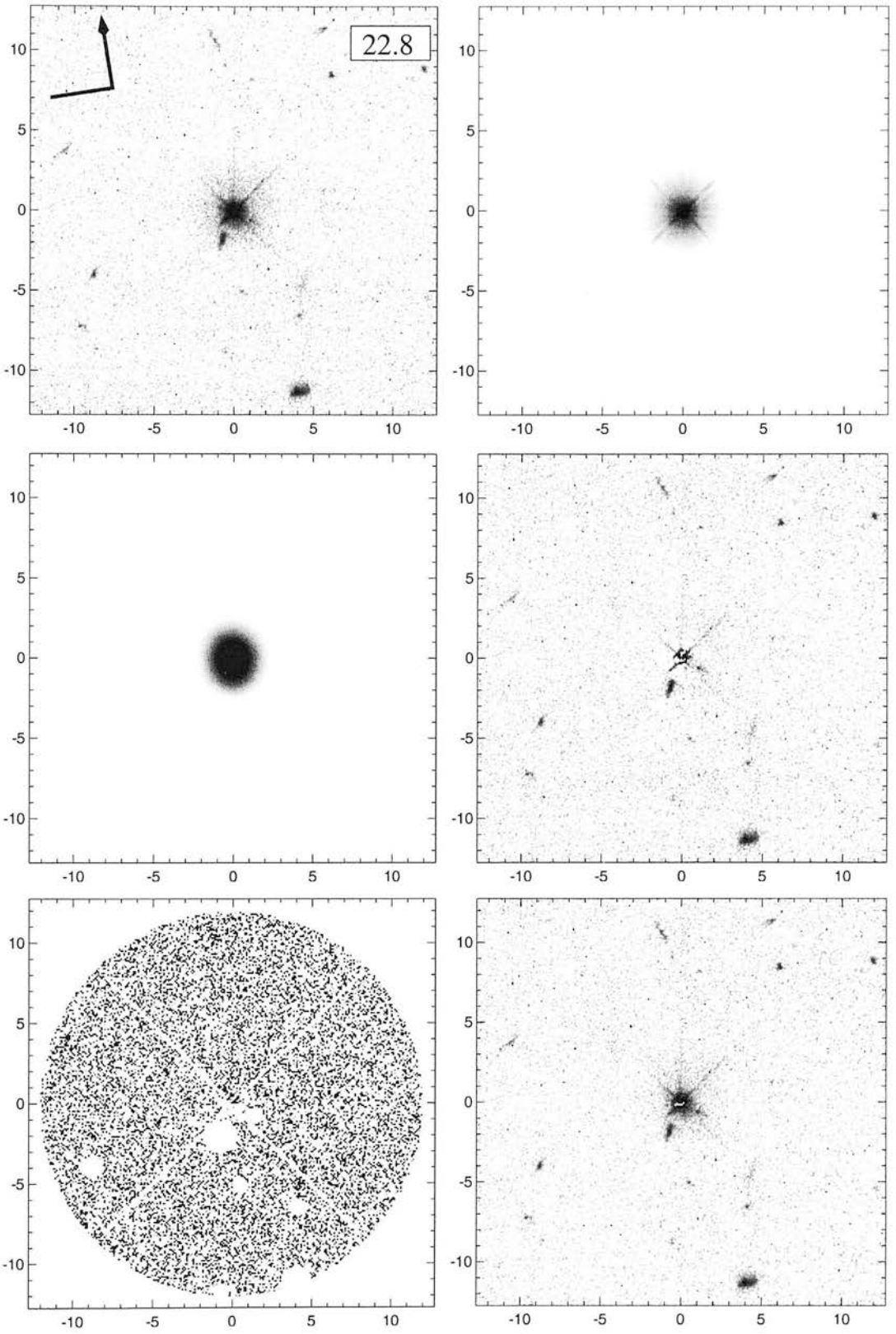

Figure B.2:
The Radio-Quiet Quasar BVF225

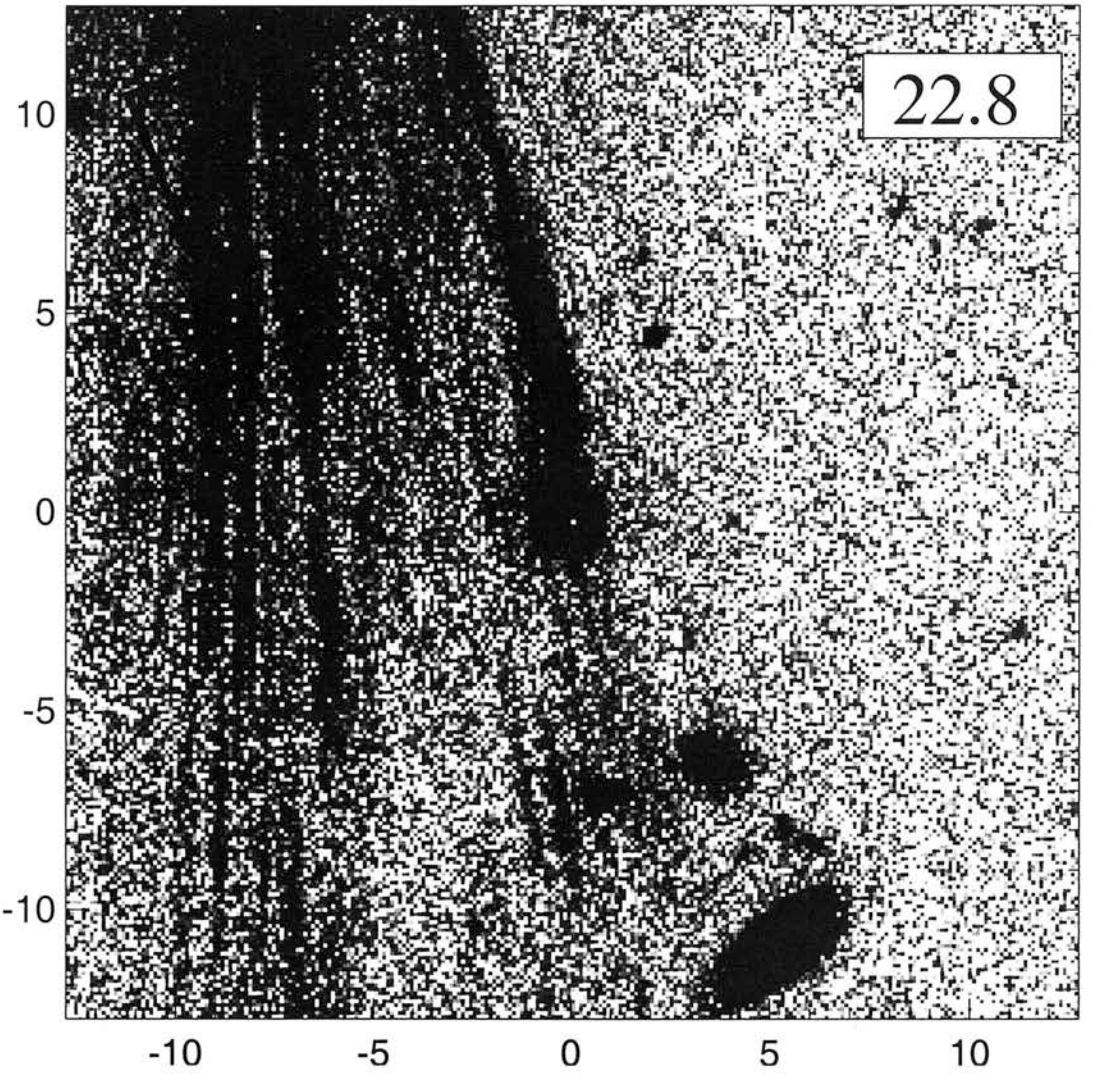

Figure B.3:
The Radio-Quiet Quasar SGP5-46

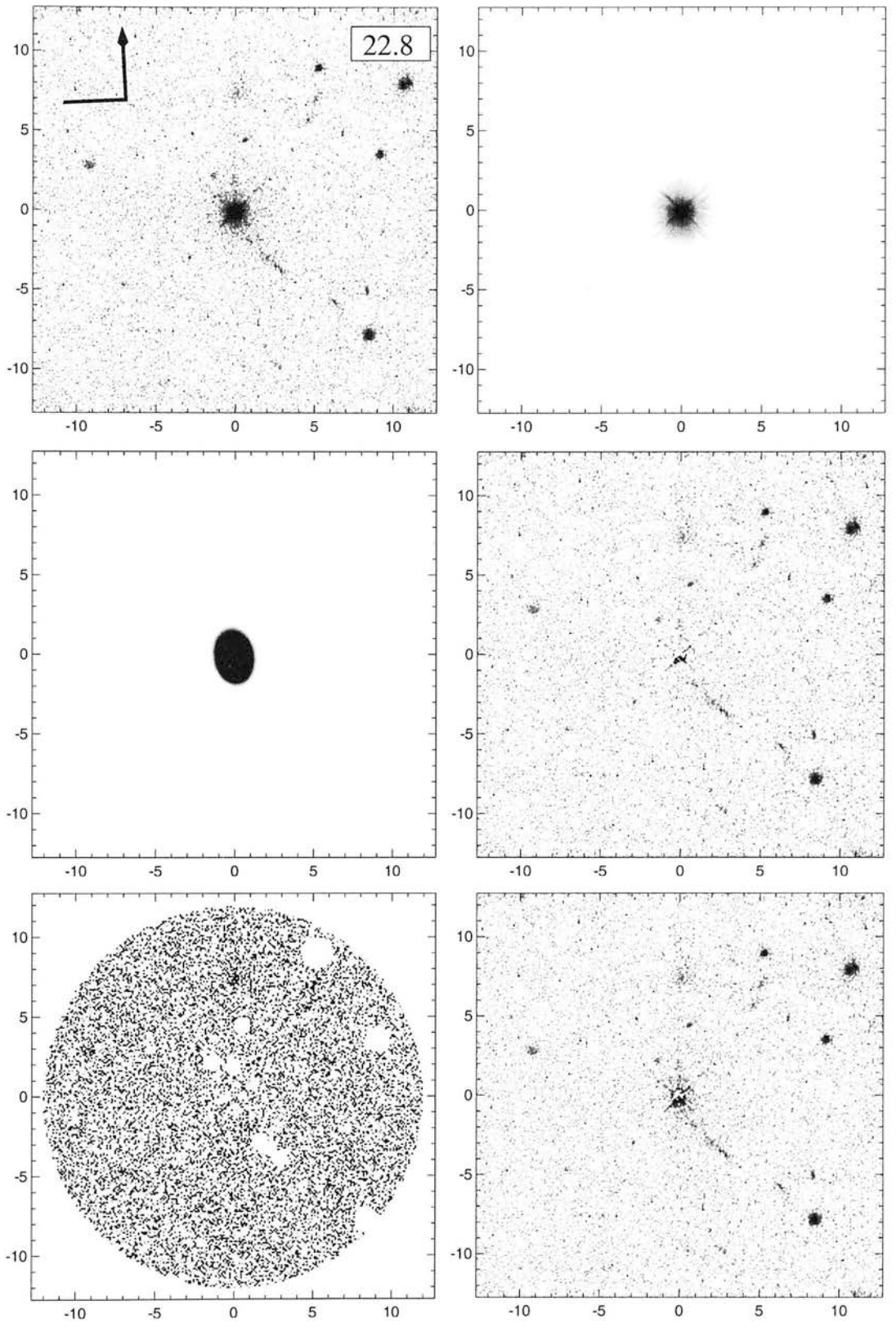

Figure B.4:
The Radio-Quiet Quasar BVF262

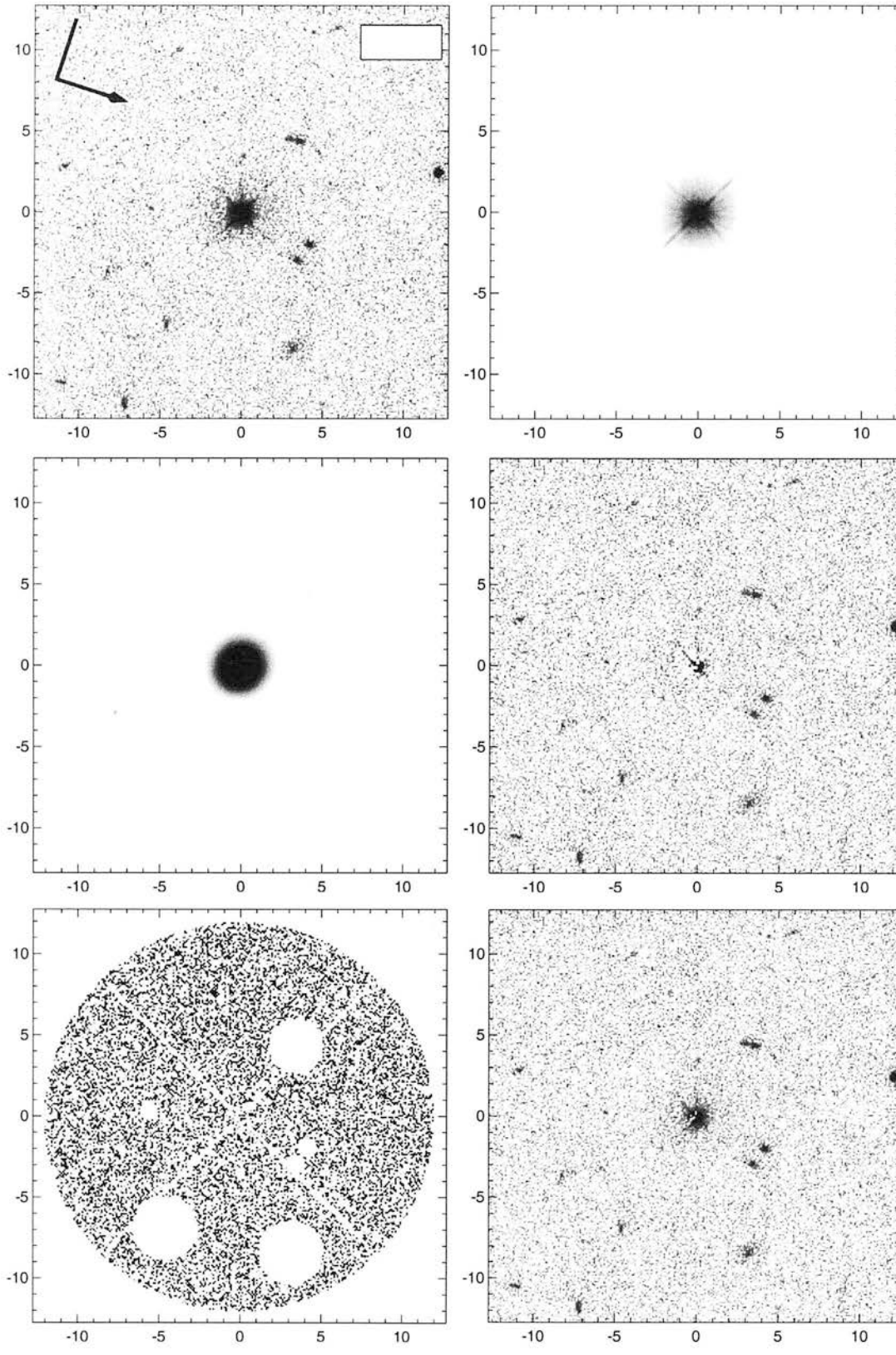

Figure B.5:
The Radio-Loud Quasar PKS0440-00

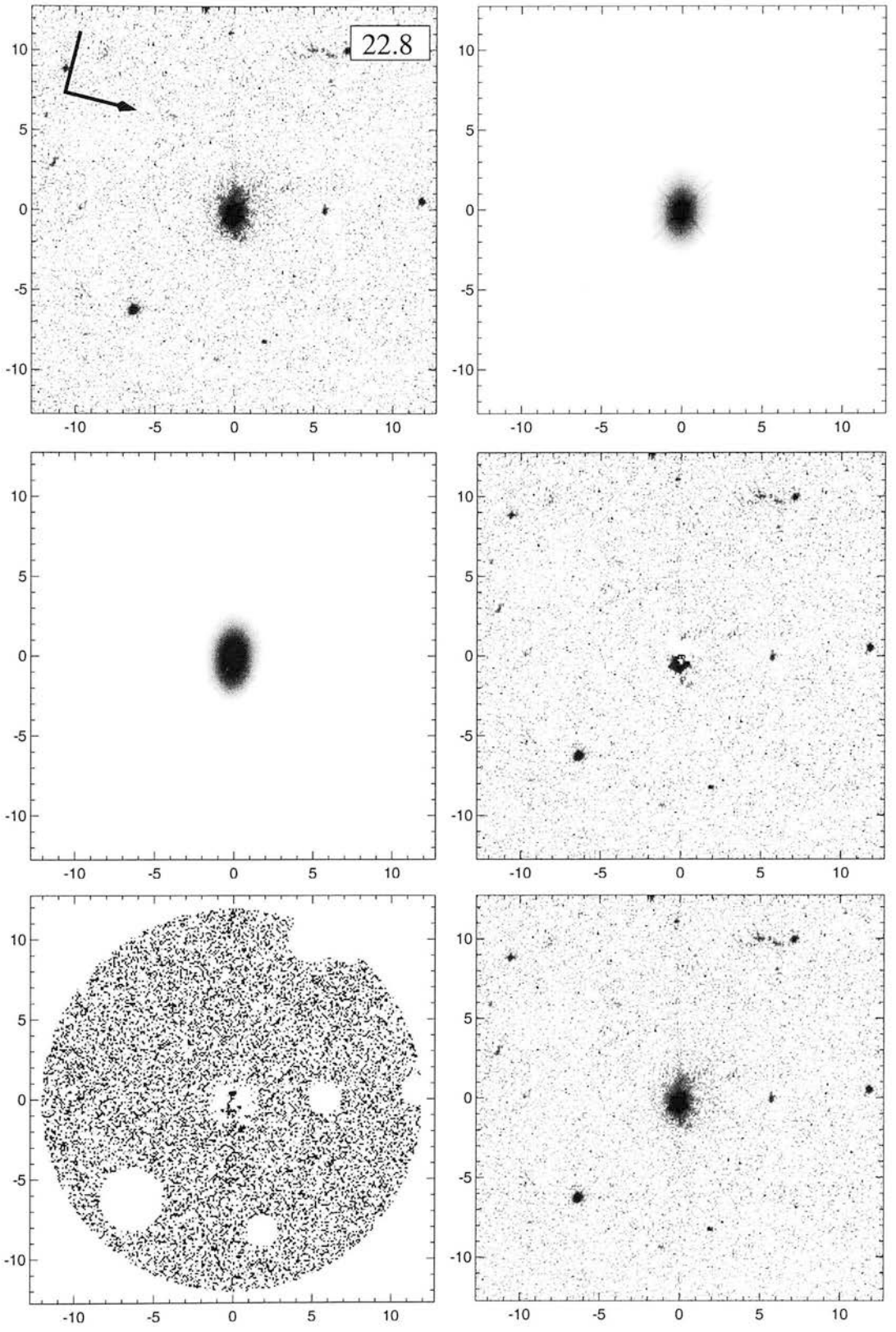

Figure B.6:
The Radio-Loud Quasar MC2112+172

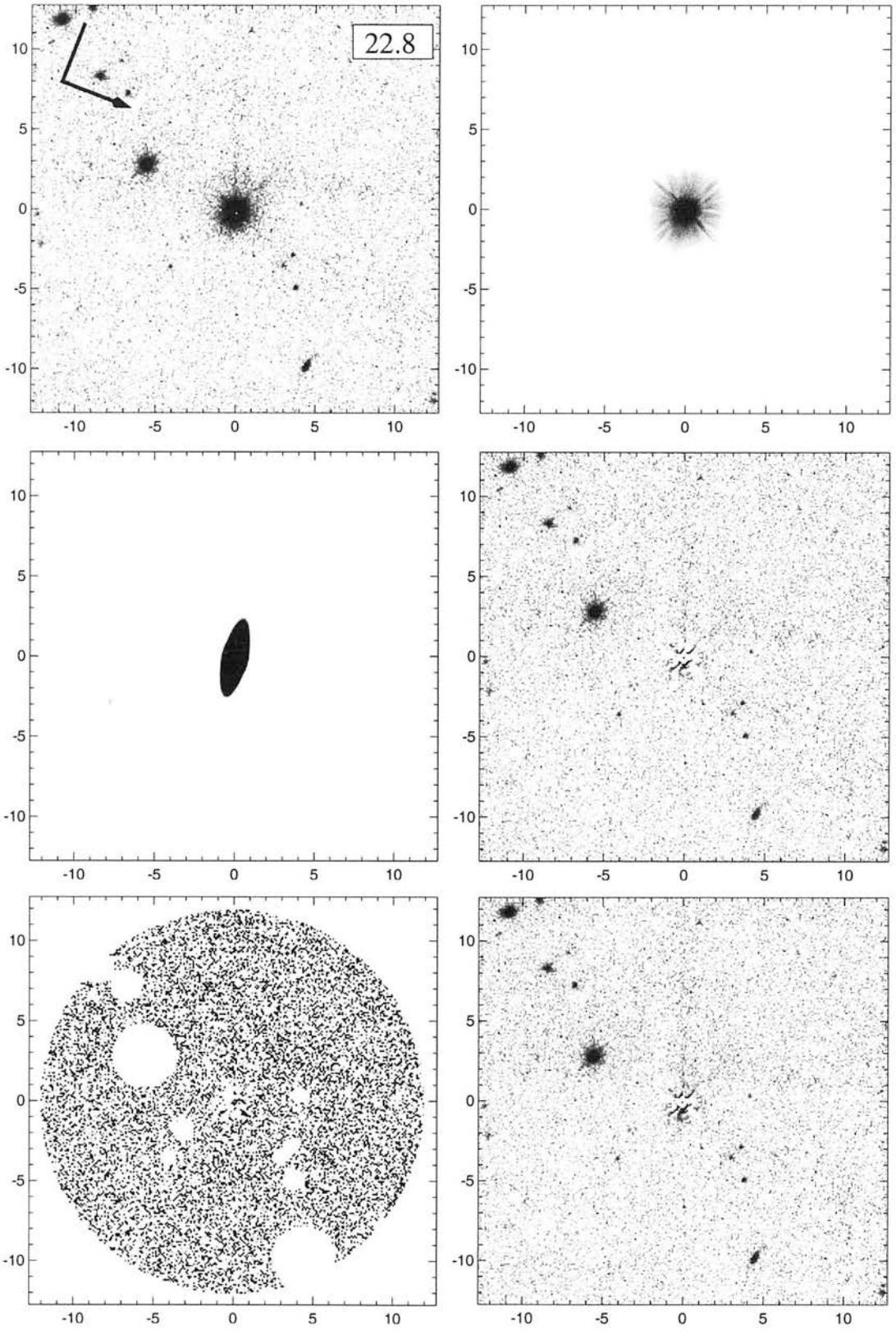

Figure B.7:
The Radio-Loud Quasar 3C422

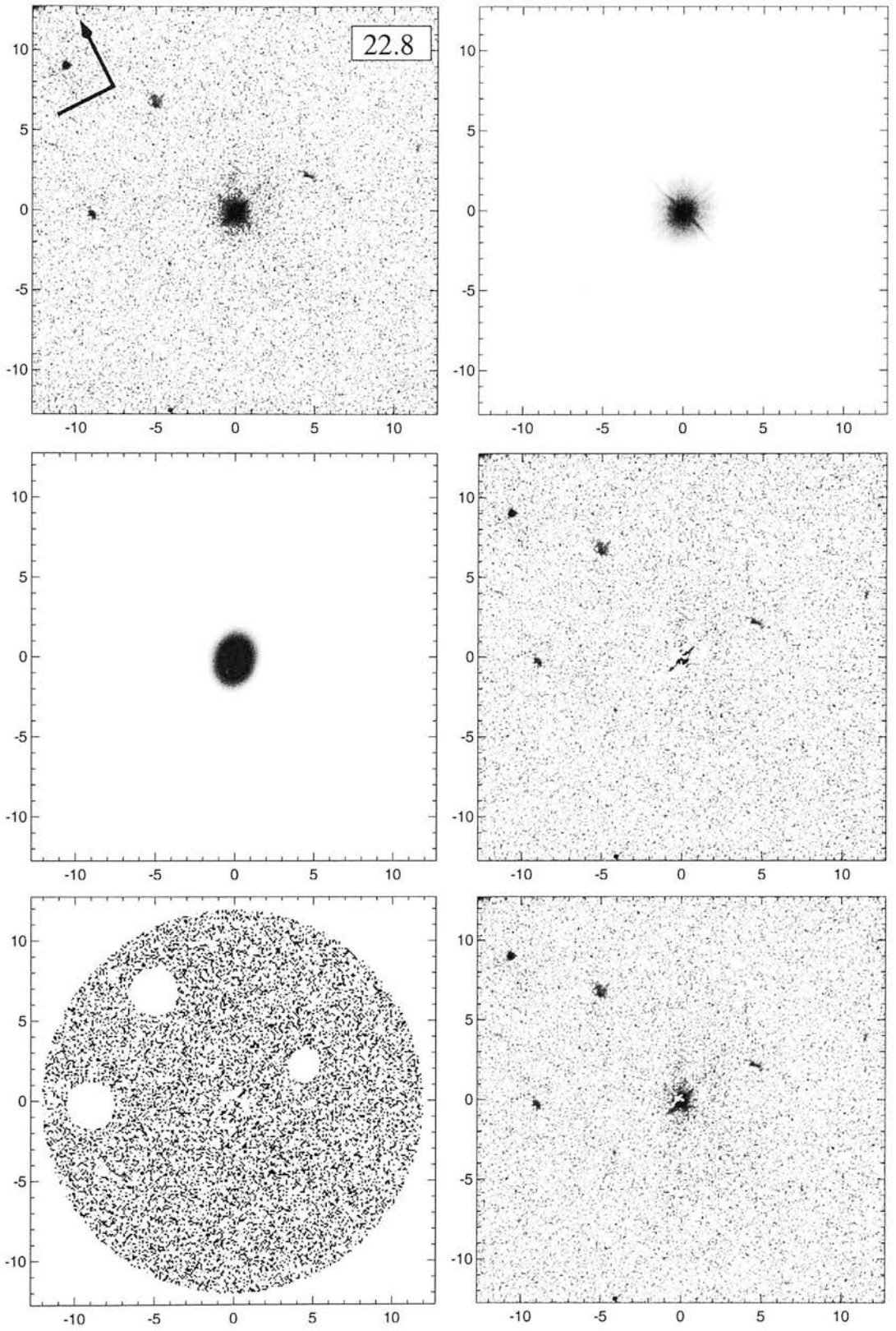

Figure B.8:
The Radio-Loud Quasar PKS0938+18

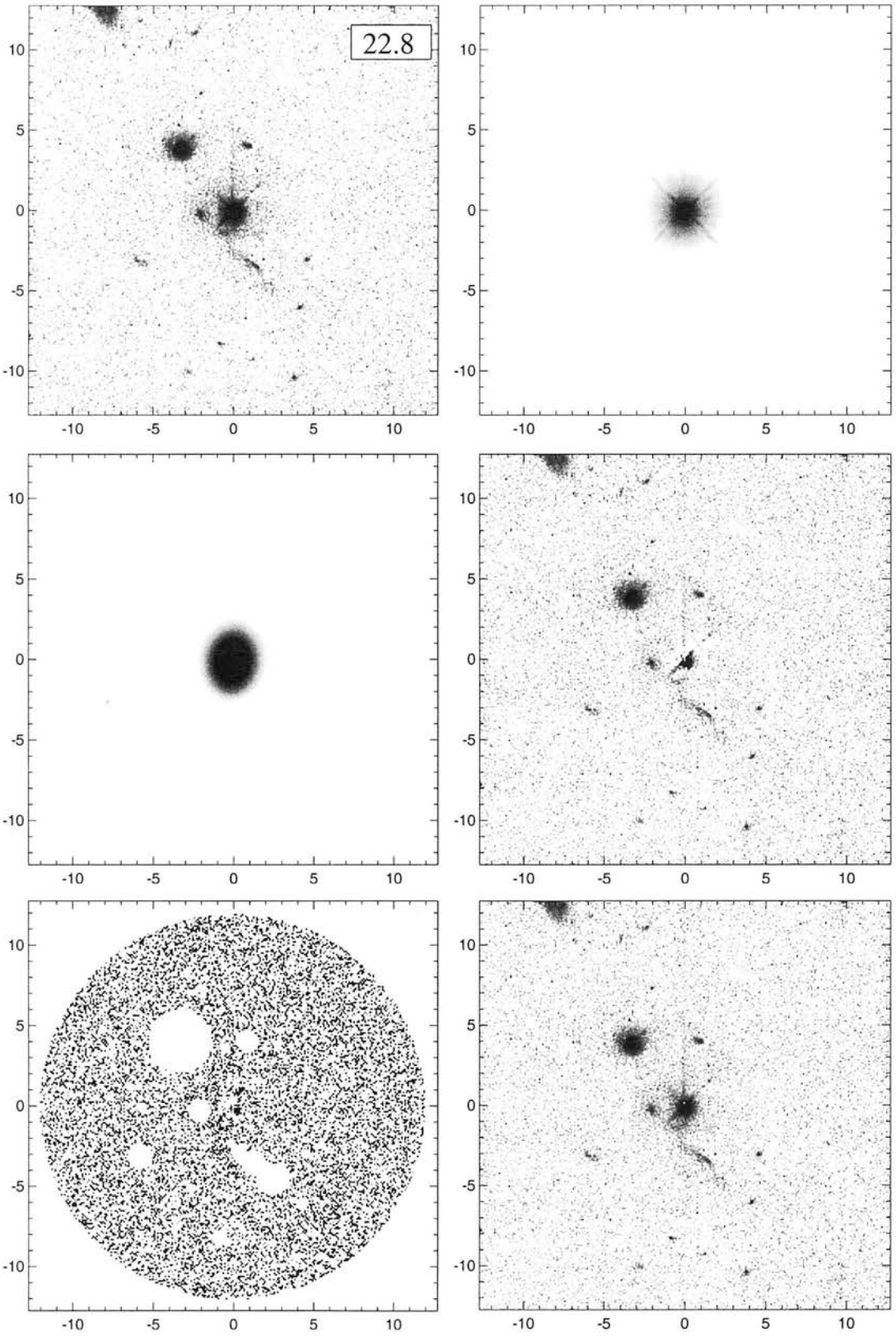

Figure B.9:
The Radio-Loud Quasar 4C02.54

APPENDIX C

Quasar images at z=2

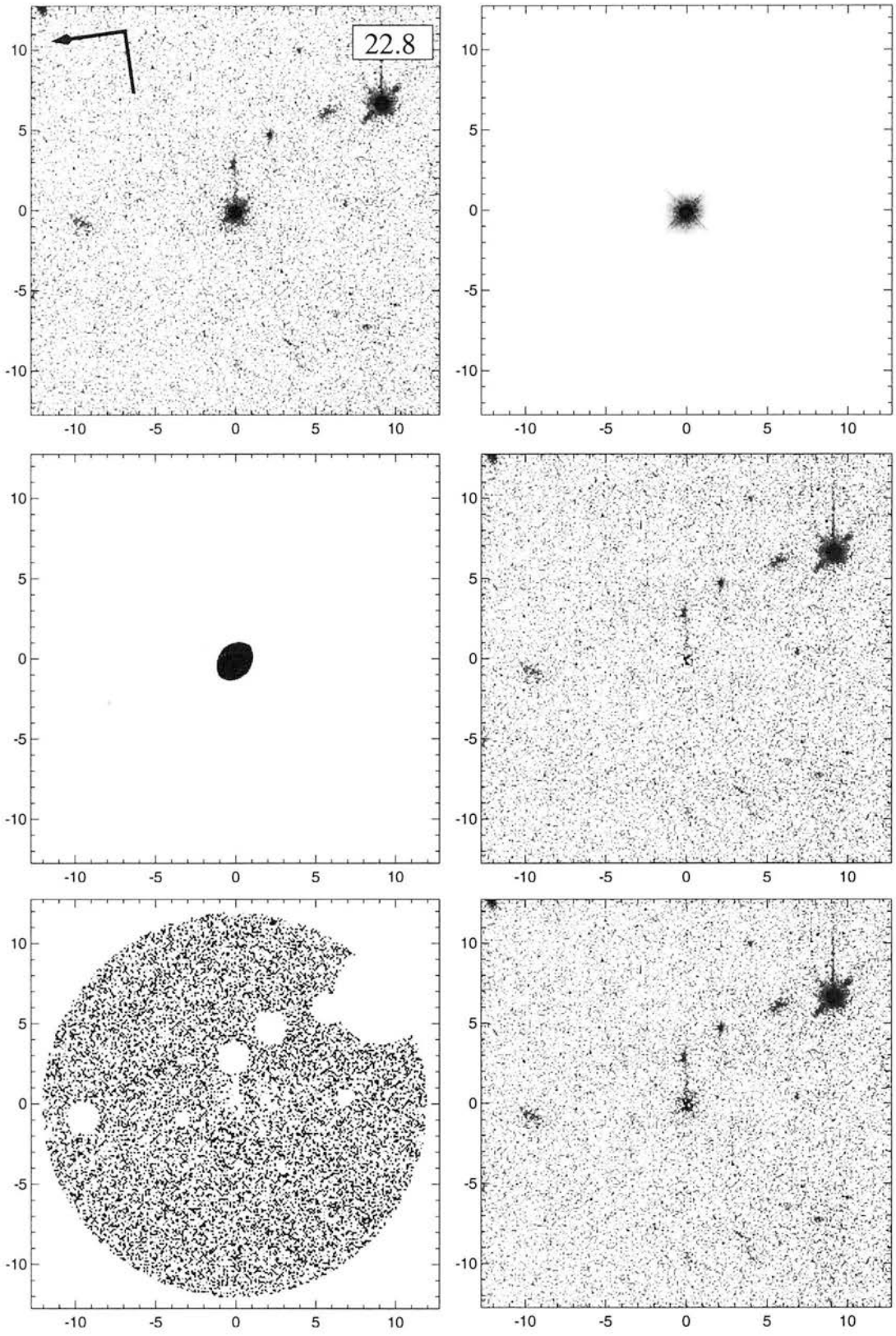

Figure C.1:
The Radio-Loud Quasar SGP4-39

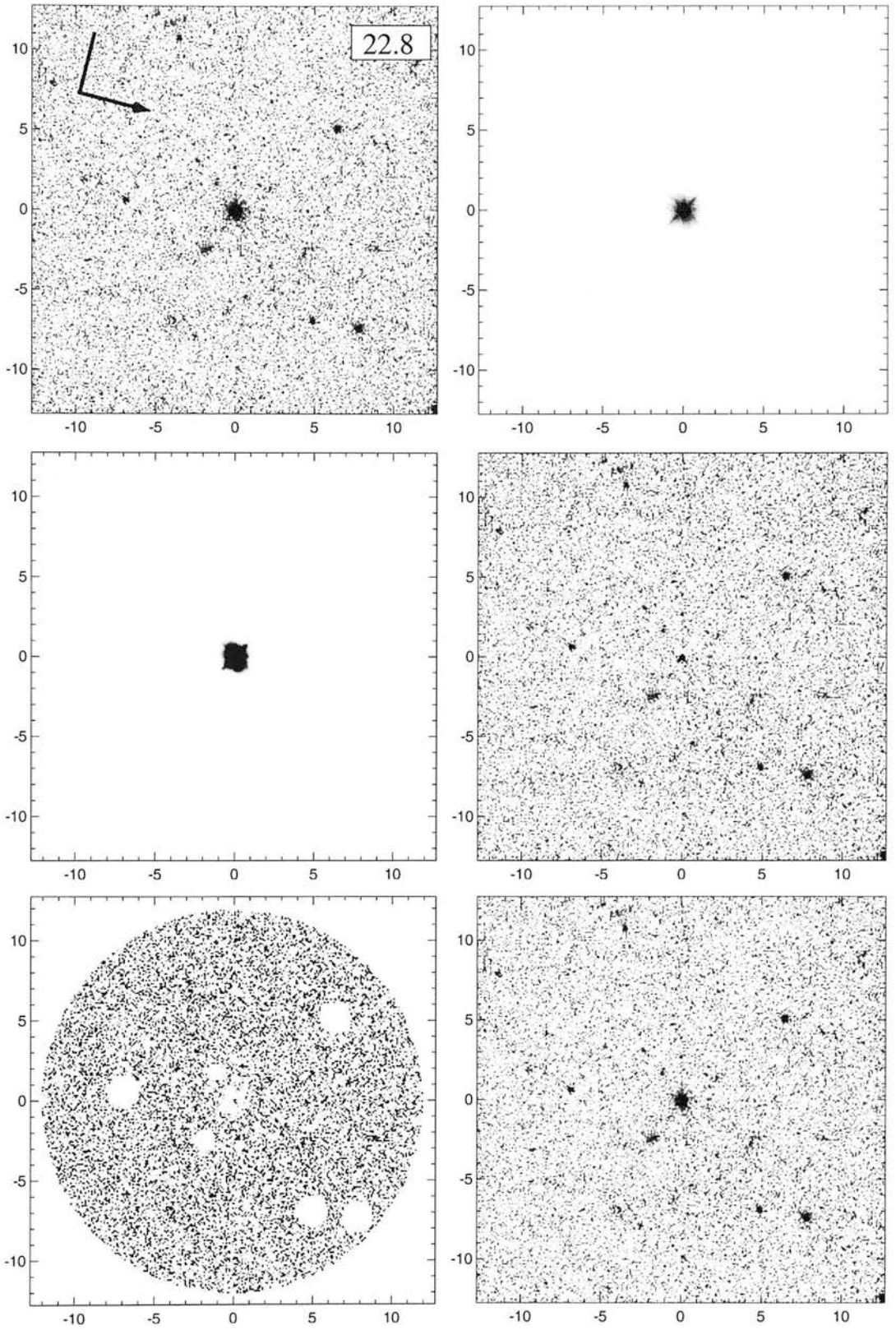

Figure C.2:
The Radio-Loud Quasar SGP2-36

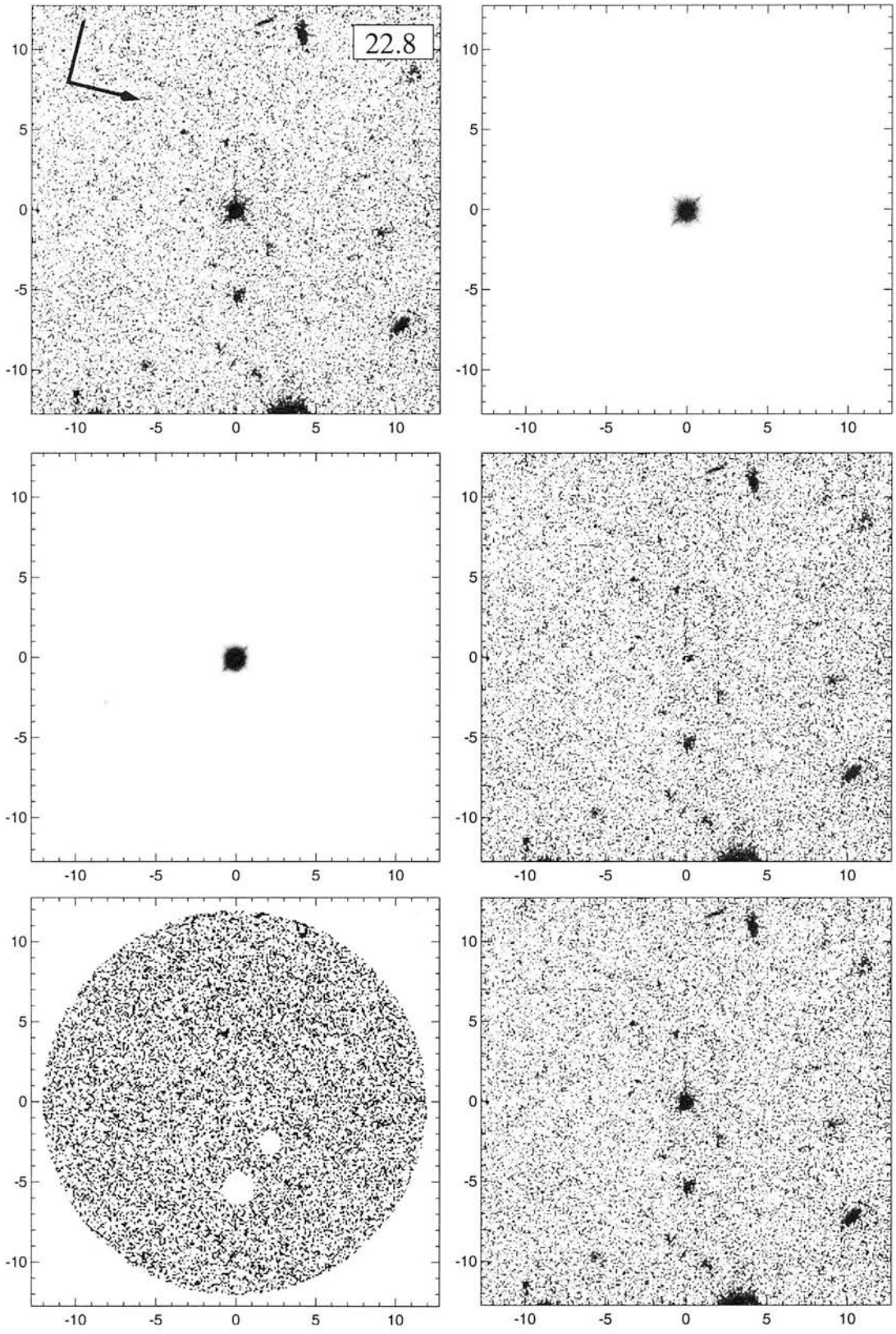

Figure C.3:
The Radio-Loud Quasar SGP2-25

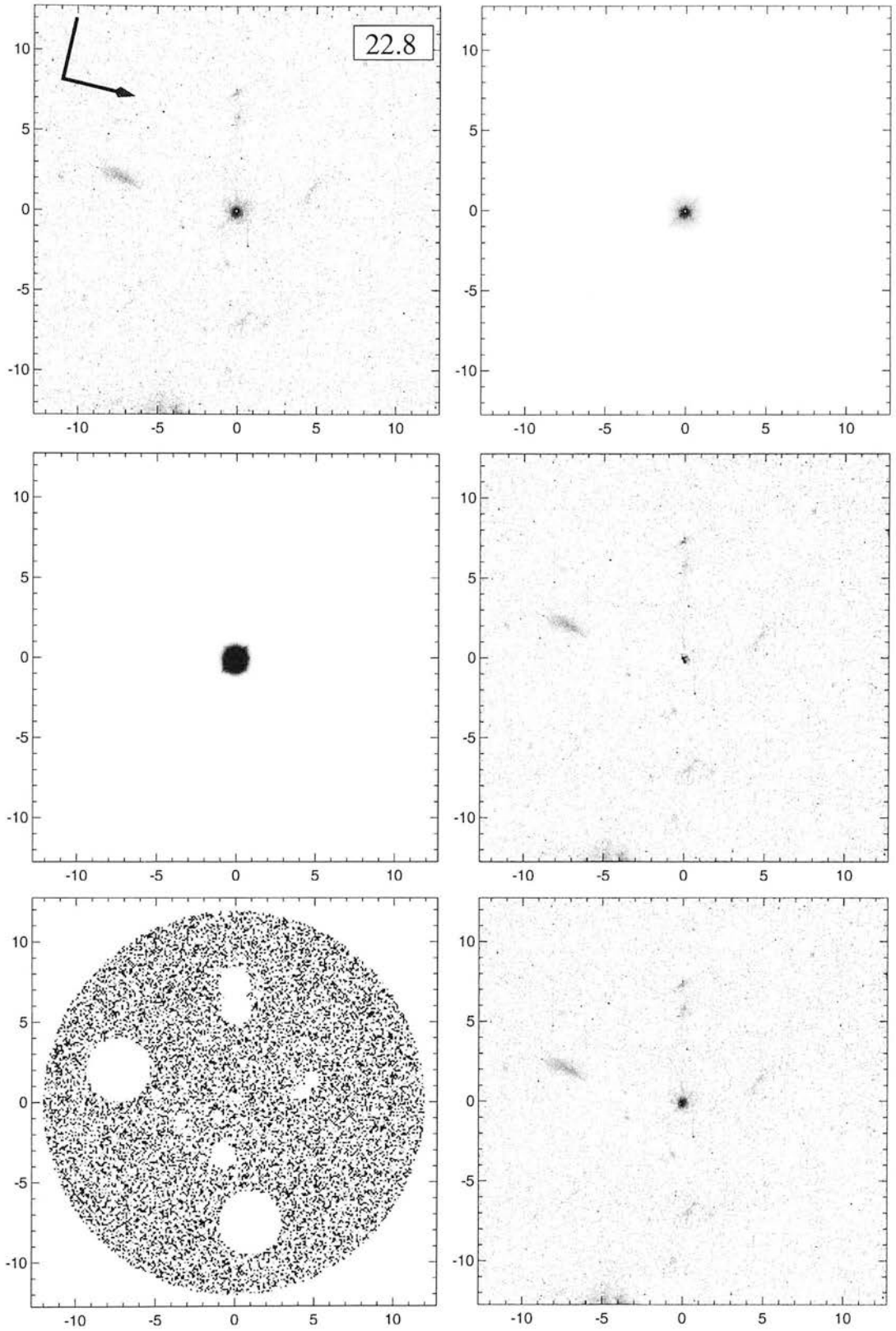

Figure C.4:
The Radio-Loud Quasar SGP3-39

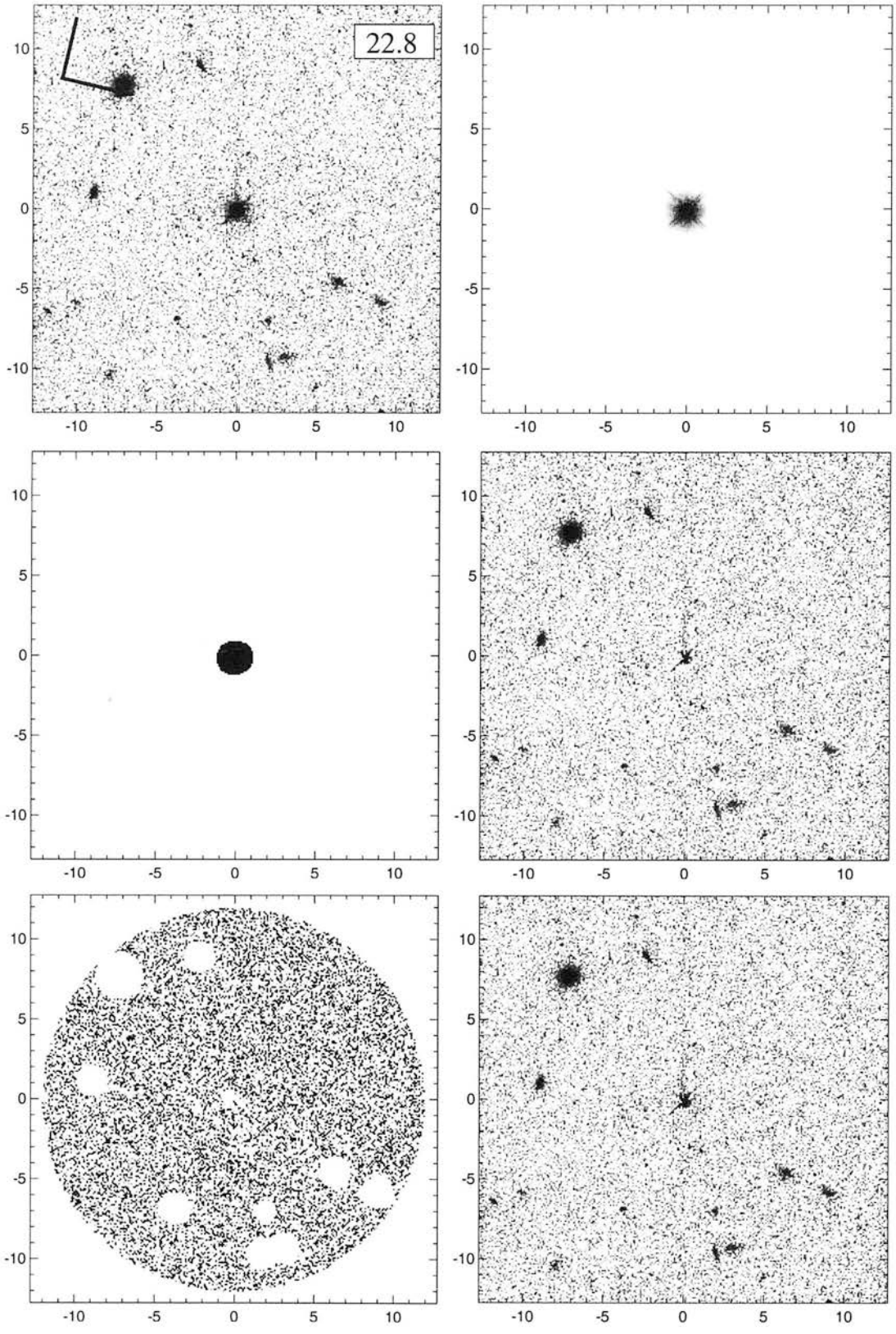

Figure C.5:
The Radio-Loud Quasar SGP2-11

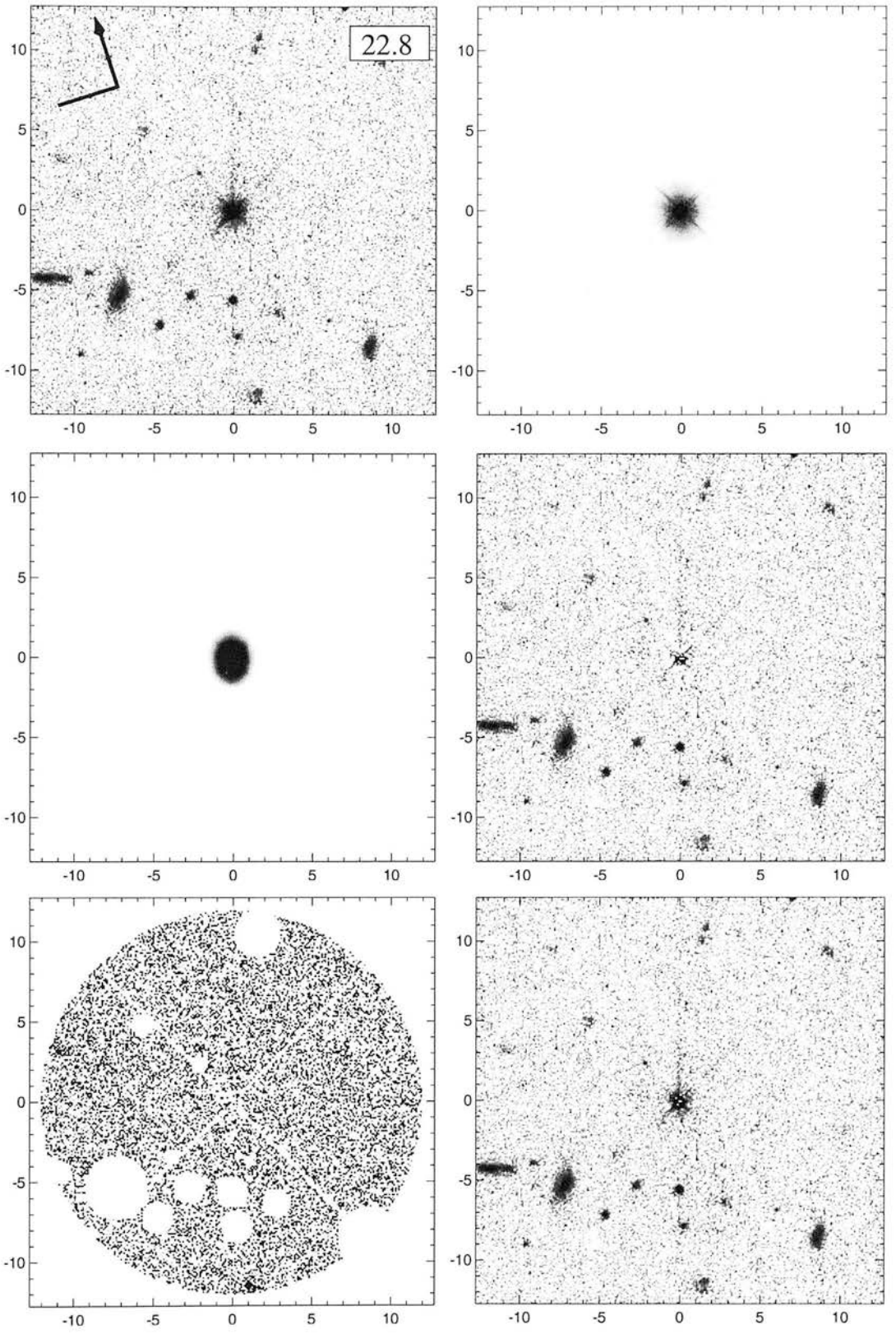

Figure C.6:
The Radio-Loud Quasar PKS1524-13

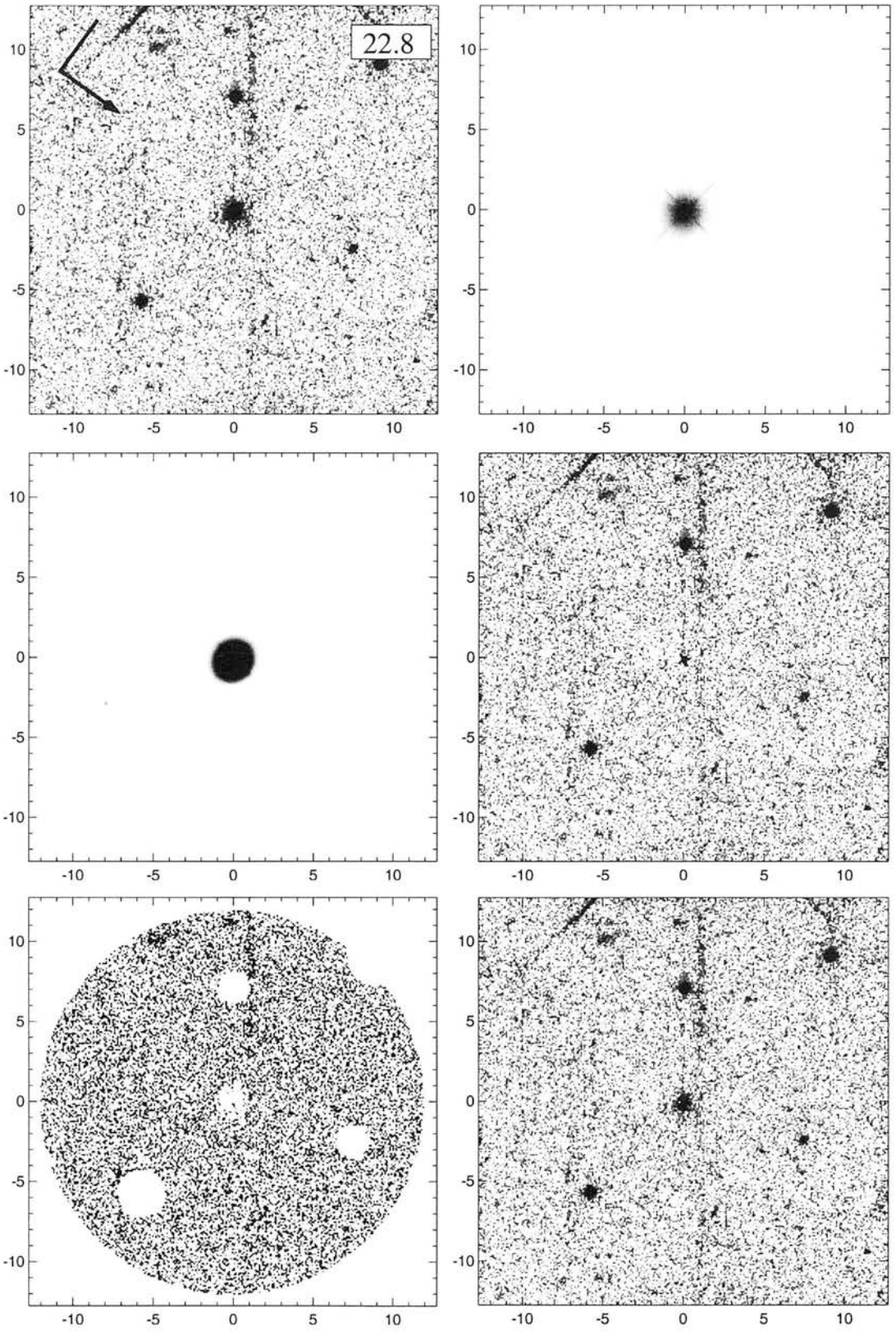

Figure C.7:
The Radio-Loud Quasar 4C45.51

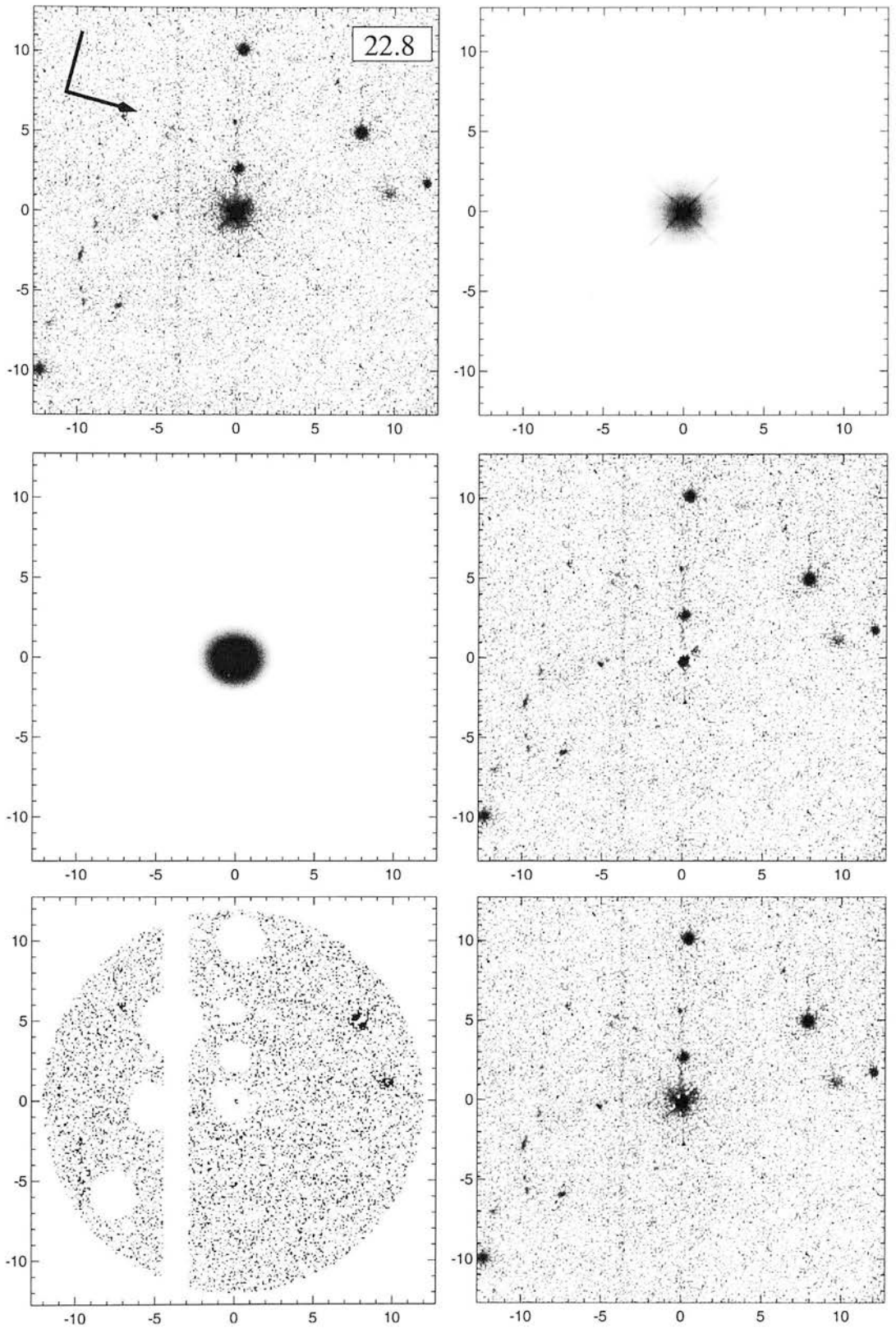

Figure C.8:
The Radio-Loud Quasar B2-2156+29

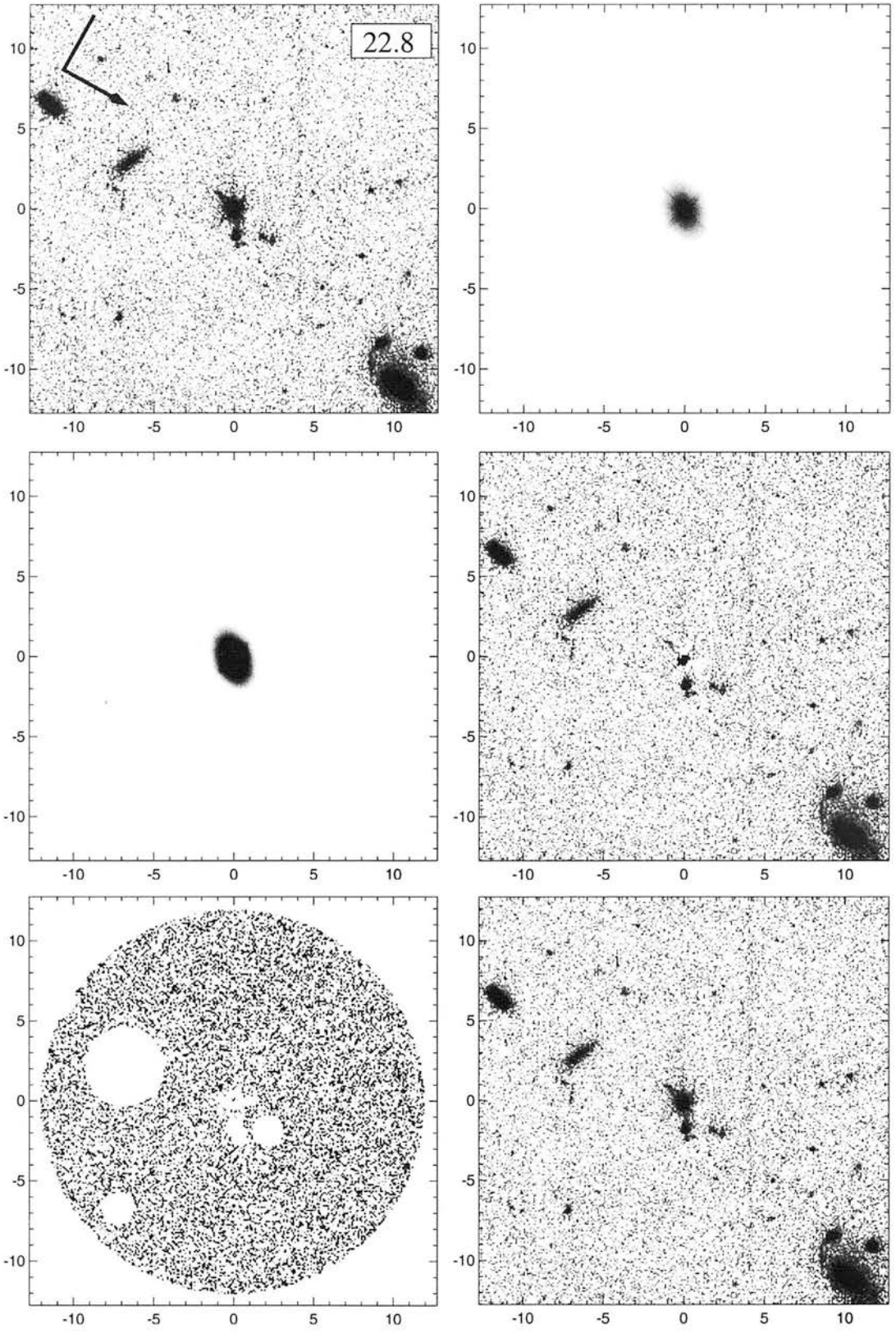

Figure C.9:
The Radio-Loud Quasar PKS2204-20

APPENDIX D

ULIRG and IRQSO images

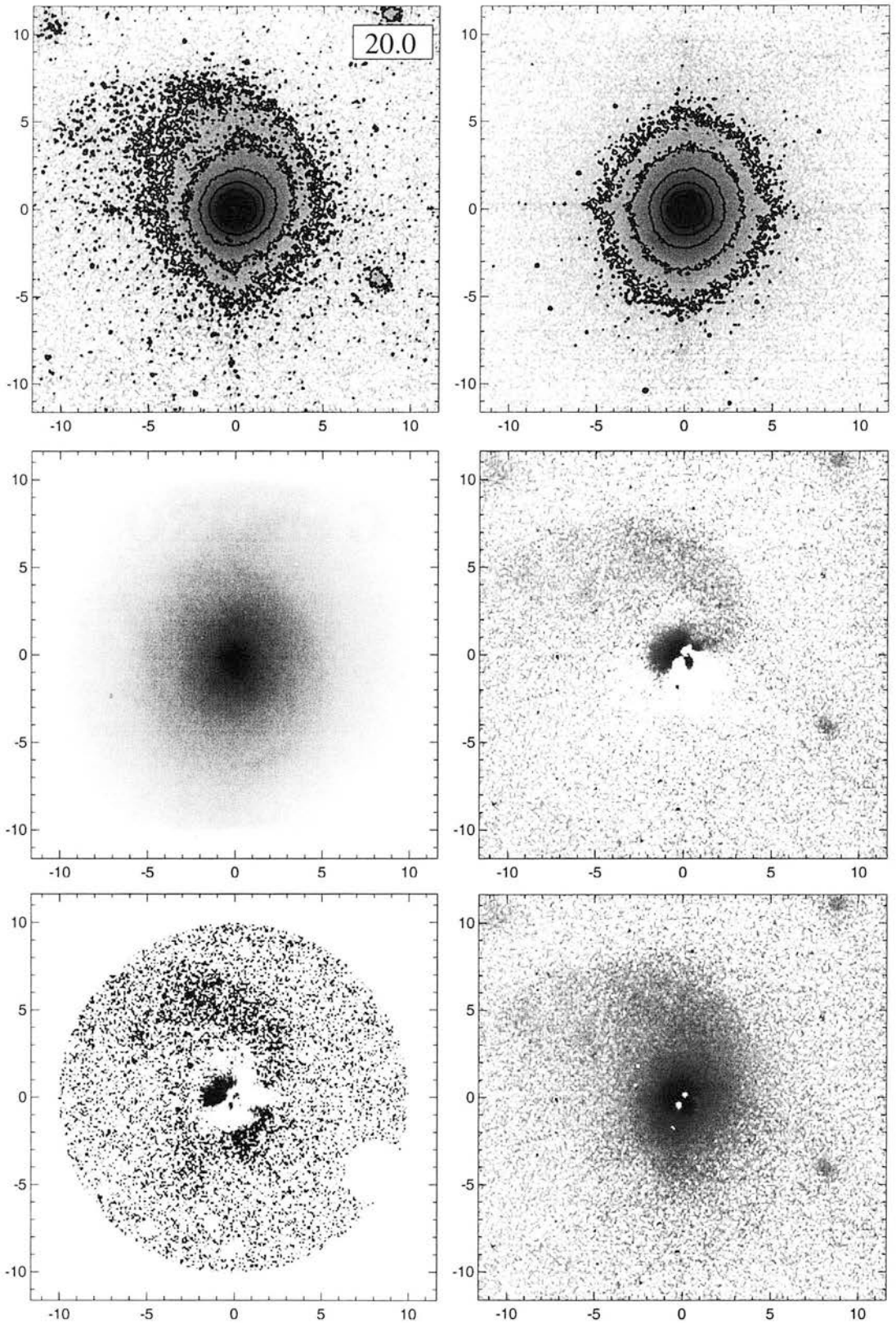

Figure D.1:
The IRQSO 0157+001

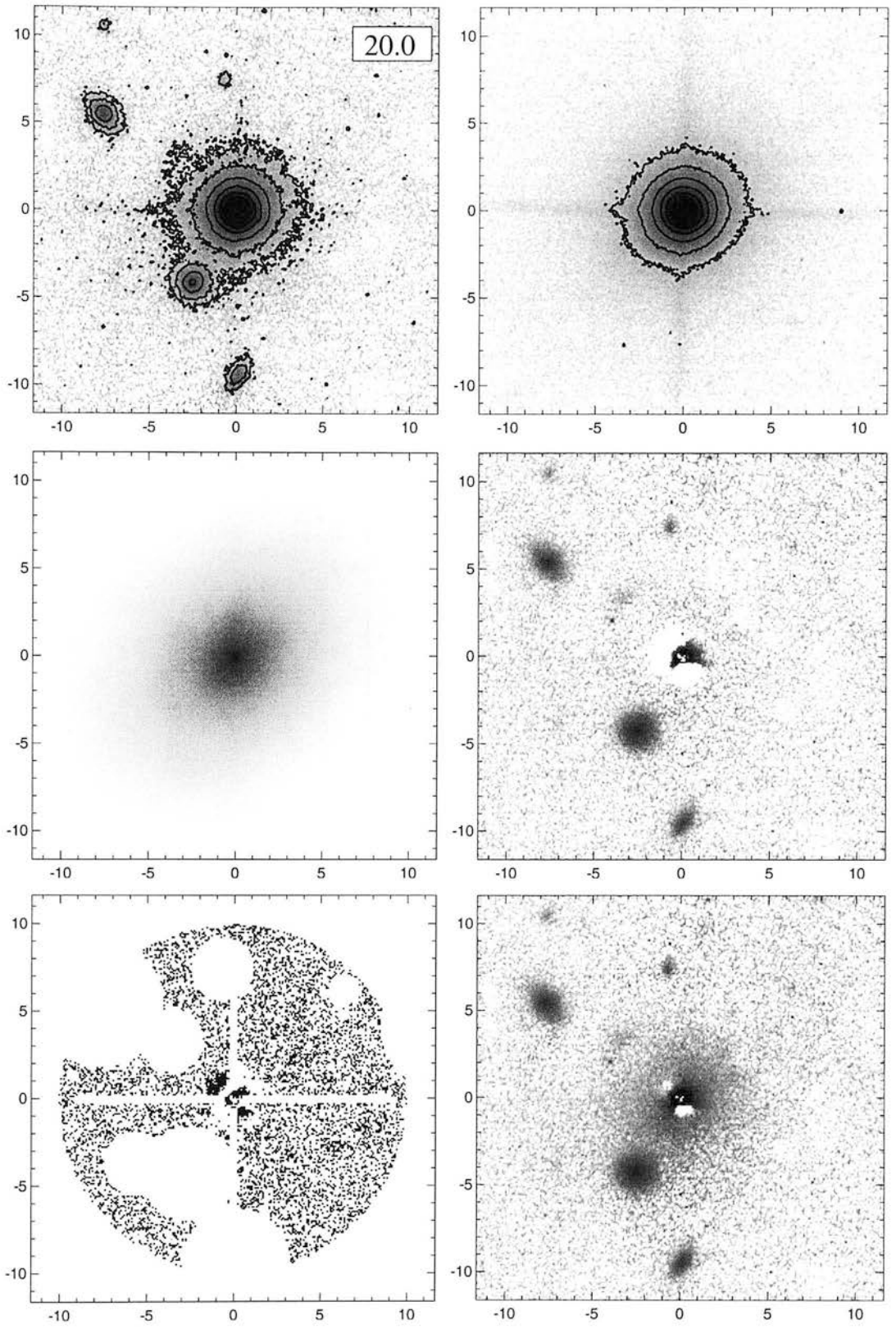

Figure D.2:
The IRQSO 0829+046

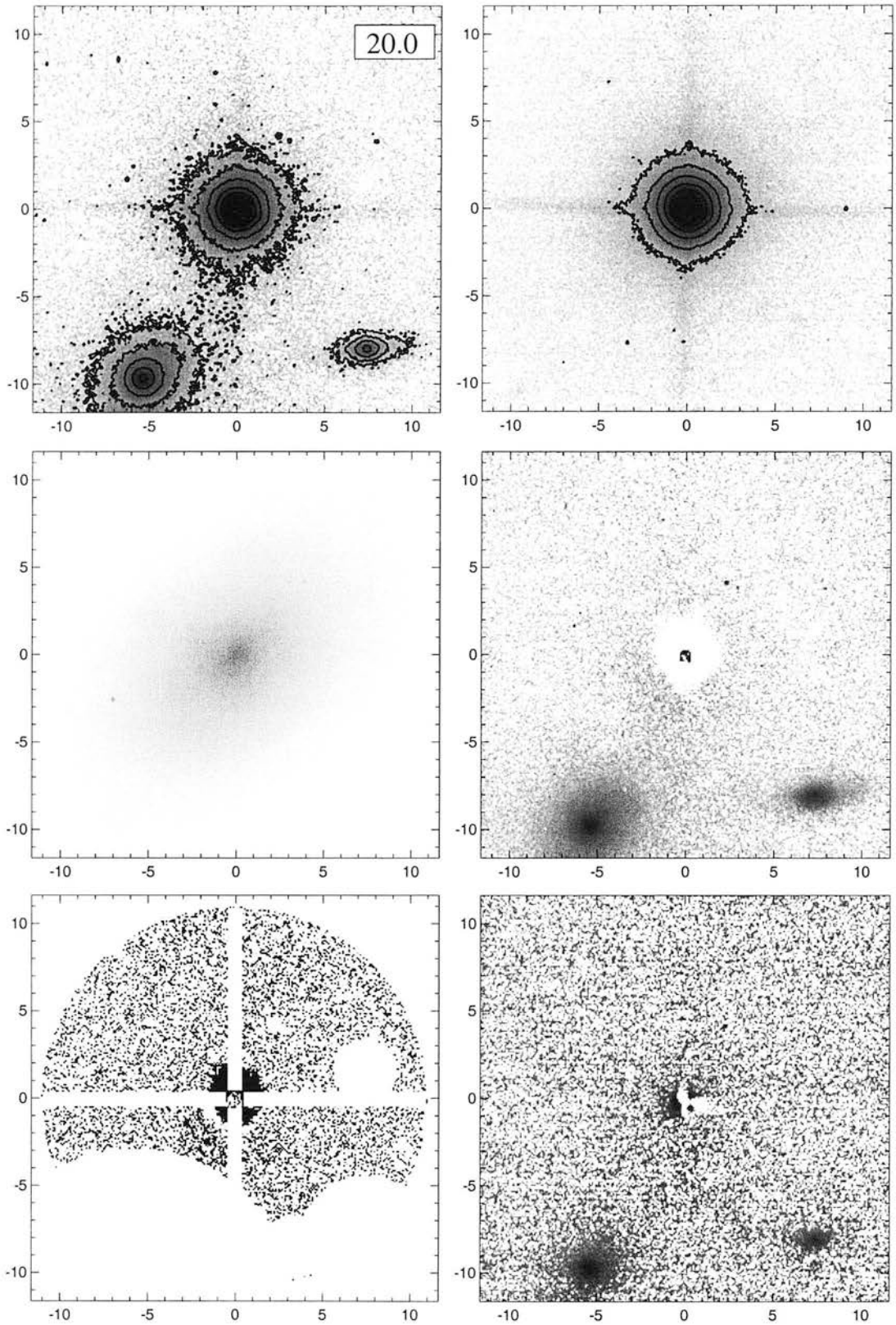

Figure D.3:
The IRQSO 0923+201

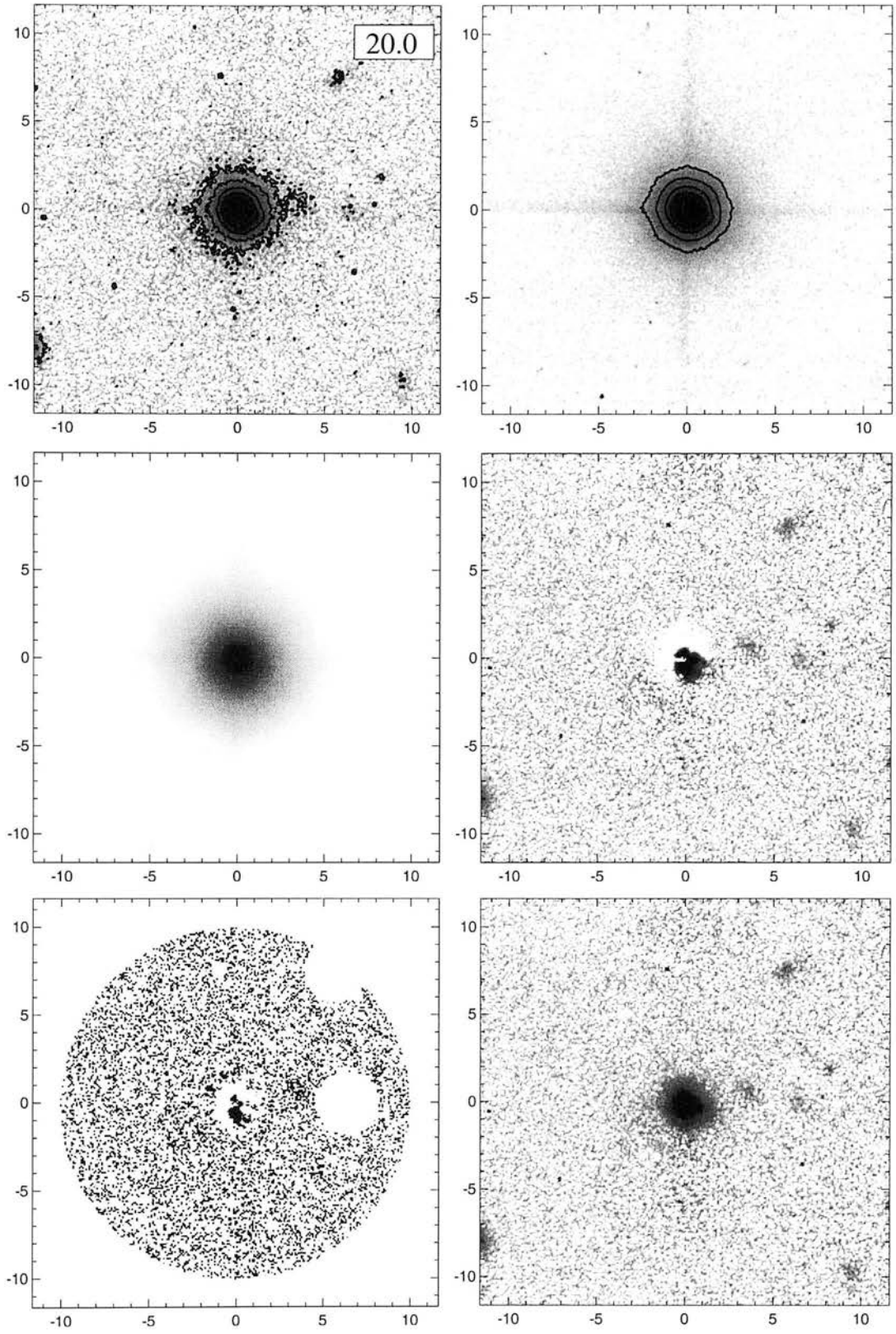

Figure D.4:
The IRQSO/ULIRG 1003+437

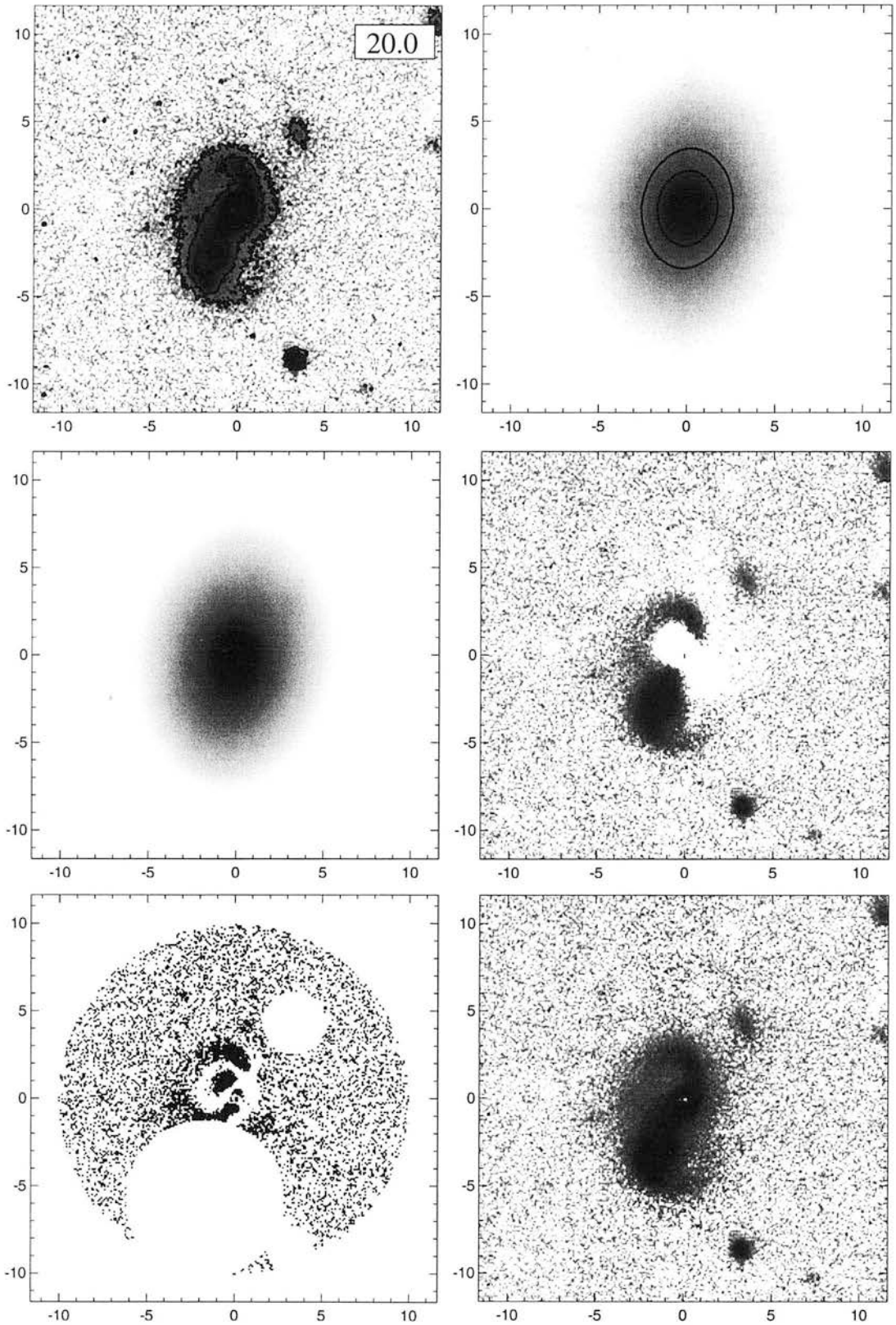

Figure D.5:
The ULIRG 06268+3509

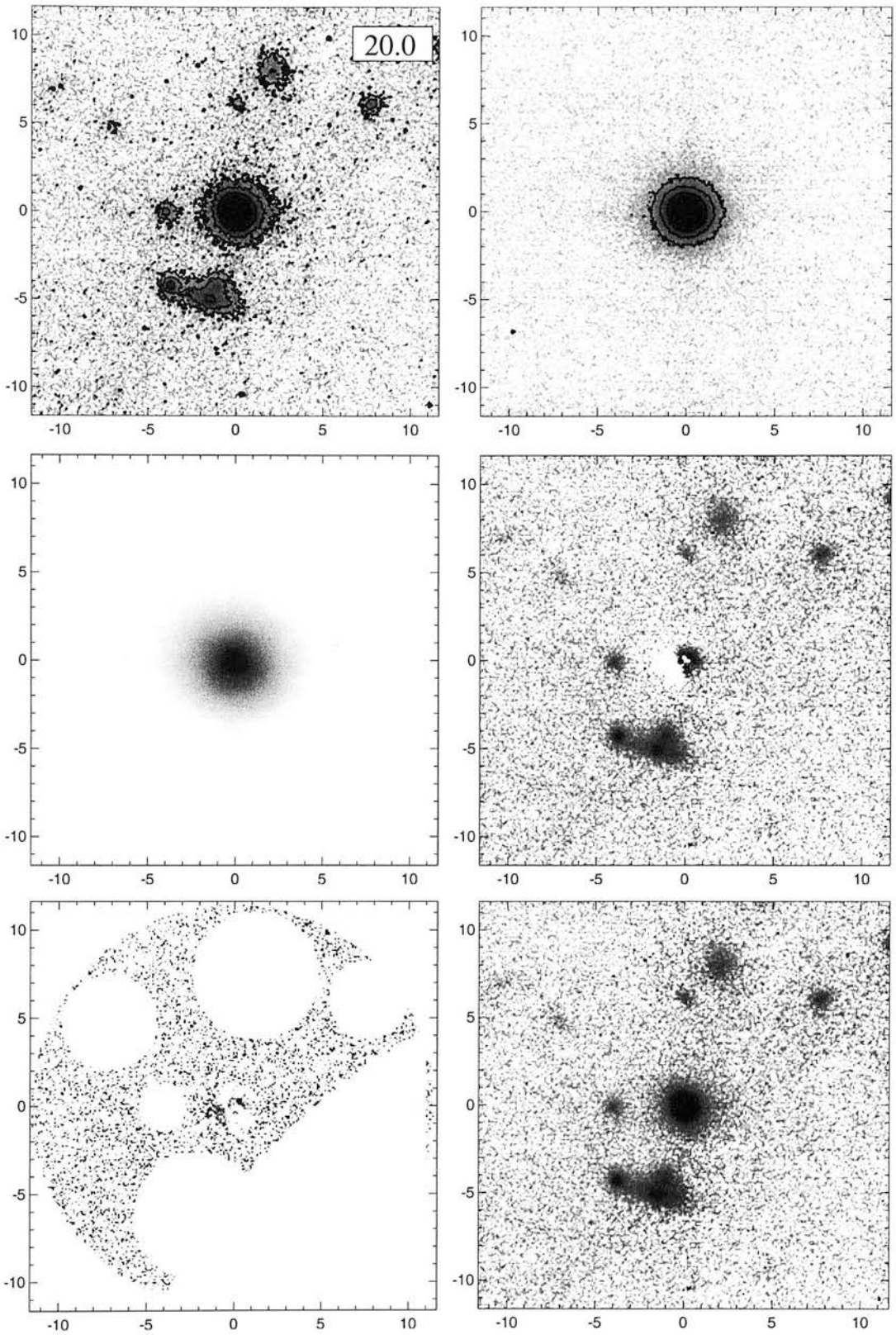

Figure D.6:
The ULIRG/IRQSO/Sy1 02054+0835

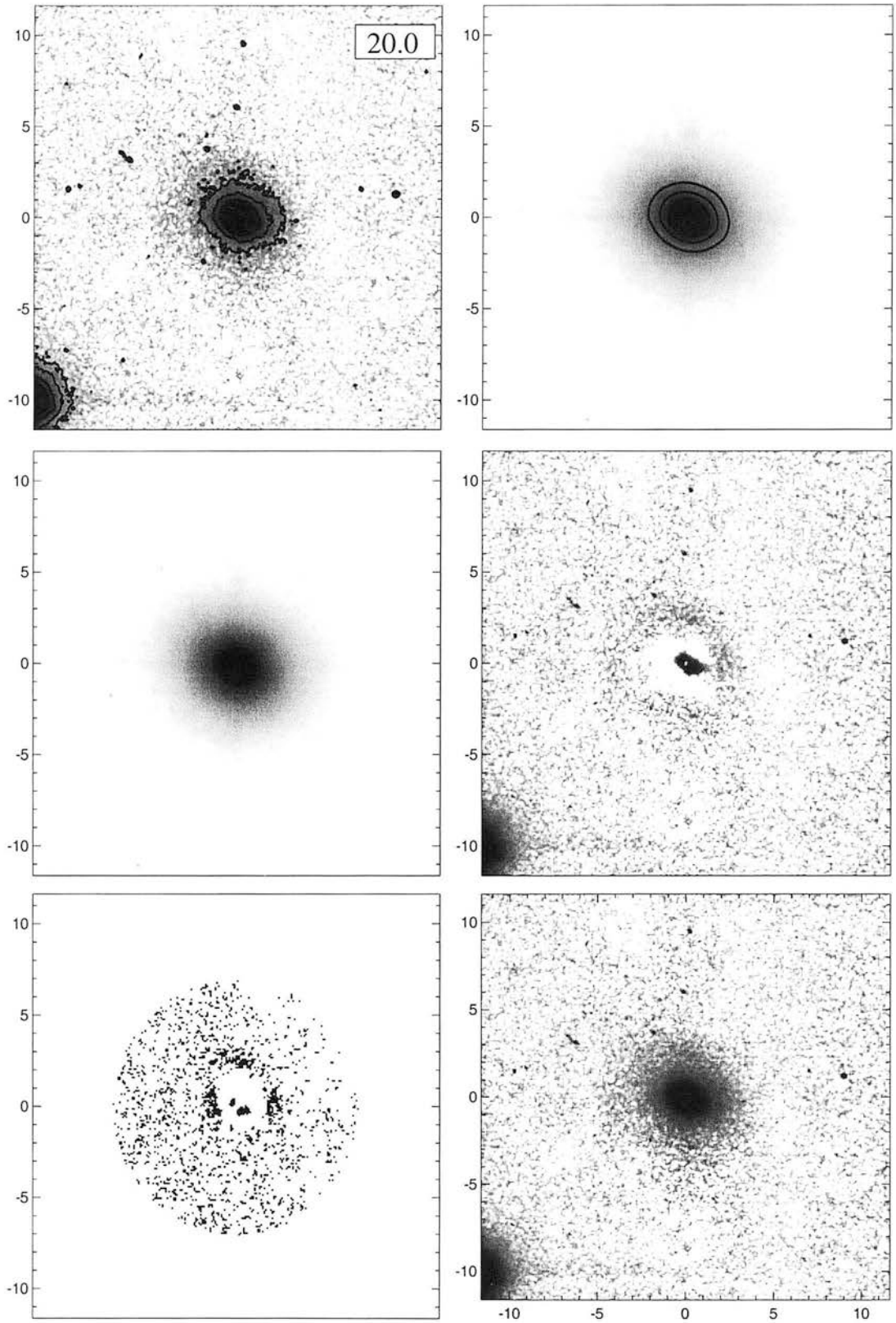

Figure D.7:
The ULIRG 07381+3215

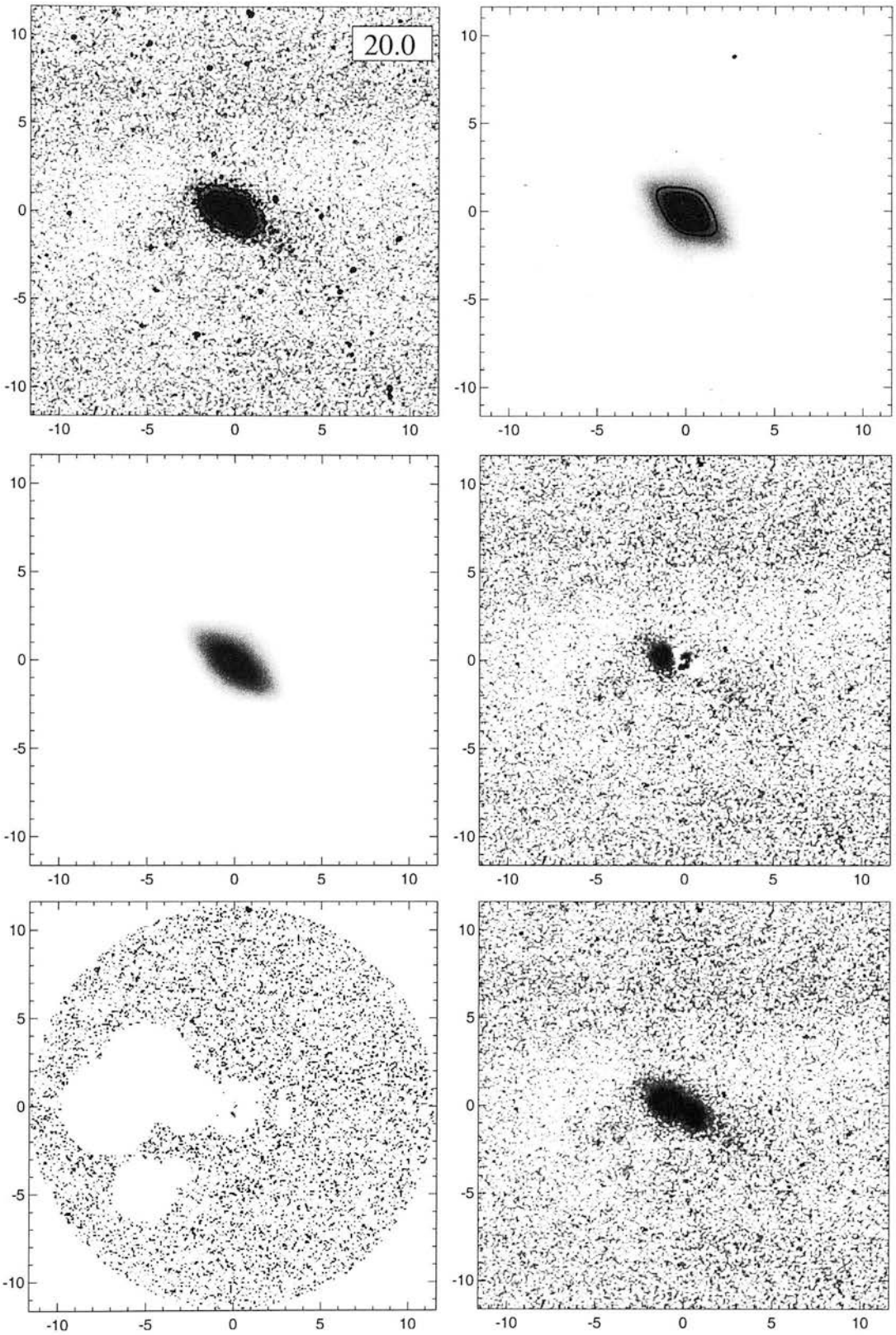

Figure D.8:
The ULIRG 10579+0438

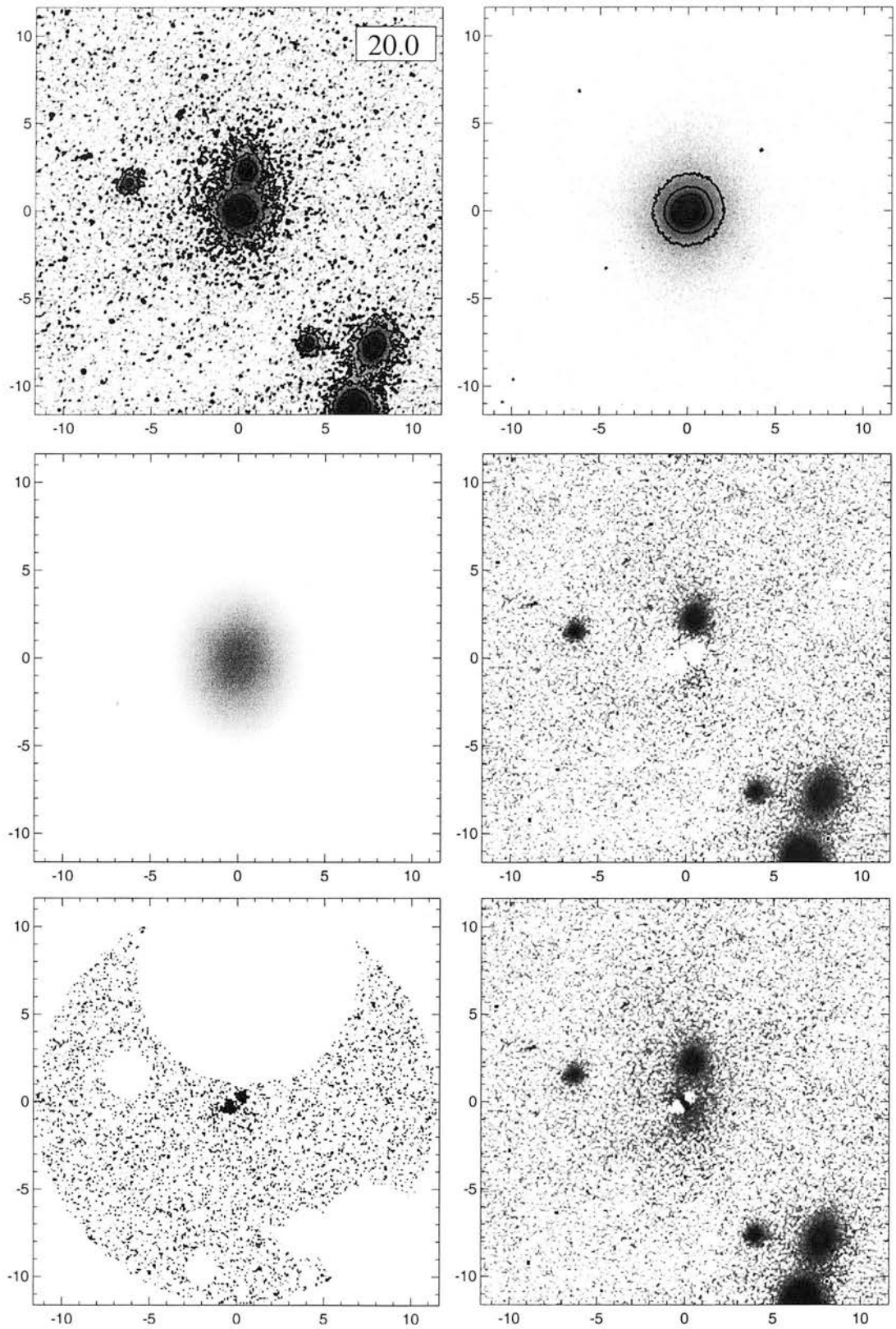

Figure D.9:
The ULIRG 06561+1902

Bibliography

Abraham, R. G., Crawford, C. S., and McHardy, I. M.: 1992, *ApJ* **401**, 474

Aldcroft, T. L., Bechtold, J., and Elvis, M.: 1994, *ApJS* **93**, 1

Alexander, D. M., Vignali, C., Bauer, F. E., Brandt, W. N., Hornschemeier, A. E., Garmire, G. P., and Schneider, D. P.: 2002, *AJ* **123**, 1149

Altschuler, D. R.: 1982, *AJ* **87**, 387

Antonucci, R.: 1993, *ARA&A* **31**, 473

Antonucci, R. R. J. and Miller, J. S.: 1985, *ApJ* **297**, 621

Aretxaga, I., Hughes, D. H., Chapin, E. L., Gaztañaga, E., Dunlop, J. S., and Ivison, R. J.: 2003, *MNRAS* **342**, 759

Baganoff, F. K., Bautz, M. W., Brandt, W. N., Chartas, G., Feigelson, E. D., Garmire, G. P., Maeda, Y., Morris, M., Ricker, G. R., Townsley, L. K., and Walter, F.: 2001, *Nature* **413**, 45

Bahcall, J. N., Kirhakos, S., Saxe, D. H., and Schneider, D. P.: 1997, *ApJ* **479**, 642+

Bahcall, J. N., Kirhakos, S., and Schneider, D. P.: 1994, *ApJ* **435**, L11

Bahcall, J. N., Kirhakos, S., and Schneider, D. P.: 1995a, *ApJ* **450**, 486+

Bahcall, J. N., Kirhakos, S., and Schneider, D. P.: 1995b, *ApJ* **447**, L1

Bahcall, J. N., Kirhakos, S., and Schneider, D. P.: 1996, *ApJ* **457**, 557+

Barger, A. J., Cowie, L. L., Sanders, D. B., Fulton, E., Taniguchi, Y., Sato, Y., Kawara, K., and Okuda, H.: 1998, *Nature* **394**, 248

Begelman, M. C.: 2003, *Science* **300**, 1898

Bernardi, M., Sheth, R. K., Annis, J., Burles, S., Eisenstein, D. J., Finkbeiner, D. P., Hogg, D. W., Lupton, R. H., Schlegel, D. J., SubbaRao, M., Bahcall, N. A., Blakeslee, J. P., Brinkmann, J., Castander, F. J., Connolly, A. J., Csabai, I., Doi, M., Fukugita, M., Frieman, J., Heckman, T., Hennessy, G. S., Ivezić, Ž., Knapp, G. R., Lamb, D. Q., McKay, T., Munn, J. A., Nichol, R., Okamura, S., Schneider, D. P., Thakar, A. R., and York, D. G.: 2003, *AJ* **125**, 1849

Blain, A. W., Kneib, J.-P., Ivison, R. J., and Smail, I.: 1999, *ApJ* **512**, L87

Block, D. L. and Stockton, A.: 1991, *AJ* **102**, 1928

Blundell, K. M.: 2003, *New Astronomy Review* **47**, 593

Blundell, K. M., Beasley, A. J., Lacy, M., and Garrington, S. T.: 1996, *ApJ* **468**, L91+

Blundell, K. M. and Rawlings, S.: 2001, *ApJ* **562**, L5

Booth, R. S., Spencer, R. E., Stannard, D., and Baath, L. B.: 1979, *MNRAS* **188**, 159

Boroson, T. A. and Oke, J. B.: 1982, *Nature* **296**, 397

Bower, G. A., Green, R. F., Gebhardt, K., Bender, R., Kormendy, J., Lauer, T., Danks, A., Gull, T., Woodgate, B., Hutchings, J., Joseph, C., Kaiser, M. E., and Weistrop, D.: 1997, *Bulletin of the American Astronomical Society* **29**, 1293

Boyce, P. J., Disney, M. J., Blades, J. C., Boksenberg, A., Crane, P., Deharveng, J. M., Macchetto, F. D., Mackay, C. D., and Sparks, W. B.: 1998, *MNRAS* **298**, 121

Boyce, P. J., Disney, M. J., and Bleaken, D. G.: 1999, *MNRAS* **302**, L39

Boyle, B. J., Fong, R., Shanks, T., and Peterson, B. A.: 1990, *MNRAS* **243**, 1

Brandie, G. W. and Bridle, A. H.: 1974, *AJ* **79**, 903

Brinchmann, J., Abraham, R., Schade, D., Tresse, L., Ellis, R. S., Lilly, S., Le Fevre, O., Glazebrook, K., Hammer, F., Colless, M., Crampton, D., and Broadhurst, T.: 1998, *ApJ* **499**, 112

Bruzual A., G. and Charlot, S.: 1993, *ApJ* **405**, 538

Burbidge, G. and Hewitt, A.: 1987, *AJ* **93**, 1

Burbidge, G. R., Burbidge, E. M., and Sandage, A. R.: 1963, *Reviews of Modern Physics* **35**, 947

Bushouse, H. A., Borne, K. D., Colina, L., Lucas, R. A., Rowan-Robinson, M., Baker, A. C., Clements, D. L., Lawrence, A., and Oliver, S.: 2002, *ApJS* **138**, 1

Casti, J.: 1996, *Five Golden Rules*, Wiley

Chapman, S. C., Windhorst, R., Odewahn, S., Yan, H., and Conselice, C.: 2003, *ApJ* **599**, 92

Chiosi, C., Vallenari, A., and Bressan, A.: 1997, *A&AS* **121**, 301

Cirasuolo, M., Magliocchetti, M., Celotti, A., and Danese, L.: 2003, *MNRAS* **341**, 993

Clements, D. L.: 2000, *MNRAS* **311**, 833

Cohen, M. H. and Kundu, M. R.: 1966, *ApJ* **143**, 621

Crampin, J. and Hoyle, F.: 1961, *MNRAS* **122**, 27

Dallacasa, D., Bondi, M., Alef, W., and Mantovani, F.: 1998, *A&AS* **129**, 219

de Koff, S., Best, P., Baum, S. A., Sparks, W., Röttgering, H., Miley, G., Golombek, D., Macchetto, F., and Martel, A.: 2000, *ApJS* **129**, 33

de Vaucouleurs, G. and Capaccioli, M.: 1979, *ApJS* **40**, 699

Disney, M.: 1998, *Scientific American* pp 37+

Djorgovski, S. and Davis, M.: 1987, *ApJ* **313**, 59

Dressler, A., Lynden-Bell, D., Burstein, D., Davies, R. L., Faber, S. M., Terlevich, R., and Wegner, G.: 1987, *ApJ* **313**, 42

Dunlop, J. S.: 2001, *New Astronomy Review* **45**, 609

Dunlop, J. S., McLure, R. J., Kukula, M. J., Baum, S. A., O'Dea, C. P., and Hughes, D. H.: 2003, *MNRAS* **340**, 1095

Dunlop, J. S., Taylor, G. L., Hughes, D. H., and Robson, E. I.: 1993, *MNRAS* **264**, 455+

Efstathiou, G., Ellis, R. S., and Peterson, B. A.: 1988, *MNRAS* **232**, 431

Efstathiou, G. and Rees, M. J.: 1988, *MNRAS* **230**, 5P

Eisenhauer, F., Schödel, R., Genzel, R., Ott, T., Tecza, M., Abuter, R., Eckart, A., and Alexander, T.: 2003, *ApJ* **597**, L121

Faber, S. M.: 1982, in *Astrophysical Cosmology Proceedings*, pp 191–214

Faber, S. M. and Jackson, R. E.: 1976, *ApJ* **204**, 668

Fabian, A. C.: 1999, *MNRAS* **308**, L39

Fabian, A. C., Vaughan, S., Nandra, K., Iwasawa, K., Ballantyne, D. R., Lee, J. C., De Rosa, A., Turner, A., and Young, A. J.: 2002, *MNRAS* **335**, L1

Falcke, H., Malkan, M. A., and Biermann, P. L.: 1995, *A&A* **298**, 375

Falomo, R.: 1996, *MNRAS* **283**, 241

Falomo, R., Kotilainen, J., and Treves, A.: 2001, *ApJ* **547**, 124

Fanaroff, B. L. and Riley, J. M.: 1974, *MNRAS* **167**, 31P

Fanti, C., Fanti, R., Ficarra, A., Gregorini, L., Mantovani, F., and Padrielli, L.: 1983, *A&A* **118**, 171

Farrah, D., Rowan-Robinson, M., Oliver, S., Serjeant, S., Borne, K., Lawrence, A., Lucas, R. A., Bushouse, H., and Colina, L.: 2001, *MNRAS* **326**, 1333

Farrah, D., Verma, A., Oliver, S., Rowan-Robinson, M., and McMahon, R.: 2002, *MNRAS* **329**, 605

Fasano, G. and Franceschini, A.: 1987, *MNRAS* **225**, 155

Ferrarese, L. and Ford, H. C.: 1999, *ApJ* **515**, 583

Ferrarese, L., Ford, H. C., and Jaffe, W.: 1996, *ApJ* **470**, 444

Ferrarese, L. and Merritt, D.: 2000, *ApJ* **539**, L9

Ferrari, A.: 1998, *ARA&A* **36**, 539

Fomalont, E. B., Frey, S., Paragi, Z., Gurvits, L. I., Scott, W. K., Taylor, A. R., Edwards, P. G., and Hirabayashi, H.: 2000, *ApJS* **131**, 95

Ford, H. C., Tsvetanov, Z. I., Kriss, G. A., Harms, R., and Dressel, L.: 1994, *Bulletin of the American Astronomical Society* **26**, 966

Franceschini, A., Vercellone, S., and Fabian, A. C.: 1998, *MNRAS* **297**, 817

Freeman, K. C.: 1970, *ApJ* **160**, 811+

Garcia, M. R., McClintock, J. E., Narayan, R., Callanan, P., Barret, D., and Murray, S. S.: 2001, *ApJ* **553**, L47

Gebhardt, K., Bender, R., Bower, G., Dressler, A., Faber, S. M., Filippenko, A. V., Green, R., Grillmair, C., Ho, L. C., Kormendy, J., Lauer, T. R., Magorrian, J., Pinkney, J., Richstone, D., and Tremaine, S.: 2000, *ApJ* **539**, L13

Gebhardt, K., Richstone, D., Tremaine, S., Lauer, T. R., Bender, R., Bower, G., Dressler, A., Faber, S. M., Filippenko, A. V., Green, R., Grillmair, C., Ho, L. C., Kormendy, J., Magorrian, J., and Pinkney, J.: 2003, *ApJ* **583**, 92

Genzel, R., Eckart, A., Ott, T., and Eisenhauer, F.: 1997, *MNRAS* **291**, 219

Genzel, R., Tacconi, L. J., Rigopoulou, D., Lutz, D., and Tecza, M.: 2001, *ApJ* **563**, 527

Ghez, A. M., Duchêne, G., Matthews, K., Hornstein, S. D., Tanner, A., Larkin, J., Morris, M., Becklin, E. E., Salim, S., Kremenek, T., Thompson, D., Soifer, B. T., Neugebauer, G., and McLean, I.: 2003, *ApJ* **586**, L127

Goldschmidt, P., Kukula, M. J., Miller, L., and Dunlop, J. S.: 1999, *ApJ* **511**, 612

Goldschmidt, P., Miller, L., La Franca, F., and Cristiani, S.: 1992, *MNRAS* **256**, 65P

Granato, G. L., De Zotti, G., Silva, L., Bressan, A., and Danese, L.: 2004, *ApJ* **600**, 580

Green, R. F. and Yee, H. K. C.: 1984, *ApJS* **54**, 495

Gregory, P. C., Vavasour, J. D., Scott, W. K., and Condon, J. J.: 1994, *ApJS* **90**, 173

Guyon, O., Sanders, D. B., Stockton, A., Baudoz, P., and Potter, D.: 2001, in *American Astronomical Society Meeting*, Vol. 198, pp 8807+

Hamilton, T. S., Turnshek, D. A., and Casertano, S.: 2000, *American Astronomical Society Meeting* **197**, 0

Harms, R. J., Ford, H. C., Tsvetanov, Z. I., Hartig, G. F., Dressel, L. L., Kriss, G. A., Bohlin, R., Davidsen, A. F., Margon, B., and Kochhar, A. K.: 1994, *ApJ* **435**, L35

Hawarden, T. G., Leggett, S. K., Letawsky, M. B., Ballantyne, D. R., and Casali, M. M.: 2001, *MNRAS* **325**, 563

Heckman, T. M., Bothun, G. D., Balick, B., and Smith, E. P.: 1984, *AJ* **89**, 958

Hook, I. M., McMahon, R. G., Boyle, B. J., and Irwin, M. J.: 1994, *MNRAS* **268**, 305

Hooper, E. J., Impey, C. D., and Foltz, C. B.: 1997, *ApJ* **480**, L95

Hubble, E. P.: 1926, *ApJ* **64**, 321

Hughes, D. H., Kukula, M. J., Dunlop, J. S., and Boroson, T.: 2000, *MNRAS* **316**, 204

Hughes, D. H., Serjeant, S., Dunlop, J., Rowan-Robinson, M., Blain, A., Mann, R. G., Ivison, R., Peacock, J., Efstathiou, A., Gear, W., Oliver, S., Lawrence, A., Longair, M., Goldschmidt, P., and Jenness, T.: 1998, *Nature* **394**, 241

Hutchings, J. B.: 1987, *ApJ* **320**, 122

Hutchings, J. B., Frenette, D., Hanisch, R., Mo, J., Dumont, P. J., Redding, D. C., and Neff, S. G.: 2002, *AJ* **123**, 2936

Hutchings, J. B., Johnson, I., and Pyke, R.: 1988, *ApJS* **66**, 361

Hutchings, J. B. and Neff, S. G.: 1990, *AJ* **99**, 1715

Hutchings, J. B. and Neff, S. G.: 1991, *AJ* **101**, 2001

Hutchings, J. B. and Neff, S. G.: 1992, *AJ* **104**, 1

Ivison, R. J., Greve, T. R., Smail, I., Dunlop, J. S., Roche, N. D., Scott, S. E., Page, M. J., Stevens, J. A., Almaini, O., Blain, A. W., Willott, C. J., Fox, M. J., Gilbank, D. G., Serjeant, S., and Hughes, D. H.: 2002, *MNRAS* **337**, 1

Jackson, C. A. and Wall, J. V.: 1999, *MNRAS* **304**, 160

Jimenez, R., MacDonald, J., Dunlop, J. S., Padoan, P., and Peacock, J. A.: 2004, *MNRAS* in press

Jimenez, R., Thejll, P., Jorgensen, U. G., MacDonald, J., and Pagel, B.: 1996, *MNRAS* **282**, 926

Jørgensen, I., Franx, M., and Kjaergaard, P.: 1996, *MNRAS* **280**, 167

Jorgensen, U. G. and Jimenez, R.: 1997, *A&A* **317**, 54

Jorgensen, U. G. and Thejll, P.: 1993, *A&A* **272**, 255

Kauffmann, G. and Haehnelt, M.: 2000, *MNRAS* **311**, 576

Kormendy, J.: 1977, *ApJ* **217**, 406

Kormendy, J.: 2001, in *Carnegie Observatories Centennial Symposium I: Coevolution of Black Holes and Galaxies*, pp 363–+

Kormendy, J. and Gebhardt, K.: 2001, in *AIP Conf. Proc. 586: 20th Texas Symposium on relativistic astrophysics*, pp 363–+

Kormendy, J. and Richstone, D.: 1995, *ARA&A* **33**, 581

Kotilainen, J. K. and Falomo, R.: 2000, *A&A* **364**, 70

Krist, J.: 1999, *TinyTim User Manual*

Kristian, J.: 1973, *ApJ* **179**, L61

Kukula, M. J., Dunlop, J., Hughes, D., and Rawlings, S.: 1997, *Bulletin of the American Astronomical Society* **29**, 1373

Kukula, M. J., Dunlop, J. S., Hughes, D. H., and Rawlings, S.: 1998, *MNRAS* **297**, 366

Kukula, M. J., Dunlop, J. S., McLure, R. J., Baum, S. A., O'Dea, C. P., and Hughes, D. H.: 1999, *Advances in Space Research* **23**, 1131

Kukula, M. J., Dunlop, J. S., McLure, R. J., Miller, L., Percival, W. J., Baum, S. A., and O'Dea, C. P.: 2001, *MNRAS* **326**, 1533

Lawrence, A., Rowan-Robinson, M., Leech, K., Jones, D. H. P., and Wall, J. V.: 1989, *MNRAS* **240**, 329

Lehnert, M. D., van Breugel, W. J. M., Heckman, T. M., and Miley, G. K.: 1999, *ApJS* **124**, 11

Lim, J., Leon, S., Combes, F., and Trung, D. V.: 2000, *ApJ* **545**, L93

Lima Neto, G. B., Gerbal, D., and Márquez, I.: 1999, *MNRAS* **309**, 481

Lynden-Bell, D.: 1969, *Nature* **223**, 690

Márquez, I., Petitjean, P., Théodore, B., Bremer, M., Monnet, G., and Beuzit, J.-L.: 2001, *A&A* **371**, 97

Macchetto, F., Marconi, A., Axon, D. J., Capetti, A., Sparks, W., and Crane, P.: 1997, *ApJ* **489**, 579

Magorrian, J., Tremaine, S., Richstone, D., Bender, R., Bower, G., Dressler, A., Faber, S. M., Gebhardt, K., Green, R., Grillmair, C., Kormendy, J., and Lauer, T.: 1998, *AJ* **115**, 2285

Malkan, M. A.: 1984, *ApJ* **287**, 555

Marconi, A., Axon, D. J., Macchetto, F. D., Capetti, A., Soarks, W. B., and Crane, P.: 1997, *MNRAS* **289**, L21

Marconi, A., Capetti, A., Axon, D. J., Koekemoer, A., Macchetto, D., and Schreier, E. J.: 2001, *ApJ* **549**, 915

Marconi, A. and Hunt, L. K.: 2003, *ApJ* **589**, L21

Matthews, T. A. and Sandage, A. R.: 1963, *ApJ* **138**, 30

McLeod, K. K. and McLeod, B. A.: 2001, *ApJ* **546**, 782

McLeod, K. K. and Rieke, G. H.: 1994a, *ApJ* **420**, 58

McLeod, K. K. and Rieke, G. H.: 1994b, *ApJ* **431**, 137

McLeod, K. K. and Rieke, G. H.: 1995, *ApJ* **454**, L77

McLeod, K. K., Rieke, G. H., and Storrie-Lombardi, L. J.: 1999, *ApJ* **511**, L67

McLure, R. J.: 1999, *Ph.D. thesis*, Institute for Astronomy, University of Edinburgh

McLure, R. J. and Dunlop, J. S.: 2002, *MNRAS* **331**, 795

McLure, R. J., Dunlop, J. S., and Kukula, M. J.: 2000, *MNRAS* **318**, 693

McLure, R. J., Kukula, M. J., Dunlop, J. S., Baum, S. A., O'Dea, C. P., and Hughes, D. H.: 1999, *MNRAS* **308**, 377

Melia, F. and Falcke, H.: 2001, *ARA&A* **39**, 309

Merritt, D. and Ferrarese, L.: 2001, *MNRAS* **320**, L30

Miller, C. J., Nichol, R. C., Gómez, P. L., Hopkins, A. M., and Bernardi, M.: 2003, *ApJ* **597**, 142

Miller, L., Peacock, J. A., and Mead, A. R. G.: 1990, *MNRAS* **244**, 207

Miyoshi, M., Moran, J., Herrnstein, J., Greenhill, L., Nakai, N., Diamond, P., and Inoue, M.: 1995, *Nature* **373**, 127

Mobasher, B., Sharples, R. M., and Ellis, R. S.: 1993, *MNRAS* **263**, 560

Mushotzky, R. F., Done, C., and Pounds, K. A.: 1993, *ARA&A* **31**, 717

Naab, T. and Burkert, A.: 1999, in *Astronomische Gesellschaft Meeting Abstracts*, Vol. 15, pp 11–+

Nelson, C. H.: 2000, *ApJ* **544**, L91

Nelson, C. H. and Whittle, M.: 1995, *ApJS* **99**, 67

Nolan, L. A., Dunlop, J. S., Kukula, M. J., Hughes, D. H., Boroson, T., and Jimenez, R.: 2001, *MNRAS* **323**, 308

Osterbrock, D. E.: 1981, *ApJ* **249**, 462

Peacock, J. A.: 1983, *MNRAS* **202**, 615

Peacock, J. A.: 1999, *Cosmological Physics*, CUP

Percival, W. J., Miller, L., McLure, R. J., and Dunlop, J. S.: 2001, *MNRAS* **322**, 843

Pesce, J. E., Falomo, R., and Treves, A.: 1994, *AJ* **107**, 494

Peterson, B. M.: 1997, *An introduction to active galactic nuclei*, CUP

Peterson, B. M., Craine, E. R., and Strittmatter, P. A.: 1978, *PASP* **90**, 386

Press, W. H., Teukolsky, S. A., Vetterling, W. T., and Flannery, B. P.: 1992, *Numerical recipes in FORTRAN. The art of scientific computing*, Cambridge: University Press, —c1992, 2nd ed.

Price, R., Gower, A. C., Hutchings, J. B., Talon, S., Duncan, D., and Ross, G.: 1993, *ApJS* **86**, 365

Puchnarewicz, E. M., Mason, K. O., Cordova, F. A., Kartje, J., Brabduardi, A. A., Puchnarewicz, E. M., Mason, K. O., Cordova, F. A., Kartje, J., Branduardi-Raymont, G., Mittaz, J. P. D., Murdin, P. G., and Allington-Smith, J.: 1992, *MNRAS* **256**, 589

Rees, M. J.: 1998, in *Black Holes and Relativistic Stars*, pp 79–+

Reimers, D., Hopp, U., Clavel, J., Chini, R., Dahlem, M., Engels, D., Fink, H., Hagen, H. ., Heber, U., Schramm, K. ., Wamsteker, W., and Wisotzki, L.: 1995, *A&A* **303**, 449+

Ridgway, S. E., Heckman, T. M., Calzetti, D., and Lehnert, M.: 2001, *ApJ* **550**, 122

Robson, I.: 1996, *Active galactic nuclei*, Wiley-Praxis Series in Astronomy and Astrophysics, New York, NY: Wiley, Chichester: Praxis Publishing, —c1996

Roche, P. F., a.: 2002, in *Instrument Design and Performance for Optical/IR Ground-Based Telescopes. Edited by Iye, M.; Moorwood, A. F. Proceedings of the SPIE, Volume 4841*

Sanders, D. B., Soifer, B. T., Elias, J. H., Madore, B. F., Matthews, K., Neugebauer, G., and Scoville, N. Z.: 1988, *ApJ* **325**, 74

Schade, D. J., Boyle, B. J., and Letawsky, M.: 2000, *MNRAS* **315**, 498

Schmidt, M.: 1963, *Nature* **197**, 1040

Schwarzschild, M.: 1979, *ApJ* **232**, 236

Scoville, N. Z., Evans, A. S., Thompson, R., Rieke, M., Hines, D. C., Low, F. J., Dinshaw, N., Surace, J. A., and Armus, L.: 2000, *AJ* **119**, 991

Sersic, J. L.: 1968, in *Atlas de Galaxes Australes; Vol. Book; Page 1*, pp 0+

Seyfert, C. K.: 1943, *ApJ* **97**, 28

Shaver, P. A., Wall, J. V., Kellermann, K. I., Jackson, C. A., and Hawkins, M. R. S.: 1996, *Nature* **384**, 439

Silk, J. and Rees, M. J.: 1998, *A&A* **331**, L1

Sitko, M. L., Schmidt, G. D., and Stein, W. A.: 1985, *ApJS* **59**, 323

Smith, E. P., Heckman, T. M., Bothun, G. D., Romanishin, W., and Balick, B.: 1986, *ApJ* **306**, 64

Smith, H. E. and Spinrad, H.: 1980, *ApJ* **236**, 419

Smith, P. S., Balonek, T. J., Elston, R., and Heckert, P. A.: 1987, *ApJS* **64**, 459

Stanghellini, C., O'Dea, C. P., Dallacasa, D., Baum, S. A., Fanti, R., and Fanti, C.: 1998, *A&AS* **131**, 303

Steidel, C. C., Adelberger, K. L., Giavalisco, M., Dickinson, M., and Pettini, M.: 1999, *ApJ* **519**, 1

Stickel, M. and Kuhr, H.: 1993, *A&AS* **101**, 521

Stickel, M., Meisenheimer, K., and Kuehr, H.: 1994, *A&AS* **105**, 211

Stickel, M., Rieke, G. H., Kuehr, H., and Rieke, M. J.: 1996, *ApJ* **468**, 556

Stockton, A. and Ridgway, S. E.: 2001, *ApJ* **554**, 1012

Tadhunter, C., Marconi, A., Axon, D., K., W., Robinson, T. G., and Jackson, N.: 2003, *MNRAS*

Tanaka, Y., Nandra, K., Fabian, A. C., Inoue, H., Otani, C., Dotani, T., Hayashida, K., Iwasawa, K., Kii, T., Kunieda, H., Makino, F., and Matsuoka, M.: 1995, *Nature* **375**, 659

Taylor, G. L., Dunlop, J. S., Hughes, D. H., and Robson, E. I.: 1996, *MNRAS* **283**, 930

Thomas, P. A., Webster, R. L., and Drinkwater, M. J.: 1995, *MNRAS* **273**, 1069

Tinsley, B. M. and Gunn, J. E.: 1976, *ApJ* **203**, 52

Tully, R. B. and Fisher, J. R.: 1977, *A&A* **54**, 661

Urry, C. M. and Padovani, P.: 1995, *PASP* **107**, 803

van der Marel, R. P., Gerssen, J., Guhathakurta, P., Peterson, R. C., and Gebhardt, K.: 2002, *AJ* **124**, 3255

Verdoes Kleijn, G. A., Baum, S. A., de Zeeuw, P. T., and O'Dea, C. P.: 1999, *AJ* **118**, 2592

Veron, M. P.: 1971, *A&A* **11**, 1

Veron-Cetty, M. . and Woltjer, L.: 1990, *A&A* **236**, 69

Veron-Cetty, M.-P. and Veron, P.: 1993a, *A Catalogue of quasars and active nuclei*, ESO Scientific Report, Garching: European Southern Observatory (ESO), —c1993, 6th ed.

Veron-Cetty, M.-P. and Veron, P.: 1993b, *A&AS* **100**, 521

Veron-Cetty, M.-P. and Veron, P.: 2000, *A catalogue of quasars and active nuclei*, A catalogue of quasars and active nuclei / M.-P. Veron-Cetty and P. Veron. Garching bei Munchen, Germany : European Southern Observatory, c2000. (Scientific report (European Southern Observatory) ; no. 19)

Voges, W., Aschenbach, B., Boller, T., Bräuninger, H., Briel, U., and Burkert, W.: 1999, *A&A* **349**, 389

Wilkes, B. J., Tananbaum, H., Worrall, D. M., Avni, Y., Oey, M. S., and Flanagan, J.: 1994, *ApJS* **92**, 53

Wills, B. J., Brandt, W. N., and Laor, A.: 1999, *ApJ* **520**, L91

Wright, S. C., McHardy, I. M., and Abraham, R. G.: 1998, *MNRAS* **295**, 799

Wyckoff, S., Gehren, T., and Wehinger, P. A.: 1981, *ApJ* **247**, 750

Xia, X.-Y., Mao, S., Wu, H., Zheng, Z., Boller, T., Deng, Z.-G., and Zou, Z.-L.: 1999, *A&A* **341**, L13

Yee, H. K. C. and Green, R. F.: 1987, *ApJ* **319**, 28

Young, P. J., Westphal, J. A., Kristian, J., Wilson, C. P., and Landauer, F. P.: 1978, *ApJ* **221**, 721

Zel'dovich, Y. B. and Novikov, I. D.: 1964, *Sov. Phys. Dokl.* **158**, 811

Zheng, Z., Wu, H., Mao, S., Xia, X.-Y., Deng, Z.-G., and Zou, Z.-L.: 1999, *A&A* **349**, 735